

European Commission

technical steel research

Steel products and applications for building, construction and industry

Natural fire safety concept – The development and validation of a CFD-based engineering methodology for evaluating thermal action on steel and composite structures

S. Kumar, S. Welch, S. Miles

BRE

Bucknalls Lane, Garston, Watford WD25 9XX, United Kingdom

L.-G. Cajot, M. Haller

ProfilArbed

66, rue de Luxembourg, L-4009 Esch/Alzette

M. Ojanguren, J. Barco

LABEIN

Cuesta de Olabeaga 16, Apartado 1234, E-48013 Bilbao

S. Hostikka

VTT

PO Box 1807, FIN-02044 Espoo

U. Max, A. Röhrle

Arbeitsgemeinschaft Brandsicherheit AGB

Au in den Buchen 90, D-76646 Bruchsal

Contract No 7210-PR/184
1 July 1999 to 31 December 2002

Final report

Directorate-General for Research

LEGAL NOTICE

Neither the European Commission nor any person acting on behalf of the Commission is responsible for the use which might be made of the following information.

***Europe Direct is a service to help you find answers
to your questions about the European Union***

**Freephone number (*):
00 800 6 7 8 9 10 11**

(*) Certain mobile telephone operators do not allow access to 00 800 numbers or these calls may be billed.

A great deal of additional information on the European Union is available on the Internet. It can be accessed through the Europa server (<http://europa.eu.int>).

Cataloguing data can be found at the end of this publication.

Luxembourg: Office for Official Publications of the European Communities, 2005

ISBN 92-894-9594-4

© European Communities, 2005
Reproduction is authorised provided the source is acknowledged.

Printed in Luxembourg

PRINTED ON WHITE CHLORINE-FREE PAPER

FINAL SUMMARY

Objectives of the project

The objective of the project was to develop an engineering methodology, exploiting the advanced capabilities of computational fluid dynamics (CFD), for determining the thermal behaviour of structural elements in steel/composite-framed buildings. Specific objectives of the project were as follows:

- To develop a verified and validated CFD-based engineering methodology for simulating the thermal action on steel/composite structures,
- To apply the methodology for evaluating the effect of fire loading, ventilation and compartment construction on the thermal action on steel/composite structures,
- To identify the essential elements of the methodology developed and provide guidance on its 'correct' use, i.e. defining the range of applicability and the sensitivity to various input parameters,
- To apply the model for the assessment of the calibration and sensitivity of empirical design parameters, such as the convective heat transfer coefficient and empirical parameters used in the design guides (Eurocodes EC1 and EC3).
- To contribute to the development of the design guides.

Annex 1 (the 'Technical Annex') includes further information and technical details.

Comparison of planned activities and work accomplished

This section summarises any major deviations from the initial work content and their effects on the project.

Due to some delays incurred in the completion of work package 2 associated with the technical work, the lead partner wrote to the Commission requesting a 6-month extension to the project.

On behalf of the Commission, Mr André Boucart (chair of the F6 committee) wrote the relevant Justification Note and supported the extension of the project. Commission Amendment No 1 to ECSC contract 7210-PR-104 was received from DG Budget in a letter of 18/03/02 which was subsequently signed and authenticated by the authorised representatives of each of the contracting parties.

Other than this, and the initial delay in formally starting the project, the contract was conformed to in its entirety.

Description of activities and discussion

This section describes the project activities and the capabilities of the methodology developed in the work, giving an idea of how it can contribute to fire safety engineering guidance and ultimately to improved efficiency and safety in structural fire design.

1. Model development

A multi-block solver to model heat conduction through composite solids was incorporated in the SOFIE CFD code. This has been written to deal specifically with structural elements such as I-beams and columns, where the standard structured grid cannot adequately resolve the flange and web for heat transfer calculations. The three-dimensional conduction equation is solved on a fine grid, where in each Cartesian direction there may be typically 10 to 100 grid points for every gas-phase grid point.

The composite solid solver is called at the end of each main (CFD) time-step, or after multiples thereof. The surface fluxes from the CFD solution are mapped onto the finer solid mesh to provide the boundary conditions for the solution of the conduction equation inside the solid. The temperature field inside the composite solid is advanced from the previous CFD time level to the current time level using an independent solid solver time-step ($\Delta\tau$) that can be defined by the user. Although this time-step can be less than the CFD one, there is no advantage in making it too small since the accuracy of the solution is still limited to some degree by the fact that the CFD-solid boundary condition information is updated only at the end of each CFD time-step.

The composite solid solver algorithm is a “multi-block” procedure, in that each composite solid is treated as a set of rectangular blocks in which the heat conduction is solved locally. At the end of each solid solver time step ($\Delta\tau$) the boundary conditions at the composite block interfaces are updated (a mixture of temperature and flux values).

At the start of the next CFD timestep the face temperatures from the composite solid solver are mapped back to the CFD grid to provide the appropriate temperature boundary conditions for the next computation of the CFD gas-phase flow and radiation solvers. From the perspective of these solvers the composite solids are isothermal blockages, with the additional feature that the temperature values are updated at the end of each time-step.

The solver has been made accessible via the graphical user interface JOSEFINE to allow users to easily set up structural elements such as I-beams and columns, with and without protection. Temperature dependent thermal properties can be defined for both the structural members themselves (normally steel) and also the protection materials. In the latter case, the effects of moisture and intumescence can be accommodated via corrections to the relevant thermal properties.

2. Model validation

This task consisted of a progressive model verification exercise, in which the engineering methodology developed for the project (above) was applied, systematically and extensively, by all partners to simulation of real fire tests. Supporting calculations were undertaken with the OZone and MRFC zone models, and other techniques.

The main fire tests simulated fall into three categories - a localised beam fire test, fire-resistance furnace tests and full-scale fire tests in compartments, involving both experimental and natural fires. The latter case relates to data to be obtained in the fire tests carried out under ECSC Research Project - Natural Fire Safety Concept (NFSC2).

In detailed studies of heat transfer to a single steel beam exposed to a localised fire reasonable agreements between predictions and experiment were eventually achieved. Sensitivities to the details of the radiation model implementation were found to be relatively low and the main influence on the computed flux distributions was attributed to the resolution of the numerical grid. The SOFIE code also

reproduced reasonably well both the gas-phase combustion and heat transfer and the solid-phase thermal characteristics of the fire-resistance furnace test.

The CFD models reproduced the large room results very reasonably, with an excellent match of doorway velocities and only a slight overprediction of temperature; the latter effect is associated with inaccuracies in the computation of conjugate heat transfer into the enclosure boundaries when using relatively large grid cells. The zone models also reproduced the fire dynamics very reasonably, though the hot layer temperatures were on the high side with MRFC. The differences between the OZone and MRFC results could not be fully reconciled, but part of the discrepancy apparently stems from differences in treatment of wall heat transfer.

For the BRE large compartment fire tests, pre-processing of experimental data was required and considerable effort was made to determine the best possible representation of the heat release rate curve, considering the simultaneous burning of two different types of fuel. Progressive burn-out of combustibles from front to rear of the compartment was also accommodated in the fire source definition. Extensive grid resolution sensitivity studies were undertaken together with examinations of the effect of other numerical and physical model choices. Again, overall, realistic results were obtained for the thermal flowfield but with generally slight overprediction of gas temperatures; as for the large room tests, this effect is probably mainly to do with weakness in description of the heat loss to and within the main enclosure boundaries when relatively large computational cells must be used.

3. Analysis and review

This task concerned the “Analysis and review” of the results.

3.1 Supplementary cases of model application

A hypothetical scenario involving car fires in the underground car parks was considered of interest to the steel industry. A further very relevant case concerning the external column fire tests performed by CTICM was also identified and studied carefully.

3.2 Results analysis: equivalent parameter values

One of the specific objectives of the project concerned application of the CFD-based methodology developed to the assessment of some of the parameters adopted in the design codes (e.g. EC1 and EC3). At the time of drafting the proposal, this objective reflected the current state of development of the draft version of that document (i.e. EC1 Part 2.2, 1996), stating:

- To apply the model for the assessment of the calibration and sensitivity of empirical design parameters, such as the convective heat transfer coefficient and safety factors used in the design guides (Eurocodes EC1 and EC3).

The project partners re-examined the relevant draft Eurocodes at the project meeting in November 2001. It was noted that no reference was now made to the "safety factors" mentioned in the earlier draft, and that the fundamental part of the "actions for temperature analysis (thermal actions)" guidance now consisted of the following set of heat transfer equations¹ (c.f. equ. 3.1 to 3.3 in EC1 Part 1.2):

$$\dot{h}_{net}^{\&} = \dot{h}_{net,c}^{\&} + \dot{h}_{net,r}^{\&} \quad (1)$$

$$\dot{h}_{net,c}^{\&} = \alpha (\theta_g - \theta_m) \quad (2)$$

$$\dot{h}_{net,r}^{\&} = \Phi \epsilon_m \sigma ((\theta_r + 273)^4 - (\theta_m + 273)^4) \quad (3)$$

¹ It was subsequently noted that the definitions changed again in the final draft of EC 1 Part 1.2 (Stage 49 10 January 2002) with reintroduction of a factor for emissivity of the fire into equation (3); however, this value is to be taken as unity so can effectively be ignored.

Following careful examination, it was agreed that the main parameters of relevance in the current project could now be defined as:

- convective heat transfer coefficient, α (c.f. equ. 2)
- configuration factor, Φ , used in the radiation equation (c.f. equ. 3); this parameter is in turn a function of the fire development/exposure history, which itself depends on factors such as the fire load, compartment geometry, protection material etc.
- the effective radiative temperature, θ_r , (assumed in EC1 to equal the gas temperature)

The latter two parameters are interrelated and are not easily decoupled.

Therefore, in order to make comparisons between the results obtained from the CFD-based methodology and some of the simpler methods available in the design guidance, it is necessary to extract from the CFD results the values of some relevant "equivalent parameters". The information generally required by simpler models includes the value of the convective heat flux, and the effective radiation temperature or flux.

In order to facilitate analysis of these parameters, the JOSEFINE post-processor was developed to permit extraction of surface values of convective heat transfer coefficient, temperature and heat fluxes. Coding was also written for the determination of an effective "radiative temperature", derived from the total radiative flux parameter. This former parameter, a field variable, is a measure of the effective temperature of radiation which can be seen from any point in space and is derived simply from the relationship, with the emissivity being taken as unity:

$$T_{rad} = \left(\frac{\dot{h}_{rad}}{\sigma} \right)^{1/4} \tag{4}$$

where: \dot{h}_{rad} is the total flux arriving at any point in space (i.e. at each grid cell)
 σ is the Stefan-Boltzmann constant [$5.67 \times 10^{-8} \text{ W/m}^2/\text{K}^4$]

The important thing to note about this temperature parameter is that it implicitly includes the spatial/angular dependence of the emissivity and configuration factors (embedded within \dot{h}_{rad}).

Using the above tools, detailed conclusions were drawn concerning the values and distributions of the main parameters of interest, i.e. the convective heat transfer coefficient, the various emissivities, including both "fire" and "member" emissivities, the configuration factor, the effective radiative temperature and flux and finally the general form of the governing heat exchange equations which draw all of these factors together. For example, summary data on convective heat transfer coefficients (in $\text{W/m}^2/\text{K}$) for certain scenarios, considering the contributions of all exposed surfaces, are as follows:

Scenario	Minimum	Maximum	Overall average
BRI localised beam fire	3.0	25	4.0
VTT scale fire-resistance furnace (column)	5.0	33	12
Standard fire-resistance furnace (wall)	4.5	7.5	6.0
VTT room – test 8	2.5	11	5.9
BRE large compartment – test 6	3.1	14	6.6
BRE large compartment – test 8	2.1	14	5.3

Table 1 – summary values on convective heat transfer coefficient for selected test cases

The averaged values for plane walls are fairly consistent at around $6 \text{ W/m}^2/\text{K}$. Where there are direct impingement flows, in the localised beam fire and the scale furnace, higher values are found.

Results for other parameters are summarised below in section 4 and described in more detail in Appendix F.

3.3 Results analysis: critical design parameters

Detailed assessment of the results for the purpose of identifying the critical design parameters affecting the thermal action on the steel/composite structures was undertaken. Results from these studies are presented below together with the assessment of the impact of the results.

The utility of the model for optimisation of the location of structural steelwork was noted in this application – specifically via prediction of the radiative temperature and flux fields which can provide a good idea of the thermal attack on a specific structural member.

4. Implications of the results – impact assessment on the Eurocodes

4.1 Review of Eurocodes methodology

A review was undertaken of the simplified models in the Eurocodes. This highlighted a number of areas where input from more detailed/advanced models could be profitably exploited, as described in the next section.

4.2 Recommendations and extension to Eurocodes methodology

Recommendations - simplified models

Recommendations have been prepared covering the treatments of a range of relevant parameters in the simpler Eurocodes methodologies. The main parameters of interest are the convective heat transfer coefficient, the various emissivities, including both “fire” and “member” emissivities, the configuration factor, the effective radiative temperature/flux and finally the general form of the governing heat exchange equations which draw all of these factors together. Summary information is presented below and justification and further explanation can be found in Appendix F.

Convective heat transfer coefficient

Structural member

- Conservative value is high
- 35 W/m²/K is a reasonable maximum value for “natural fire”
- This may apply in impingement zone
- Lower value might be supported by fundamentally-based modelling, e.g. CFD

Enclosure boundaries

- Conservative value is low (if used for zone model)
- 5-10 W/m²/K is typical value for "natural fire"
- 4 W/m²/K is a reasonable minimum value for “natural fire”
- Adiabatic boundary (no convective heat transfer) is a still more conservative limit

Emissivities

- Fire (ϵ_f) and member (ϵ_m) emissivities should be distinguished
- ϵ_f can be approximated as function of path length (L), stoichiometry (η) and soot yield:

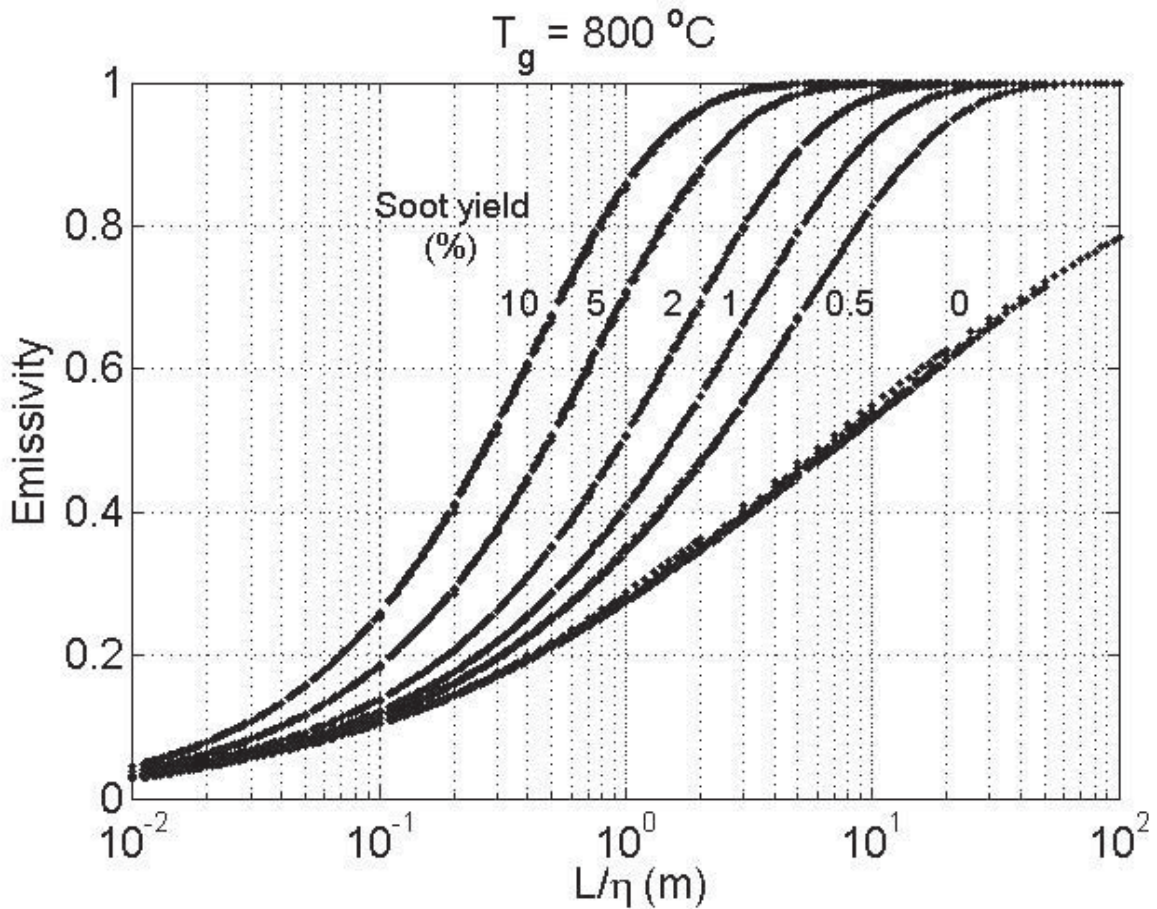


Figure 1 – fire gas emissivity dependence on path length (L), stoichiometry (η) and soot yield

- A conservative value of ϵ_f is unity
- A conservative value of ϵ_m is unity
- More precise values of ϵ_m can be used but value may tend to unity under fire conditions due to smoke deposition

Configuration factor

- A value of unity is generally applicable when member is fully engulfed
- In localised fire the “position effect” gives lower values
 - assumes no impingement
 - orientation must also be considered
 - shielding must be considered in non-convex objects

Heat transfer equations

The radiative transfer equation is more exactly written:

$$\dot{h}_{net,r} = \Phi_f \epsilon_m \epsilon_f \sigma T_f^4 + (1 - \Phi_f) \epsilon_m \epsilon_a \sigma T_a^4 - \epsilon_m \sigma T_m^4 \quad (5)$$

For typical fire conditions, use of the Eurocode equation:

$$\dot{h}_{net,r} = \Phi \epsilon_m \epsilon_f \sigma (T_r^4 - T_m^4) \quad (6)$$

can introduce errors >10% with the following parameter values:

$\Phi_f = 0.1$	$T_f = 900\text{ }^\circ\text{C}$
$\varepsilon_f = 1$	$T_m = 100\text{ }^\circ\text{C}$
$\varepsilon_a = 1$	$T_a = 20\text{ }^\circ\text{C}$

1. Configuration factor, Φ_f , <0.1
2. Fire emissivity, ε_f , <0.5
3. Fire temperature, T_f , $< 750^\circ\text{C}$
4. Member temperature, T_m , $> 300^\circ\text{C}$
5. Ambient temperature, T_a , $> 150^\circ\text{C}$

Of these, condition 4 is potentially most serious.

Effective radiation temperature/flux

- Thermal severity can be mapped by “effective radiative flux”
- An effective radiation temperature can also be derived from the radiative flux:

$$T_{rad} = \left(\frac{\dot{q}_{rad}}{\sigma} \right)^{1/4} \quad (7)$$

- Latter is closely related to thermocouple temperature in radiation-dominated flows
- Both parameters implicitly include spatial/angular dependence of gas emissivity and configuration factor

Recommendations - CFD models

A further set of recommendations have been developed as draft “best practice” guidance for the engineering methodology developed within the current project. These extend to:

- scope - area of application, e.g. localised fire, or post-flashover fire; requirements and applicability, e.g. domain size/computational limits/cell size/accuracy balance; transient versus pseudo “steady-state” and distributed burning;
- fire/structural specific issues, such as smoke, high-temperature material properties, moisture/intumescence effects, ventilation control, fuel chemistry, etc.;
- detailed guidance on the use of CFD codes from the practitioner’s point of view, covering the determination of conservative bounds on solutions (e.g. by assuming adiabatic boundaries), choice of physical models, numerical modelling issues, guidance on the modelling process as a procedure, including sensitivity studies etc., and validation work.

5. Information dissemination

Dissemination of the project work and results has included authoring of various articles for publications with wide building industry circulation and publicity via the project website (<http://projects.bre.co.uk/frsdiv/ecsc/>).

Conclusions

- A robust CFD-based engineering modelling methodology has been developed for evaluating thermal action on steel and composite structures. The methodology has been validated by using a systematic approach of progressive verification and validation, starting with simple fire scenarios and proceeding to more complex applications.
- To ensure reliability and robustness of the methodology, every partner has contributed to the model verification and validation exercise and have managed to reproduce reasonably satisfactorily the results for each scenario. Partners have used both the main CFD-based methodology and supporting calculations from the OZone and MRFC zone models and other techniques.
- Detailed studies of heat transfer to a single steel beam were performed using CFD codes, with some supporting analyses using other methods. Reasonable agreements between predictions and experiment were eventually achieved. Sensitivities to the details of the radiation model implementation were found to be relatively low and the main influence on the computed flux distributions was attributed to the resolution of the numerical grid.
- The SOFIE code reproduced reasonably well the gas-phase and solid-phase thermal and chemical characteristics of the fire-resistance furnace tests.
- For the large room test case, the OZone zone model was shown to reproduce the fire dynamics very reasonably, whilst the MRFC zone model was shown to reproduce reasonably well the interface height of the hot gas layer and to provide conservative estimates of the hot layer temperature.
- The differences between the OZone and MRFC results were carefully examined. It seems that whilst they could not be fully reconciled, part of the discrepancy stems from differences in treatment of wall heat transfer.
- The CFD models also reproduced the large room results reasonably well, with an excellent match of doorway velocities and only a slight overprediction of temperature; the latter effect is associated with inaccuracies in the computation of conjugate heat transfer into the wall when using relatively large grid cells.
- The BRE large compartment fire tests were the most challenging test of CFD validation simulation. For this case, pre-processing of test data was required and considerable effort was made to determine the best possible representation of the heat release rate considering the simultaneous burning of two different types of fuel. Progressive burn-out of combustibles from front to rear of the compartment was also accommodated in the fire source definition.
- Realistic results were obtained for the thermal flowfield but with generally slight overprediction of gas temperatures; again, this effect is probably mainly to do with weakness in description of the heat loss to the boundaries when relatively large computational cells are used in the wall. Extensive grid resolution sensitivity studies were undertaken.
- The utility of the model for optimisation of the location of structural steelwork was noted in this application – specifically via prediction of the radiative temperature and flux fields which can provide a good idea of the thermal insult on a structural member.
- In each validation case it is noted that the performance of the modelling methodology should be viewed within the constraints of the experimental data (e.g., accuracy of the fire growth curve using mass loss measurements, gas temperature measurements using thick unshielded thermocouples, etc.).
- The project has examined the values and distributions of the main parameters of interest, i.e., the convective heat transfer coefficient, the various emissivities, including both “fire” and “member”

emissivities, the configuration factor, the effective radiative flux and finally the general form of the governing heat exchange equations which draw all of these factors together.

- Results obtained for effective model parameters have proved useful in assessing the robustness and range of validity of simpler heat transfer models, such as those embodied in the structural Eurocodes. The radiative temperature parameter was earlier shown to provide an interesting insight into the way the thermal conditions imposed by a fire flowfield might influence temperature development in structural components. This is achieved by effectively decoupling the complicating effects of radiative loss from such a member, which is a function of the member's temperature and hence the way it responds to a particular heating regime.
- A study of the Eurocodes radiative heat transfer analysis has determined the sensitivities of the simple model; the results show clearly that, in some situations, the theoretical ambiguities of the basic governing heat transfer equation, and its definition, may lead to considerable errors in the calculated heat flux.
- A study of the fire emissivity parameter with respect to its dependence on path length, soot concentration and fire/ambient temperatures has resulted in a useful generalised chart which can be used both to examine parametric sensitivities and as a lookup to obtain specific values.
- By use of the methodology developed, design efficiencies can be achieved whilst maintaining or improving levels of safety. Adoption of such intelligent and targeted design approaches naturally leads to a reduction of waste and conservation of natural resources.

Assessment of exploitation and impact of the research results

The technical and economic potential for the use of the results

There is great technical potential for use of the methodology developed in this work. In application to fire safety engineering design, a simulation tool which is sufficiently well-validated can be used to provide a scientifically-robust and reliable methodology for performance-based fire safety design and hazard analysis. Considering the typical costs of fire protection materials the potential economic savings are also large, as has already been proven in related areas, for example in application of fire safety engineering methods in smoke ventilation design (SHEVS).

Actual practical applications

Project partners have already used the methodology both in other relevant research projects and in ordinary engineering consultancy. The former includes use by ProfilARBED for the project on “Development of design rules for the fire behaviour of external steel structures”, funded by the ECSC (7210-PR-380), and the latter includes fire design of a sports centre undertaken by partner LABEIN.

A list of patents applied for or of filed patents

IPR was defined as follows:

- (a) Improved version of SOFIE (CFD software), including STELA solid solver, and JOSEFINE (graphical user interface for fire engineering).
- (b) Design rules for the use of CFD software.

Publications and conference presentations resulting from the project

- "Fire Simulation using Computational Fluid Dynamics", Finnish Steel Construction Magazine, vol. 4/2002, The Finnish Constructional Steelwork Association, 2002.
- “CFD for fire design”, Building Services Journal, February 2003
- “CFD for fire design”, in Constructing the future, BRE quarterly digest, Issue 16, Spring 2003

Further publications are being prepared.

Other aspects concerning dissemination of results

The project website (at <http://projects.bre.co.uk/FRSdiv/ecsc/>) has had a steady stream of visitors during the duration of the project, averaging 3 per day.

Nomenclature

A	-	area [m ²]
a_e	-	effective mean absorption coefficient [-]
$a_{k,b}$	-	absorption coefficient for grey gas band b [-]
c	-	concentration [kg/m ³]
C_μ	-	coefficient of turbulent viscosity [-]
c_p	-	specific heat capacity [J/kg/K]
D	-	cylinder diameter [m]
	-	doorway temperature measurement location [-]
	-	fire diameter [m]
d_{wire}	-	thermocouple wire diameter [m]
g	-	acceleration due to gravity [m/s ²]
G	-	predicted thermocouple temperature [°C]
\dot{q}	-	heat flux [W/m ² /K]
h	-	height [m]
h_{eq}	-	weighted average of window heights on all walls [m]
H	-	height [m]
i	-	radiative intensity [W/m ²]
K	-	thermal diffusivity [m ² /s]
k	-	thermal conductivity [W/m/K]
$k_{g,b}$	-	combustion products absorption constant for band b [-]
$k_{g,s}$	-	soot absorption constant for band b [-]
l	-	local path length [m]
L	-	path length [m]
m	-	mass [kg]
m_s	-	surface mass flux [kg/m ² /s]
\dot{m}	-	mass loss rate [kg/s]
Nu	-	Nusselt number (hx/k) (dimensionless heat transfer coefficient) [-]
O	-	opening factor ($A_v\sqrt{h_{eq}}/A_t$) [m ^{1/2}]
p	-	pressure [N/m ²]
p_0	-	reference pressure [N/m ²]
p_{cp}	-	partial pressure of the combustion products [N/m ²]
p_{floor}	-	reference pressure at the height of the floor [N/m ²]
Pr	-	Prandtl number ($\mu c_p/k$) (kinematic viscosity/thermal diffusivity) [-]
q	-	heat flux [W/m ²]
Q	-	heat release rate [kW]
Q^*	-	non-dimensional heat release rate ($Q/\rho T c_p g^{1/2} D^{5/2}$) [-]
r	-	ray vector [-]
Re	-	Reynolds number ($\rho U x/\mu$) (inertial force/viscous force) [-]
S	-	radiative energy source term [W/m ²]
s	-	distance along a line-of-sight in DTRM model [m]
T	-	temperature [K]
	-	horizontal thermocouple rake location [-]
t	-	time [s]
TC	-	measured thermocouple temperature [°C]
U	-	velocity [m/s]
u	-	streamwise velocity [m/s]
V	-	velocity measurement location [-]
w	-	weighting factor/coefficient in DTRM model [-]
x	-	x-coordinate direction [m]
Y	-	mass fraction [-]
y	-	y-coordinate direction; distance from the wall [m]
Z	-	height [m]
z	-	z-coordinate direction/height above floor [m]
z'	-	interface height above floor [m]

Greek letters

α	-	convective heat transfer coefficient [W/m ² /K]
χ	-	combustion efficiency [-]
Δ	-	difference or change [-]
ΔH_c	-	heat of combustion [MJ/kg]
δ	-	thermal penetration depth [m]
ε	-	emissivity [-]
Φ	-	configuration factor [-]
ϕ	-	azimuthal angle [radians]
η	-	air excess factor ($\eta=1$ for stoichiometry) [-]
μ	-	coefficient of viscosity [kg/m/s]
π	-	pi constant, 3.141592654 [-]
θ	-	temperature [°C]
	-	polar angle [radians]
ρ	-	density [kg/m ³]
σ	-	Stefan-Boltzmann constant [5.67x10 ⁻⁸ W/m ² /K ⁴]
	-	turbulent Prandtl-Schmidt number [-]
τ	-	transmissivity [-]
	-	time in solid solver [s]
	-	$T/1000$ [K/1000]
τ_s	-	shear stress [N/m ²]
Ω	-	solid angle [-]

Subscripts

<i>a</i>	-	ambient
<i>b</i>	-	black-body radiation
<i>c</i>	-	convective
<i>conv</i>	-	convective
<i>FL</i>	-	flashover
<i>f</i>	-	fire, floor
<i>fi</i>	-	fire
<i>g</i>	-	gas
<i>ignition</i>	-	ignition
<i>l</i>	-	lower layer
<i>m</i>	-	member
<i>max</i>	-	maximum
<i>min</i>	-	minimum
<i>net</i>	-	in context of flux, net flux, i.e. absorbed minus emitted
<i>q</i>	-	combustible material
<i>r</i>	-	radiative
<i>S</i>	-	layer
<i>s</i>	-	soot
	-	solid surface
<i>soot</i>	-	soot
<i>rad</i>	-	radiative
<i>sur</i>	-	surface
	-	surroundings
<i>t</i>	-	total surface, i.e. walls, ceiling and floor, including openings
<i>TC</i>	-	thermocouple
<i>U</i>	-	upper layer
<i>u</i>	-	upper layer
<i>v</i>	-	vertical openings on all walls
<i>+</i>	-	outgoing/emitted
	-	normalised parameter
<i>-</i>	-	incoming/incident

Glossary

1ZM	-	one-zone model
2ZM	-	two-zone model
BICCG	-	Incomplete-Cholesky preconditioned bi-conjugate gradient numerical solver
BRE	-	<u>B</u> uilding <u>R</u> esearch <u>E</u> stablishment Ltd., UK
BRI	-	<u>B</u> uilding <u>R</u> esearch <u>I</u> nstitute, Japan
CFD	-	<u>c</u> omputational <u>f</u> luid <u>d</u> ynamics
CH ₄	-	methane
CO	-	carbon monoxide
CO ₂	-	carbon dioxide
CGSTAB	-	<u>c</u> onjugate <u>g</u> radient <u>s</u> tabilised numerical solver
DTRM	-	<u>d</u> iscrete <u>t</u> ransfer <u>r</u> adiation <u>m</u> odel
EBU	-	<u>e</u> ddy <u>b</u> reakup combustion model
F	-	opening at the <u>f</u> ront only
F+B	-	openings at both <u>f</u> ront and <u>b</u> ack
GUI	-	<u>G</u> raphical <u>U</u> ser <u>I</u> nterface
HI	-	<u>h</u> ighly <u>i</u> nsulating compartment lining
H ₂ O	-	water
I	-	<u>i</u> nsulating compartment lining
ICCG	-	Incomplete-Cholesky preconditioned conjugate gradient numerical solver
ILUCCG	-	ILU preconditioned conjugate gradient numerical solver
JASMINE	-	CFD code (<u>A</u> nalysis of <u>S</u> moke <u>M</u> ovement <u>i</u> n <u>E</u> nclosures)
JOSEFINE	-	Graphical User Interface (<u>J</u> ASMINE or <u>S</u> OFIE <u>F</u> ire <u>I</u> nterface)
MMA	-	<u>m</u> ethyl <u>m</u> ethacrylate
NAF	-	<u>n</u> on- <u>a</u> diabatic <u>f</u> lamelet
N ₂	-	nitrogen
NFSC	-	<u>N</u> atural <u>F</u> ire <u>S</u> afety <u>C</u> oncept
O ₂	-	oxygen
OZone	-	zone model developed and validated under NFSC1 & NFSC2
QUICK	-	Quadratic Upwind numerical interpolation scheme
RHR	-	rate of <u>h</u> eat <u>r</u> elease
RTE	-	<u>r</u> adiation <u>t</u> ransfer <u>e</u> quation
SGDH	-	<u>s</u> ingle <u>g</u> radient <u>d</u> iffusion <u>h</u> ypothesis turbulence model
SIMPLE	-	pressure correction algorithm (<u>s</u> emi <u>i</u> mplicit <u>p</u> ressure <u>l</u> inked <u>e</u> quation)
SIMPLEC	-	variant on the SIMPLE pressure correction algorithm (<u>S</u> IMPLE <u>c</u> orrected)
SIMPLEST	-	variant on the SIMPLE pressure correction algorithm (<u>S</u> IMPLE <u>s</u> hortened)
sip3d	-	Stone's <u>s</u> trongly <u>i</u> mplicit solver (numerical solver)
SOFIE	-	CFD code (<u>S</u> imulation of <u>F</u> ires in <u>E</u> nclosures)
SOUP	-	<u>S</u> econd <u>O</u> rders <u>U</u> Pwind numerical interpolation scheme
SP	-	constant <u>s</u> tatic <u>p</u> ressure boundary
STELA	-	Embedded mesh solid-phase solver (<u>S</u> olid <u>T</u> hermal <u>A</u> nalysis)
tdma	-	tri-diagonal matrix algorithm numerical solver
TVD	-	van Leers flux-limited second-order numerical interpolation scheme
W	-	100% wood
W+P	-	80% wood, 20% plastic
WSGG	-	radiation emission model based on <u>w</u> eighted <u>s</u> um of <u>g</u> rey <u>g</u> ases

List of figures and tables

Figures

- Fig. 1 – fire gas emissivity dependence on path length (L), stoichiometry (η) soot yield
- Fig. A.1 – OZone organisation chart of the combination strategy
- Fig. A.2 – OZone modification of $RHR(t)$ in case of flashover
- Fig. A.3 – conventional discretization of the solid angle hemisphere for DTRM
- Fig. A.4 – Bressloff discretization scheme
- Fig. A.5 – original + polar discretization scheme
- Fig. B.1 – representation of an I-beam in SOFIE with the STELA composite solid solver
- Fig. B.2 – SOFIE and STELA composite solid solver solution algorithm
- Fig. B.3 – JOSEFINE windows for specification of beam and protection information
- Fig. D.1 – schematic of test
- Fig. D.2 – computational mesh in region of beam
- Fig. D.3 – SOFIE prediction of heat flux distribution and flowfield in impingement region on underside of beam/ceiling slab assembly ^[BRE]
- Fig. D.4 – predictions versus experiment for different size/beam height combinations ^[BRE]
- Fig. D.5 – incident heat flux to lower flange upward-facing surface ^[LABEIN]
- Fig. D.6 – incident heat flux to lower flange upward-facing surface ^[LABEIN]
- Fig. D.7 – incident heat flux to ceiling ^[LABEIN]
- Fig. D.8 – incident heat flux to upper flange ^[LABEIN]
- Fig. D.9 – temperatures in the lower flange ^[LABEIN]
- Fig. D.10 – temperatures in the upper flange ^[LABEIN]
- Fig. D.11 – lower flange width-averaged convective heat transfer coefficient variation with distance and dependence on fire exposure (symmetry is used) ^[BRE]
- Fig. D.12 – lower flange width-averaged heat flux breakdown ^[BRE]
- Fig. D.13 – lower flange width-averaged convective heat flux ^[BRE]
- Fig. D.14 – VTT scale furnace schematic
- Fig. D.15 – overview of the scale furnace model
- Fig. D.16 – overview inside the scale furnace; the fuel and air inflow boundaries are indicated
- Fig. D.17 – modification of the steel column cross-section from rectangular to I-shape [mm]
- Fig. D.18 – finite-volume grid inside the columns
- Fig. D.19 – overview of simulated flowfield inside scale furnace and exhaust tube ^[VTT]
- Fig. D.20 – simulated "thermocouple error" $T_{TC} - T_{gas}$ inside scale furnace ^[VTT]
- Fig. D.21 – measured and simulated thermocouple temperatures inside scale furnace ^[VTT]
- Fig. D.22 – measured and simulated CO_2 volume fraction inside exhaust tube ^[VTT]
- Fig. D.23 – development of the steel column surface temperatures ^[VTT]
- Fig. D.24 – net heat flux into the columns ^[VTT]
- Fig. D.25 – comparison of measured and simulated temperatures in cross-section of the black steel column located approximately in the middle of the column ^[VTT]
- Fig. D.26 – convective heat transfer coefficient on the surface of the columns ^[VTT]
- Fig. D.27 – histogram of values of convective heat transfer coefficient on furnace boundaries ^[VTT]
- Fig. D.28 – schematic of VTT large room with instrumentation locations
- Fig. D.29 – heptane pool locations in the test room
- Fig. D.30 – horizontal thermocouple rake locations for gas temperature measurement
- Fig. D.31 – vertical locations of the thermocouples for gas temperature measurement
- Fig. D.32 – locations of the door gas temperature (D) and velocity (V) measurements
- Fig. D.33 – VTT Test 4 results ^[AGB]
- Fig. D.34 – VTT Test 6 results ^[AGB]
- Fig. D.35 – VTT Test 8 results ^[AGB]
- Fig. D.36 – rate of heat release VTT test #7 ^[AGB]
- Fig. D.37 – interface height VTT test #7 ^[AGB]
- Fig. D.38 – temperature of hot gas layer VTT test #7 ^[AGB]
- Fig. D.39 – temperature of lower layer VTT test #7 ^[AGB]
- Fig. D.40 – rate of heat release VTT test #8 ^[AGB]
- Fig. D.41 – interface height VTT test #8 ^[AGB]

- Fig. D.42 – temperature of hot gas layer VTT test #8 ^[AGB]
- Fig. D.43 – temperature of lower layer VTT test #8 ^[AGB]
- Fig. D.44 – rate of heat release VTT test #9 ^[AGB]
- Fig. D.45 – interface height VTT test #9 ^[AGB]
- Fig. D.46 – temperature of hot gas layer VTT test #9 ^[AGB]
- Fig. D.47 – temperature of lower layer VTT test #9 ^[AGB]
- Fig. D.48 – SOFIE monitor window at 600 seconds ^[AGB]
- Fig. D.49 – temperature iso-surface (800K) and velocity vectors ^[AGB]
- Fig. D.50 – comparison of grid effect on door jet velocities at four time points ^[VTT]
- Fig. D.51 – vertical velocity profile in doorway ^[BRE]
- Fig. D.52 – vertical temperature profile in doorway ^[BRE]
- Fig. D.53 – convective heat transfer coefficient inside rear wall of compartment ^[AGB]
- Fig. D.54 – convective heat transfer coefficient inside side wall of compartment ^[AGB]
- Fig. D.55 – convective heat transfer coefficient on underside of ceiling of compartment ^[AGB]
- Fig. D.56 – convective heat transfer coefficient inside front wall of compartment ^[AGB]
- Fig. D.57 – right-hand opening in BRE large compartment prior to test 8 (17/2/00)
- Fig. D.58 – right-hand opening showing early fire development in test 8
- Fig. D.59 – front openings showing later fire development in test 8
- Fig. D.60 – front openings showing flashed-over burning in test 7 (6/1/00)
- Fig. D.61 – approximate heat release rate curve for BRE large compartment test 6
- Fig. D.62 – approximate heat release rate curve for BRE large compartment test 8
- Fig. D.63 – doorway centreline velocity curves from test for which thermocouple temperatures (original) and estimated gas temperatures (corrected) where used ^[BRE]
- Fig. D.64 – comparison of MRFC prediction and experiment for BRE large compartment test 8 ^[AGB]
- Fig. D.65 – comparison of MRFC velocity prediction and experiment for BRE large compartment test 8 ^[AGB]
- Fig. D.66 – SOFIE monitor window for BRE large compartment test 8 ^[BRE]
- Fig. D.67 – comparison between prediction (SOFIE and JASMINE CFD codes) and experiment for velocities on doorway centreline, BRE large compartment test 8 ^[BRE]
- Fig. D.68 – comparison between prediction (SOFIE CFD code) and experiment for temperatures (°C) on doorway centreline, BRE large compartment test 8 ^[BRE]
- Fig. D.69 – comparison of predicted gas, thermocouple and radiative temperatures (°C) on doorway centreline, BRE large compartment test 8 ^[BRE]
- Fig. D.70 – predicted gas temperatures (K) on doorway centreline at 10 minutes, BRE large compartment test 8 ^[BRE]
- Fig. D.71 – convective heat transfer coefficient inside rear wall of compartment, BRE large compartment test 8 ^[BRE]
- Fig. D.72 – convective heat transfer coefficient inside side wall of compartment, BRE large compartment test 8 ^[BRE]
- Fig. D.73 – convective heat transfer coefficient on underside of ceiling of compartment ^[BRE]
- Fig. D.74 – convective heat transfer coefficient inside front wall of compartment ^[BRE]
- Fig. D.75 – temperature development within protected indicative - BRE large compartment test 8 ^[BRE]
- Fig. D.76 – protective indicative temperatures at point P2 - grid & DT ray effects ^[LABEIN]
- Fig. D.77 – computed gas temperature field for BRE test 6 (front and rear openings) ^[BRE]
- Fig. D.78 – effective radiative temperature profiles at three positions in the compartment at 500s, BRE large compartment test 6 ^[BRE]
- Fig. D.79 – computed convective heat transfer coefficient values on underside of ceiling (front of compartment towards top of page) at 500s, BRE large compartment test 6 ^[BRE]
- Fig. D.80 – convective heat transfer coefficient for 51000 cells and 8 rays SOFIE simulation at 600 seconds (ceiling) ^[LABEIN]
- Fig. D.81 – effect of soot concentration and soot model choice on heat loss from simple fire plume ^[BRE]
- Fig. D.82 – an open car park ^[ProfilARBED]
- Fig. D.83 – surface temperature distributions in open car park ^[ProfilARBED]
- Fig. D.84 – convective heat transfer coefficient distributions in open car park ^[ProfilARBED]
- Fig. D.85 – CTICM external column fire test rig ^[ProfilARBED]
- Fig. D.86 – numerical grid for CTICM external column fire test case ^[ProfilARBED]

- Fig. D.87 – temperature isosurfaces for CTICM external column fire test case:
a) 927 °C, b) 1227°C ^[ProfilARBED]
- Fig. D.88 – thermocouple temperatures (K) after 14 minutes (plane YZ) ^[ProfilARBED]
- Fig. D.89 – thermocouple temperatures (K) after 14 minutes (plane YZ) ^[ProfilARBED]
- Fig. D.90 – comparison with test data for CTICM external column test ^[ProfilARBED]
- Fig. F.1 – schematic picture of the geometry assumed in the emissivity computation
- Fig. F.2 – emissivity of a soot-gas mixture in reaction region, where $\eta \approx 1$; results are given for different soot yields and gas temperatures of 1000°C (top) and 300°C (bottom)
- Fig. F.3 – emissivity of the mixture of soot and combustion products at temperature of 800 °C, for different soot yields
- Fig. F.4 – dependence of air excess factor η on the heat release rate and height
- Fig. F.5 – integration element of the solid angle
- Fig. F.6 – the effect of the radiation parameters Φ_f , ε_f and ε_a on the error in Eurocode equ. 3.3
- Fig. F.7 – the effect of the radiation parameters T_f , T_m and T_a on the error in Eurocode equ. 3.3

Tables

- Table 1 – summary values on convective heat transfer coefficient for selected test cases
- Table A.1 – SOFIE CFD technical summary
- Table A.2 – SOFIE radiation model options
- Table D.1 – localised beam fire test cases
- Table D.2 – base parameters for SOFIE simulations
- Table D.3 – SOFIE localised beam fire simulation test cases
- Table D.4 – summary of parametric study findings for localised beam fire test case
- Table D.5 – normalised radiation computation periods for localised beam fire test
- Table D.6 – SOFIE input details for VTT scale furnace test
- Table D.7 – fire types in the NFSC2 Room Test series in VTT (Fire type 10 is the Inter-laboratory calibration test)
- Table D.8 – NFSC2 Room Test series in VTT; Δm_{fuel} is the change of the load cell reading during the fire
- Table D.9 – summary of VTT room test 8
- Table D.10 – model parameters for SOFIE simulation of VTT room test 8
- Table D.11 – summary information on convective heat transfer coefficients (W/m²/K) for VTT test 8
- Table D.12 – BRE large compartment test series
- Table D.13 – BRE large compartment test series - ventilation characteristics
- Table D.14 – summary of BRE large compartment test 6
- Table D.15 – summary of BRE large compartment test 8
- Table D.16 – model parameters in SOFIE simulation of test 8
- Table D.17 – summary information on convective heat transfer coefficients (W/m²/K), BRE test 8
- Table D.18 – model parameters in SOFIE simulation of test 6
- Table D.19 – summary information on convective heat transfer coefficients (W/m²/K), BRE test 6
- Table D.20 – soot mass fraction with prescribed scalar models at various heights
- Table E.1 – summary values on convective heat transfer coefficient
- Table F.1 – convective heat transfer coefficients from EC1 section 3

References

1. Abbas, A.S. & Lockwood, F.C. (1984) "The prediction of the combustion and heat transfer performance of a refinery heater", *Combust. Flame*, vol. 58, pp. 91-101
2. Alpert, R.L. (1975) "Turbulent ceiling-jet induced by large-scale fires", *Combust. Sci. and Tech.*, vol. 11, pp. 197-213
3. Anderson, D., Tannehill, J. & Pletcher, R. (1994) "Computational fluid mechanics and heat transfer", McGraw-Hill
4. Bilger, R.W. (1994) "Computational field models in fire research and engineering", *Proc. of the 4th Int. Symp. on Fire Safety Science*, Ottawa, 13-17 July, 1994, pp. 95-110
5. Blevins, L.G. & Pitts, W.M. (1999) "Modelling of bare and aspirated thermocouples in compartment fires", *Fire Safety J.*, vol. 33, pp. 239-259
6. Blevins, L.G. (1998) "Modelling of thermocouple behaviour in room fires", NIST annual conference on fire research, Gaithersburg, MD, Nov. 2-5, 1998, pp. 17-18
7. Blevins, L.G. (1999) "Behaviour of bare and aspirated thermocouples in compartment fires", *Proc. of the 33rd National Heat Transfer Conf.*, Albuquerque, New Mexico, 15-17 August 1999
8. Bradley, D. & Matthews, K.J. (1968) "Measurement of high gas temperatures with fine wire thermocouples", *J. Mech. Eng. Sci.*, vol. 10, no. 4
9. Bressloff, N.W., Moss, J.B. & Rubini, P.A. (1996) "Assessment of a differential total absorptivity solution to the radiative transfer equation as applied in the discrete transfer radiation model", *Numerical Heat Transfer, Part B: Fundamentals*, vol. 29, part 3, pp. 381-397
10. Carvalho, M.G. & Coelho, P.J. (1989) "Heat transfer in gas turbine combustors", *J. Thermophysics*, vol. 3, no. 2, pp. 123-131
11. Cox, G. & Chitty, R. (1985) "Some source-dependent effects of unbounded fires", *Combust. & Flame*, vol. 60, pp. 219-232
12. Cox, G. & Kumar, S., "Field modelling of fire in forced ventilation enclosures", *Combustion Science and Technology*, vol. 52, pp. 7-23, 1987
13. Cox, G. & Kumar, S. (2002) "Modelling enclosure fires using CFD modelling", *SFPE Handbook*, 3rd ed., pp. 3-194 to 3-218
14. Cumber, P.S. (2000) "Ray effect mitigation in jet fire radiation modelling", *Int. J. of Heat and Mass Transfer*, vol. 43, pp. 935-943
15. Eurocode 1: Basis of design and actions on structures, Part 1.2: Actions on structures - actions of structures exposed to fire, prEN 1991-1-2, 2001, BSi/CEN
16. Eurocode 1: Basis of design and actions on structures, Part 2.2: Actions on structures - actions of structures exposed to fire, prEN 1991-1-2, 1996, BSi/CEN
17. Eurocode 3: Design of steel structures, Part 1.2: General rules, Structural fire design, prEN 1993-1-2:2002, BSi/CEN
18. Fairweather, M., Jones, W.P. & Lindstedt, R.P. (1992) "Predictions of radiative transfer from a turbulent reacting jet in a cross-wind", *Combust. Flame*, vol. 89, pp. 45-63
19. Ferziger, J.H. & Peric, M. (1996) "Computational methods for fluid dynamics", Springer-Verlag
20. Grosshandler, W. (1993) "RadCal: A narrow band model for radiation calculations in a combustion environment. NIST Technical Note (TN 1402)", National Institute of Standards and Technology, Gaithersburg, Maryland 20899, 1993
21. Heskestad, G. (1984) "Engineering relations for fire plumes", *Fire Safety J.*, vol. 7, pp. 25-32
22. Hinze, J.O. (1959) "Turbulence", McGraw-Hill, New York
23. Hostikka, S., Kokkala, M. & Vaari, J. (2000) "Experimental study of the localized room fires: NFSC2 tests series", VTT research notes, 2104, Espoo 2001
24. Jayatilleke, C.L.V. (1969) "The influence of Prandtl number and surface roughness on the resistance of laminar sub-layer to momentum and heat transfer", *Prog. in Heat and Mass Transfer*, vol. 1, Pergamon Press, 1969, pp. 193-329
25. Kramers, H. (1946) "Heat transfer from spheres to flowing media", *Physica*, vol. 12, pp. 61-80
26. Kumar, S. & Cox G. (2001) "The development of best practice for the 'correct' use of CFD for fire applications with examples", *Proc. Interflam 2001 conference*, Edinburgh, UK, 17-19 September 2001, pp. 823-834
27. Lockwood, F.C. & Shah, N.G. (1981) "A new radiation solution method or incorporation in general combustion prediction procedures", 18th Symp. (Int.) on Combustion, pp. 1405-1414, The Combustion Institute, Pittsburgh

28. McAdams, W.H. (1954) "Heat Transmission", 3rd edition, McGraw-Hill, New York
29. McCaffrey, B. (1983) "Momentum implications of buoyant diffusion flames", *Combust. Flame*, vol. 52, pp. 149-167
30. Moss, J.B. & Stewart, C.D. (1998) "Flamelet-based smoke properties for the field modelling of fires", *Fire Safety J.*, vol. 30, pp. 229-250
31. Nam, S. & Bill, R.G. Jr. (1993) "Numerical simulation of thermal plumes", *Fire Safety J.*, vol. 21, pp. 231-256
32. Pchelintsev, A., Hasemi, Y., Wakamatsu, T. & Yokobayashi, Y. (1997) "Experimental and numerical study on the behaviour of a steel beam under ceiling exposed to a localised fire", *Proc. 5th Int. Symp. on Fire Safety Science*, Melbourne, Australia, 5-7 Apr., 1997, pp. 1153-1164
33. Pettersson, O., Magnusson, S.E. & Thor, J., *Fire Engineering Design of Structures*, Swedish Institute of Steel Construction, Publication 50, 1976.
34. Rodi, W. (1982) "Turbulent buoyant jets and plumes", Pergamon
35. Welch, S. & Rubini, P. (1997) "Three-dimensional simulation of a fire-resistance furnace", *Proc. 5th Int. Symp. Fire Safety Science*, Melbourne, Australia, 5-7 Apr., 1997, pp. 1009-1020
36. Schleich, J.B. (2000) "Natural Fire Safety Concept - Full scale test, implementation in the Eurocodes and development of an userfriendly design tool", Technical Report no. 6, Semestrial report, period from 01.01.2000 to 30.06.2000, CEC agreement 7210-PA/PB/PC/PD/PE/PF/PR-060, ProfilARBED – Recherches
37. Tanaka, T. (1985) "Smoke Control in large scale spaces. Part 1: Analytic theories for simple smoke control problems. Part 2: Smoke control experiments in a large scale space", *Fire Sci. & Tech.*, vol. 5, no. 1
38. Tewarson, A. (1995) "Generation of heat and chemical compounds in fires". In *SFPE Handbook of Fire Protection Engineering*, Section 3/Chapter 4, NFPA, pp. 3/53-3/124.
39. Thomas, P.H., Hinkley, P.L., Theobald, C.R. & Simm, D.L. (1963) "Investigations into the flow of hot gases in roof venting", *Fire Research Technical Paper No. 7*, London, HMSO
40. Welch, S. (2000) "Developing a model for thermal performance of masonry exposed to fire", *Proc. 1st Int. Workshop on "Structures in Fire"*, Copenhagen, Jun. 2000
41. Welch, S. & Marshall, N.R. (2003) "Development and validation of a comprehensive model for flame spread and toxic products in full-scale scenarios", *Proc. 4th Int. Sem. on Fire and Explosion Hazards*, Derry, Sept. 8-12, 2003
42. Williams, G.C. (1942) ScD thesis in chemical engineering, MIT

APPENDICES – Scientific and Technical Description of the Results

Appendix A – Technical background

Appendix B – Model Development

Appendix C – Thermocouple temperatures

Appendix D – Model Verification

Appendix E – Analysis and Review

Appendix F – Implications of the Results

Annex 1 – Technical Annex

Appendix A – Technical background

The overall objective of the project concerns what are termed “advanced” or “general” methodologies, typified here by the Computational Fluid Dynamics (CFD) models. However, other methods and engineering tools can be used to shed light on the performance of the more sophisticated procedures, as described below for the case of the zone models. A brief summary of the background of both is set out below, starting with the zone models, before more details are given of the specific codes used in this project.

Zone models

Zone models are numerical tools commonly used for the evaluation of the temperature development of the gases within a compartment during the course of a fire. Based on a limited number of hypotheses, they are easy to use and provide a good evaluation of the situation if they are used within their field of validated application. Since the first numerical one-zone models have been made by Pettersson, major developments of the numerical fire modelling have been done. For example, multi-zone, multi-compartment zone models have been developed. Although less sophisticated than CFD models (c.f. below), they have their own role in fire safety engineering and thus essential tools in fire safety engineering applications.

The main hypothesis in zone models is that the compartments are divided into geometrical regions which correspond to physical zones in which the temperature distribution is uniform at any point in time. In one-zone models, the temperature is considered to be uniform within the whole compartment. This type of model is thus a reasonable approximation in case of fully developed fires, contrary to two-zones models which are more appropriate to the case of localised fires. In the latter case, there is a hot layer, which is close to the ceiling, and a cool layer, which is close to the floor.

CFD models

The next section provides more detail about the main modelling methodology based on Computational Fluid Dynamics (CFD), which provides a more detailed, general and sophisticated approach than zone models. The basic remit of a CFD model is to solve the underlying conservation equations describing the fluid and heat transfer processes within each of a large number of control volumes, typically numbering anywhere between about 1,000 and 1,000,000. This provides for a very detailed solution, with considerably less recourse to empirical assumptions than for the zone modelling approach.

CFD models take as their starting point the system of coupled partial differential equations that describe the conservation of mass, momentum, energy and chemical species. These equations, known as the Navier-Stokes equations (momentum and mass conservation) and the related general advection-diffusion transport equation (energy and species conservation), describe both laminar and turbulent fluid flow. A solution, in time and space, is obtained by integrating and discretizing the equation set over a spatial and temporal grid, and then solving the resultant set of algebraic equations by an appropriate numerical method. This yields a discrete set of solution values for velocity, temperature etc. at each spatial grid point (each one corresponding to one control volume) at each time step.

Although CFD models are more general than zone models, particularly for large volume buildings involving large flashed-over or underventilated fires, they require longer processing times and greater knowledge of fluid dynamics, and care and nursing in numerical solution to avoid divergence and to minimise numerical errors. Furthermore, users of CFD models should exercise proper care especially in the choice of fire specification, grid design, sub-models of combustion and radiation, and treatment of heat exchange at gas-solid boundaries. For ensuring quality and trust in CFD models, adequate validation should be demonstrated for the appropriate fire application.

Thus, from the practitioner’s point of view, a combination of zone and CFD models offers a practical solution to a typical performance-based fire safety design of a building.

In this study, the zone models OZone and MRFC and the CFD model SOFIE have been compared within the context of an engineering modelling methodology for determining the thermal behaviour of structural elements in steel/composite-framed buildings subjected to natural fires. The detailed technical description of these models can be found below.

It was perceived that further technical development of the zone models, particularly OZone, was not necessary, which has been covered, to some extent, as part of the previously ECSC-funded projects (NFSC1,2). However, further development of the CFD model SOFIE was necessary for accurate reproduction of the thermal response of the structural elements. In addition, further development of the user interface JOSEFINE was required in order to facilitate pre-processing of the input data and speedier analysis of the results data. This is described in more detail in Appendix B.

Zone model OZone

The zone model “OZone” has been developed and validated in the scope of the ECSC research "*Natural Fire Safety Concept*" (NFSC1) and "*Natural Fire Safety Concept - Full Scale Tests, Implementation in the Eurocodes and Development of a User Friendly design tool*" (NFSC2). The probabilistic approach to defining the action of fire, developed in the scope of NFSC1, has been included in the code.

In the software OZone several improvements on basic zone models have been made. OZone version 1 is a one-zone model developed in the NFSC1 research. OZone version 2 is an improvement on version 1 and includes both two-zone and one-zone models, with a possible switch from two zones to one zone if certain criteria are encountered. It therefore caters for both localised and fully engulfed fires. The wall model is made by the finite-element method and is implicit. OZone takes into account window breakage. And finally different combustion models, considering the ventilation conditions of the fire, have been developed to cover different situations of use of the code, i.e. tests or design simulations. A Graphical User Interface (GUI) has been developed to define the input data.

Within the same ECSC research a database of natural fire tests has been created (see NFSC2) and a series of full-scale fire tests have been carried out for validation. The code has been validated on more than 80 tests and a comparison of the one-zone model of OZone and another independent one-zone model has been made.

The two-zone and one-zone models are based on different hypotheses and it cannot be said that one model is necessarily better than the other. Indeed they correspond to different types of fires or different stages of the same fire. They simply have different application domains and are in fact complementary. When modelling a fire in any given compartment, and at a particular stage in its development, it is important to know whether a two-zone model or a one-zone model is more appropriate.

The fire load can be considered to be uniformly distributed if the combustible material is present more or less over the whole floor surface of the fire compartment and when the fire load density (quantity of fuel per floor area) is more or less uniform. By contrast, the fire load is said to be “localised” if the combustible material is concentrated on quite a small surface compared to the floor area with the rest of the floor area being free of fuel.

Fire ignitions are in most cases localised and therefore a fire tends to remain localised for a certain period of time. If temperatures are sufficiently high as to provoke spontaneous ignition of all the combustible present in the compartment, a phenomenon known as “flashover” occurs. Generally two-zone models are valid in case of localised fires or pre-flashover fires and one-zone models are valid in case of fully-engulfed fires or post-flashover fires. Also if the thickness of the lower layer is small compared to the height of the compartment, the two-zone assumption becomes inapplicable and a one-zone model becomes more appropriate. Moreover if the fire area is big compared to the floor area, the one-zone model assumption is usually better than the two-zone one.

These considerations imply that in order to model fires in a compartment with a uniformly distributed fire load, a two-zone model is well adapted for the first stages of the fire and a one-zone model can be a better assumption if some conditions on temperatures, fire area and smoke layer thickness are

encountered. In many cases, it is difficult to know exactly if a fire will remain localised during its entire burning period, if flashover will happen etc., and in general to know whether a two- or a one-zone model is most appropriate.

It can be imagined to make a manual combination strategy. It implies to make at first a two-zone model simulation, to check until when it is valid (i.e. to find the time of transition from two zones to one zone) and then to restart a one-zone model simulation with new initial condition obtained from the results of the first two-zone simulation at transition time. The last step is particularly difficult, especially concerning the initial partition temperatures, and is not permitted by existing one-zone models.

For this reason an automatic combination strategy is proposed. With this strategy, the simulation always begins with the two-zone model assumption and if one of the above described conditions is encountered, the simulation switches from the two-zone model to a one-zone model and/or modifies the mass and energy released by the fire. It may be that only one of these two modifications happens during the fire simulation or they can happen successively or simultaneously.

In case of localised fire loads, when the upper layer temperature is sufficiently high to ignite the fuel by radiation, fuel in the complete fire area is deemed to have started to burn and the rate of heat release is modified. In this case the fire stay localised and a two-zone phenomenon is continuing and the two-zone model is still applied. A one-zone model can become more realistic when the upper layer thickness becomes large compared to the compartment height.

It is also still possible to choose to follow a two-zone or a one-zone strategy for the entire duration of a fire. With these strategies, the whole simulation is made considering two or one zones, from the initial time to the end of the calculation. No modification of the rate of heat release is made by the code, except via the combustion models.

The burning model in OZone is modified according to the criterion that flashover has occurred. There are different criteria to be checked:

- Criterion 1 (C1) : $T_U > T_{FL}$
High temperature of the upper layer gases, composed of combustion products and entrained air, leads to a flashover. All the fuel in the compartment is ignited by radiative flux from the upper layer. The flashover temperature (T_{FL}) is set to 500°C.
- Criterion 2 (C2) : $Z_s < Z_q$ and $T_z > T_{ignition}$
If the gases in contact with the fuel have a temperature higher than the ignition temperature of fuel ($T_{ignition}$), the propagation of fire to all the combustibles of the compartment will occur by convective and radiative ignition. The gases in contact (at temperature T_z) can belong to either the lower or upper layers of a two-zone model (in the latter case, if the decrease of the interface height (Z_s) leads to combustible material being in the smoke layer - Z_q is the maximum height of the combustible material) or the unique zone of a one-zone model. $T_{ignition}$ is assumed here to be 300°C.
- Criterion 3 (C3) : $Z_s < 0.2 H$
The interface height (H) descends and produces a very small lower layer thickness, i.e. less than 20% of room height, which is not representative of a two-zone phenomenon.
- Criterion 4 (C4) : $A_{fi} > 0.25 A_f$
Compared to the floor area of the compartment (A_f), the fire area is too high to be considered as a localised fire, i.e. it is more than 25% of the former.

The strategy is rather complicated (c.f. fig. A.1). The effects of the choice between the various model options, resulting in different paths, can usually be appreciated directly from the results plots. If there is the possibility of checking these with real test data, it can be decided which choice fits the results best. Whilst this may be a good choice for the case of interest, it need not be a good choice for other configurations. Nevertheless, after these adjustment procedures the default set of parameters can be used for design purposes in normal configurations.

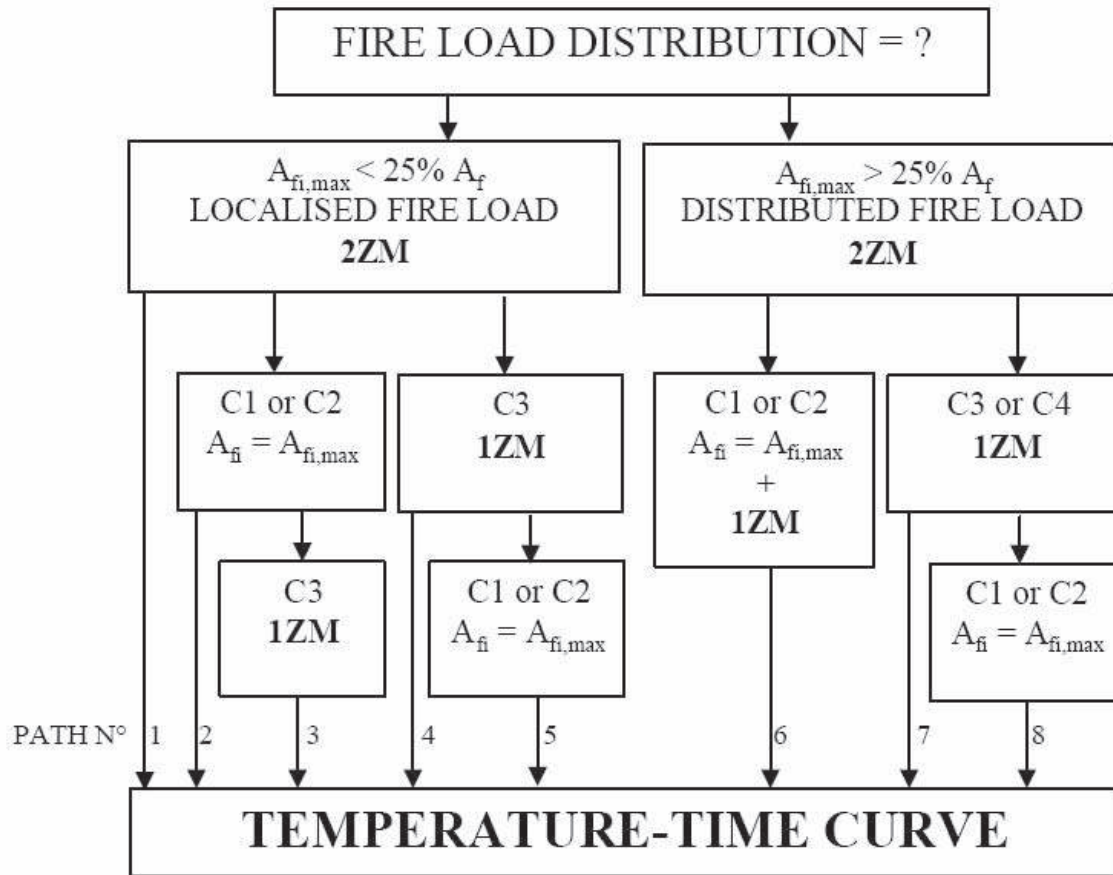


Figure A.1 – OZone organisation chart of the combination strategy

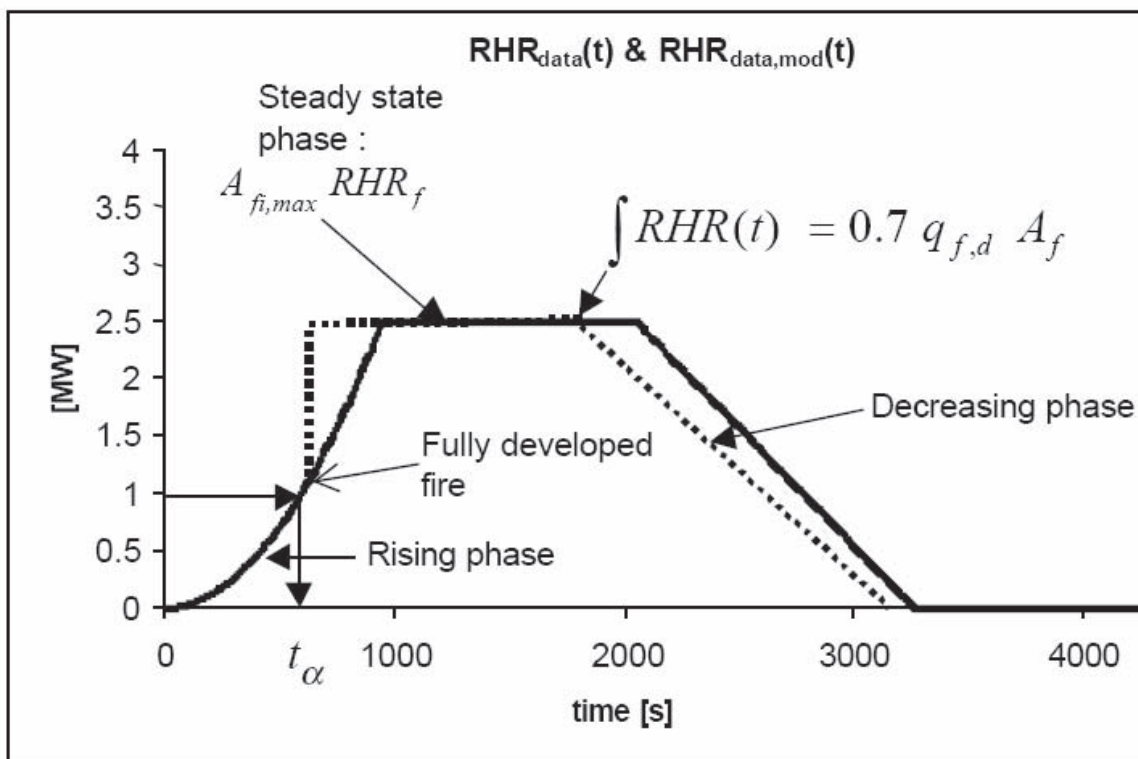


Figure A.2 – OZone modification of $RHR(t)$ in case of flashover

The rate of heat release specified by input data is modified if the model switches to a fully-developed fire (c.f. fig. A.2). In this case the mass loss rate is calculated according to the maximum specified value, i.e. the ventilation-limited rate. The fire duration is therefore shortened according to the predicted burn-out time of the rest of the amount of fuel.

Zone model MRFC

MRFC (Multi Room Fire Code) is a zone model to calculate the physical data during a fire such as the temperature distribution in gases and structures and smoke transport inside a complex building and between the building and outside. It is the kernel of the zone fire model that is supported by AGB. Included in the package are data editors and reporting tools for the model results.

The modelling equations used in MRFC take the mathematical form of an initial value problem for a system of ordinary differential equations (ODE). These equations are derived using the conservation of mass, the conservation of energy, the ideal gas law and relations for density and internal energy. These equations predict, as functions of time, quantities such as pressure, layer heights and temperatures, given the accumulation of mass and enthalpy in the two layers. The MRFC model then solves a set of equations to compute the environment in each compartment and a collection of algorithms to compute the mass and enthalpy source terms. The model incorporates the evolution of the species, such as carbon monoxide, which are important to the safety of individuals subjected to a fire environment.

MRFC is used to calculate the evolving distribution of smoke, fire gases and heat throughout a constructed facility during a fire. In the model, each compartment consists of one layer (fully developed fires) or is divided into two layers, and many zones for detailed interactions. The size of the fire is variable during the simulation. The rate of heat release is computed in the code according to the specified mass loss rate and the amount of oxygen which is available for complete combustion. The specified mass loss rate is not changed by the code during the simulation if a specified fire is used as input data. This is also valid if there is not enough oxygen available. The included switch between a two-zone and a one-zone model for the room of fire origin doesn't affect the specified mass loss rate. This switch cannot be affected by the user. The model goes from normal two-zone modelling of one room to one-zone modelling, if only 5% of the room volume is occupied by the lower layer, or if 95% of the room area is covered by the actual burning area.

Version 2.7.3 of MRFC can handle up to 40 compartments, 100 openings, fan or duct systems, several individual fires, possibility of a flame-spread object, multiple plumes, ceiling jets, multiple sprinklers, and the seven species considered most important in toxicity of fires. The geometry includes variable area/height relations, thermo-physical and pyrolysis databases, multi-layered walls, external wind, the stack effect, building leakage, and flow through holes in floor/ceiling connections. The distribution includes text report generators, facilities for graphics with common plotting packages and a system for comparing many runs done for sensitivity analysis.

According to the above, it is possible to directly compare the test results of MRFC and OZone only if in both models the same assumptions according to the development of the rate of heat release are made. This aspect should be checked when undertaking any comparisons.

CFD model SOFIE

SOFIE (Simulation of Fires in Enclosures) is based on the principles of computational fluid dynamics (CFD). It employs a finite-volume pressure-correction procedure to solve the governing density-weighted Navier-Stokes equations in a general curvilinear co-ordinate system. The SIMPLEC scheme is used together with momentum interpolation for pressure smoothing in the non-staggered numerical grid. Second-order interpolation schemes are available and there are several conjugate-gradient solvers (c.f. Ferziger, 1999).

Turbulent closure is effected through the two-equation k- ϵ model with buoyancy modifications. A standard wall-function approach is used to model convective heat transfer to solid surfaces but this is modified over regions of actively pyrolysing material to accommodate mass loss through volatile

release. Outgassing is treated in the same manner as a transpiring wall, following the approach of Spalding with simplified closed form solutions for normalised streamwise velocity, $u_+ \equiv u/\sqrt{(\tau_s/\rho)}$, and surface mass flux, $m_+ \equiv m_s/\sqrt{(\tau_s/\rho)}$, in laminar and turbulent flow, partitioned dependent upon the normalised distance from the wall, $y_+ \equiv y\sqrt{(\rho\tau_s)}/\mu \leq 11.5$.

The process of combustion is modelled either by an eddy break-up or flamelet-based combustion model. The simulation of fire spread and the thermal response of structures requires accurate prediction of radiation heat fluxes. Emission and absorption due to soot is significant and must account for a number of physical phenomena, including transport effects, turbulent fluctuations of temperature, species concentrations and the effect on the gas temperature (in turn coupled to the soot kinetics) due to local radiation loss.

Radiative heat transfer is based on a deterministic ray-tracing approach using the discrete transfer algorithm (DTRM) with incorporation of soot effects via non-adiabatic laminar flamelets together with appropriate ‘weighted sum of grey gas’ (WSGG) representations of the absorption-emission characteristics of the participating media. More details of the radiation model are provided in the next section. Soot distributions are described either by convection of a conserved scalar (the “prescribed soot” model) or by modelling the formation and oxidation either according to simple rate equations or via laminar flamelets source term modelling. Heat transfer to and within solid boundaries utilises the conjugate heat transfer approach with temperature-dependent material properties.

Published work has demonstrated the importance of calculating the radiation loss rather than by approximating it as a correction to heat release rate. However, particular care is required in developing and validating the radiation heat transfer predictive capability, especially within the context of soot-laden environments. For SOFIE, previous studies have demonstrated that the radiation heat transfer model can provide reasonable predictions of heat fluxes, provided the soot concentration can be quantified [Bressloff et al., 1996].

SOFIE has a simple internal Cartesian grid generator and the boundary and initial conditions for a simulation are also assigned within the code. As with the other aspects of problem specification, these definitions can be handled via a simple text-driven input, used either interactively or in batch mode. Alternatively, all of the same features are available via the Graphical User Interface (GUI) known as JOSEFINE. This interface has been developed to make the code more accessible to design engineers.

Finally, it should also be noted that SOFIE has been written to handle general curvilinear co-ordinates. However, to date the program has not been extensively validated for this type of grids (most fire scenarios for validation are in rectangular compartments) and therefore no interfaces to general pre-processors have been written.

Table A.1 (over) provides a summary of the main technical capabilities of SOFIE.

Radiation model

The basic method known as the “discrete transfer radiation model” (DTRM) has become very popular for solution of radiation heat transfer in combustion problems and is available in the main commercially-available codes in the field. Applications include furnaces [Abbas & Lockwood, 1984], combustors [Carvalho & Coelho, 1989], flames [Fairweather et al., 1992] and fires [Fletcher et al., 1994]. Recently some detailed investigations into the performance of such models have been reported, e.g. Bressloff (1996), Cumber (2000). However, the performance of such models is rather problem-specific, so it is not possible to be prescriptive about the particular implementation or optional parameters to be used in any given case. Rather, the informed modeller must establish a satisfactory performance in each application by means of sensitivity studies and other checks.

DTRM is particularly well-suited to coupled flow and heat transfer calculations in arbitrarily-shaped geometries. This is because it is superimposed, without modification, upon the CFD grid, and because boundary conditions are easily incorporated. However, if insufficient rays are specified, the distribution of the predicted fluxes may show irregularities resulting from numerical errors called the “ray effect”.

Numerical Features
Finite-volume, non-orthogonal curvilinear co-ordinates
Non-staggered Cartesian velocity components
Interpolation schemes – Upwind, Hybrid, Power-Law, QUICK, SOUP, TVD
Pressure correction – SIMPLE, SIMPLEC
Steady state and first-order fully-implicit transient
Solvers – TDMA, BICCG, ILUCCG, Point, ICCG, CGSTAB, SIP3D
Arbitrary passive scalars
Dynamic memory allocation at run-time
Turbulence Model
k-e turbulence model with buoyancy modifications
Combustion Models
Simple eddy breakup
Laminar flamelet
Laminar flamelet prescribed pdf description
Flamelet state relationships: CO ₂ , H ₂ O, O ₂ , N ₂ , CO, density, temperature, enthalpy etc.
Analytical/numerical integration or pre-computed lookup tables
Non-adiabatic flamelets via enthalpy interpolation
Soot models
Prescribed soot (passive scalar)
Magnussen (Tesner)
Moss transport (flamelet rate source terms)

Table A.1 – SOFIE CFD technical summary

Radiation model fundamentals

The specification of ray directions in the original weighting set is described in fig. A.3:

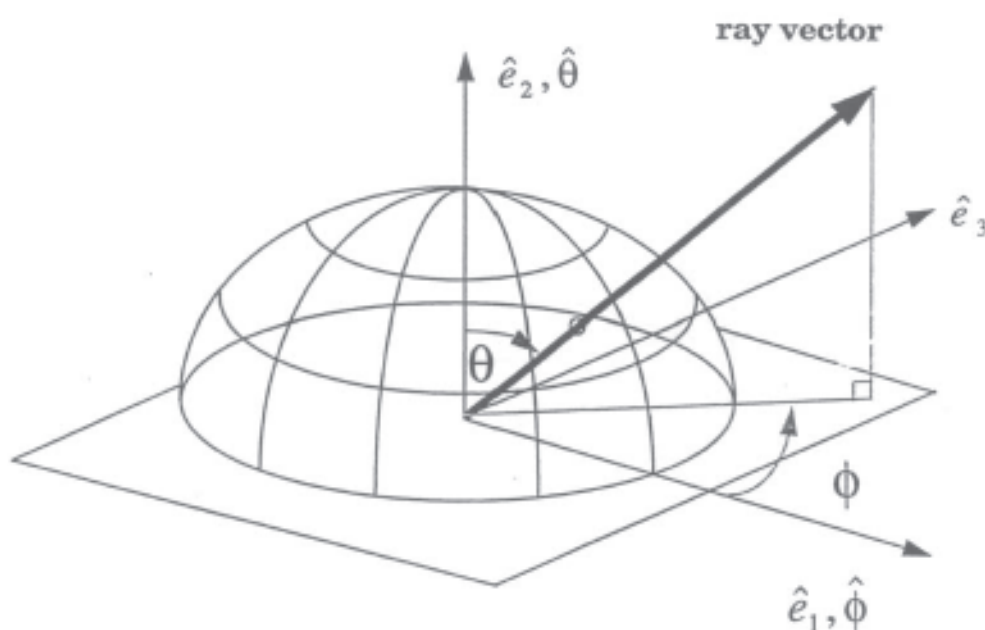


Figure A.3 – conventional discretization of the solid angle hemisphere for DTRM

This alignment of axes yields:-

$$\vec{r}_{rel} = (\sin \theta \cos \phi, \cos \theta, \sin \theta \sin \phi) \quad (A.1)$$

and then discrete solid angles are defined by equal divisions of the polar and azimuthal angles θ and ϕ . Each solid angle is represented by a ray located at the centre of the angle and the radiation transfer equation (RTE) is solved along all directions for every solid surface element.

The radiative intensity along a single line of sight is evaluated from the integrated form of the radiative transfer equation:

$$i_n(s) = \int_0^\infty i_v(0) \tau_v(0 \rightarrow s) dv + \int_0^s \int_0^\infty i_{b,v}(s') \frac{\delta \tau_v(s' \rightarrow s)}{\delta s'} ds' dv \quad (A.2)$$

where τ_v and $i_{b,v}$ are the spectral transmissivity and black body intensity, respectively.

The first term in equ. A.2 represents radiance at the start of a path that is transmitted to s , and the second term is the sum of energy emitted from intermediate points, s' , that is then transmitted across the remaining path to s . For a grey, homogeneous medium equ. A.2 simplifies to a recurrence relation expressing the intensity at the end of a path segment, i_{r-1} , in terms of that at the start of the segment. τ and i are now total properties of the R -th cell.

$$i_r = i_{r-1} \tau_R + i_{b,R} (1 - \tau_R) \quad (A.3)$$

Equ. A.3 can be expanded to the origin of the line of sight so as to represent the total path from one solid surface to another:

$$i_r = i_0 \prod_{m=1}^M \tau_m^T + \sum_{m=1}^M i_{b,m} \varepsilon_m \prod_{m'=m+1}^M \tau_{m'}^T \quad (A.4)$$

where ε is the emissivity of the m -th cell.

Eqs. A.3 or A.4 are applied twice along each ray direction; away from solid surfaces to calculate energy source terms within the solution domain, and towards surfaces to calculate the incident flux. Since the start value, i_0 , in either direction is unknown, other than for black walls with prescribed temperatures, the process is iterative. i_0 is calculated from the radiative heat flux leaving a surface which, for a grey Lambert surface, is:

$$i_0 = \frac{q_+}{\pi} = \frac{1}{\pi} (\sigma T_w^4 - q_-) \quad (A.5)$$

q_+ and q_- are total outgoing and incident fluxes, respectively, σ is the Stefan-Boltzmann constant and T_w is a solid surface temperature. The incident flux for the n -th ray is assumed to be constant for the elemental solid angle, $d\Omega_n$ such that:

$$dq_{i,n} = i_{i,n} \cos \theta_n d\Omega_n \quad (A.6)$$

Hence, integration for this solid angle yields:-

$$q_{i,n} = i_{i,n} \sin \theta_n \cos \theta_n \sin \Delta \theta_n \Delta \phi_n \quad (A.7)$$

where θ_n is the angle between the n -th ray and the surface normal, and $\Delta\theta_n$ and $\Delta\phi_n$ specify the solid angle polygon. When the radiative recurrence relation is solved across all intersected cells from the hit surface back to the firing surface, the incoming intensity, $i_{i,n}$, is assumed constant within each of the N solid angles, and the total incident flux is:

$$q_i = \sum_{n=1}^N i_{i,n} w_n \quad (\text{A.8})$$

where

$$w_n = \sin \theta_n \cos \theta_n \sin \Delta\theta_n \Delta\phi_n \quad (\text{A.9})$$

represents the weighting applied to $i_{i,n}$.

Radiative energy source terms in a control volume are calculated from:

$$\Delta S_n = \Delta i_n w_n \Delta A \quad (\text{A.10})$$

and summed for all intersecting rays. It is assumed that each ray occupies a "pencil" equal in area to the projection of the firing surface, and that the "pencil" completely overlaps every control volume that it intersects. These assumptions are justified by Lockwood & Shah (1981) in terms of the expensive computational penalties that are incurred, for a small improvement in accuracy, when the source terms are calculated according to the exact proportion of a control volume overlapped by a ray.

This procedure is performed for each surface in turn, q_+ , the radiative flux leaving a surface, is updated using equ. A.5 and a convergence criterion is tested based upon the absolute change in the net wall heat flux.

The weighting coefficients, w_n , in equ. A.8 are each functions of ray direction and the solid angles represented by each ray. They also depend on the alignment of the axes (used to discretize the hemispherical solid angle) relative to a solid surface. Hence, the specification of ray directions completely determines a weighting set.

Discretization scheme

The method used to determine the distribution of the ray directions in the discretization of the solid angle hemisphere, and hence weighting coefficients, has been studied by Bressloff (1996). In the original formulation, the discretization is based on divisions of the polar and azimuthal angles, θ and ϕ , as shown above in fig. A.1. There are two potential problems with this approach. The first is that the effective non-uniformity of the resultant distribution may lead to problems of insufficient coverage, known as the 'ray effect'. This simply means that insufficient information may be received by some surfaces due to the lack of sufficient rays arriving there which have also traversed a good selection of the control volumes of interest in the gas phase. The second potential problem relates to computations of axisymmetric jets/plumes, where there may be insufficient rays close to the centreline which may have a disproportionate influence on the accuracy of the solution along the plume axis.

Bressloff put forward two alternative discretization models in an attempt to combat these problems. The first was to propose a completely new weighting set producing a more uniform distribution of rays, and this is illustrated in fig. A.4. The second was to add a single polar ray, launched perpendicular to the solid surface, to the original weighting set. This option is shown in fig. A.5.

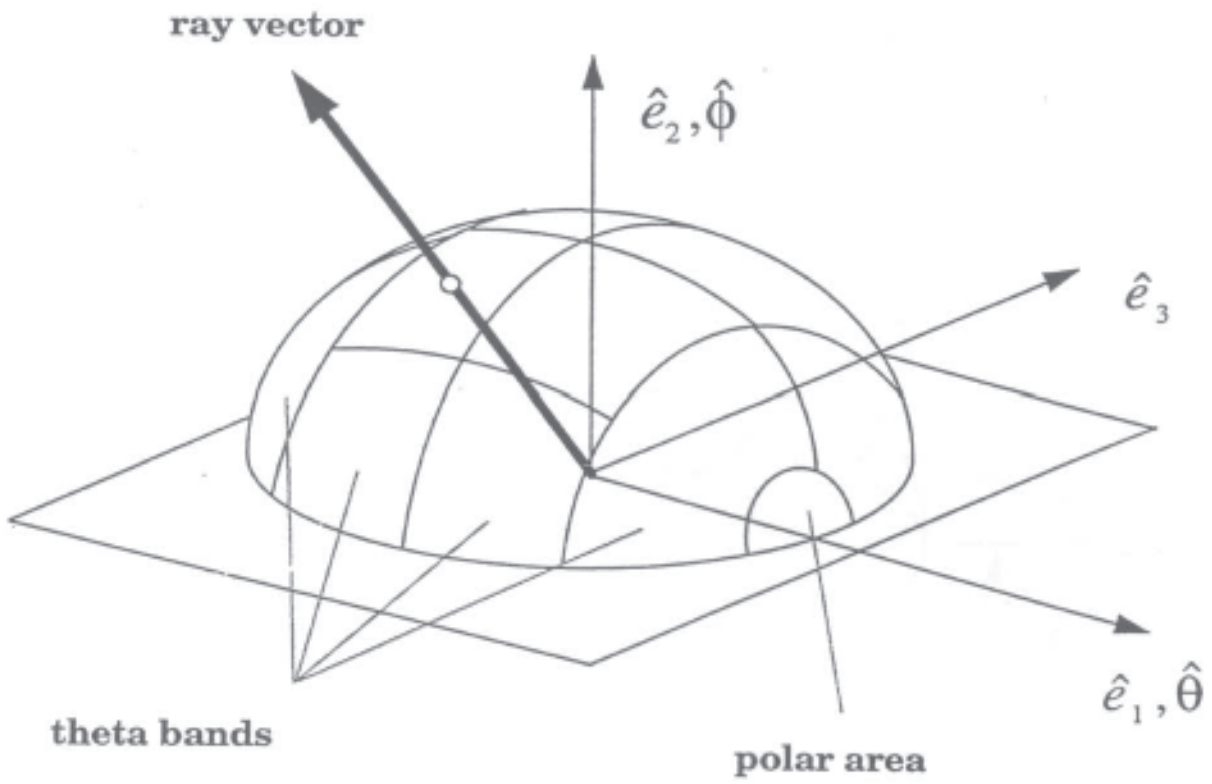


Figure A.4 – Bressloff discretization scheme

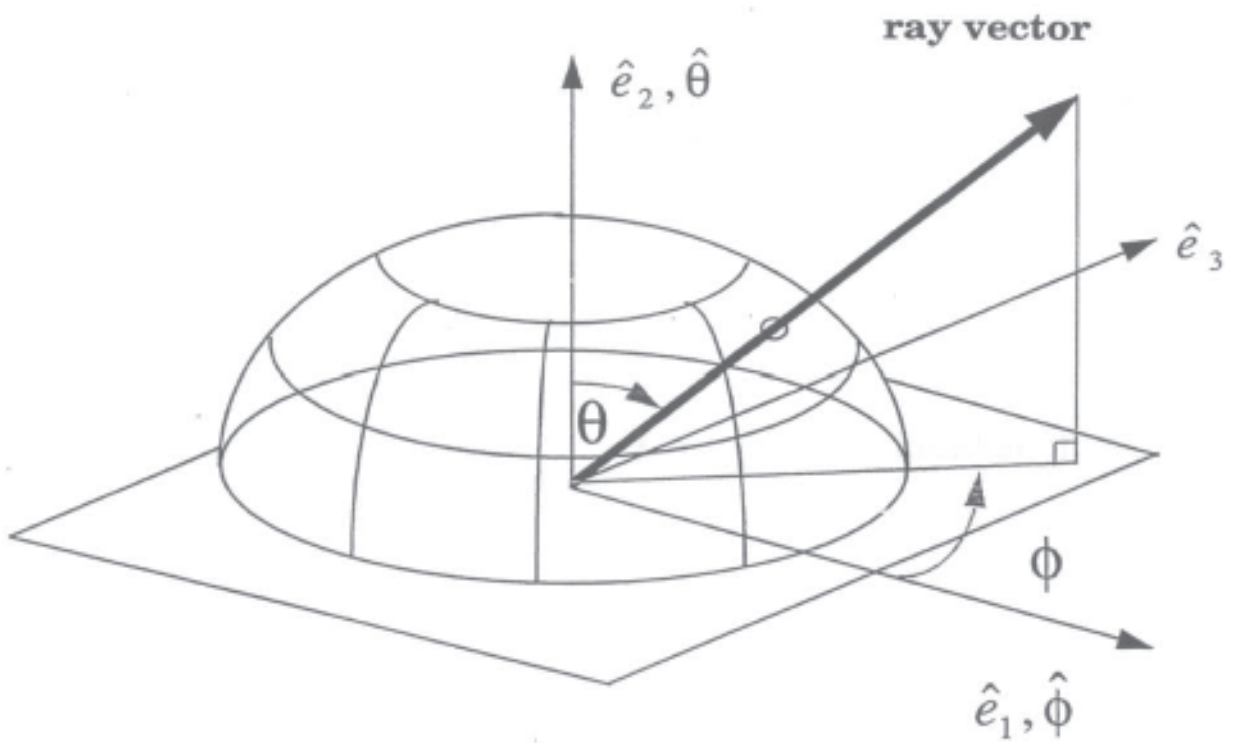


Figure A.5 – original + polar discretization scheme

Radiation transfer equation (RTE) solution

The main SOFIE models for solving the radiation transfer equation (i.e. equ. A.4 above) are based around a representation of the absorption/emission characteristics of the gases (and soot) known as a "mixed grey gas model". This type of model sits in a hierarchy of different methods which may be used to supply this essential information, and represents a good compromise between accuracy and computational expense in the problems of interest in this study (Bressloff et al. (1996)).

The basic concept of such models is to represent the gas properties in a series of bands which correspond in some way to postulated grey gas components. The models of interest generally have 3 or 4 bands, which might be taken as clear gas, optically thin, optically intermediate and optically thick, though the introduction of soot may double the number of bands required. These bands are correlated in some manner to the actual emission spectra of water and carbon dioxide, such that the characteristic peaks corresponding to their main emission bands are approximately represented. Thus the model type is a significant simplification over 'wide band' and 'narrow band' models respectively, which map the emission spectra to a much greater number of spectral bands.

The way the model works is to determine an effective absorption coefficient for each grey gas band, which will be a function of the local combustion products and soot concentrations:

$$a_{k,b} = k_{g,b} p_{cp} + k_{s,b} c_{soot} \quad (\text{A.11})$$

where: $a_{k,b}$ is the absorption coefficient for grey gas band b
 $k_{g,b}$ is the combustion products absorption constant for band b
 $k_{s,b}$ is the soot absorption constant for band b
 p_{cp} is the partial pressure of the combustion products
 c_{soot} is the soot concentration

This is used to evaluate the effective emissivity which is fed into the computation of the RTE (equ. A.4) at each increment along the ray path:

$$\epsilon_b = 1 - e^{-a_{k,b} l} \quad (\text{A.12})$$

where: ϵ_b is the effective emissivity of band b
 l is the local path length

In addition, a coefficient is provided to determine the proportion of black-body radiation actually emitted in this band, $i_{b,R}$ in eqs. A.3 and A.4. This coefficient is represented purely as a polynomial function of the local temperature.

In implementing this type of model, various approximations may be made (for the sake of computational expediency), and this leads to the hierarchy of models available in SOFIE. The distinguishing features of the models are summarised in table A.2 below.

In the most detailed model, the banded weighted sum of grey gases (WSGG), the RTE is evaluated on a band-by-band basis using the corresponding banded absorption coefficient and the exact path length of the ray passing through each cell. By contrast, the 'total properties WSGG' model simplifies the solution by integrating the RTE on a 'total properties' basis, i.e. only once, though the absorption coefficient is still evaluated in the same way.

The simplification implicit in the banded absorptivity solution is the approximate representation of the ray path length in the evaluation of the absorption coefficient. Since this is not determined exactly, i.e. it is calculated once and for all such that the exponential term in equ. A.12 need not be evaluated, there is a considerable saving in computation time. The banded transmissivity model takes this a step further by using the approximate path length in the RTE solution too. In each of the models, the user may also

specify a constant absorption coefficient rather than that evaluated from the total property WSGG model (c.f. equ. A.11).

The lumped absorption coefficient model 'lumps' the solution of the RTE equation itself into a single computation, i.e. it is computed on an 'averaged' basis. The exact path length is still used in the RTE equation, whilst the absorption coefficient uses the same approximation as before. The final basic variant, the lumped transmissivity model is the same except that it does not use the exact path length in the RTE solution either. Again, both of the lumped RTE models may use either constant absorption coefficients or a total property WSGG representation.

Further, in each case where approximate path lengths are specified, the user has three options in SOFIE - either to use the 'cell size' (which is evaluated as the cube root of the cell volume), or the 'mean beam length' which is a constant value proportional to the ratio of fluid volume to surface area, or to specify a 'user defined' constant value.

Model	RTE solution	RTE path length	Absorption coefficient	Absorption coefficient path length
lumped transmissivity	lumped	cell size	constant ²	n/a
		mean beam length	WSGG total property	cell size mean beam length
lumped absorption coefficient	lumped	exact	constant	n/a
			WSGG total property	cell size mean beam length
banded transmissivity	banded	cell size	Constant	n/a
		mean beam length	WSGG total property	cell size mean beam length
banded absorptivity	banded	Exact	Constant	n/a
			WSGG total property	cell size mean beam length
WSGG total property	lumped	exact	WSGG banded	exact
WSGG banded	banded	Exact	WSGG banded	exact

Table A.2 – SOFIE radiation model options

CFD model JASMINE

The JASMINE (Analysis of Smoke Movement in Enclosures) CFD code was exercised within the scope of the project to provide comparisons and checks on the predictions obtained with SOFIE. This code has many similar capabilities to SOFIE, but is based upon a staggered numerical grid representation of the pressure-velocity coupling, which renders its treatment of gas flows over static pressure boundaries significantly more robust [Cox & Kumar, 1987]. The grid is Cartesian structured and boundary heat losses are accommodated by either thermal conduction depth expressions or using a one-dimensional heat transfer calculation (c.f. SOFIE's 3-D conjugate heat transfer). It also differs from SOFIE in using the SIMPLEST pressure correction algorithm. The convection terms are discretized using the Upwind interpolation by default (c.f. the various SOFIE code options in Table A.1 above). More details about the technical basis of the code can be found in Cox & Kumar, 1987.

A major strength of this code is its extensive validation. This has extended to a range of fire problems dealing with the various stages of fire development and over a range of scales, from bench-scale tests up to very large buildings/tunnels, but with particular emphasis on smoke movement in full-scale buildings, over a period of more than 20 years [c.f. Cox & Kumar, 2002].

² In the current study, the value of the constant absorption coefficient was assumed to be 0.3 by default

Appendix B – Model development

This task is concerned with the development of specific submodels in the CFD model SOFIE to facilitate analysis of the applications of interest. This development allows the code to treat more efficiently and accurately the behaviour of structural elements in steel/composite-framed buildings exposed to natural fires.

STELA Composite solid solver

A multi-block solver to model heat conduction through composite solids has been added to SOFIE named STELA (Solid Thermal Analysis). This has been written initially to deal specifically with structural elements such as I-beams and columns, where the standard SOFIE grid cannot be expected to adequately resolve the flange and web for large-scale problems. This constraint arises because in common with many other CFD codes SOFIE uses a structured grid, and typical cell sizes might be in the range 0.1 to 0.5m for the gas-phase solution, much larger than typical I-beam flange and web thicknesses for instance. The limitation on representing the structural components is overcome, with at least partial decoupling, by introducing an independent mesh for the solid-phase regions.

In order to adequately resolve the solid-phase heat transfer, the grid for solution of the three-dimensional conduction equation must be much higher resolution, so that in each Cartesian direction there may be typically 10 to 100 grid points for every SOFIE gas-phase grid point (the typical cell size therefore being 1 to 10 mm).

Assuming isotropic properties, the differential form of the heat conduction equation can be written in Cartesian co-ordinates (x, y, z) as:

$$\frac{\partial T}{\partial t} = K(x, y, z) \left(\frac{\partial^2 T}{\partial x^2} + \frac{\partial^2 T}{\partial y^2} + \frac{\partial^2 T}{\partial z^2} \right) \quad (\text{B.1})$$

Here T is the temperature and K the thermal diffusivity, which is expressed as a function of the thermal conductivity (k_s), density (ρ_s) and heat capacity (c_s) of the solid material:

$$K = \frac{\rho_s c_s}{k_s} \quad (\text{B.2})$$

Fig. B.1 illustrates the general concept, showing how an I-beam may be represented within both the CFD (SOFIE) and composite solid grids. The one-to-many mapping between the two grids is shown.

Fig. B.2 shows the logic of solution procedure. At the end of each main (CFD) time-step (Δt) the composite solid solver is called. The surface fluxes from the CFD solution are mapped onto the finer solid mesh to provide the boundary conditions for the solution of the conduction equation inside the solid. The temperature field inside the composite solid is advanced from the previous CFD time level to the current time level using a solid solver time-step ($\Delta \tau$) that can be defined by the user. Although this time-step can be less than the CFD one, there is little advantage in making it very small since the accuracy of the solution is still limited to some degree by the fact that the CFD-solid boundary condition information is updated only at the end of each CFD time-step.

The right hand loop in fig. B.2 illustrates the STELA solid solver algorithm. This is a multi-block algorithm in that each composite solid is treated as a set of rectangular blocks in which the heat conduction is solved locally. At the end of each solid solver time step ($\Delta \tau$) the boundary conditions at the composite block interfaces are updated (a mixture of temperature and flux values).

At time t (the current CFD time level) the face temperatures from the composite solid solver are mapped back to the CFD grid to provide the appropriate temperature (isothermal) boundary conditions for the next time-step of the CFD and radiation solvers. From the perspective of the CFD and radiation

solvers the composite solids are isothermal blockages, with the additional feature that the temperature values are updated at the end of each time-step.

The conduction solver has been developed to allow the full range of Dirichlet (temperature specification) and Neumann (flux specification) boundary conditions that may be required in fire simulation. Technically this is described as a “mixed boundary condition initial value problem”, using both value (temperature) and flux boundary values. In practice, fluxes are used by default with temperature boundary values applied only at some block-to-block interfaces. Overall, the most important boundary conditions include the flux from the fluid phase 'seen' at the solid, the surface temperature 'seen' by the fluid, the boundary conditions between blocks (or groups of blocks) and the isothermal or flux boundary condition on the outer surface of a wall or ceiling.

The conduction solver itself is a time-dependent, three-dimensional finite-volume model that works on single or multiple geometrical blocks, each with its own numerical mesh on which the heat conduction is solved. The integral form of the conduction equation is discretized on the mesh, and the resultant linear system of algebraic equations is solved using a multi-dimensional form of the tri-diagonal matrix algorithm. Time advancement is by a fully-implicit method that ensures stability. Spatial- and temperature-dependent material properties can be specified, allowing a full range of structural and insulating materials to be modelled.

Quantitative testing of the conduction solver algorithm was initially performed for 'simple' combinations of shape and boundary conditions, e.g. specified temperatures and fluxes at the surfaces of a rectangular element. Further qualitative testing was performed for more complex shapes and boundary conditions for which the analytical solution is not known. Satisfactory performance was demonstrated, thereby ensuring internal verification of the new code.

The composite solid solver has been written in Fortran90, allowing dynamic array allocation to be used. This is more convenient than using the original SOFIE stack arrays that are necessary in Fortran77 coding. The solid solver coding has been integrated with the CFD solver to produce a single executable. The solid solver acts on input data which is generated via the common Graphical User Interface (GUI), known as JOSEFINE (JASMINE or SOFIE Fire Interface), in parallel with the setup for the CFD fluid flow solution. The interface allows users easy access to definition of structural elements such as I-beams and columns which are automatically included in the main CFD simulation, as described in the next section.

JOSEFINE Graphical User Interface (GUI)

During the course of the work it has been necessary to enhance some aspects of the JOSEFINE GUI so that it creates for the user the blocks required to represent the various structural elements. This would otherwise be a time consuming, error-prone task. The user is able to select the type of beam, its dimensions and location, any insulating material, and then the interface creates the block information automatically

Some of the new GUI windows for communication with the solid-phase solver are shown in fig. B.3 below. The main beam/column selection window allows the basic orientation of the beam/column to be defined, together with the choice of materials, heat transfer solution method and geometry of protection. A beam/column type selection button is provided, giving the user access to a default library of 80 beams and 30 columns (which can easily be extended and can be added to by the user), with full geometrical details provided in a further information window.

In the final phase of the model verification exercise, the composite solid solver was tested in conjunction with the CFD solver in the context of the full-scale test cases identified for the model verification exercise. The results of this study are reported under “model validation” in Appendix D.

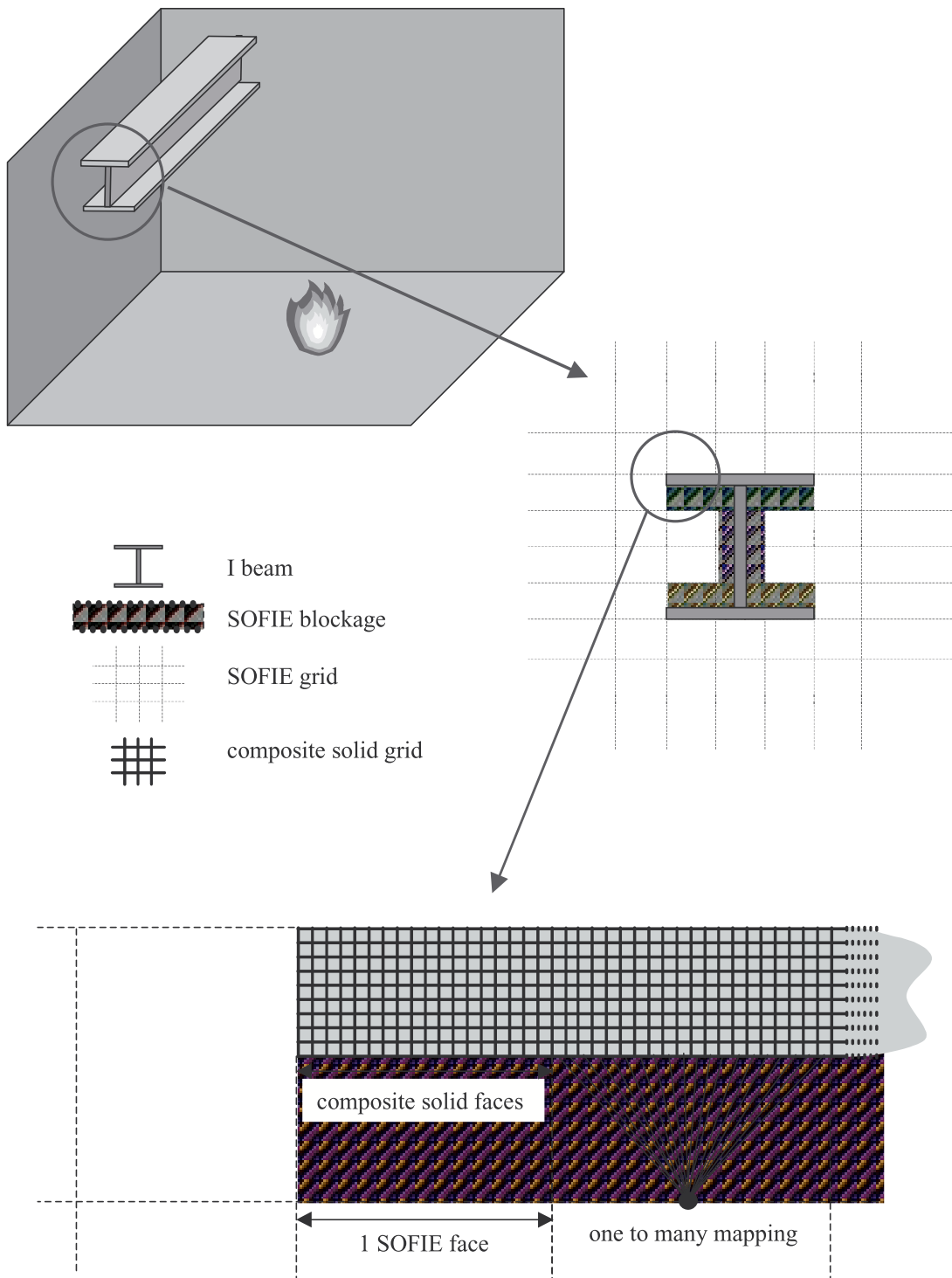


Figure B.1 – representation of an I-beam in SOFIE with the STELA composite solid solver

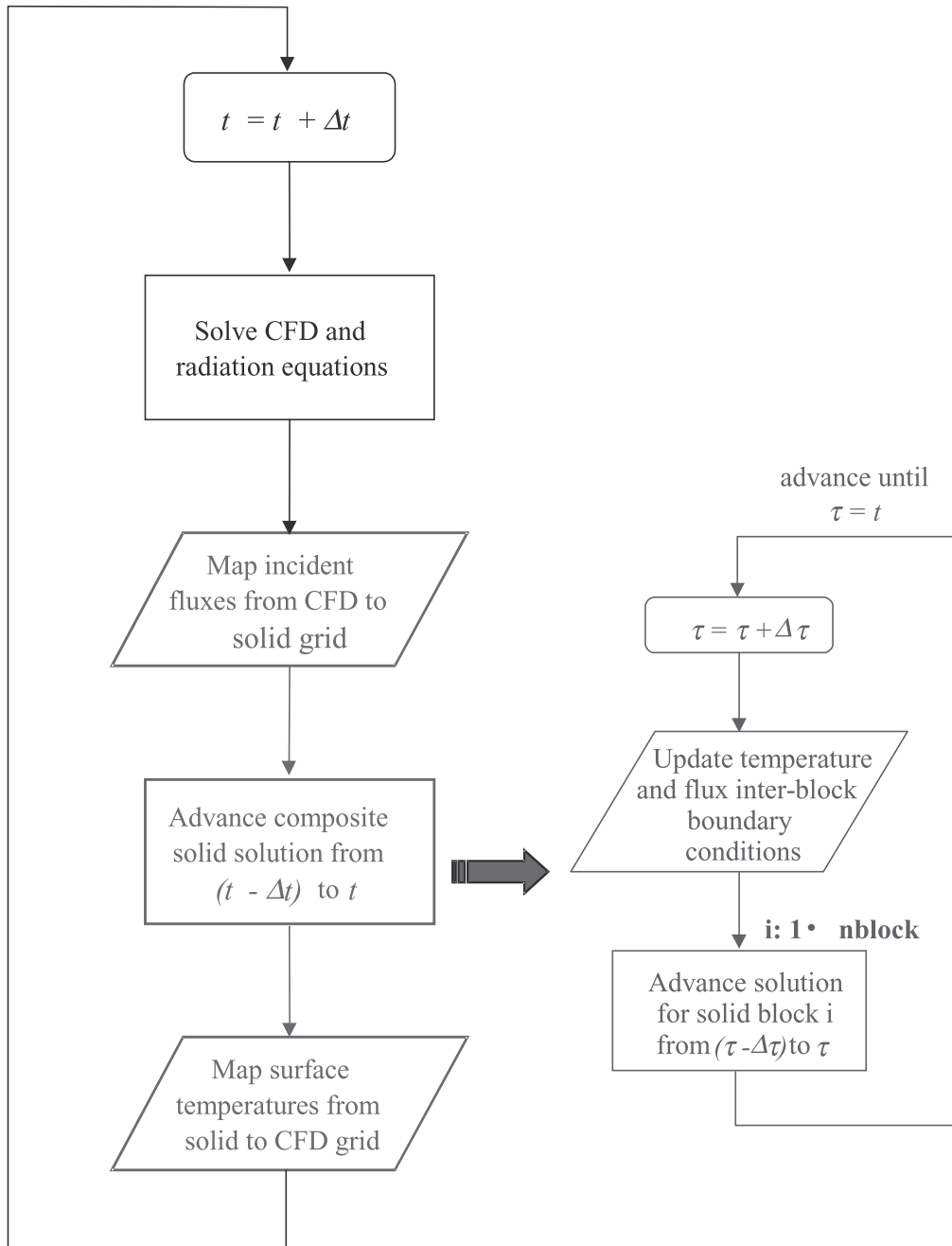


Figure B.2 – SOFIE and STELA composite solid solver solution algorithm



Figure B.3 – JOSEFINE windows for specification of beam and protection information

Appendix C – Thermocouple temperatures

The temperature indicated by a bare thermocouple near a fire differs from the true gas temperature because the bead exchanges radiation with its effective thermal environment, and also due to conduction of heat along the thermocouple wire itself. In certain circumstances, such errors can be very significant and it is always necessary to give due consideration to this phenomenon.

This section briefly describes the underlying theory and looks at typical error predictions. The errors arising from conduction effects are often less significant in fully flashed-over fires and are not dealt with here.

Theory

The basic theory is covered for example by: McAdams (1954) p. 261, Bradley & Matthews (1968), Blevins (1998, 1999), Blevins & Pitts (1999) and Hostikka (2000).

With the neglect of conduction losses, the basic governing equations are rather simple, as follows.

Heat loss from the thermocouple by radiation is:

$$q_{rad} = \frac{A_{TC}\sigma(T_{TC}^4 - T_{sur}^4)}{1 - \frac{A_{TC}}{A_{sur}}\left(\frac{1 - \epsilon_{sur}}{\epsilon_{sur}}\right)} \quad (C.1)$$

where the symbols have their conventional meanings and the subscripts *TC* and *sur* stand for “thermocouple” and “surroundings” respectively.

If the thermocouple bead area is very small compared to that of the thermal environment with which it is exchanging heat, then the above equation reduces to:

$$q_{rad} = \epsilon_{TC} A_{TC} \sigma (T_{TC}^4 - T_{sur}^4) \quad (C.2)$$

Heat gain by the thermocouple via convection is:

$$q_{conv} = \alpha_{TC} A_{TC} (T_{TC} - T_{sur}) \quad (C.3)$$

Neglecting any other heat exchange (i.e. conduction loss) and also, for the sake of simplicity, transient heating effects, the net heat transfer to the thermocouple will be equal to the net radiative loss.³ Thus we can derive the governing equation:

$$\epsilon_{TC} \sigma (T_{TC}^4 - T_{sur}^4) = \alpha_{TC} (T_{TC} - T_{sur}) \quad (C.4)$$

The value of the convective heat transfer coefficient is conventionally obtained from a Nusselt number correlation, noting that:

$$\alpha = \frac{kNu}{d_{wire}} \quad (C.5)$$

³ Where transient effects are important, the reported temperature will be further underestimated; however, this ‘thermal lag’ will normally be quite small when narrow-wire thermocouples are used and when the timescales of the test itself are relatively long can normally be neglected.

which for convenience may be re-expressed as:

$$\alpha = \frac{\mu c_p Nu}{d_{wire} Pr} \quad (C.6)$$

The viscosity of the fluid can be obtained for example from Sutherland's law [Anderson et al., 1994]:

$$\mu = \frac{C_1 T^{1.5}}{T + C_2} \quad (C.7)$$

In the SOFIE code, Kramers' expression is used for the case of a cylinder [c.f. Hinze (1959) p. 76 and McAdams (1954) p. 267]:

$$Nu = 0.42 Pr^{0.2} + 0.57 Pr^{0.33} Re^{0.5} \quad (C.8)$$

(valid for air and diatomic gases for $0.01 < Re < 10000$)

whilst Williams/Kramers expression is used for a sphere [c.f. McAdams (1954) p. 265]:

$$Nu = 0.37 Re^{0.6} \quad (C.9)$$

Overall solution can be obtained by a simple numerical procedure (e.g., 1st-order Newton-Raphson method).

Thus, it can be seen that the direction of the error depends on the relationship between the local temperature and the effective temperature of the surrounding regions:

- flame temperatures are underpredicted as the thermocouple head radiates heat to the relatively cold surroundings
- the lower layer gas temperatures are typically overpredicted because of the radiation from the main combustion regions

In order to correct the measurements to provide estimates of the true gas temperature a number of parameters are required:

- temperature and composition of effective thermal environment
- emissivity of effective thermal environment
- convective heat transfer coefficient (a function of the local gas velocity)
- thermocouple bead emissivity
- thermocouple bead diameter (may increase with soot deposition)

These parameters may be estimated in order to obtain qualitative predictions of the trends and dependencies of the thermocouple errors, or alternatively obtained from CFD solutions as more fundamental predictions. It should be noted that in a post-flashover environment, the first parameter, in conjunction with the second, will be the dominant influence; the convective term is usually small and when convection can be neglected, the remaining parameters cancel from the governing equations, i.e. T_{TC} simply tends to T_{sur} in equ. C.4.

Thermocouple model

A thermocouple simulator model is already available in the CFD code SOFIE. In the current work, the accuracy of the treatment for the radiative flux to the thermocouple bead was improved and the predictions of the model were carefully analysed. Additional checks were made by means of a simple one-dimensional thermocouple simulation implemented in a spreadsheet.

In the SOFIE model, the parameters specified by the user of the model are the bead diameter, shape and emissivity. The calculation does not require any information about the assumed temperature and composition of the surrounding thermal environment since it is based on a fundamentally-derived prediction of the total incoming radiative flux to the bead. Thus the influence of both radiation from the surrounding gases and from any solid surfaces is automatically taken into account, as well as the effects of arbitrary variation in the temperature and composition fields.

The spreadsheet model considers radiation only, neglecting convection. On the basis of predicted temperature in a vertical profile, the model simply integrates, in each direction, the fluxes traversing the vertical path at that location. Gas emissivity/absorptivity is not modelled but is crudely represented as a linear function of the temperature rise. The adequacy of the model developed was demonstrated and the predictions satisfactorily cross-checked by means of this simple spreadsheet-based model.

Appendix D – Model validation

This subject comprises the main phase of the programme of work. It consists of a progressive model validation exercise, in which the engineering methodology developed for the project is applied by all partners to simulation of real fire tests, and additional zone model simulations are carried out to provide supporting information and comparisons.

The fire tests simulated fall into three categories - a localised beam fire test, fire-resistance furnace tests and full-scale tests involving both pool fires and natural fires. The last case mentioned relates to data obtained in the fire tests carried out under 'ECSC Research Project - Natural Fire Safety Concept (NFSC2) - CEC agreement 7210-PR-060' in the "large compartment" at BRE Cardington.

Numerical simulations for verification of the CFD model were carried out for all of the above cases in two stages.

In the first stage, the main emphasis of the verification was on the reproduction of the gas-phase conditions (i.e. neglecting the heat transfer within individual constructional components, such as I-beams).

In the second stage, the emphasis of the verification was on the representation of the temperature development within solid components (i.e., normally steel beams and columns, including "composite" components and those involving other forms of protection) and the derivation of the distributions of certain equivalent model parameters by post-processing the results data. The results of the simulations were also used to identify some of the critical design parameters.

For the BRI beam case, full details of the radiation model sensitivities and requirements are reported, whilst for the VTT large room and the BRE large compartment the sensitivity of the certain numerical parameters, such as grid dependency of the simulation results, is described.

Issues of importance as regards the gas-phase modelling include the following:

- thermocouple temperature simulation
- effect of soot loading
- comparison of "prescribed source" and "flamelet" soot models
- examination of overall heat balance

Localised beam fire tests (BRI beam fire test)

The purpose of initial phase of the validation work was to establish the baseline performance of the CFD model in terms of its prediction of the combustion and heat transfer, rather than the details of the temperature distribution with the steel component. This is reported below following a brief description of the test apparatus.

Experimental details

The experiment was performed at BRI, Japan and is described for instance in Pchelintsev et al. (1997). The setup consists of a gas burner located beneath the centre of a ceiling slab resting on top of a single steel beam, see fig. D.1.

The I-section steel beam has overall dimensions 3.6 m x 0.075 m x 0.15 m with a web of thickness 5 mm and flange thickness 6 mm. The beam was positioned below a ceiling slab consisting of perlite (mineral fibre) board of dimensions 3.6 m x 1.83 m x 0.024 m. A 0.5 m diameter round burner was located below the centre of the ceiling assembly.

The experiments covered 6 different combinations of fire size and beam height, ranging from 95 to 200 kW and with the beam located either 0.6 m or 1.0 m above the fire. These details are summarised in table D.1:

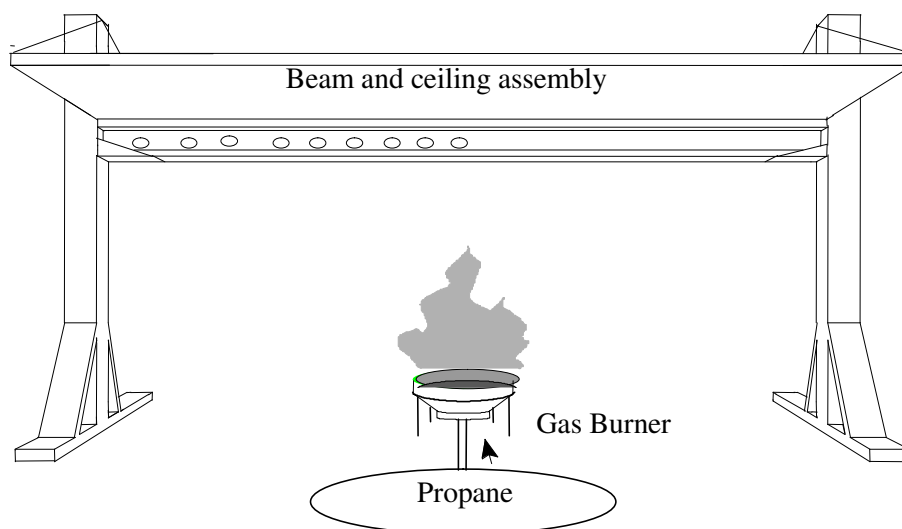


Figure D.1 – Schematic of localised beam fire test

Label	Fire size (kW)	Beam height (m)
95kW-0.6m	95	0.6
130kW-0.6m	130	0.6
160kW-0.6m	160	0.6
100kW-1m	100	1.0
150kW-1m	150	1.0
200kW-1m	200	1.0

Table D.1 – localised beam fire test cases

The test was instrumented to measure total heat fluxes and surface temperatures on the steel beam. The measurement locations were arranged symmetrically about the beam mid-point. The face temperature was recorded on the lower surfaces of both upper and lower flanges and on the web, and at nine positions along the half-length of the beam. The 0.2 mm K-type thermocouples were embedded 0.5 mm below the surface of the beam. Total heat flux measurements were made at the nine corresponding locations along the symmetric half-length of the beam, using water-cooled Schmidt-Boelter gauges. Four gauges were located at each cross-section, positioned to record the heat flux to the downward and upward-facing surfaces of the lower flange, to the web and to the downward-facing surface of the upper flange. The gauges were installed flush with the beam surface through holes in the web and flange; the temperature of the cooling water was measured at 55°C.

Altogether, this set of fire tests provides an excellent set of experimental data for testing the performance of key aspects of the CFD-based methodology. Since the flowfield is relatively simple, the performance of key aspects of the model, such as the plume development and the radiation and convective heat transfer distributions can be studied in detail. Furthermore, because of the relative simplicity of the CFD calculations, parametric and sensitivity studies can easily be undertaken. These have highlighted some of the critical factors in application of the model to this type of problem, and providing useful guidance for the subsequent phases of the work concerned with more complex structures and flowfields.

CFD simulations with SOFIE

The simulations were undertaken mainly with the SOFIE CFD code, though the FLUENT code was also used by one partner. The following description concerning sensitivity studies pertains to the simulation details for the SOFIE runs. In this case, the default structured Cartesian mesh was used, which in early work was described by means of the interpreted input text file and in later work was defined via the JOSEFINE interface in a semi-automatic manner. Since the purpose of the initial studies was to establish the baseline performance of the model in terms of its prediction of the combustion and heat transfer, rather than the details of the temperature distribution with the steel component, the effects of additional mesh refinement in certain regions was not considered at this stage. Base parameters and details of the simulation are set out in table D.2 below.

Two planes of symmetry were used to reduce the size of the simulation domain. By default the whole of the top surface of the calculation domain was defined as a static-pressure boundary, and it was located at a distance of one metre above the ceiling slab. In most cases, the vertical side-wall which runs parallel to the beam axis was also defined as a static-pressure boundary, whilst the other (end) wall was defined as a solid; however, in one case, this order was reversed, with only the end-wall being defined as a pressure boundary. The pressure boundaries/walls were all located at a (horizontal) distance of one metre from the edge of the perlite ceiling slab.

Code	SOFIE 3 (version '24-May-2000')
Default grid	19 x 64 x 17 = 20672 cells
Combustion model	Eddy breakup
Turbulence model	High Reynolds number k-ε model with buoyancy corrections (SGDH)
Radiation model	Discrete transfer (DTRM)
Solver	CGSTAB solver
Interpolation scheme	SOUP for velocity, Hybrid for other solved variables

Table D.2 – base parameters for SOFIE simulations

In the default case described here, 10 cells were used to define a symmetric half of the beam (each of length 0.15 m) along the direction of the axis and there were a total of 17 grid cells along the full length of the calculation domain up to the boundary. A total of 15 cells were used in the horizontal direction perpendicular to the beam and there were 64 vertical cells, with 40 over the 1 m height between the burner surface and the underside of the beam (each of height 0.025 m, i.e. finer than the horizontal dimensions).

In cross-section, the I-section steel beam was represented using six cells vertically and two horizontally as shown in fig. D.2. Because a minimum of two cells must be used in all directions within a solid, it was necessary to represent each of the flanges and the web using a pair of cells in the vertical direction. Since a uniform grid spacing was assumed, this gives a mesh which is a poor match to the true geometry, an inevitability with the relatively narrow steel thicknesses compared to the overall dimensions of the test rig. More cells could have been used, at the expense of computational time, but this was not a priority for the initial sensitivity study.

Combustion was described here by the eddy break-up sub-model, with propane being taken as the fuel. The standard k-ε turbulence model was employed with buoyancy modifications, and with optional Rodi centre-line corrections [Rodi, 1982]. In the radiation model (see next section for more details), the 'theta' and 'phi' band ray number combinations used were as follows:

$$1 \times 4 = 4, 2 \times 4 = 8, 2 \times 8 = 16, 4 \times 8 = 32, 4 \times 16 = 64, 8 \times 16 = 128, 8 \times 32 = 256$$

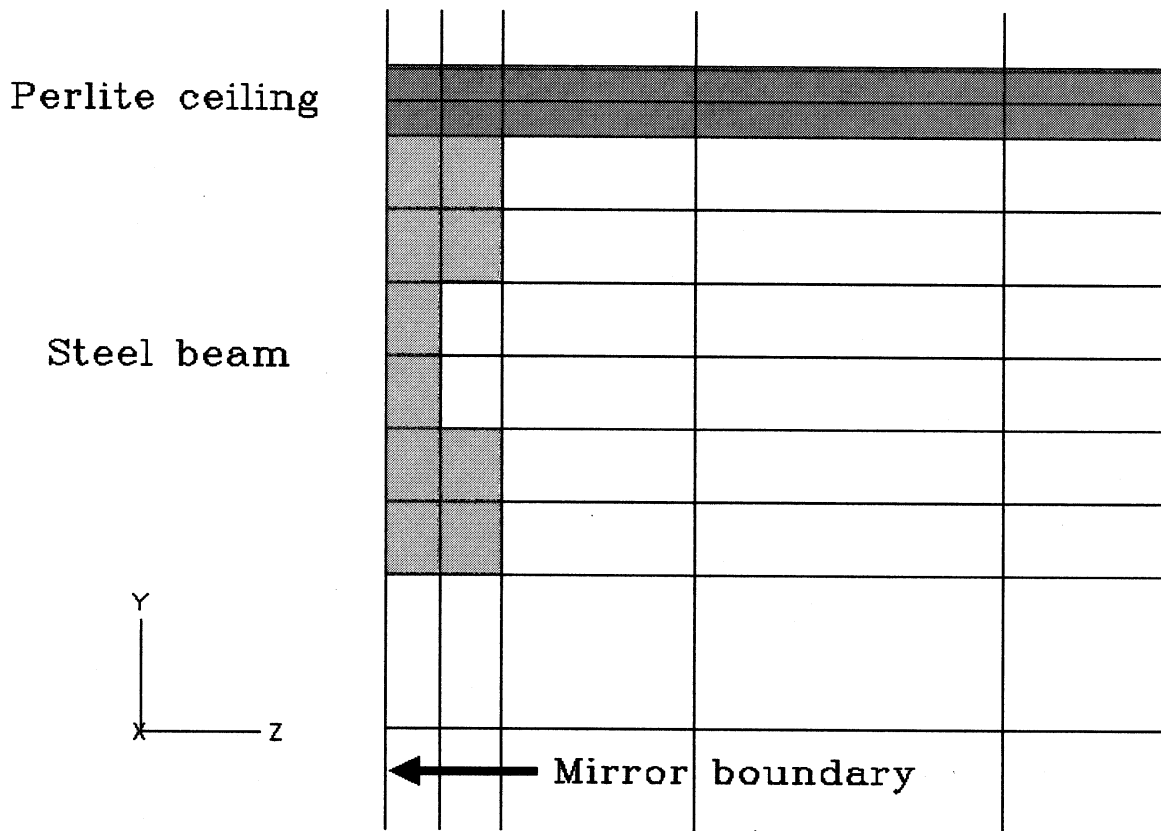


Figure D.2 – computational mesh in region of beam

The CGSTAB conjugate-gradient solver was used for the pressure correction equation in all cases. The HYBRID interpolation scheme was used for all solved variables except velocities, for which the SOUP (Second-Order UPwind) scheme was the default choice.

Three active solids were used - steel for the beam, perlite for the ceiling slab and high-density concrete for the floor. The properties for the steel and perlite were derived from experimental measurements and expressed as 4th-order polynomials of temperature as follows:

$$c_{p,steel} = 582.3 - 889.6\tau + 2289\tau^2 - 1486\tau^3 + 297\tau^4$$

$$c_{p,perlite} = 1493 - 4658\tau + 13743\tau^2 - 14585\tau^3 + 5128\tau^4$$

$$k_{steel} = 70.45 - 27.67\tau - 48.47\tau^2 + 47.22\tau^3 - 10.68\tau^4$$

$$k_{perlite} = 0.3314 - 0.8834\tau + 1.932\tau^2 - 1.960\tau^3 + 0.7226\tau^4$$

where

$$\tau = T / 1000$$

The densities were taken as 7850, 789 and 2800 kg m⁻³ for the steel, perlite and concrete respectively. A value of 0.9 was taken for the emissivity of all solid surfaces except the underside of the lower flange, for which a value of 0.8 was used.

The initial simulations were run as steady-state for simplicity. In fact, the experimental data was obtained at a time of 20 minutes from start-up, at which point the thermal behaviour will not quite have reached steady-state (see fig. 13 in Pchelintsev et al. (1997)). However, the difference in steel surface temperatures is not likely to be large, so this approximation is acceptable.

Satisfactory convergence was always obtained after less than 1000 iterations⁴.

Parameter changed	Details of parameters used
Baseline	EBU, DTRM 32rays, banded WSGG RTE solution, Truelove CH ₄ coefficients, 40 cells at 25 mm below beam, 'original' DTRM discretization
DTRM rays	4, 8, 16, 32, 64, 128, 256 rays Polar ray, + 4, 8, 16, 32, 64, 128 rays
RTE solution method	Lumped transmissivity/constant absorption coefficient Lumped transmissivity/total property WSGG absorption coefficient Lumped absorption coefficient/constant absorption coefficient Banded transmissivity/total property WSGG absorption coefficient Banded absorptivity/total property WSGG absorption coefficient Total property WSGG Banded WSGG
WSGG coefficients	Truelove CH ₄ coefficients Truelove oil coefficients Taylor & Foster CH ₄ coefficients Taylor & Foster oil coefficients Smith oil coefficients
Pressure boundary	Moved the SP boundary from side wall to end wall Increased turbulence level in inflow
Plume/turbulence	Nam & Bill's modifications ($C_{\mu}=0.18$, $\sigma=0.85$) [Nam & Bill, 1993] Reducing turbulent Prandtl-Schmidt number to 0.5 Rodi centre-line corrections [Rodi, 1982] Bilger density factor in the k- ϵ source term [Bilger, 1994] Reduced eddy breakup constants by factor of 2 and 10

Table D.3 – SOFIE localised beam fire simulation test cases

The performance of SOFIE's DTRM radiation model was first investigated in detail. Also, some factors affecting plume spread rate were examined. Grid resolution effects were also investigated. Details of some of the test cases examined are listed in table D.3.

An illustrative plot of the predictions is shown in fig D.3. Initial quantitative analysis of the radiative heat flux distribution suggested that reasonable predictions had been achieved, particularly for locations far from the fire plume and also near the stagnation point. However, just outside the fire plume, the predicted flux was about a factor of two lower than the experimental value. Overall, the prediction showed a somewhat different flux profile compared to the experimental result.

⁴ Optimised constant under-relaxations of 0.4 were used for solved variables & 0.5 for mixture fraction

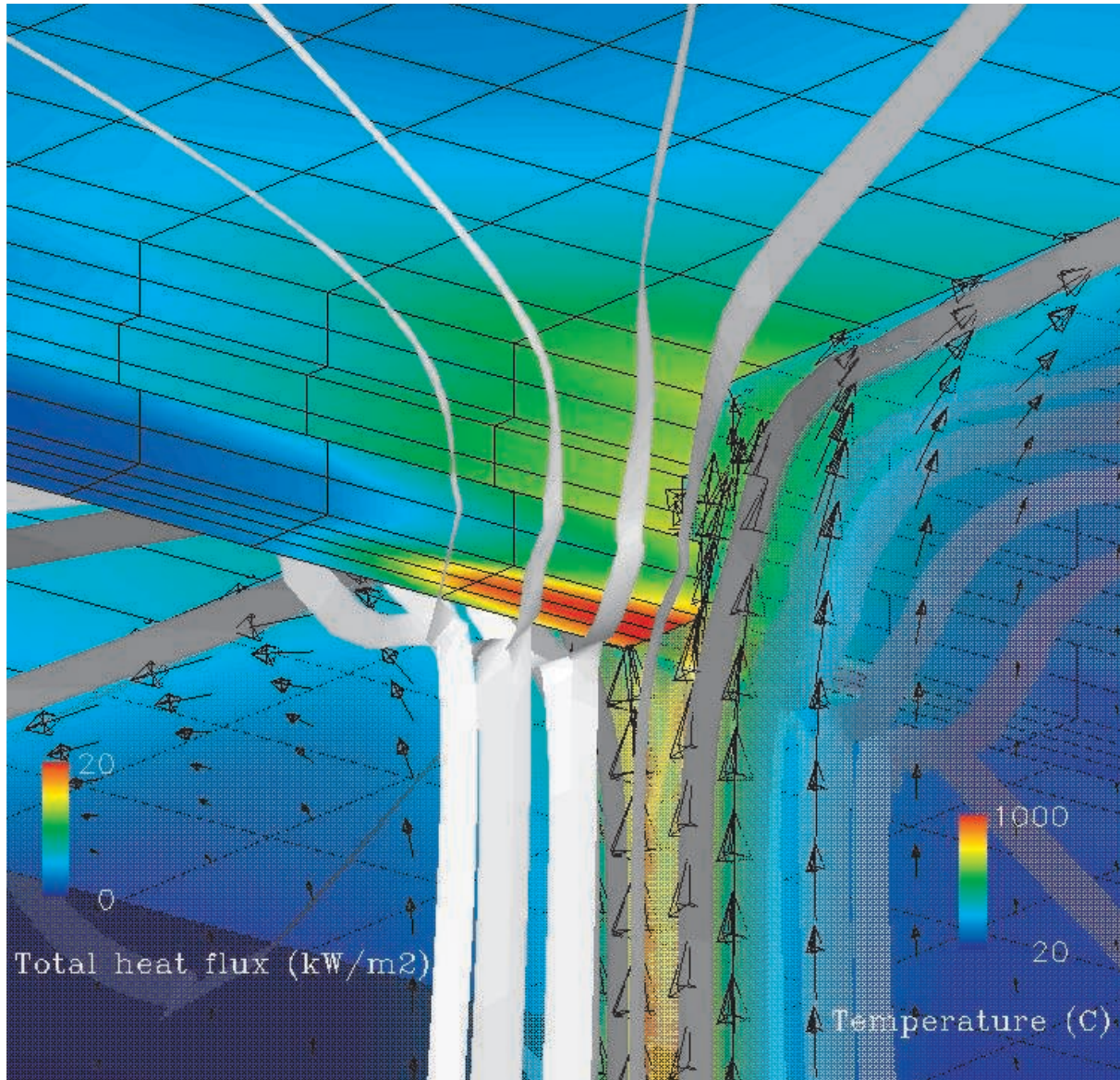


Figure D.3 – SOFIE prediction of heat flux distribution and flowfield in impingement region on underside of beam/ceiling slab assembly ^[BRE]

In order to investigate this apparent flux underprediction, careful investigations of the performance of the radiation model were undertaken, and many more simulations were run to examine the sensitivity of the predicted flux to the various variable parameters in the discrete transfer radiation model. Some fundamentals regarding the radiation model and the options available in SOFIE are described in Appendix A.

Another relevant aspect in the case of a localised fire is the predicted plume spreading rate. There are well-known uncertainties associated with modelling axisymmetric plumes using the standard k-ε turbulence model and the effect of various proposed modifications was investigated (c.f. last section of table D.3).

Determining which is the appropriate model for a given application can only really be done by trial and error. Thus, in this study, the prediction of the different model variants and the run-time overhead associated with radiation were compared. Space precludes presentation of detailed results here, but a summary of the findings is presented in tables D.4 and D.5.

Parameter changed	Effect
DTRM rays	8 or more rays were sufficient Polar ray boosted peak flux but by less than 20%
RTE solution method	Very little influence on peak fluxes but 40% higher remote fluxes using the most detailed banded model
WSGG coefficients	Good agreement between all models with exception of Smith oil model; more detailed analysis of latter identified an inconsistency in the expression of the model
Pressure boundary	Moving the static pressure boundary to the end caused a slight modification in the flowfield with higher peak fluxes but little difference further from the impingement point
Plume/turbulence	Nam & Bill's modifications gave a slightly reduced peak flux but little evidence of a wider plume

Table D.4 – summary of parametric study findings for localised beam fire test case

Lumped transmissivity/constant absorption coefficient	100.7
Lumped transmissivity/total property WSGG	100
Lumped absorption/ constant absorption coefficient	141
Lumped absorption/ total property WSGG	137
WSGG/ total property WSGG	697
WSGG banded	896

Table D.5 – normalised radiation computation periods for localised beam fire test

The next part of the study examined the performance of the model for the other fire size and beam height combinations, with heat release rates ranging between 95kW and 200kW and beam heights of 1m and 0.6m. The basic simulation parameters adopted were identical to those for the 100kW-1m default case (see table D.2), though the number of cells below the beam was reduced in the case of the lower beam height, such that the cell size was maintained constant. Results for these cases are shown in fig. D.4. It can be seen that the results for the other fire sizes with the 1 m beam height (150kW-1m and 200kW-1m) bear out the original results with regard to the underprediction of fluxes just outside the fire plume region. The results for the reduced beam height (0.6 m) on the other hand (95kW-0.6m, 130kW-0.6m, 160kW-0.6 m) show a general underprediction of the fluxes in the fire region.

Overall, the results called for a more detailed examination of the predicted flowfield. Visual examination, see for example fig. D.4, clearly showed that the fire plume does not spread out in a symmetrical manner upon impingement, but rather divides laterally around the steel beam. Thus, the bulk of the flow moves out radially over the underside of the ceiling, and there is no appreciable flow along the underside of the beam itself. If this phenomenon had not been observed in the experiment, then the underprediction of fluxes just outside the fire plume region might be simply explained. However, the tests had been recorded on video and the flame extensions determined visually, as reported for instance in Pchelintsev (1997). An analysis based on the resultant correlations determined that the expected flame extension should be of the order of 0.38m for the default 100kW-1m case. This is apparently in agreement with the value observed in the simulations. Therefore it seems that underprediction of the extent of the flame length is not a major contributor to any discrepancies in the heat flux profile. On the other hand, the correlated flame length beneath the ceiling itself also seems to be rather short at 0.40m - i.e. all of the hot flow leaves the ceiling slab to the sides, with none reaching the edge at the end of the beam axis. Though it is harder to determine the equivalent flame length from the simulation in this case, since a very thin hot flow layer does persist along the entire length of the ceiling, it does seem likely that this value has been overpredicted by the simulation. To clarify this matter, it would be necessary to examine the videotape footage.

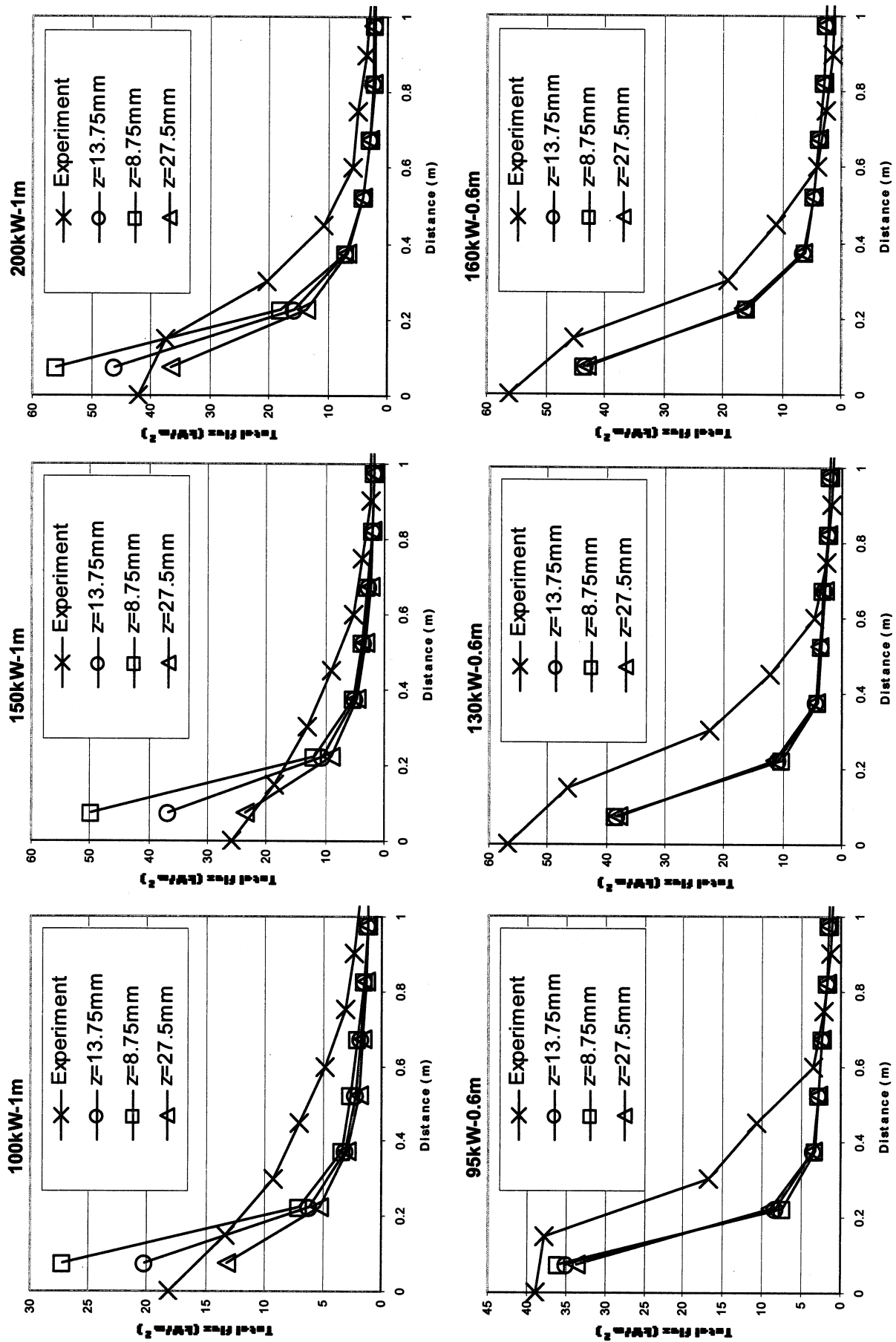


Figure D.4 – predictions versus experiment for different size/beam height combinations [BRE]

The predictions of ceiling jet thickness were assessed by exploiting the theoretical model developed by Alpert (1975). This suggested a value of about 5% of the rise height to the impingement point, corresponding to a height of 50mm in the case of the 1m beam height test, only a third of the height of the steel beam itself. Though the presence of the I-section beam itself will clearly have some influence on the jet thickness, it seems that it could be safely assumed that the ceiling jet thickness applicable away from the impingement point region would not be sufficient to expose the lower surface of the beam to the hot flow. This is in accord with the experimentally-derived correlation for flame length extension below the beam and also with the CFD model flowfield prediction. Hence there is no reason to suspect that there is any significant modelling inaccuracy in this area.

In order to investigate the sensitivities of the predictions to the numerical grid used in the study further simulations were run for different grids:

- doubled vertical grid resolution
- quadrupled vertical grid resolution

The findings show quite a significant influence of grid resolution on plume temperature, with lower temperatures near the impingement point with the finer meshes. The influence was less when the beam and ceiling assembly was removed so it seems that the effect arises from the influence of the beam and ceiling on the predicted flowfield, and must be consistent with some balance between the calculated turbulence and temperature fields (each parameter influences the other). The main consequence of the reduction of the plume temperature was a lower peak radiative flux, though the levels along the beam axis were little changed. Also, due to the influence of turbulence, the convective heat flux was increased, such that total fluxes were also slightly increased away from the impingement point and increased by about 20% at the impingement point with the finer y-grid.

A more detailed study was required to fully clarify the reasons for the observed discrepancies and to resolve the remaining differences. The above simulations adopted a simplified ‘coarse grid’ representation of the steel I-beam geometry, together with “equivalent” material thermal properties. With the latter, the thermal conductivity is scaled up by the ratio of the flange (or web) thickness in the model versus the real geometry, whilst the specific heat is scaled down by the same ratio. This approximation is not ideal where axial conduction is important since heat transfer in the third (correctly represented direction) is also scaled by the same ratio and in the current case should give artificially high levels of axial conduction. This factor would not of course affect the incident radiative fluxes but it would have a second-order influence on the total flux on which experimental comparisons are based via the surface temperature influence in the convection term.

To overcome this last-mentioned problem, further simulations were run in which the real geometry of the beam was defined and which used sufficient cells in the computational domain that the cell aspect ratio nowhere exceeded 60. The results of these simulations are shown in figs. D.5 - D.10. These figures show the comparison of the predicted and measured incident fluxes, and figs. D.9 - D.10 show the comparison of the predicted and measured surface temperatures in the lower and upper flanges. It can be seen that the predicted temperatures agree quite well with the experimental values. The fluxes are more variable but are generally better for the real beam geometry. This difference in sensitivities arises because the steel member is a good conductor of heat, thus tending to quickly smooth out any variations in incident flux profiles.

A further study of the effect of the fire size on the heat transfer was also undertaken. The peak convective heat transfer coefficient value showed quite a low sensitivity to the fire heat release rate as shown in fig. D.11.

Fig. D.12 shows the breakdown of the total heat flux to an hypothetical lower flange Gardon gauge (taken to be 55°C, as reported in the experiment), including both convective and radiative components. Two sets of curves are included encompassing trial modifications of the inflow turbulence intensity, i.e. 5% and 100% (the former is more realistic whilst the latter is perhaps excessive). This figure also shows the total heat flux curve from the original simulations described above (labelled “coarse”).

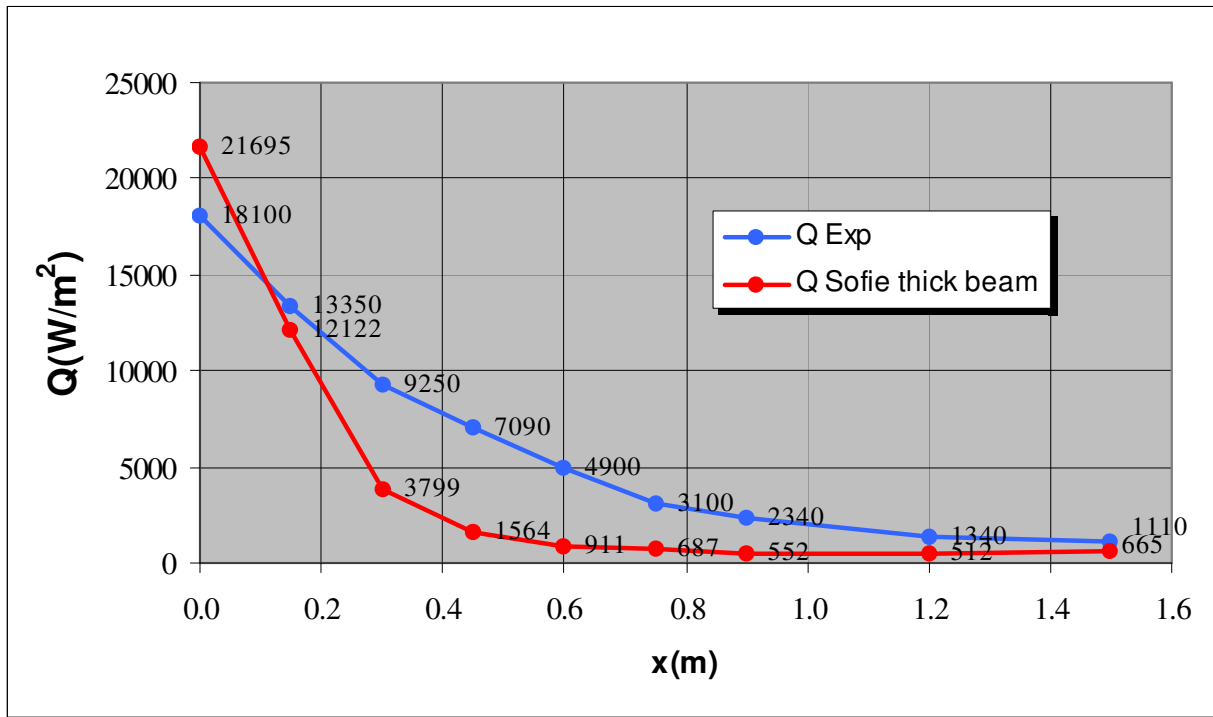


Figure D.5 – incident heat flux to lower flange upward-facing surface [LAFBEIN]

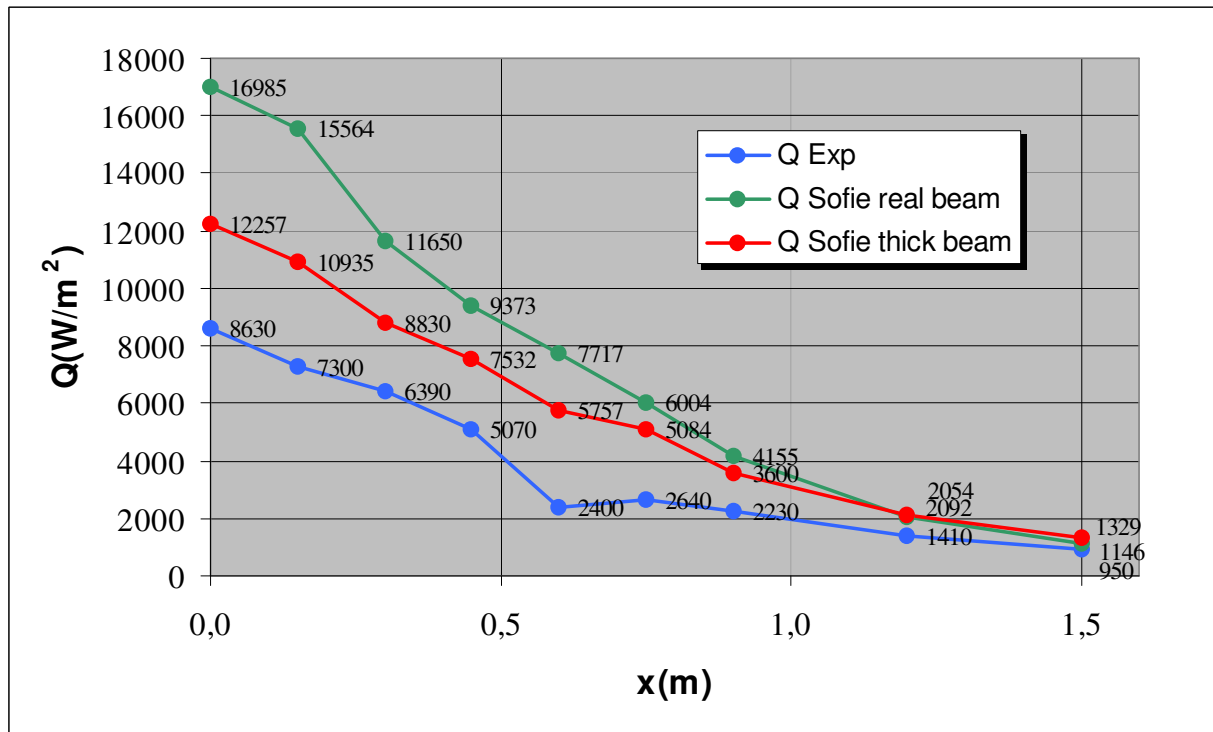


Figure D.6 – incident heat flux to lower flange upward-facing surface [LAFBEIN]

By comparison, the results now indicate a much higher flux further from the impingement point. The low values in this region were a puzzle earlier in the project and the subject of detailed investigations. The reason for the difference in the results must be primarily associated with the more finely resolved grid in the burner region which is now described with 40 cells in quarter symmetry, i.e. equivalent to 160 cells overall. By contrast, the baseline case had only 5 cells in the burner source in quarter symmetry, but a similar number of cells overall, and the grid sensitivity studies performed for this grid tended to look at each co-ordinate direction in turn.

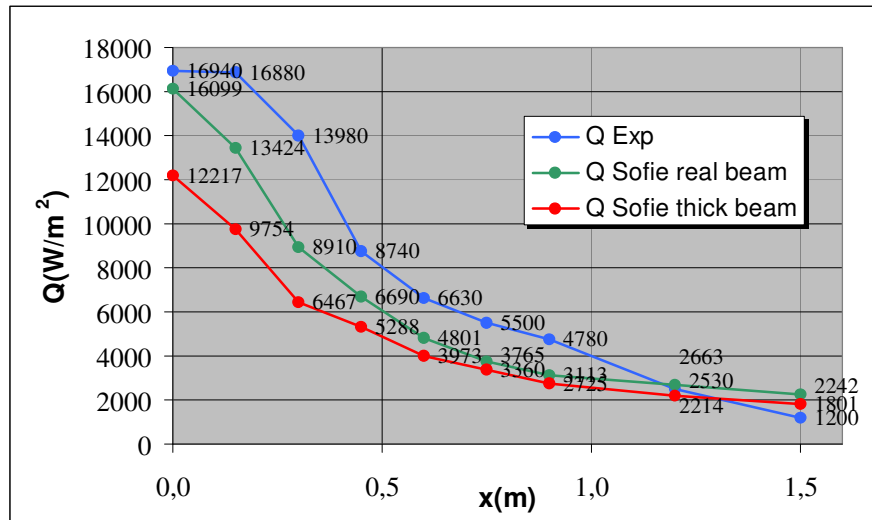


Figure D.7 – incident heat flux to ceiling [LABEIN]

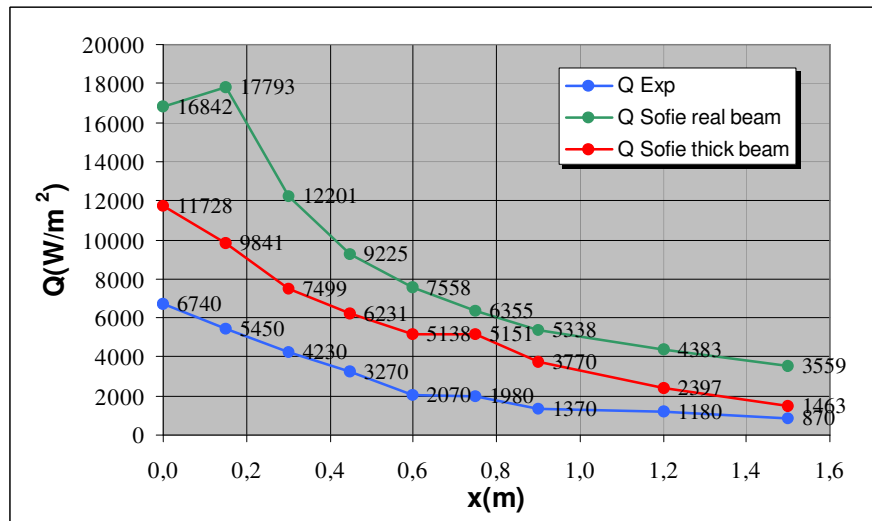


Figure D.8 – incident heat flux to upper flange [LABEIN]

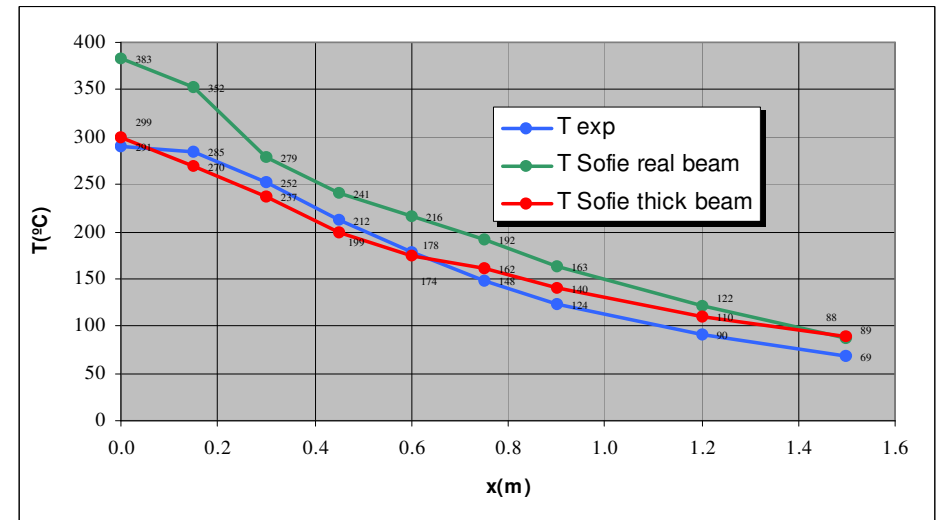


Figure D.9 – temperatures in the lower flange [LABEIN]

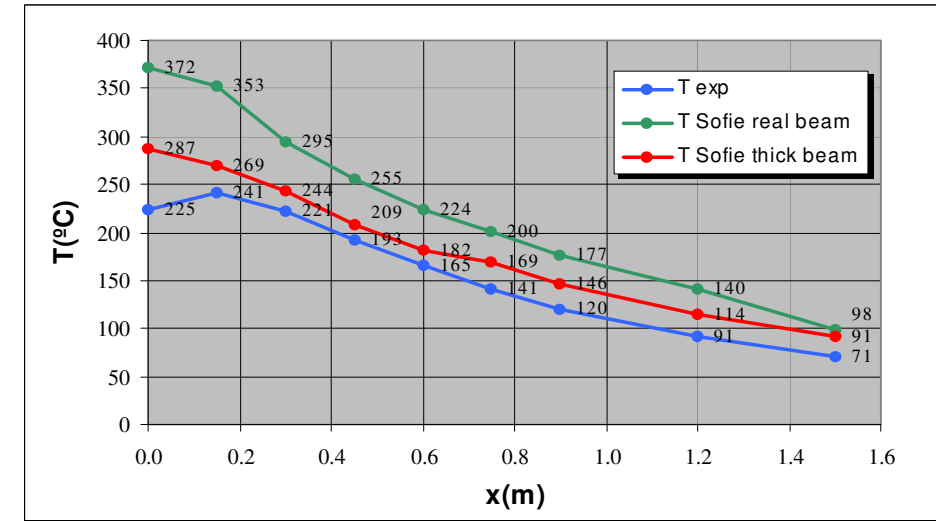


Figure D.10 – temperatures in the upper flange [LABEIN]

The fact that the grid has affected the plume width can be clearly appreciated from fig. D.13 which provides the breakdown of the calculated convective flux to a water-cooled gauge. In this figure the flux labelled “convective” is extracted directly from the SOFIE calculation and is the value pertaining to convective transfer to the heated steel member; the “correction” term is the additional flux which would be present if the heated surface were in fact a water-cooled flux gauge (with temperature 55°C as in the test); the “convective gauge” curve represents the sum of the two, i.e. the predicted flux to a water-cooled gauge. This data is consistent with that shown in fig D.11 which indicates a flame extension beneath the lower flange of over a metre either side of the impingement point.

These findings suggest that a more detailed resolution of the fire source is required for accurate results when considering localised heating, particularly where plume spread rates are critical. The ease of problem set up with the JOSEFINE interface and the improvements in computer speed even within the duration of this project has made this type of problem considerably easier to analyse than it was during the earlier studies. The remaining discrepancy between the experiment and the predictions may well disappear entirely when the fire source is resolved further.

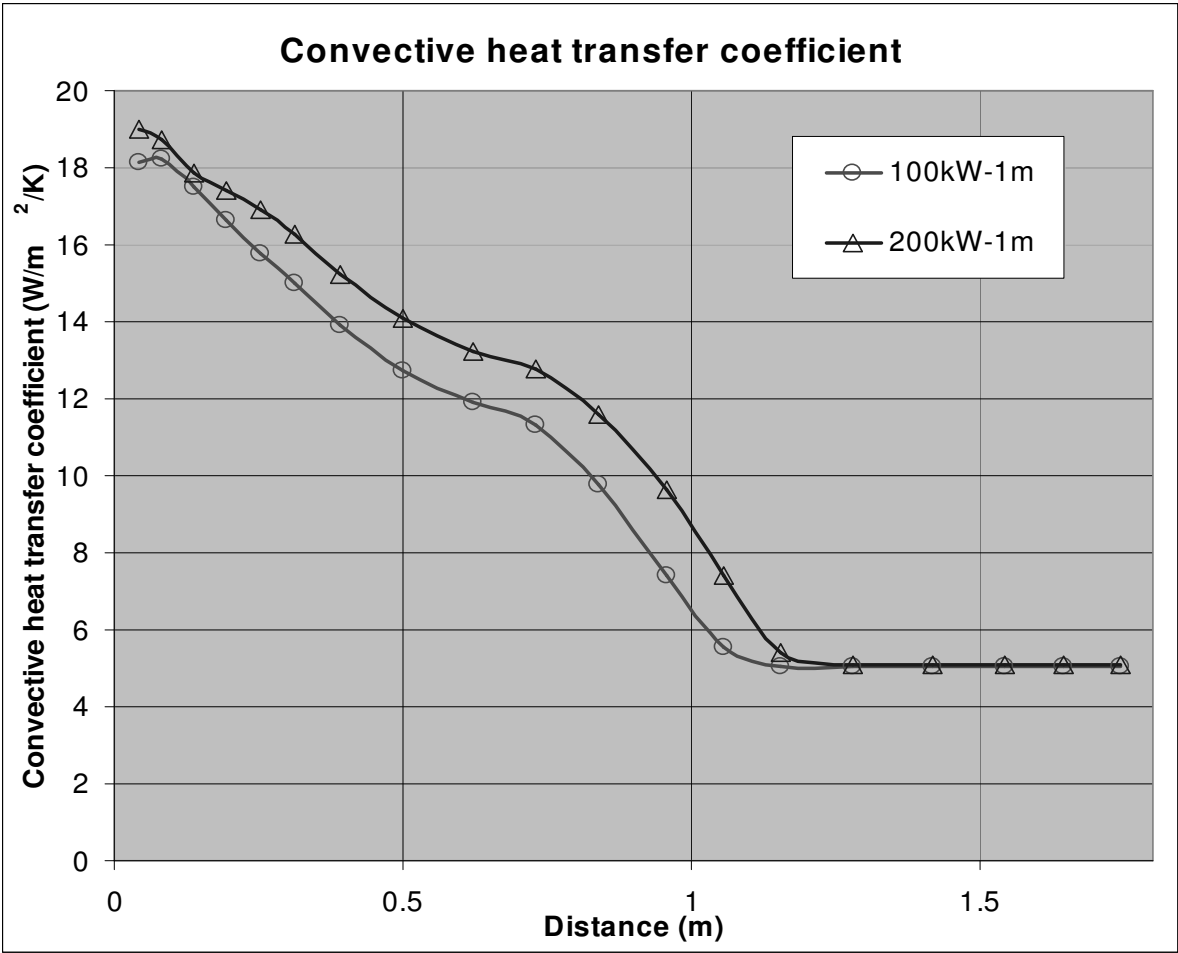


Figure D.11 – lower flange width-averaged convective heat transfer coefficient variation with distance and dependence on fire exposure (symmetry is used) ^[BRE]

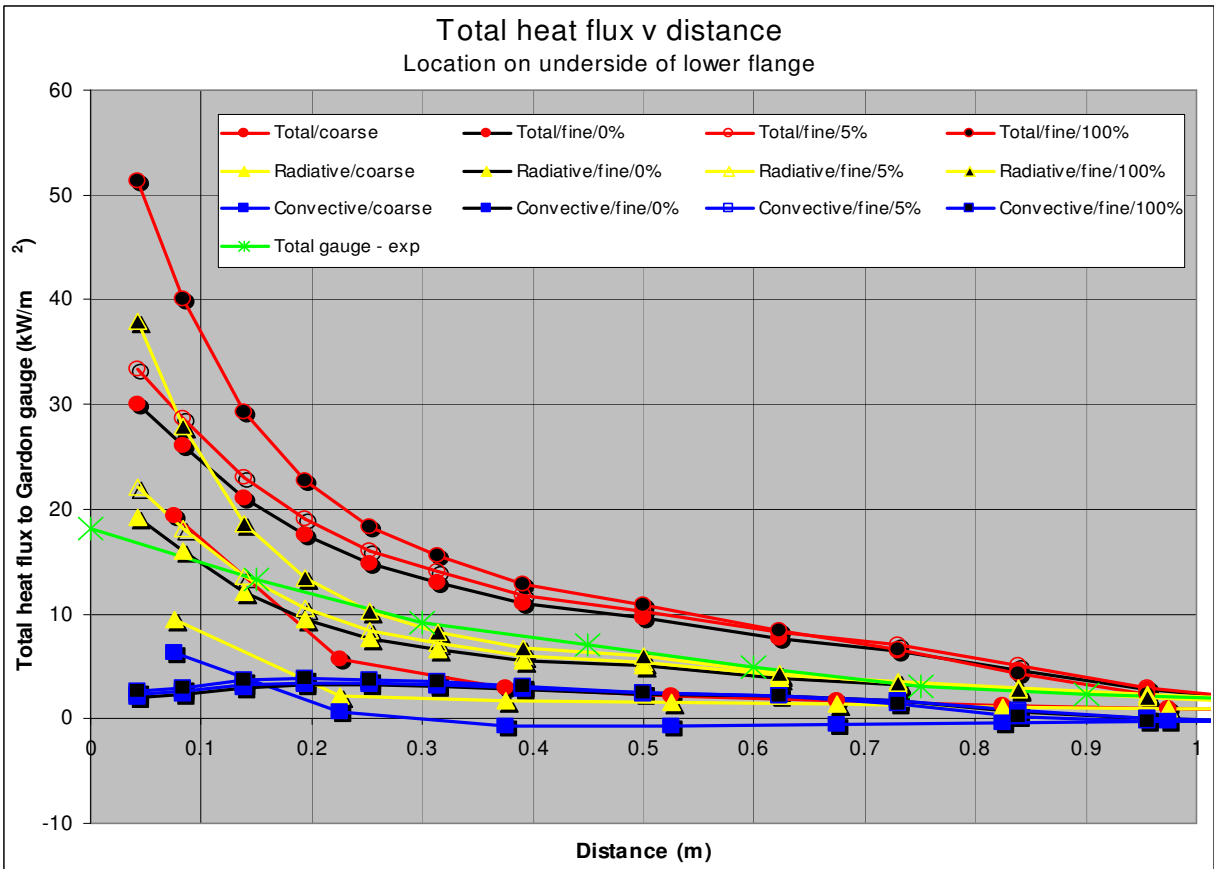


Figure D.12 – lower flange width-averaged heat flux breakdown ^[BRE]

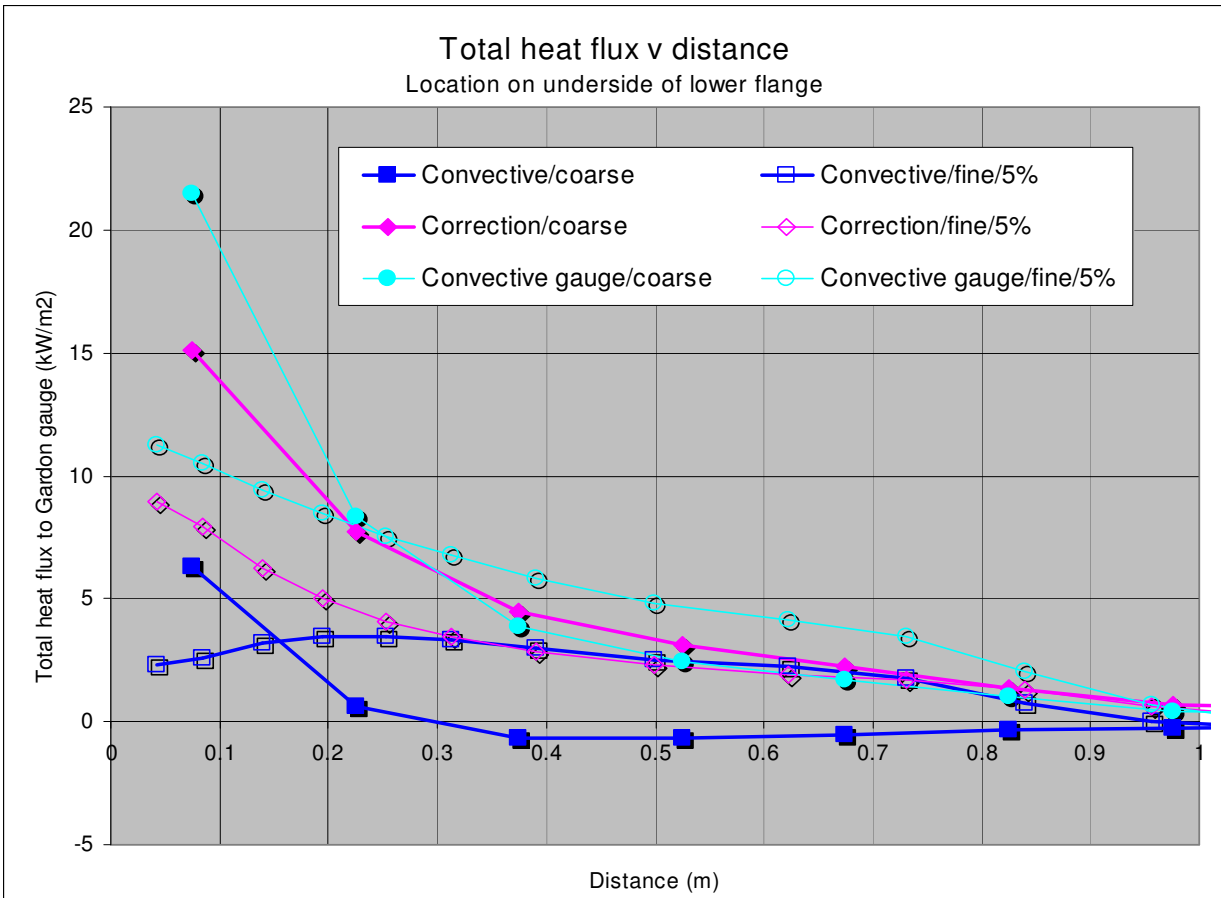


Figure D.13 – lower flange width-averaged convective heat flux ^[BRE]

Fire-resistance furnace tests (VTT scale furnace; Standard fire-resistance furnace)

VTT scale furnace

Experimental details

The experiments were conducted in the scale furnace of VTT Building Technology, which is a 1.5 m × 1.5 m × 1.3 m (height) chamber with four oil burners. A side elevation of the furnace is shown in fig. D.14 (the four burners, which are not quite axially-opposed, are indicated by the circles on the furnace wall).

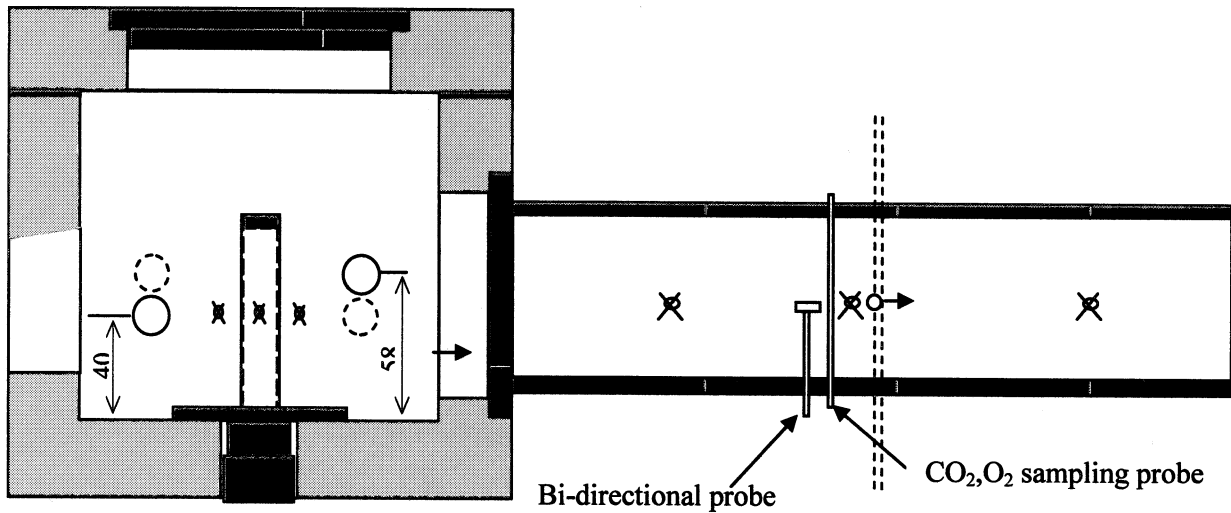


Figure D.14 – VTT scale furnace schematic

The combustion products were exhausted freely through a circular duct attached to the front wall of the furnace. Two steel columns were used as test specimens, one black and one made of stainless steel.

The fuel of the furnaces is light heating oil (light diesel oil). The oil mass flow into the furnace was measured during the experiment, but the air flow was not. However, for the boundary conditions of the CFD-model, the air flow can be estimated by looking at the simple chemistry of the furnace combustion.

The second test of the series, where only one burner was used, was used in the simulations.

CFD simulations with SOFIE

The simulations of the experiment were carried out using the SOFIE CFD-code with default model parameters as detailed in table D.6 below. A three-dimensional model of the furnace, shown in fig. D.15, was created using the JOSEFINE graphical user interface. The exhaust gases flow to the positive x -direction, the bottom of the furnace lies on the $y = y_{min}$ boundary and the fire (burner) is located on the $z = z_{min}$ boundary. $60 \times 32 \times 42 = 80640$ cells were used in a non-uniform grid, corresponding to an approximately average cell size of 5 cm inside the furnace.

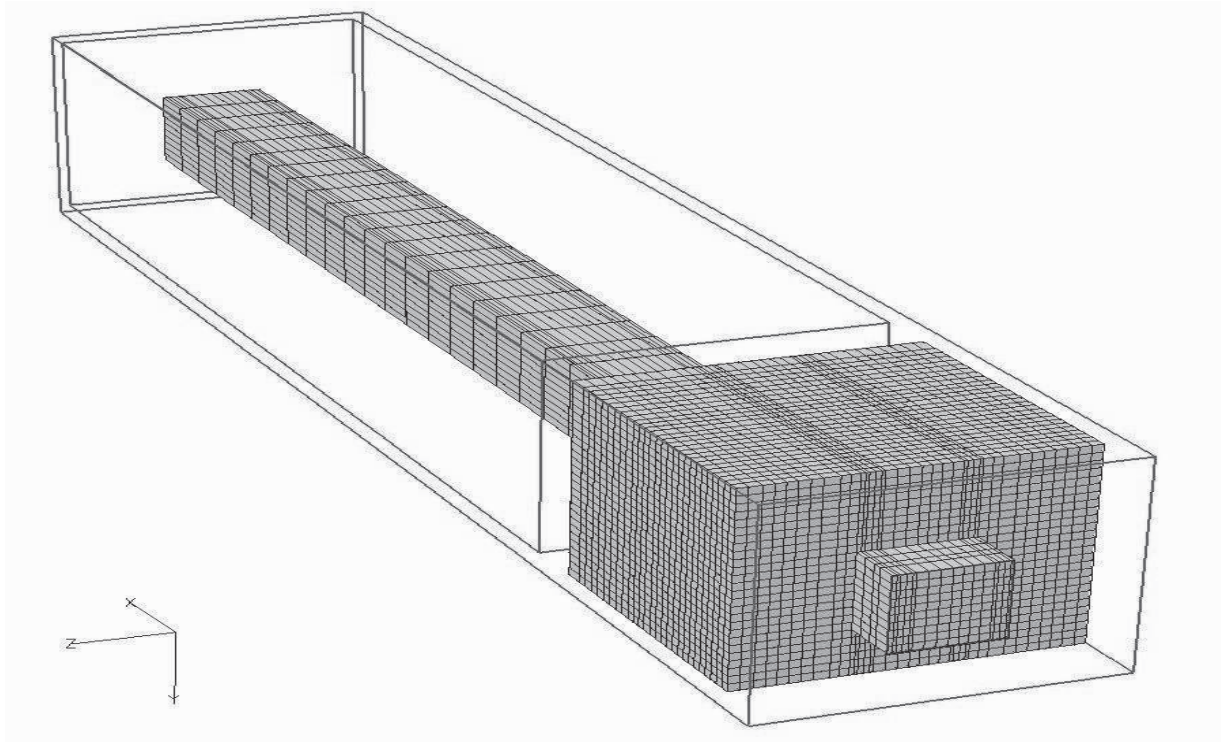


Figure D.15 – overview of the VTT scale furnace model

CFD Model		
<i>Solution Model</i>	Solver Viscous Turbulent Model Energy Gravity Combustion Radiation	SOFIE - 3D - transient flow High Reynolds k-epsilon (2 equations) Standard wall functions Active Active (+y direction) Eddy breakup model Discrete Transfer – Truelove absorption coefficient model – 2 theta rays, 8 phi rays
<i>Material</i>	Kerosine Brick Steel	Net heat of combustion: 43.434 MJ/kg Molecular weight: 167.0 Density: 2100 kg/m ³ cp= 889 J/kg/K k= 1.1 W/m/K emissivity = 0.90 Density: 7850 kg/m ³ cp = 460 J/kg/K k = 45.8 W/m/K emissivity = 0.98
<i>Boundary Conditions</i>	Inlet: fuel inlet Inlet: air inlet Outlet: pressure outlet	Material: kerosine Velocity: time dependent Temperature: 293 K Turbulent kinetic energy : 5.0 m ² /s ² Turbulent dissipation rate : 0.7 m ² /s ³ Material: air Velocity: 9.4 m/s Temperature: 293 K Turbulent kinetic energy : 5.0 m ² /s ² Turbulent dissipation rate : 0.7 m ² /s ³ Turbulent kinetic energy : 1.0% Dissipation length scale: 3.0x10 ⁻⁶ m

Table D.6 – SOFIE input details for VTT scale furnace test

Boundary conditions

The furnace burner was modelled with a fuel inflow boundary of two by two cells, surrounded by an air inflow region which was two cells wide. The fuel inflow rate was defined based on the time-dependent heat release rate. The airflow rate was set to 0.32 kg/s. The location of the burner boundaries is shown in fig. D.16. The end of the exhaust tube was modelled as a static pressure boundary.

The furnace surface material was brick. Active solids which were four cells thick were therefore defined around the furnace space. The blockages around the exhaust tube were defined to be "inactive".

Steel columns

The STELA solid solver developed in this work was used to calculate the heat transfer in the two steel columns. The original rectangular shape of the columns was replaced by the I-shape, which was the only option in the model at the time. The thickness of the steel in the original columns was 4 mm. To conserve the mass in the model, the flanges and web were defined 4 mm and 8 mm thick, respectively. The idea is shown in fig. D.17.

The default rules were used for the generation of the finite volume grid inside the columns. The resulting grid is shown in fig. D.18.

In the experiment, the column which was close to the burner was made of stainless steel AISI 304 (see Appendix A) and the second one was made of black steel S355. In the simulation, the emissivities of stainless and black steel columns were set to 0.2 and 0.9, respectively. The initial temperatures were set to 50 °C and 56 °C, based on the measured mean temperatures.

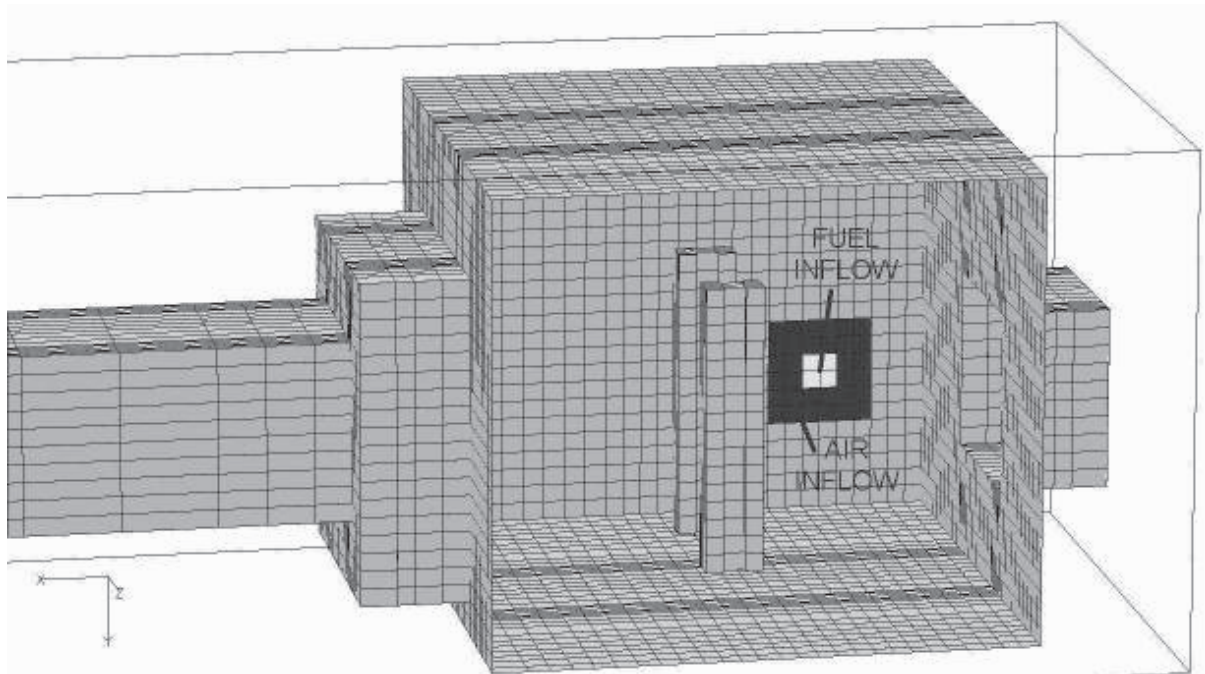


Figure D.16 – overview inside the VTT scale furnace; the fuel and air inflow boundaries are indicated

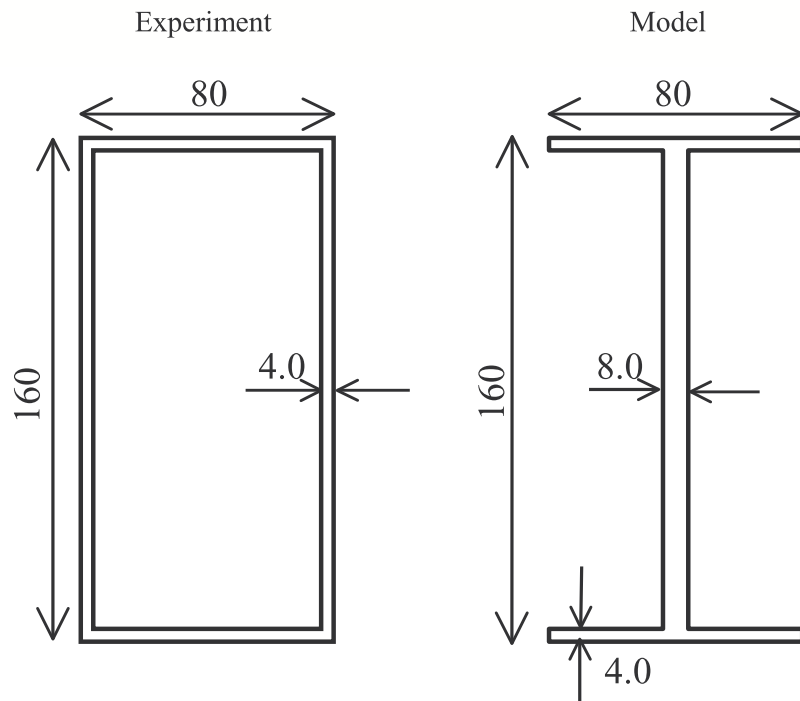


Figure D.17 – modification of the steel column cross-section from rectangular to I-shape [mm]

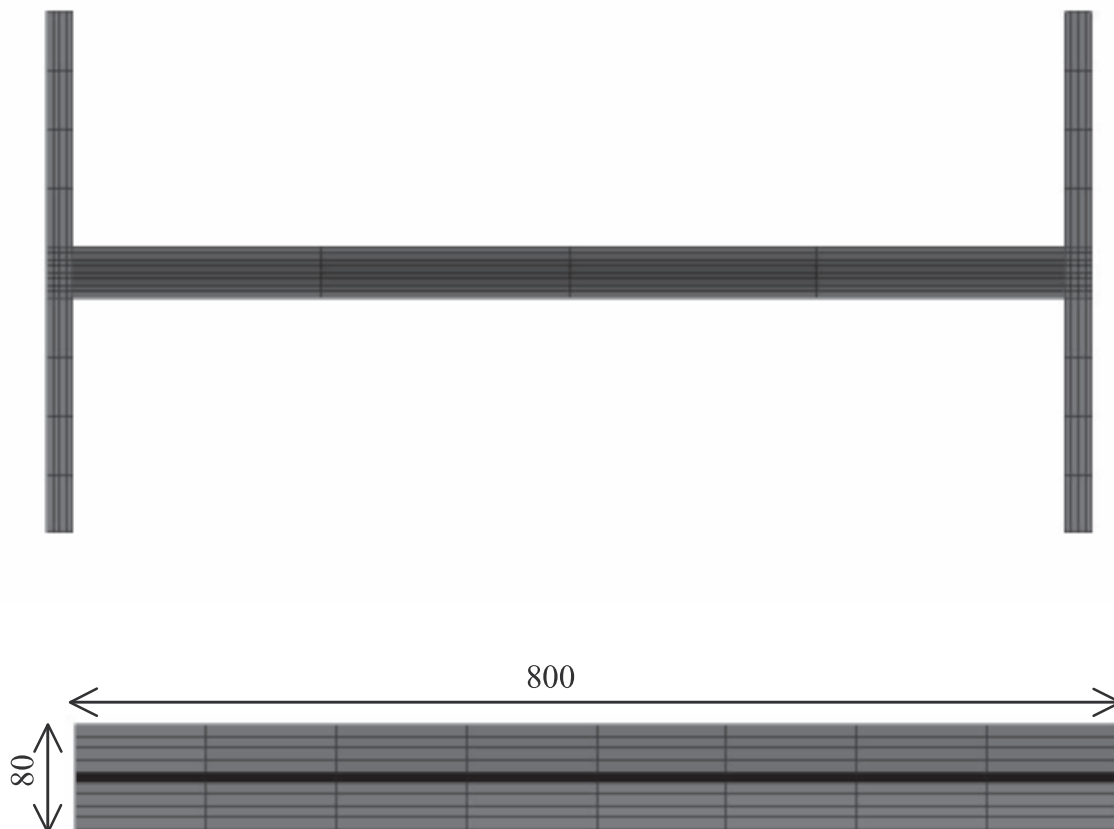


Figure D.18 – finite-volume grid inside the columns

Simulation results – gas phase

Transient simulation of the first 15 minutes of the Test 2 was done. This simulation took approximately 3 days on a 1.7 MHz PC, having Windows 2000 operating system, and 1 GB memory.

An overview of the flowfield at the vertical plane cutting through the centre of the furnace is shown in fig. D.19 at three time levels. It can be seen that there is a strong circulation zone inside the furnace, with high temperatures in the flame. There is very little difference in the flowfield between the time points.

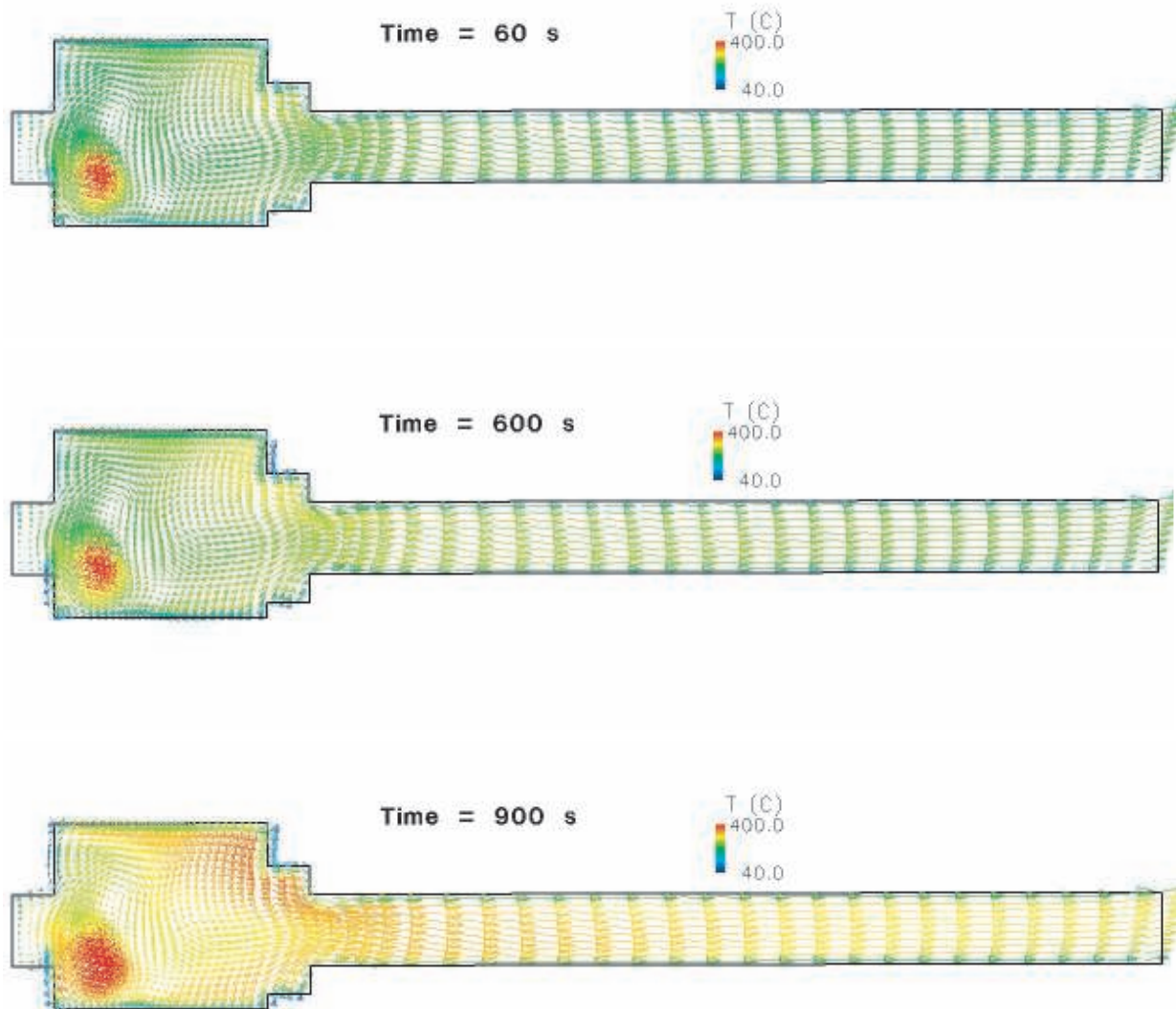


Figure D.19 – overview of simulated flowfield inside scale furnace and exhaust tube ^[VTT]

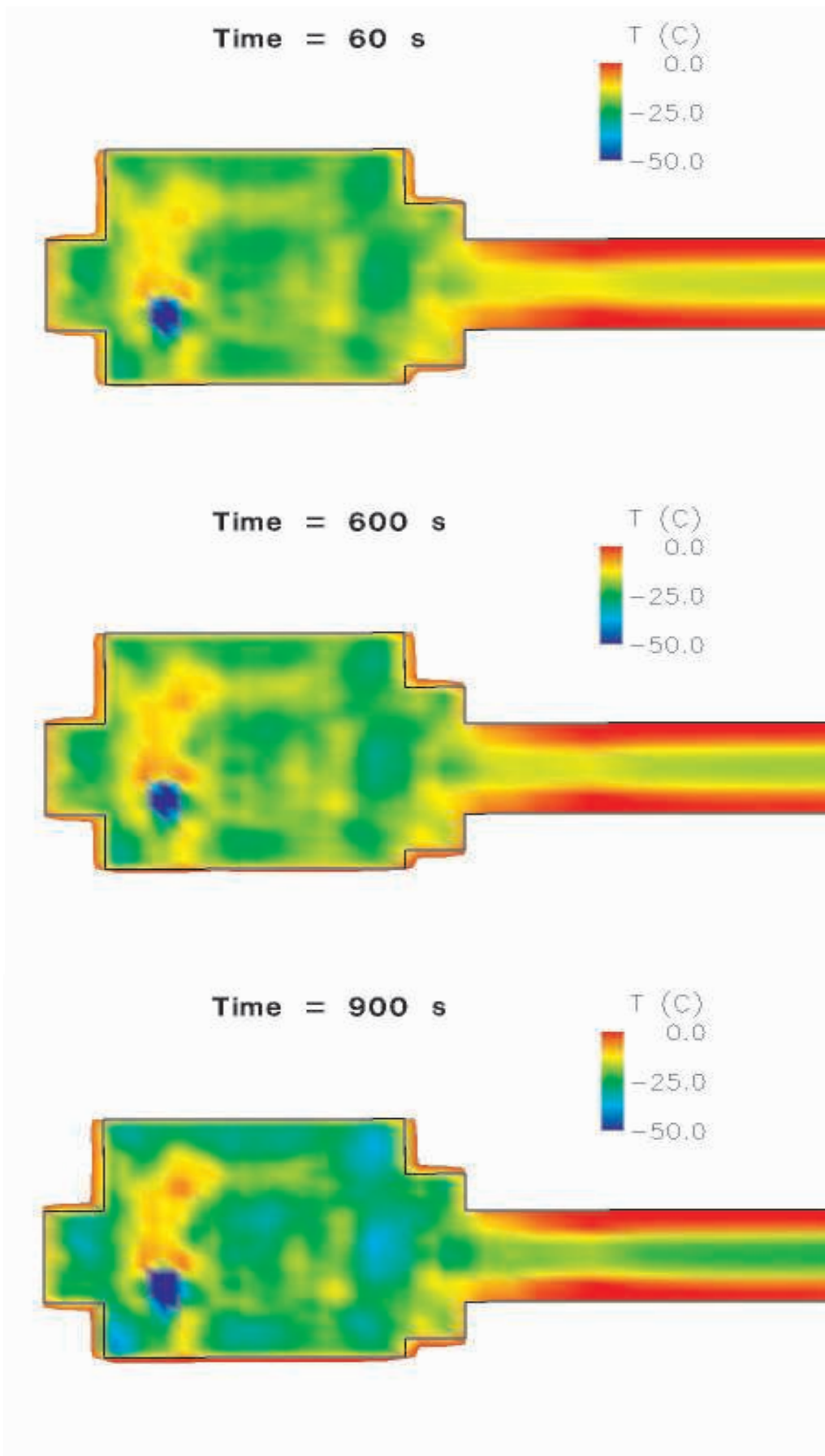


Figure D.20 – simulated "thermocouple error" $T_{TC}-T_{gas}$ inside scale furnace ^[VTT]

For the comparison with the experiments, the simulated thermocouple temperatures were stored. The difference between the simulated thermocouple temperatures and gas temperatures, which is often called "thermocouple error" is shown in fig. D.20. For most parts of the domain the thermocouple values are about 25 °C lower than the gas temperature, due to the influence of the relatively cold walls. Inside the flame domain, this difference is much bigger as the loss here is from a smaller high temperature region.

Fig. D.21 shows a comparison between the measured and simulated thermocouple temperatures inside the furnace. The measured and simulated CO₂ volume fractions in the middle of the exhaust tube are compared in fig. D.22. Both comparisons show excellent agreement, though the air inflow, which is uncertain anyway, had to be adjusted slightly to give the best match. However, as the adjustment was very small (from 0.32 kg/s to 0.35 kg/s), this shows that the overall heat transfer and combustion processes are predicted well.

Simulation results – solid phase

As the steel is a very good conductor of heat, all the temperature fields were very uniform over the cross-sections. However, the transient behaviour can be seen even from the surface temperatures, shown in fig. D.23. It is apparent that the spatial differences within one column and between the columns are very small.

The net heat flux into the columns is shown in fig. D.24. The value is highest at the beginning of the fire, when the steel is cold. It decreases to nearly zero when the steel temperature approaches the steady-state condition. After the increase of the burning rate, the heat flux increases again.

The measured and simulated temperatures of the black steel column are compared in fig. D.25. The comparison is made at one cross-section, located approximately at the mid-height of the column. The simulation results shown correspond to minimum and maximum temperature over the cross-section, at the corresponding time step. The overall temperature level is rather low, because the initial temperature of the simulation (20 °C) was smaller than in the experiment. However, the trend of the heating is very well captured.

Figs D.26 and D.27 show the predicted convective heat transfer coefficient as a surface plot and a histogram respectively. The dominant value is in the range 10-15 W/m²/K though values up to 33 W/m²/K were recorded at specific locations and the lowest value was about 5 W/m²/K.

In summary, the SOFIE CFD code has reproduced reasonably well both the gas-phase combustion and heat transfer and the solid-phase thermal characteristics of the fire-resistance furnace test.

Standard fire-resistance furnace

Reference was also made to the results of simulations undertaken on a full-scale wall furnace used for standard fire-resistance testing, as reported in Welch & Rubini, 1997. The specimen had dimensions 3m x 3m and the width of the furnace is 1m, so that the total enclosed volume is 9m³. There were two sets of seven burners arranged opposite each other in the end walls, orientated perpendicularly to the specimen and exhaust walls.

In the simulations the time variation of the averaged values of the convective heat transfer coefficient over the specimen wall, and the opposite exhaust wall, was recorded. Despite the progressively increasing temperatures during the first hour of the test, the derived values remained very steady in the range 6.0±0.5 W/m²/K. Some spatial variation over the surface of the specimen was observed, but this was relatively small, being in the range ±1.5 W/m²/K.

It is likely that the values quoted for the VTT scale furnace above, averaging 12 W/m²/K, are enhanced due to the impingement flow onto the column (c.f. also localised beam fire results in previous section). The value for the full-scale furnace is lower, both as an average and at the peak, due to the lack of a direct impingement flow from the burner jets onto the specimen and exhaust walls.

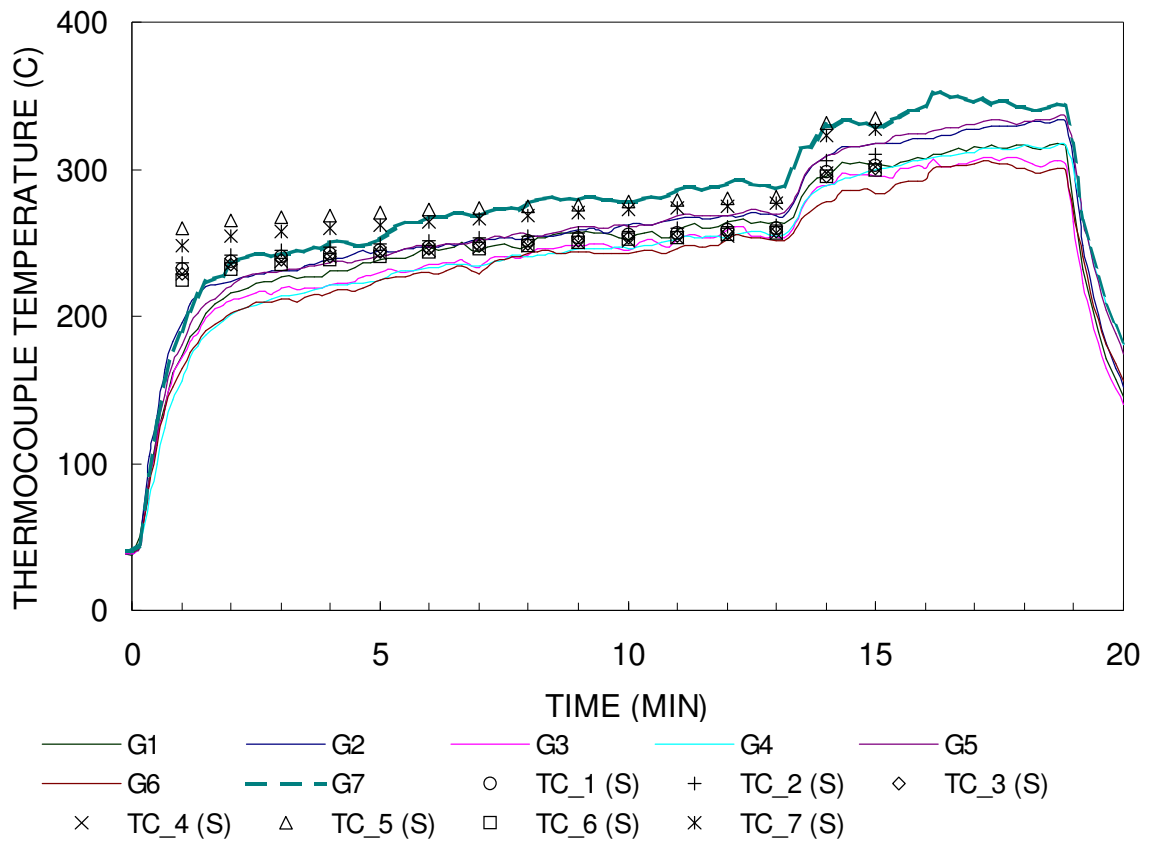


Figure D.21 – measured and simulated thermocouple temperatures inside scale furnace ^[VTT]

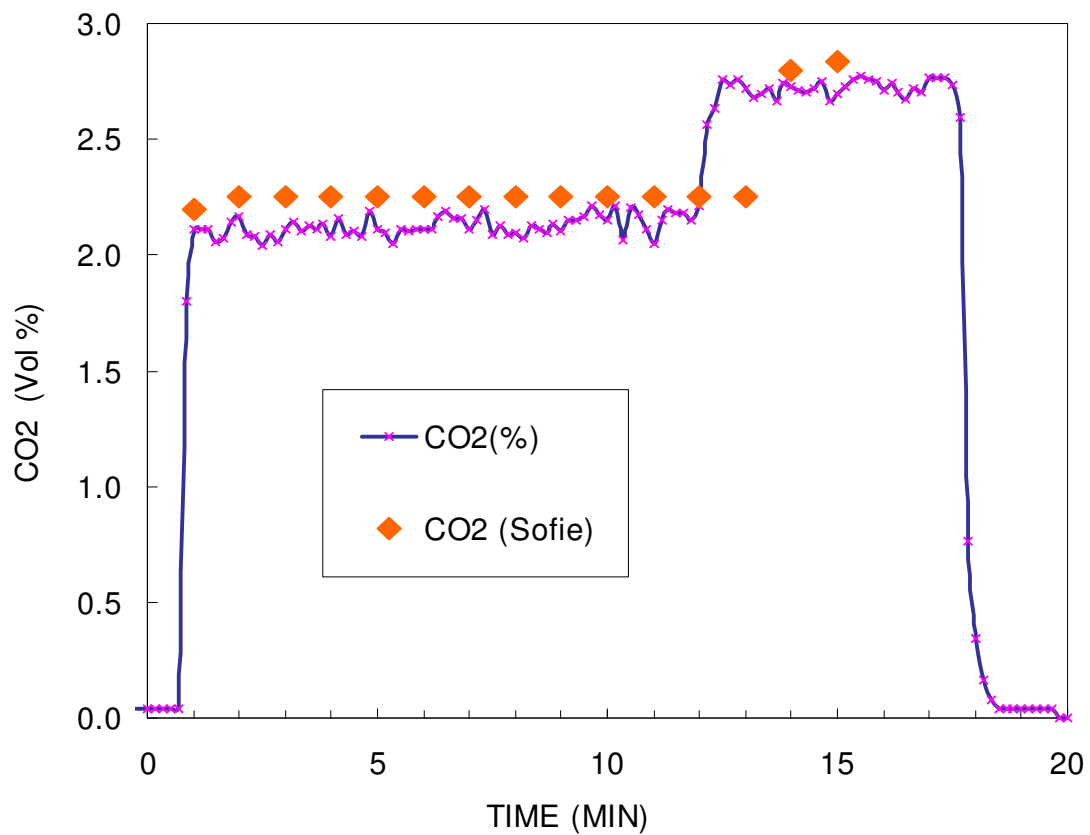


Figure D.22 – measured and simulated CO₂ volume fraction inside exhaust tube ^[VTT]

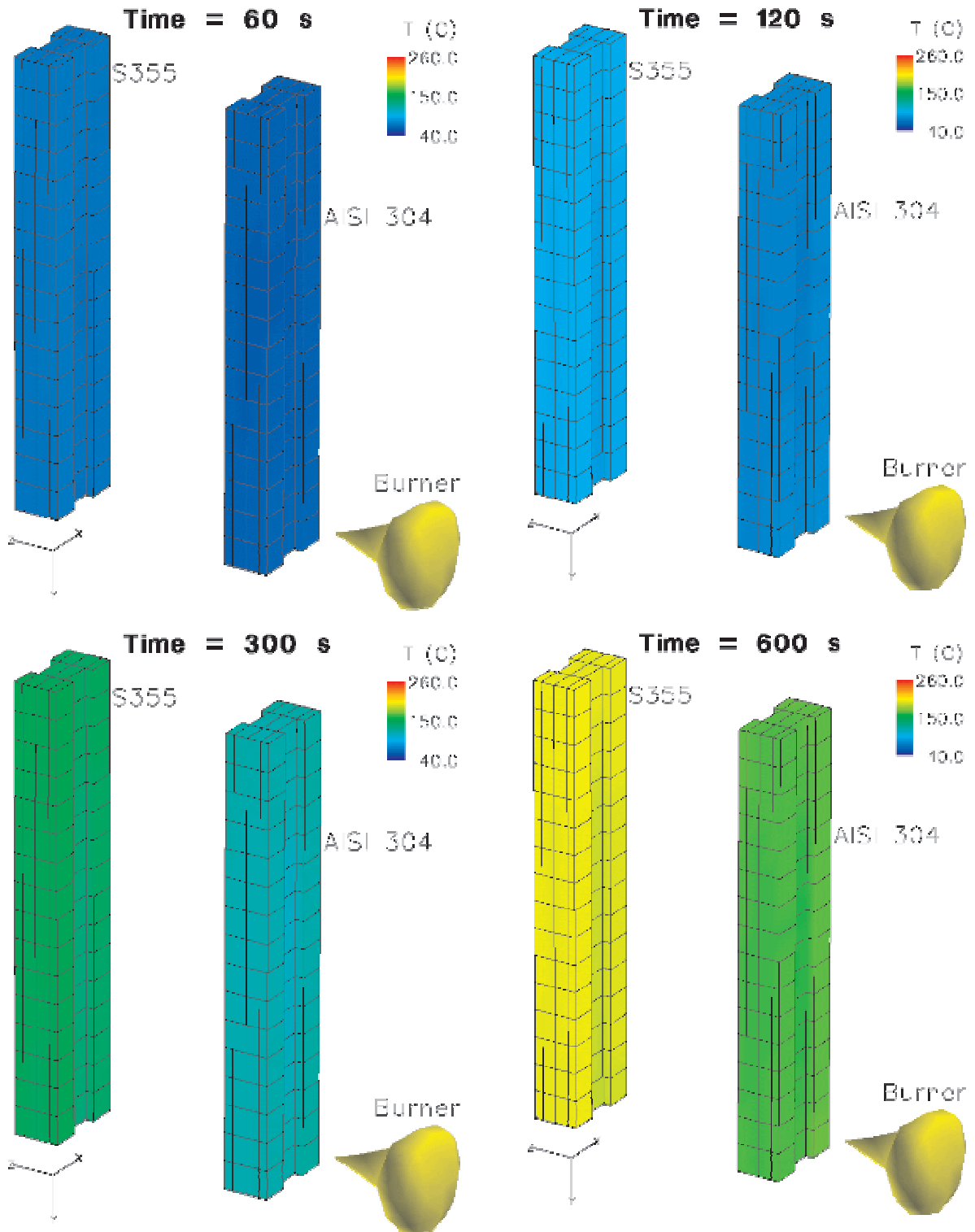


Figure D.23 – development of the steel column surface temperatures ^[VTI] (continues)

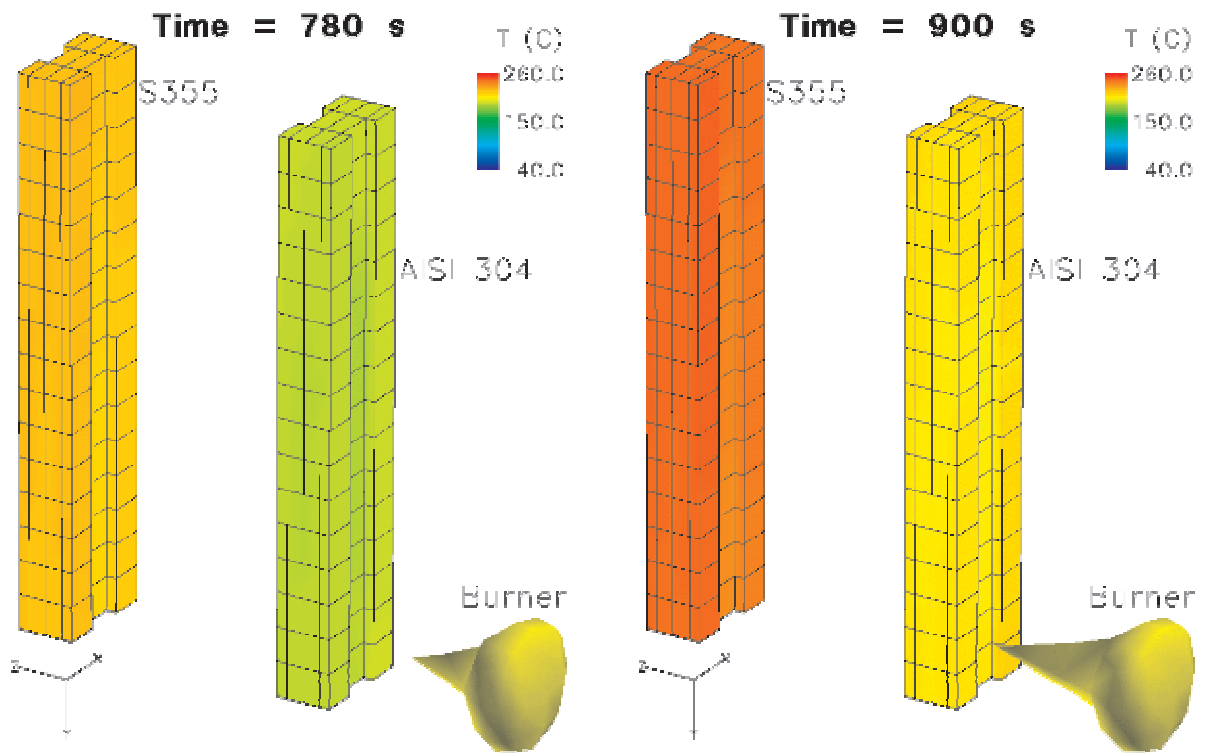


Figure D.23 – development of the steel column surface temperatures ^[VTI] (continued)

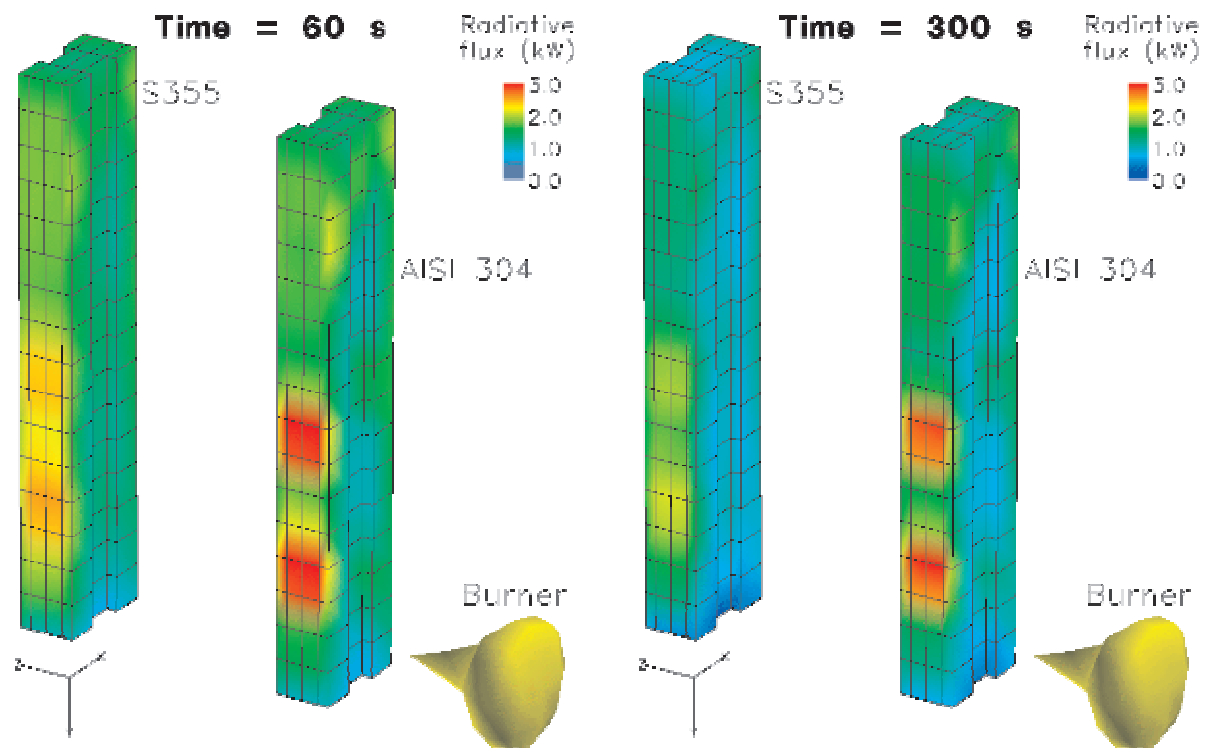


Figure D.24 – net heat flux into the columns ^[VTI] (continues)

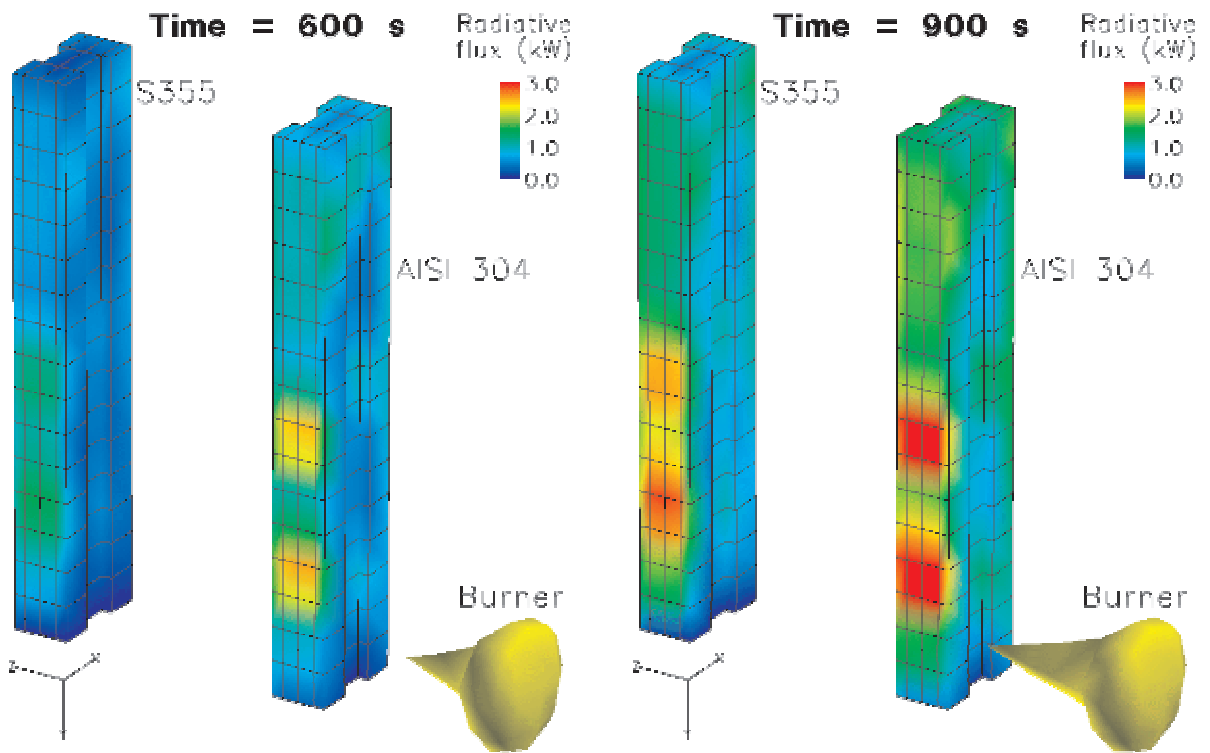


Figure D.24 – net heat flux into the columns ^[VTT] (continued)

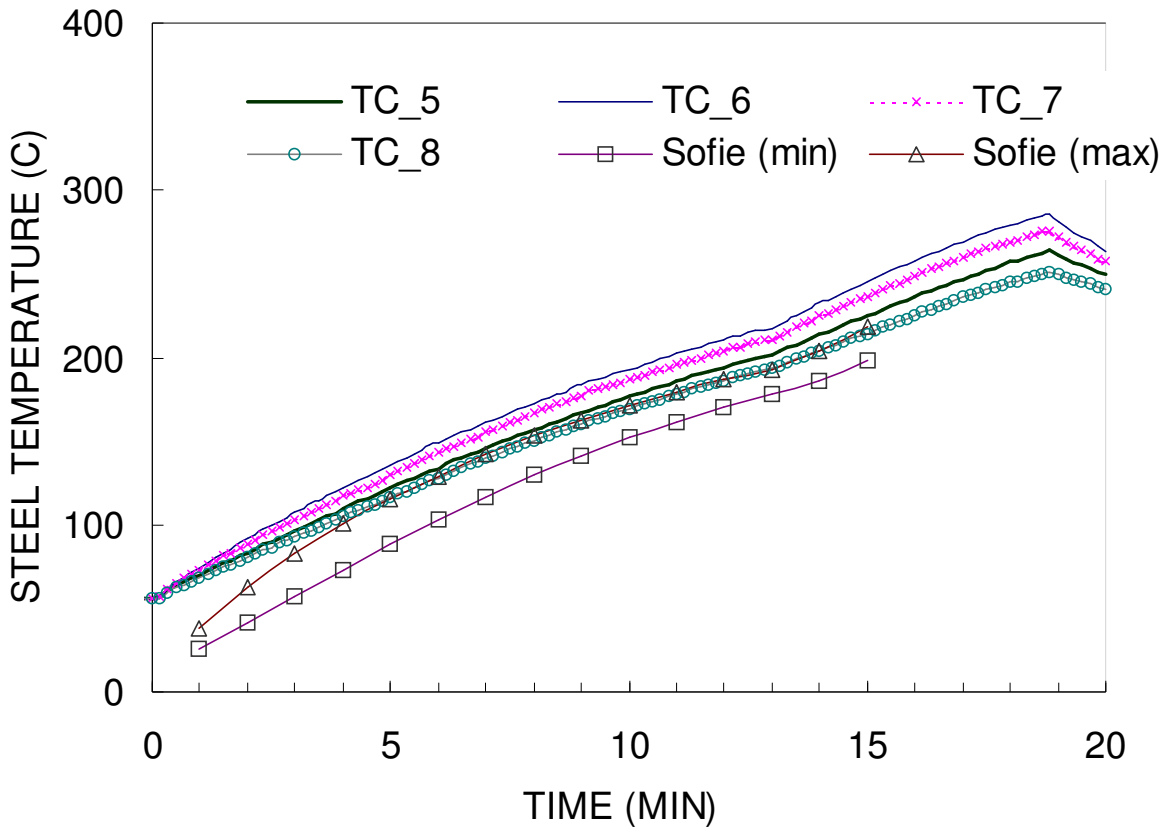


Figure D.25 – comparison of measured and simulated temperatures in cross-section of the black steel column located approximately in the middle of the column ^[VTT]

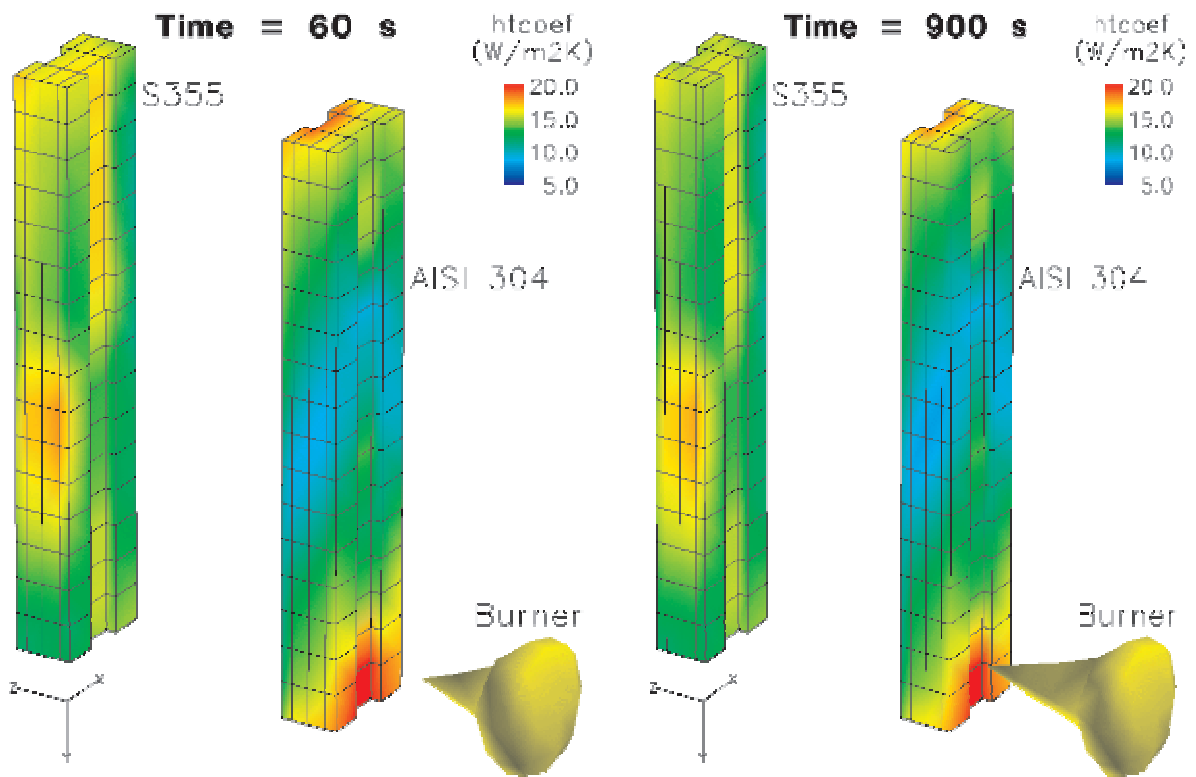


Figure D.26 – convective heat transfer coefficient on the surface of the columns ^[VTT]

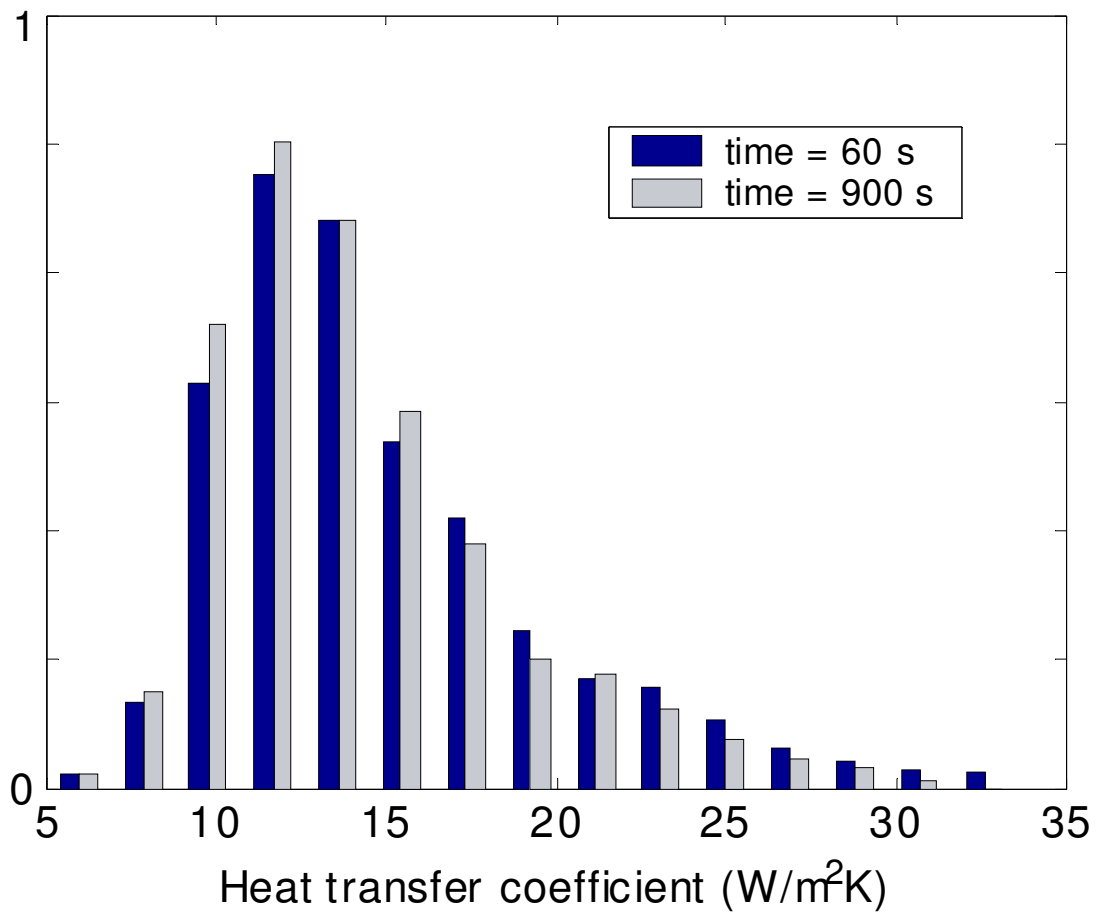


Figure D.27 – histogram of values of convective heat transfer coefficient on furnace boundaries ^[VTT]

Large room and large compartment fire tests (VTT large room; BRE large compartment)

VTT large room fire tests

Experimental details

A series of 21 fire tests were carried out in 1998 and 1999 at VTT Building Technology in a large room under the ECSC-funded NFSC2 enclosure test programme. The tests were targeted at supplying data for zone and CFD model validation. In particular, the test series was intended to examine the influence of the location and size of the fire source when calculating the thermal exposures of structures.

The large test room (10 m x 7 m in plan and 5 m in height) was situated centrally in a large test hall (27 m x 14 m in plan and 19 m in height) that acted as a calorimeter to collect combustion products from the test room. A further 8 fire tests were carried out in the large test hall, where the test room was removed from the test hall and fire was placed directly on the floor of the test hall. The large room fire tests will hereafter be referred to as the “VTT room tests”, and the fire tests in the large test hall as the “VTT hall tests”.

A schematic of the VTT test room is illustrated in fig. D.28 showing a fire plume and some of the measurement devices. The walls and ceiling of the test room were made of lightweight concrete ($\rho = 475 \text{ kg/m}^3$, $k \approx 0.12 \text{ W/m/K}$, $c_p \approx 900 \text{ J/kg/K}$) and the floor was normal concrete. The thickness of the walls was 0.30 m and the ceiling 0.25 m. In the beginning of the test series the moisture content of the walls and ceiling material was quite high, but an actual moisture measurement was not made. Approximately 10% of the floor area was covered by steel plates blocking the air channels inlet under the floor. The width and height of the door were 2.4 m and 3.0 m, respectively. However, the door width was changed to 1.2 m for some tests to find out the effect of the opening size.

The key features of the fires are shown in table D.7, and the whole test series, consisting of 10 different fires and 21 experiments, i.e. including repeats, is summarised in table D.8. The latter table also provides information about the duration of the fire and the mass of fuel burnt in each case. The parameters varied in the test series were pool size (0.40 m², 0.61 m², 1.07 m² and 2.0 m²), pool location (centre, side wall, rear corner and front corner) and door width (2.4 m and 1.2 m).

Fire Type	Pool-Location	Pool area	Pool diameter	Pool surface height from the floor	Door width
1	# 2 side wall	0.40 m ²	0.71 m	0.20 m	2.40 m
2	# 2 side wall	0.61 m ²	0.88 m	0.21 m	2.40 m
3	# 3 rear corner	0.61 m ²	0.88 m	0.21 m	2.40 m
4	# 1 centre	0.61 m ²	0.88 m	0.21 m	2.40 m
5	# 4 front corner	0.61 m ²	0.88 m	0.21 m	2.40 m
6	# 2 side wall	1.07 m ²	1.17 m	0.44 m	2.40 m
7	# 1 centre	1.07 m ²	1.17 m	0.44 m	2.40 m
7B	# 1 centre	1.07 m ²	1.17 m	0.44 m	1.20 m
8	# 2 side wall	1.07 m ²	1.17 m	0.44 m	1.20 m
9	# 2 side wall	2.00 m ²	1.60 m	0.25 m	2.40 m
10	# 2 side wall	Wood cribs	- / -	- / -	2.40 m

Table D.7 – fire types in the NFSC2 Room Test series in VTT (Fire type 10 is the Inter-laboratory calibration test)

Fire type	Test no. & date	Pool location	Pool size	Duration [min.]	Nominal amount of fuel	Nominal RHR [kW]	Δm_{fuel} [kg]
1	Test 0 12.10.98	# 2	0.40 m ² D=0.71 m	4:00	4 l (20 mm)	950	2.92
1	Test 1 13.10.98	# 2	0.40 m ² D=0.71 m	4:00	4 l (20 mm)	950	3.03
1	Test 2 14.10.98	# 2	0.40 m ² D=0.71 m	8:27	10 l (50 mm)	1440	7.22
2	Test 3 15.10.98	# 2	0.61 m ² D=0.88 m	7:45	15 l (20 mm)	1440	11.09
2	Test 4 15.10.98	# 2	0.61 m ² D=0.88 m	7:55	15 l (20 mm)	1440	11.48
2	Test 5 16.10.98	# 2	0.61 m ² D=0.88 m	8:14	15 l (20 mm)	1440	11.39
3	Test 6 16.10.98	# 3	0.61 m ² D=0.88 m	7:55	15 l (20 mm)	1440	11.04
4	Test 7 19.10.98	# 1	0.61 m ² D=0.88 m	8:00	15 l (20 mm)	1440	10.92
4	Test 8 19.10.98	# 1	0.61 m ² D=0.88 m	7:45	15 l (20 mm)	1440	10.97
5	Test 9 20.10.98	# 4	0.61 m ² D=0.88 m	7:18	15 l (20 mm)	1440	11.10
10	Test 10 20.10.98	# 2	Wood cribs	21:30 (extinguished)	50 kg	700	38.21
6	Test 11 21.10.98	# 2	1.07 m ² D=1.17 m	5:15	20 l	2500	15.28
6	Test 12 21.10.98	# 2	1.07 m ² D=1.17 m	5:07	20 l	2500	14.60
6	Test 13 22.10.98	# 2	1.07 m ² D=1.17 m	5:21	20 l	2500	15.02
10	Test 14 22.10.98	# 2	Wood cribs	≈ 40	50 kg	700	51.09
7	Test 15 23.10.98	# 1	1.07 m ² D=1.17 m	5:15	20 l	2500	14.79
7B	Test 16 23.10.98	# 1	1.07 m ² D=1.17 m	5:20	20 l	2500	14.33
8	Test 17 26.10.98	# 2	1.07 m ² D=1.17 m	5:20	20 l	2500	14.37
8	Test 18 26.10.98	# 2	1.07 m ² D=1.17 m	5:29	20 l	2500	14.72
9	Test 19 27.10.98	# 2	2.00 m ² D=1.60 m	5:30	40 l	2500	21.81
9	Test 20 27.10.98	# 2	2.00 m ² D=1.60 m	9:30	80 l	2500	59.27

Table D.8 – NFSC2 Room Test series in VTT; Δm_{fuel} is the change in load cell reading during the fire

Fire Source

For most of the tests, the fuel was heptane, floated on water for stabilising heat release rate, located in circular steel pools placed on load cells for mass loss measurement. The only exceptions were two tests in which a wood crib was burned for inter-laboratory comparisons. The size of the pool fire was varied from 0.40 m² to 2.00 m². The four different locations used for the pool fire are shown in fig. D.29.

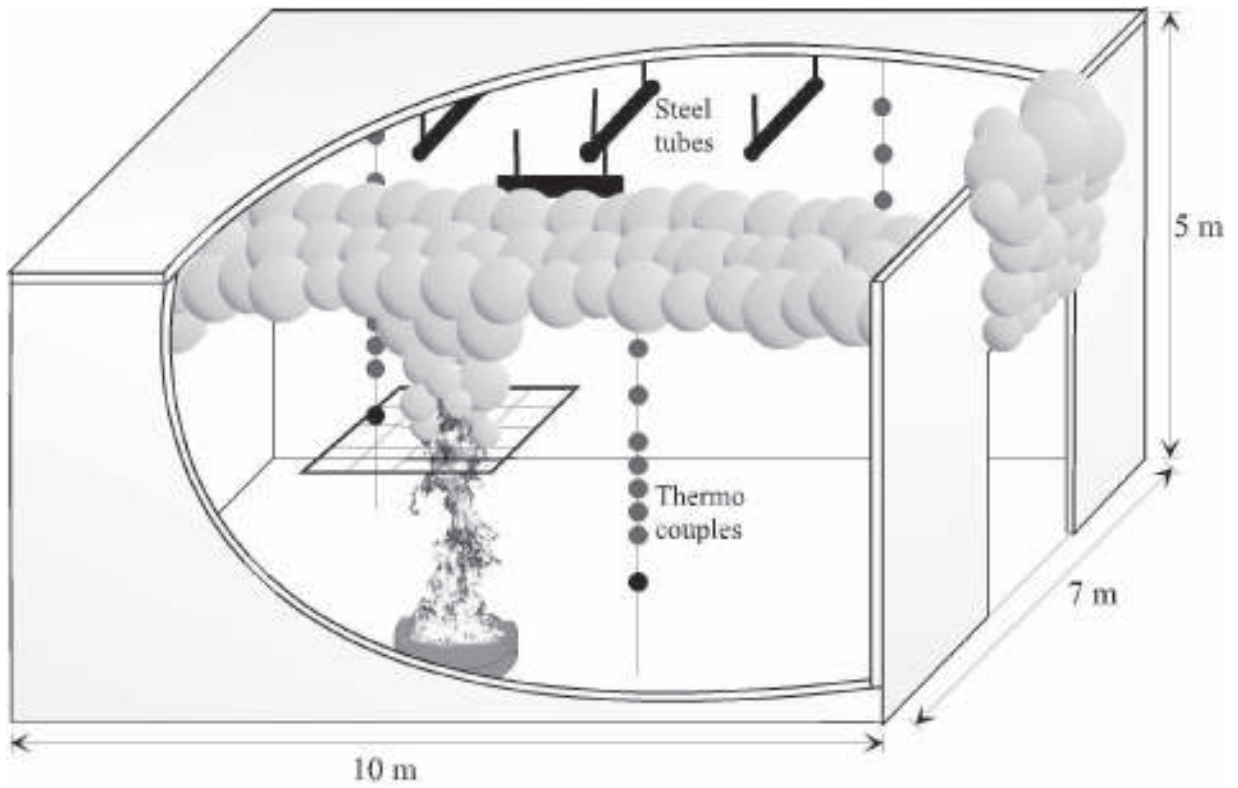


Figure D.28 – schematic of VTT large room with instrumentation locations

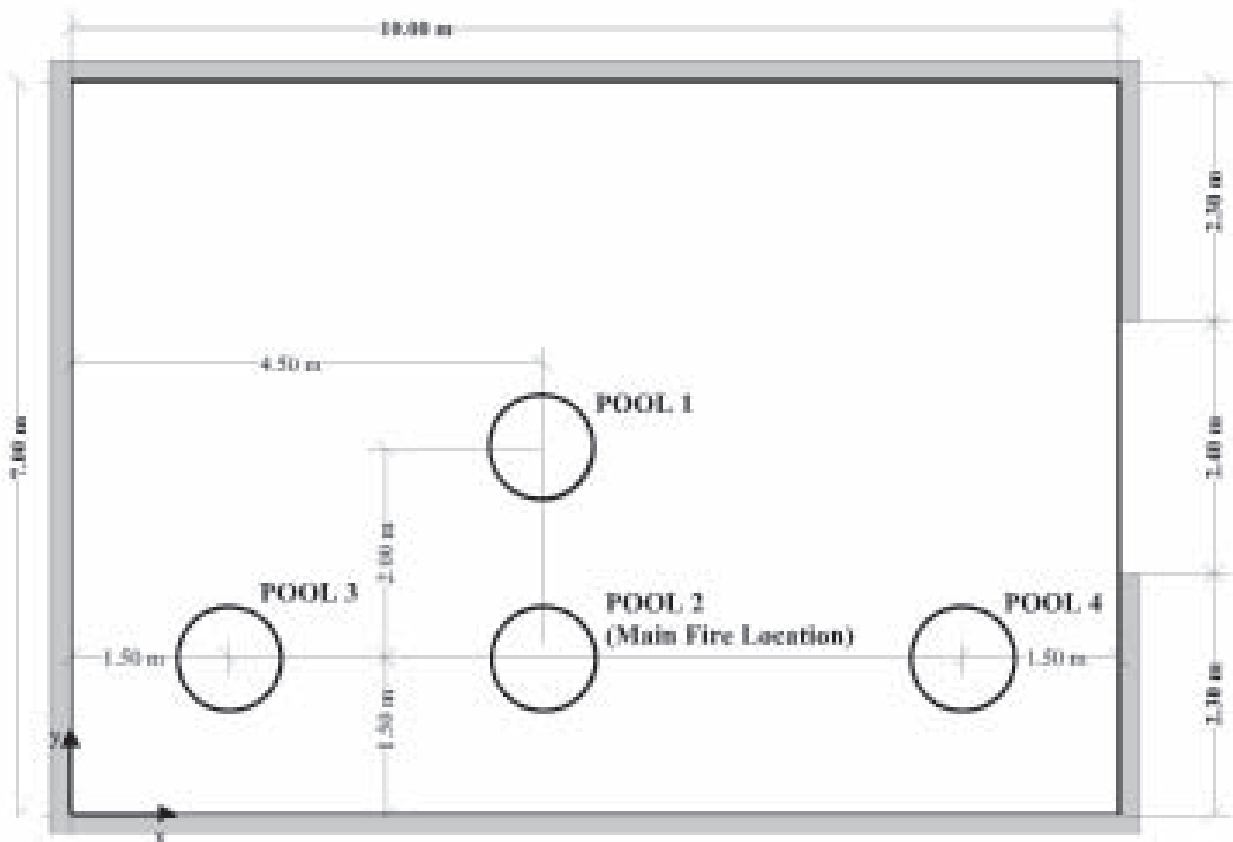


Figure D.29 – heptane pool locations in the test room

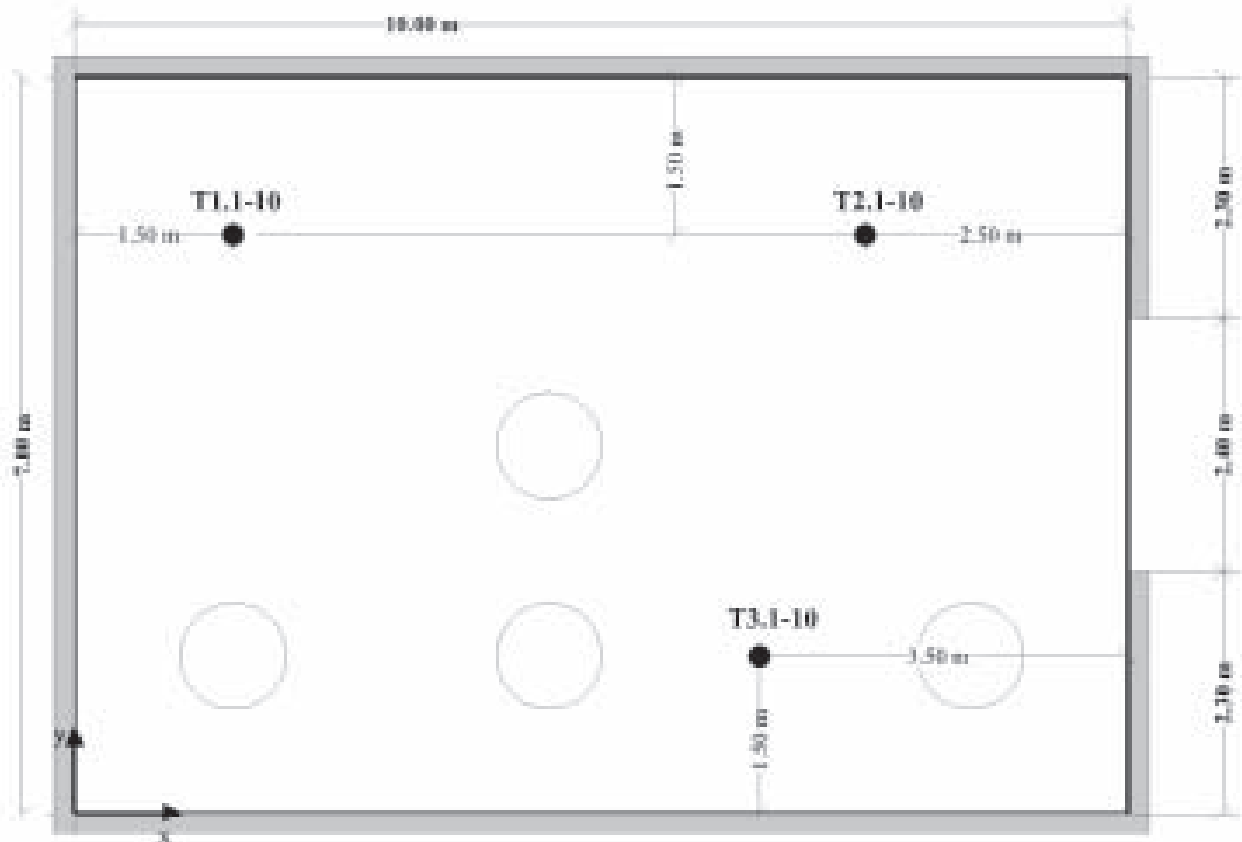
The rate of heat release was not measured precisely during the tests. However, an estimate for the heat release rate can be calculated from the measured burning rates with the equation:

$$\dot{Q} = \chi \cdot \dot{m} \cdot \Delta H_c \tag{D.1}$$

where χ is the efficiency of the combustion inside the room, \dot{m} is the measured mass loss rate and ΔH_c is the heat of combustion of heptane. The suggested values for χ and ΔH_c are 0.80 ± 0.10 and 44.6 MJ/kg, respectively.

Instrumentation

The test room was instrumented with thermocouples and heat flux gauges and included 'plate thermocouples' at some locations. The gas concentrations were measured in some of the tests to determine the completeness of combustion. About 150 channels of measurements and a video recording from the door side were made for each test. Gas temperatures were measured in three vertical rakes T1, T2 and T3 as shown in figs. D.30 and D.31. Each of these rakes consisted of 10 bare thermocouples (TCs) at different heights. In the beginning of the test series 0.1 mm TCs were used but starting from Test 12 0.5 mm TCs had to be used because the wires partially melted during Test 11. Ceiling jet temperatures were measured using 0.5 mm diameter thermocouples placed 0.10 m below the ceiling. Gas flow velocities were measured with bi-directional probes. Two probes (V1 and V2) were placed into the ceiling jet, 0.10 m below the ceiling. Six probes (V3 to V8) were placed to the door jet, as shown in fig. D.32.



Gas temperature measurements

Figure D.30 – horizontal thermocouple rake locations for gas temperature measurement

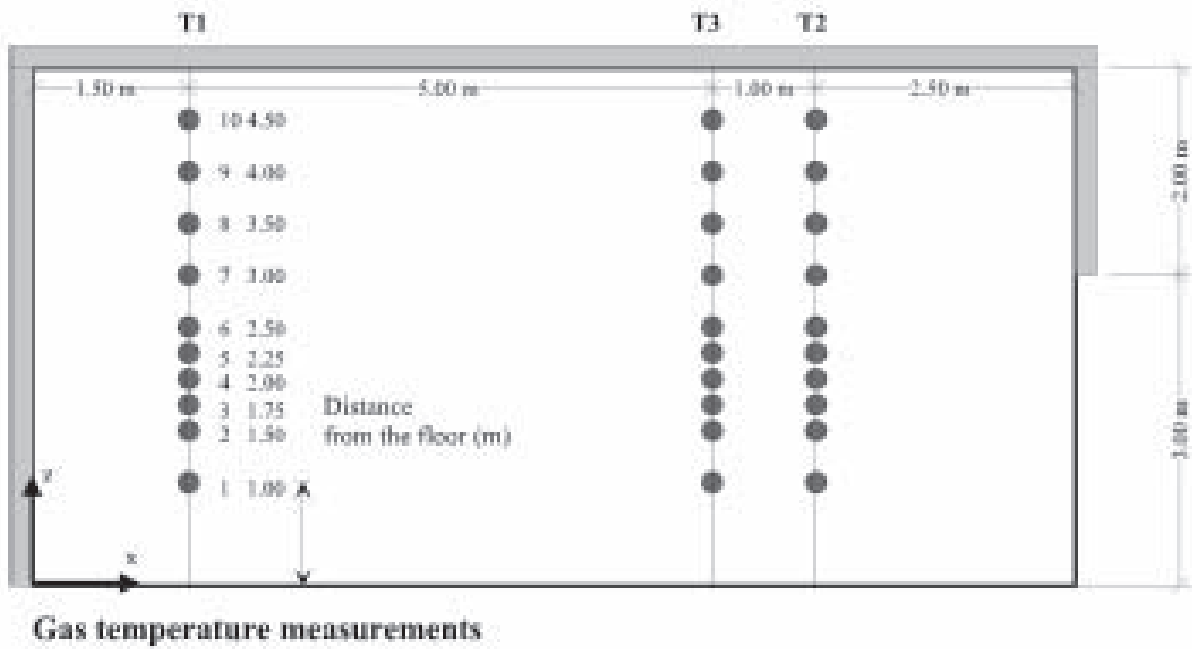


Figure D.31 – vertical locations of the thermocouples for gas temperature measurement

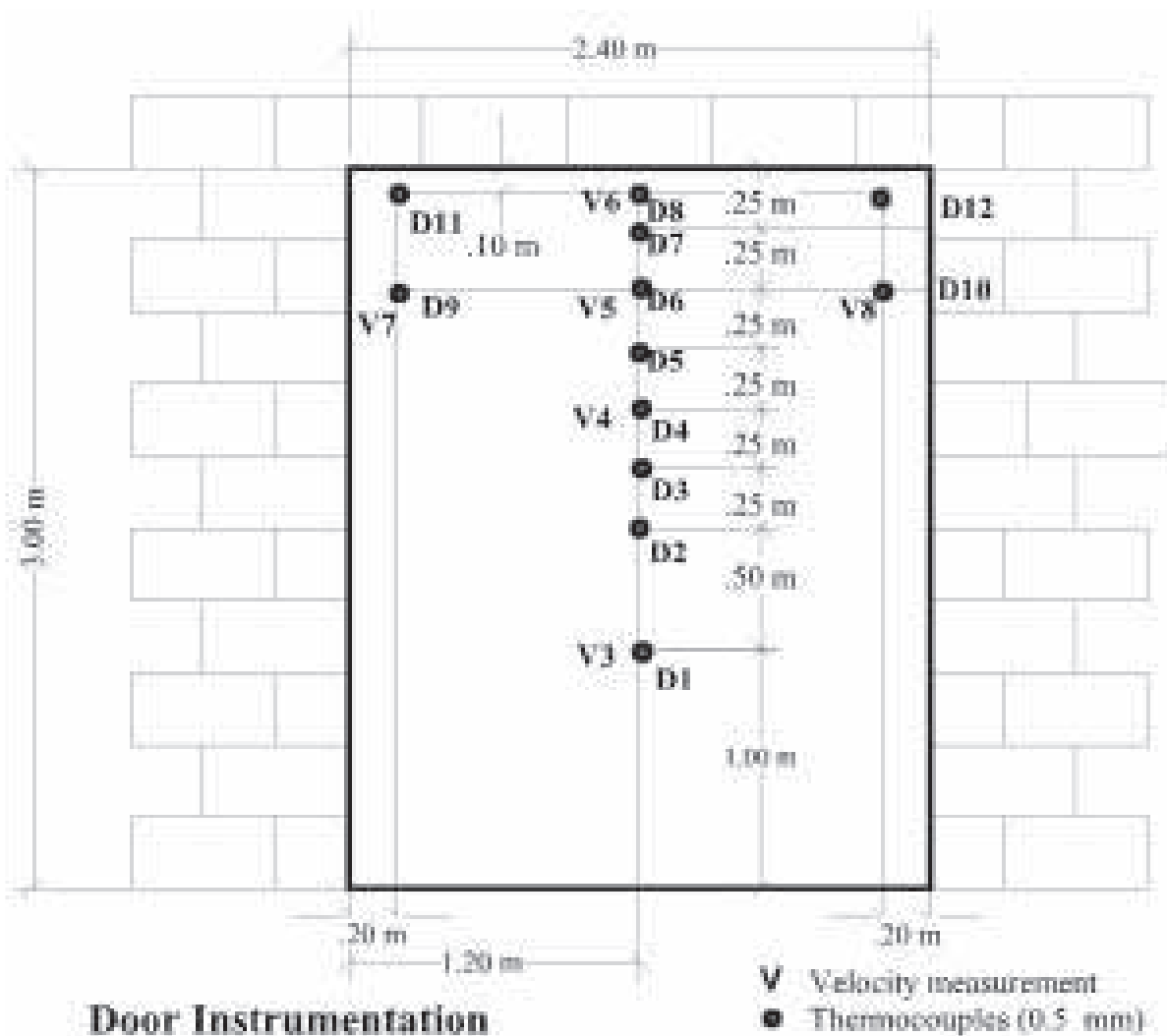


Figure D.32 – locations of the door gas temperature (D) and velocity (V) measurements

Zone model simulations with Ozone and MRFC

Zone model OZone (version 2.0.85) was used to perform computer simulations for all 29 VTT tests (including the eight VTT hall fire tests of NFSC2 series). The principle outputs of the calculations were the hot zone gas temperature and the smoke thickness, which were compared with the measured data from the tests. As an illustration, the results for the selected tests (nos. 4, 7, 8 and 9) from the series are presented in figs. D.33 – D.35. A reasonable agreement is shown between prediction and experiment.

Simulations were run with MRFC to compare with the OZone results. For the following simulations a foam concrete, included in the databank, was modified to represent the light-weight concrete walls. For the floor, a normal concrete of 0.5 m thickness was assumed. MRFC uses a discharge coefficient to consider the gas flow through the opening. A value of 0.70 was defined, which is equivalent to the default value of the computer code. The burning scenarios differed from test to test and are described below.

Initial simulations examined the various different plume models available in the code (McCaffrey, Thomas/Hinkley, Cox/Chitty, Heskestad & Tanaka). This made clear that the plume model has to be chosen very carefully. The calculated interface height is not very sensitive to the model choice for this relatively simple case and the transition model between McCaffrey and Thomas/Hinkley used in MRFC seems to fit the entrainment very well.

Subsequent simulations with MRFC and OZone have been done for VTT tests #7, #8 and #9 using McCaffrey's plume model. The results are presented in figs. D.36 – D.47 (#7). These are tests with a localized fire with moderate hot gas temperatures. No flashover conditions have been occurred during this tests. The same input data have been used for both codes. The rate of heat release has been set according to the reported values.

The results for test #7 are presented in figs. D.36 – D.39. There is a very good match of heat release rate data as shown in fig. D.36. Fig. D.37 shows a good agreement between the calculations of MRFC and OZone for the interface height with the measurement. The comparison of MRFC and OZone calculations with the measured hot layer temperatures in fig. D.38 shows that MRFC calculations fit the upper limit of the measured data, while OZone meets the lower limit of the measurement. The mean value of the measured data is nearly in the middle between the calculations. The difference between the calculated and the measured data is in the range of nearly 15%. The results for the lower layer temperature shown in fig. D.39 show the opposite trend with MRFC temperatures near the lower limit of the measurement and OZone temperatures meeting the mean value. It seems that the experimental upper limit here is influenced by oscillations of the interface height. Therefore some temperature measurements are also included, which are near the calculated interface height.

The comparison of the calculations for test #8 (figs. D.40 to D.43) and test #9 (figs. D.44 to D.47) show similar results. In each case the interface height is calculated with a very good agreement. The hot gas temperatures are in a range of $\pm 15\%$ to the mean value of the measurement, while MRFC calculations are higher and OZone calculations are lower than the measured values.

NFSC2 Tests at VTT

Series 1: Room tests

Test 4

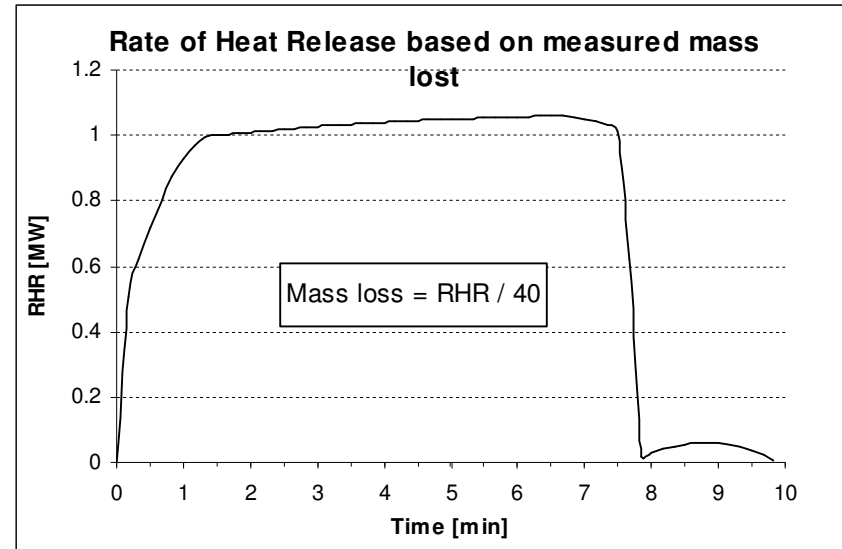
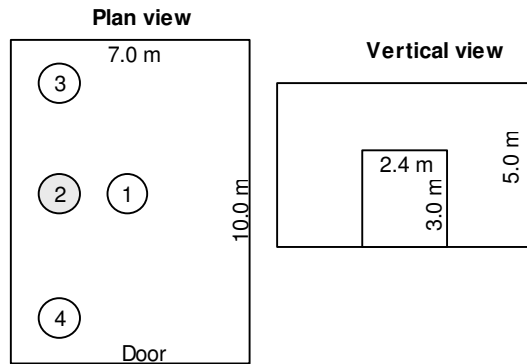
Room width: 7.0 m
 Room depth: 10.0 m
 Room height: 5.0 m

 Fuel: Heptane
 Fuel mass: 11.48 kg
 Fuel surface height: 0.21 m

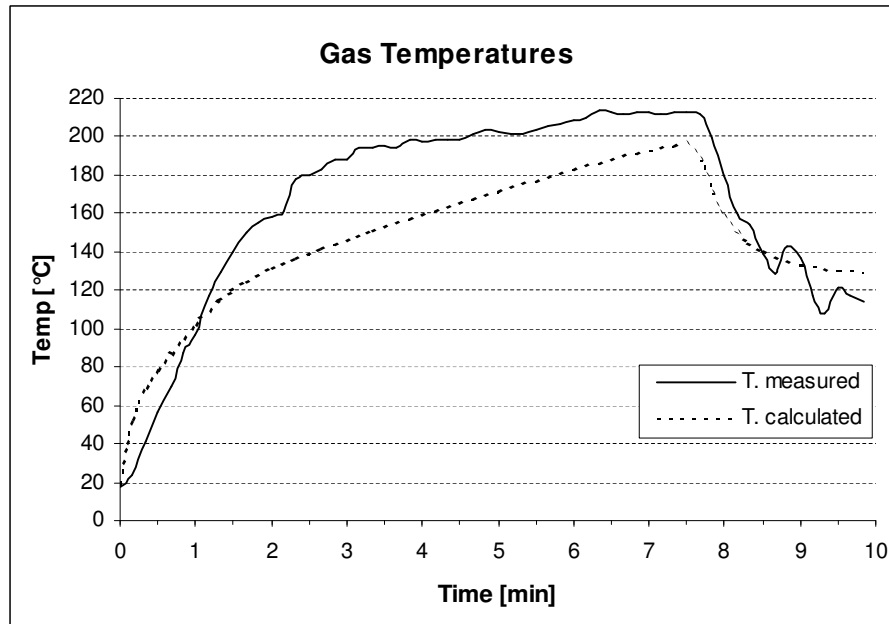
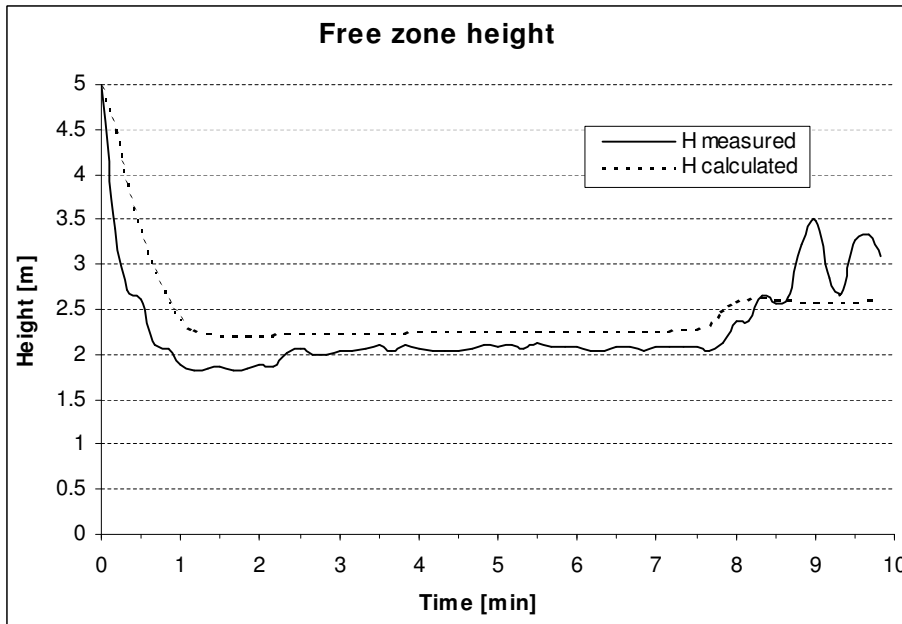
 Pool size: 0.61 m²
 Pool location: 2
 Door height: 3.00 m
 Door width: 2.40 m

 Combustion heat: 40 MJ/kg

Figure D.33 – VTT Test 4 results [AGB]



08



NFSC2 Tests at VTT
Series 1: Room tests

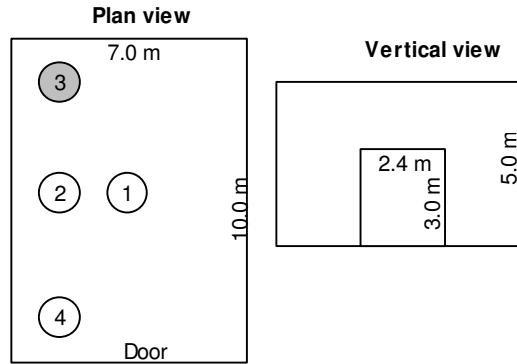
Test 6 #####

Room width: 7.0 m
 Room depth: 10.0 m
 Room height: 5.0 m

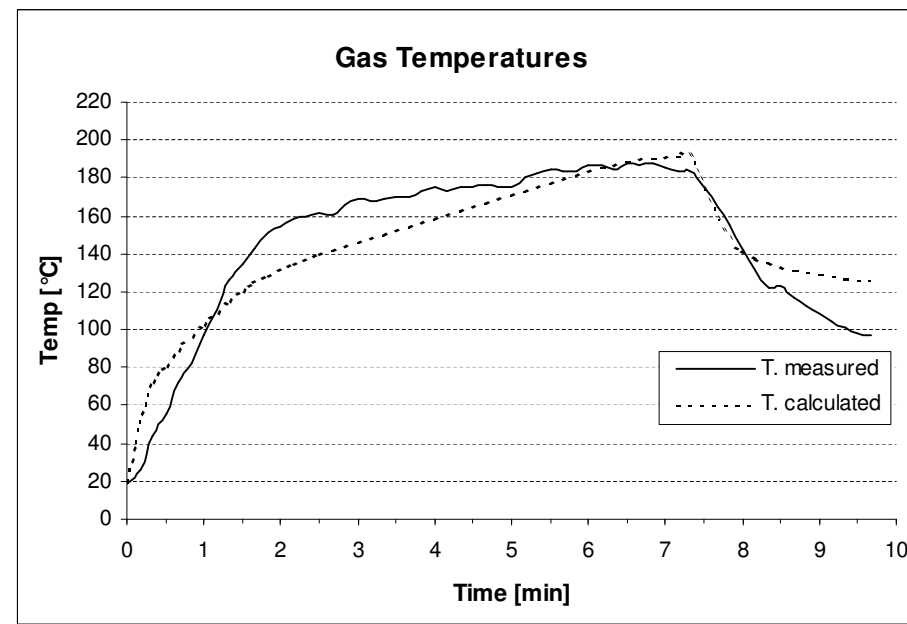
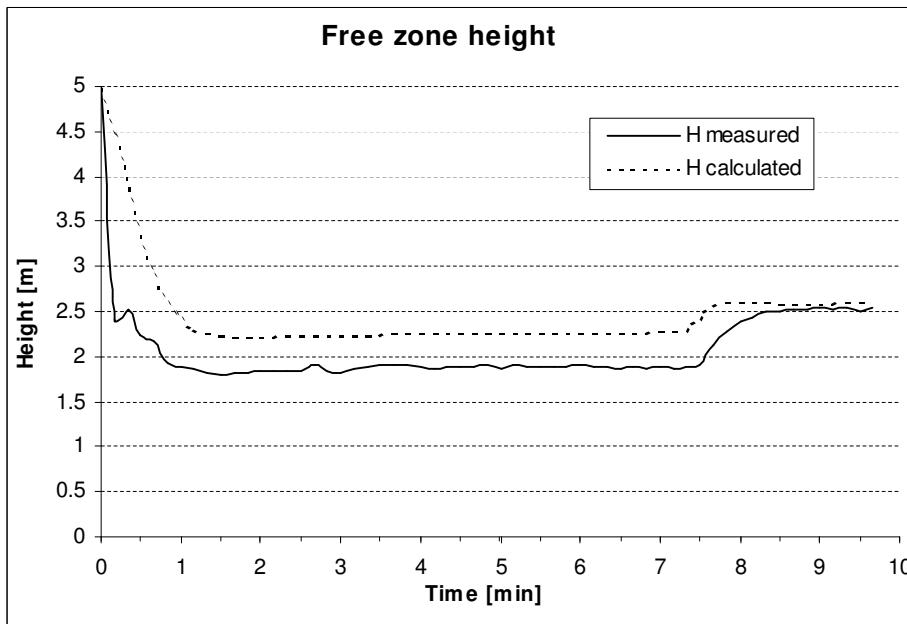
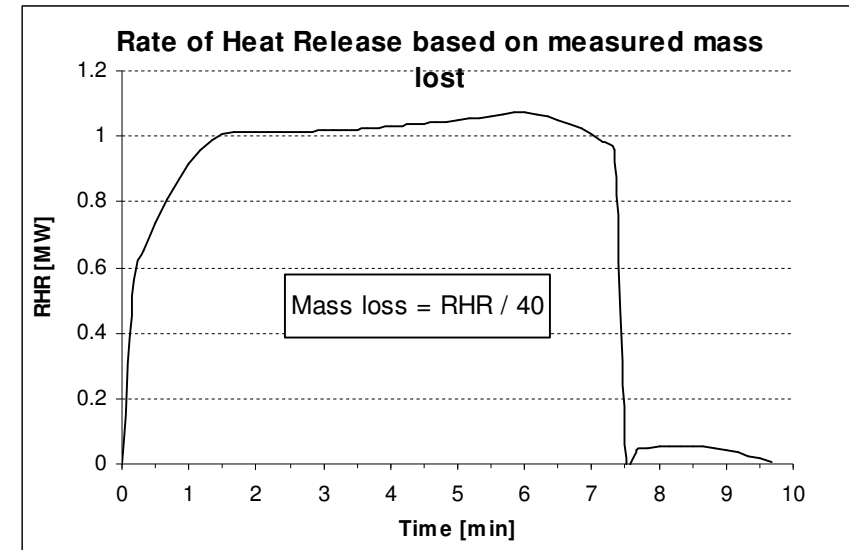
Fuel: Heptane
 Fuel mass: 11.04 kg
 Fuel surface height: 0.21 m

Pool size: 0.61 m²
 Pool location: 2
 Door height: 3.00 m
 Door width: 2.40 m

Figure D.34 – VTT Test 6 results ^[AGB]



Combustion heat: 40 MJ/kg

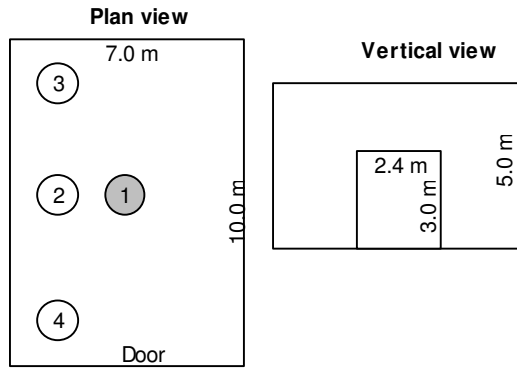


**NFSC2 Tests at VTT
Series 1: Room tests**

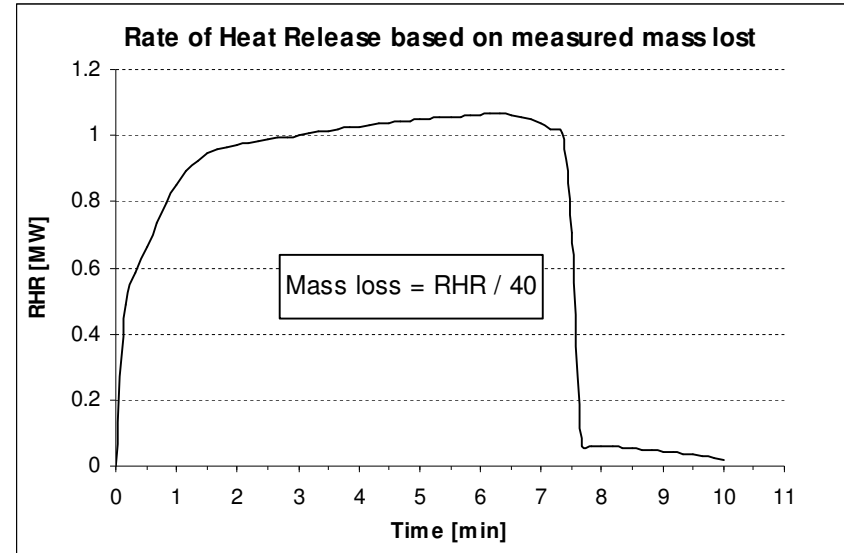
Test 8 #####

Room width: 7.0 m
 Room depth: 10.0 m
 Room height: 5.0 m
 Fuel: Heptane
 Fuel mass: 10.97 kg
 Fuel surface height: 0.21 m
 Pool size: 0.61 m²
 Pool location: 2
 Door height: 3.00 m
 Door width: 2.40 m

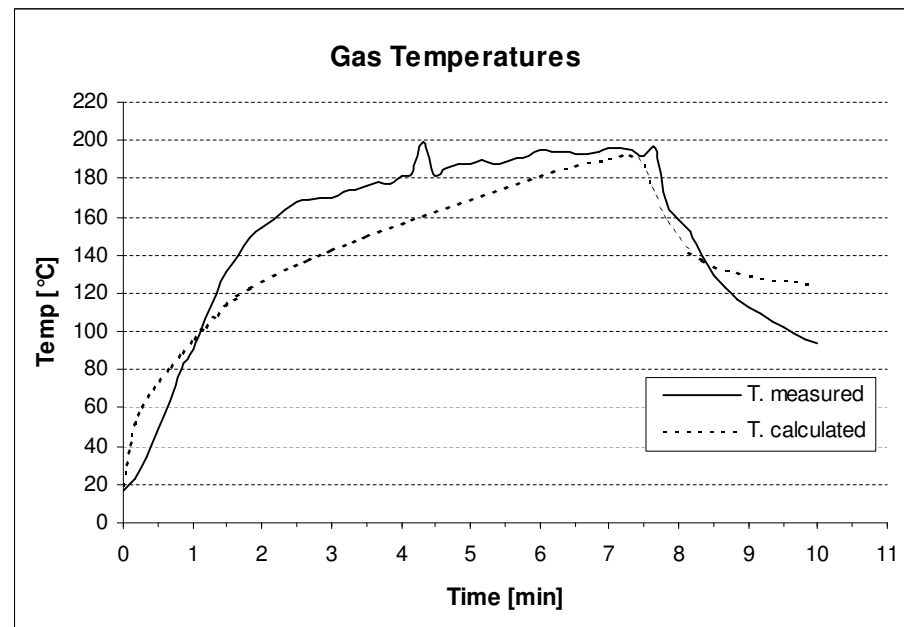
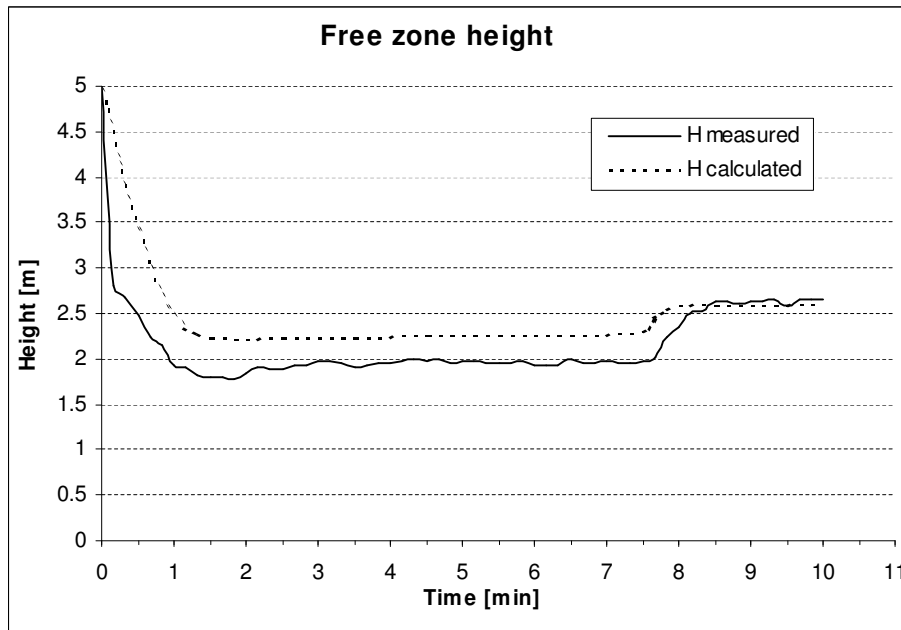
Figure D.35 – VTT Test 8 results [AGB]



Combustion heat: 40 MJ/kg



82



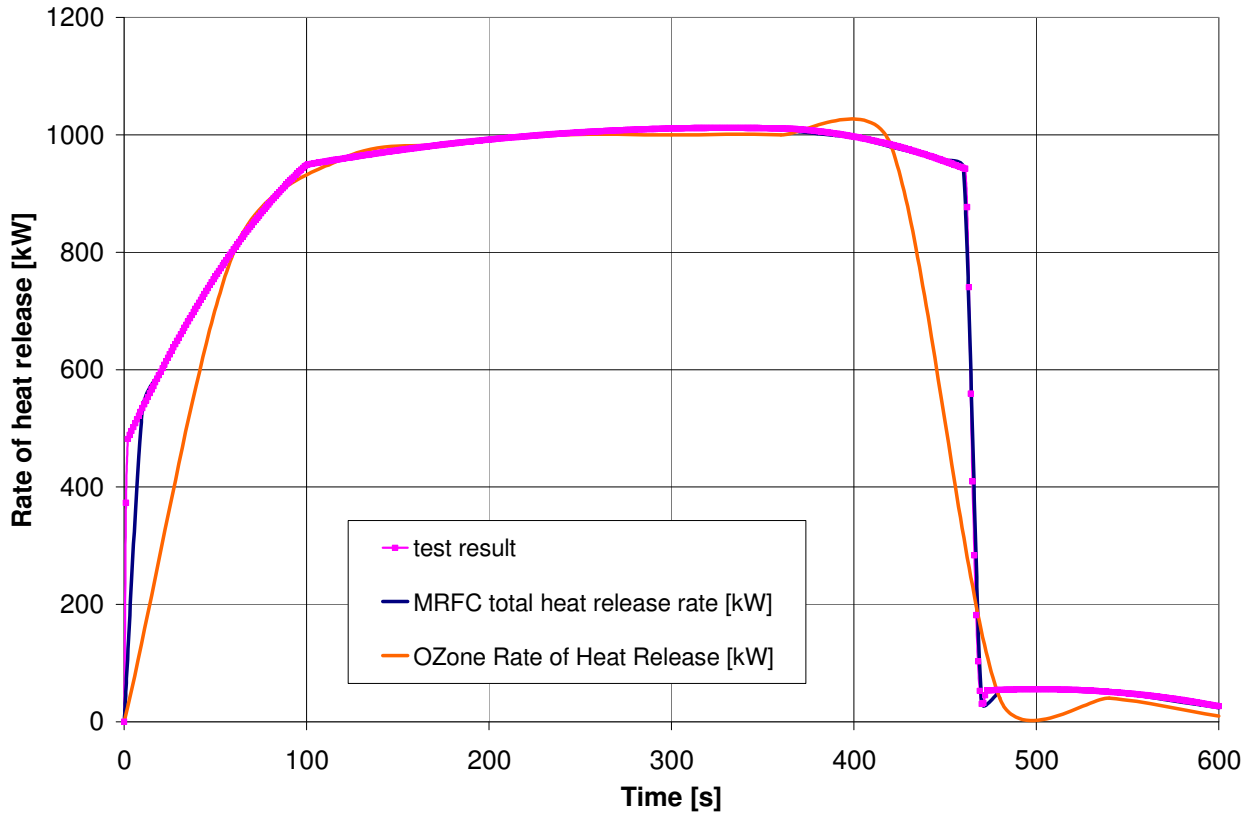


Figure D.36 – rate of heat release VTT test #7 ^[AGB]

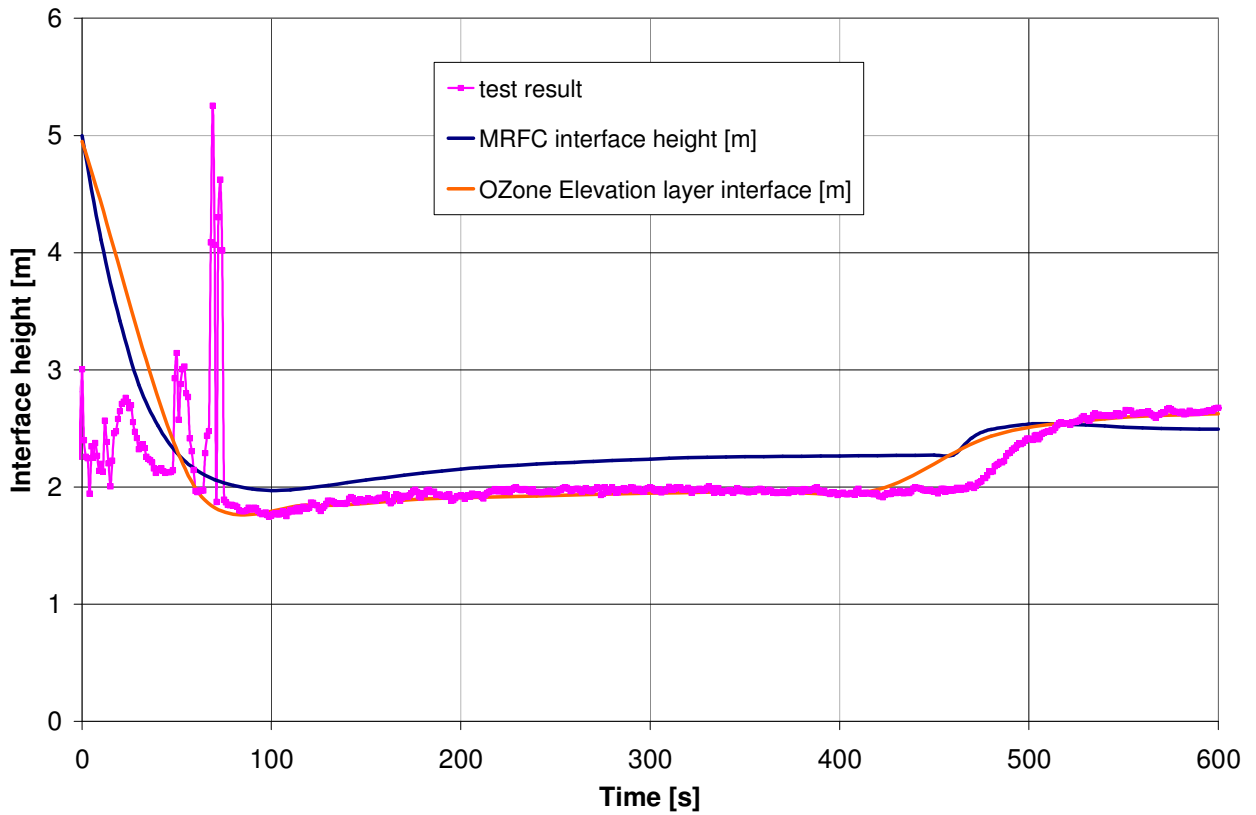


Figure D.37 – interface height VTT test #7 ^[AGB]

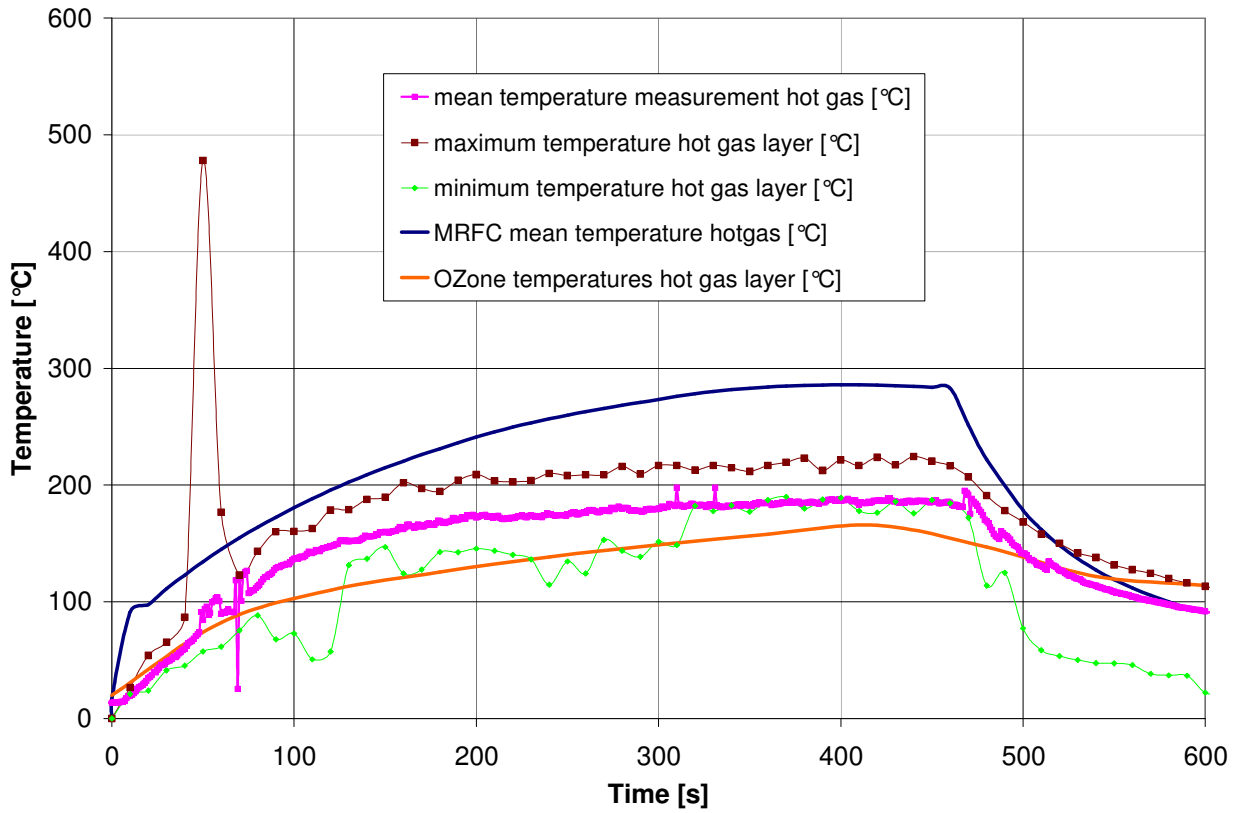


Figure D.38 – temperature of hot gas layer VTT test #7 ^[AGB]

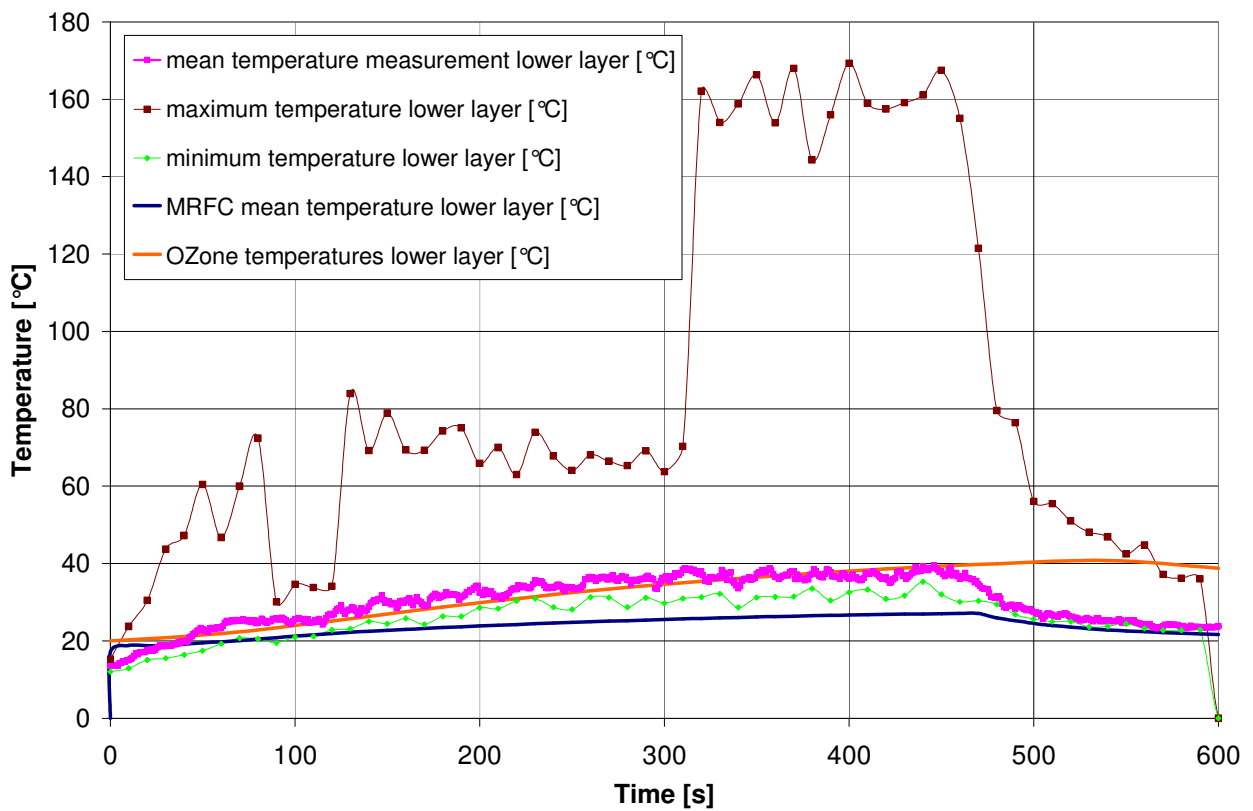


Figure D.39 – temperature of lower layer VTT test #7 ^[AGB]

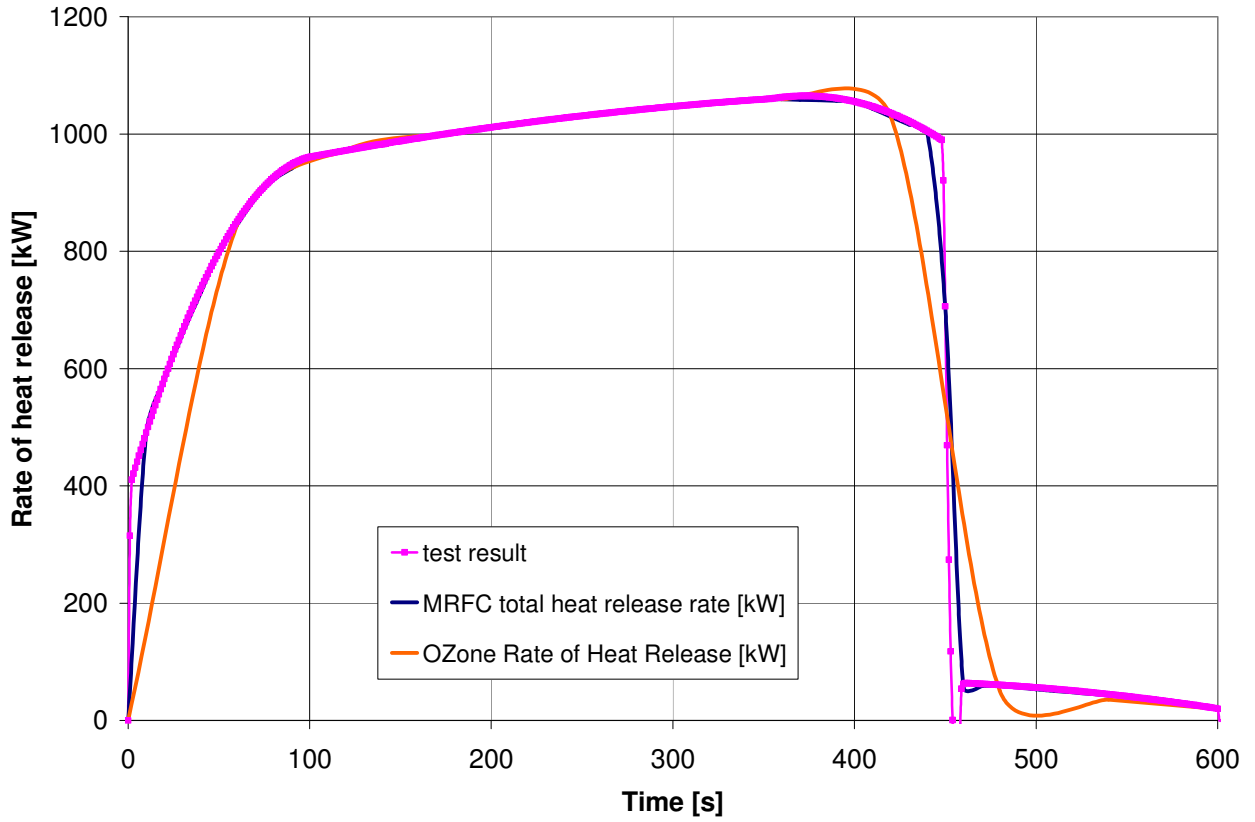


Figure D.40 – rate of heat release VTT test #8 ^[AGB]

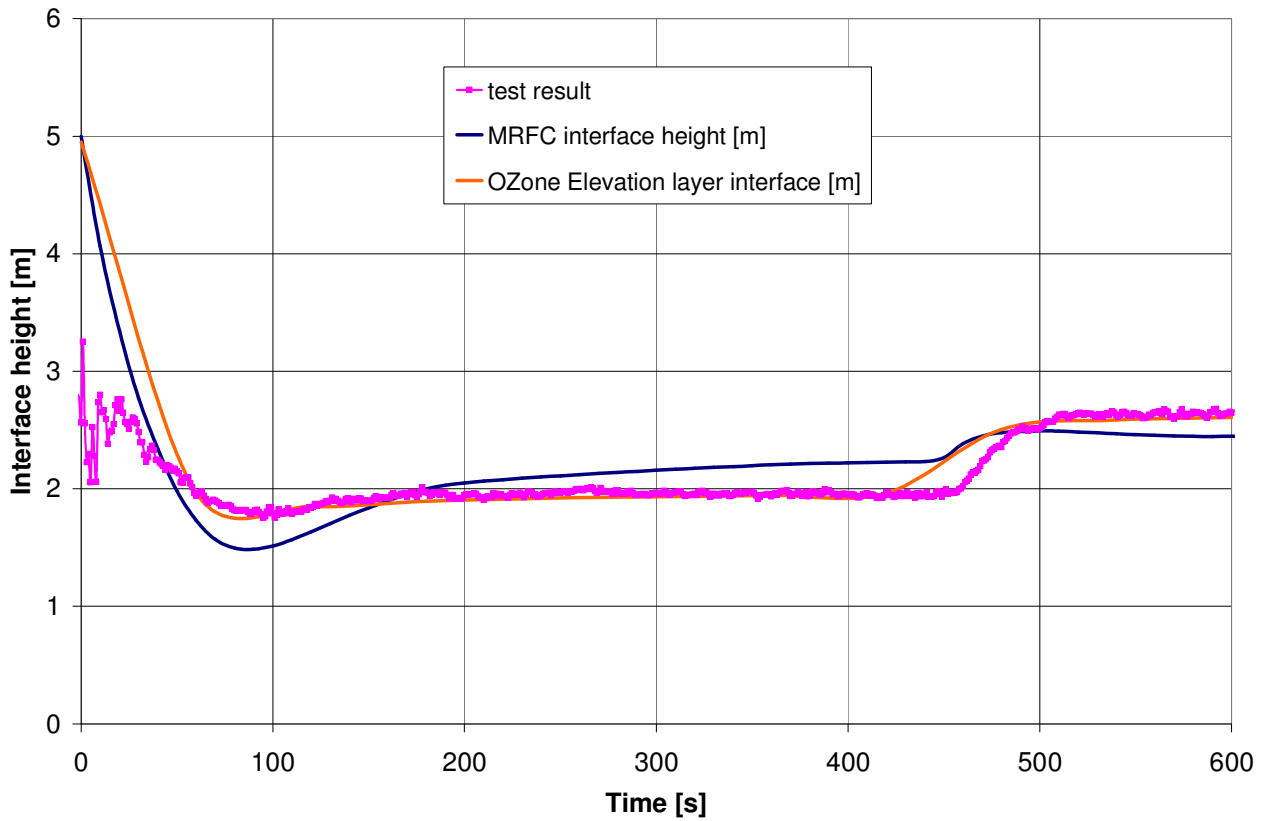


Figure D.41 – interface height VTT test #8 ^[AGB]

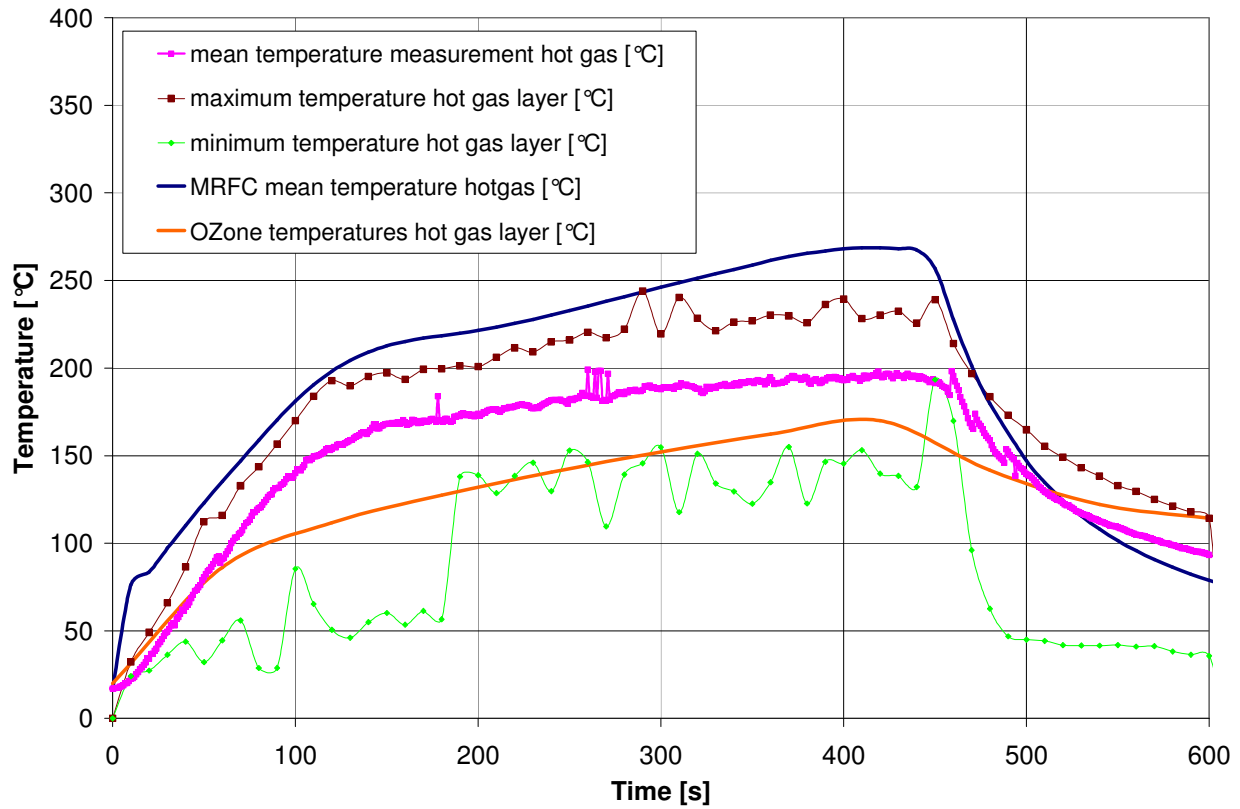


Figure D.42 – temperature of hot gas layer VTT test #8 ^[AGB]

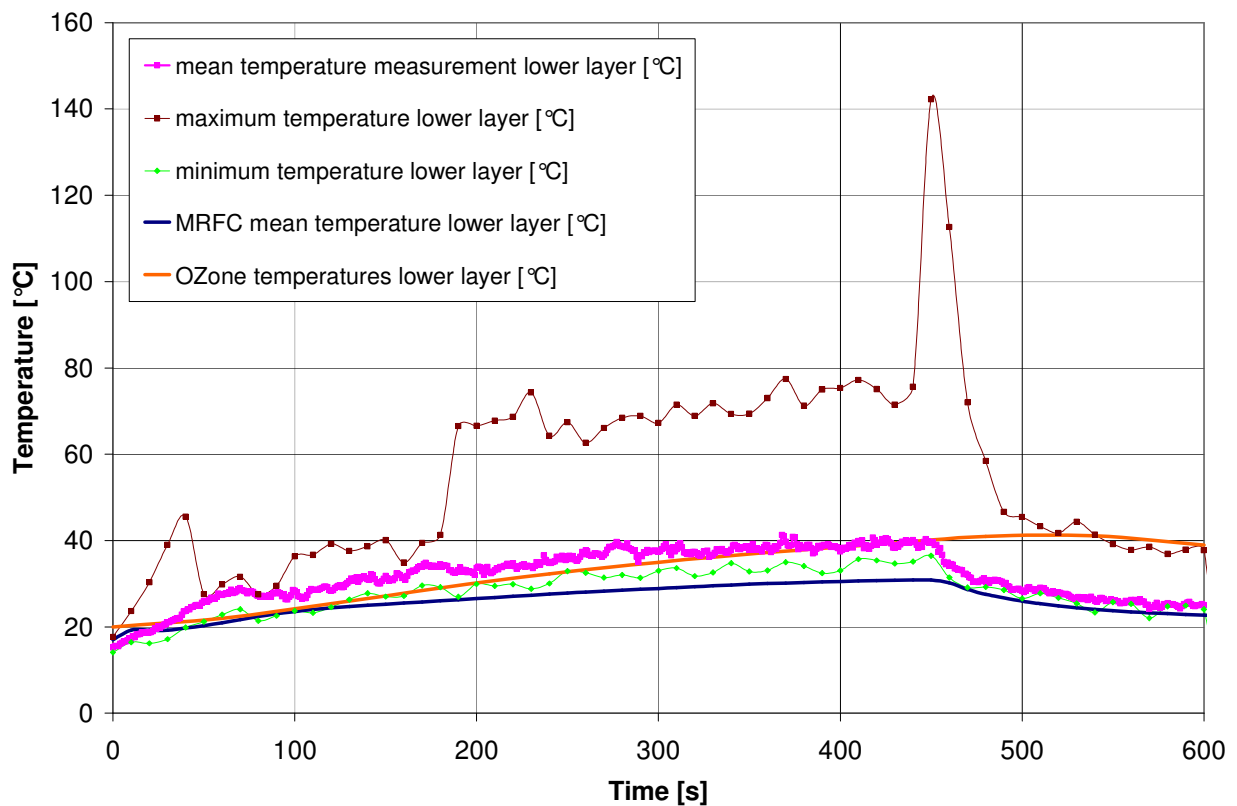


Figure D.43 – temperature of lower layer VTT test #8 ^[AGB]

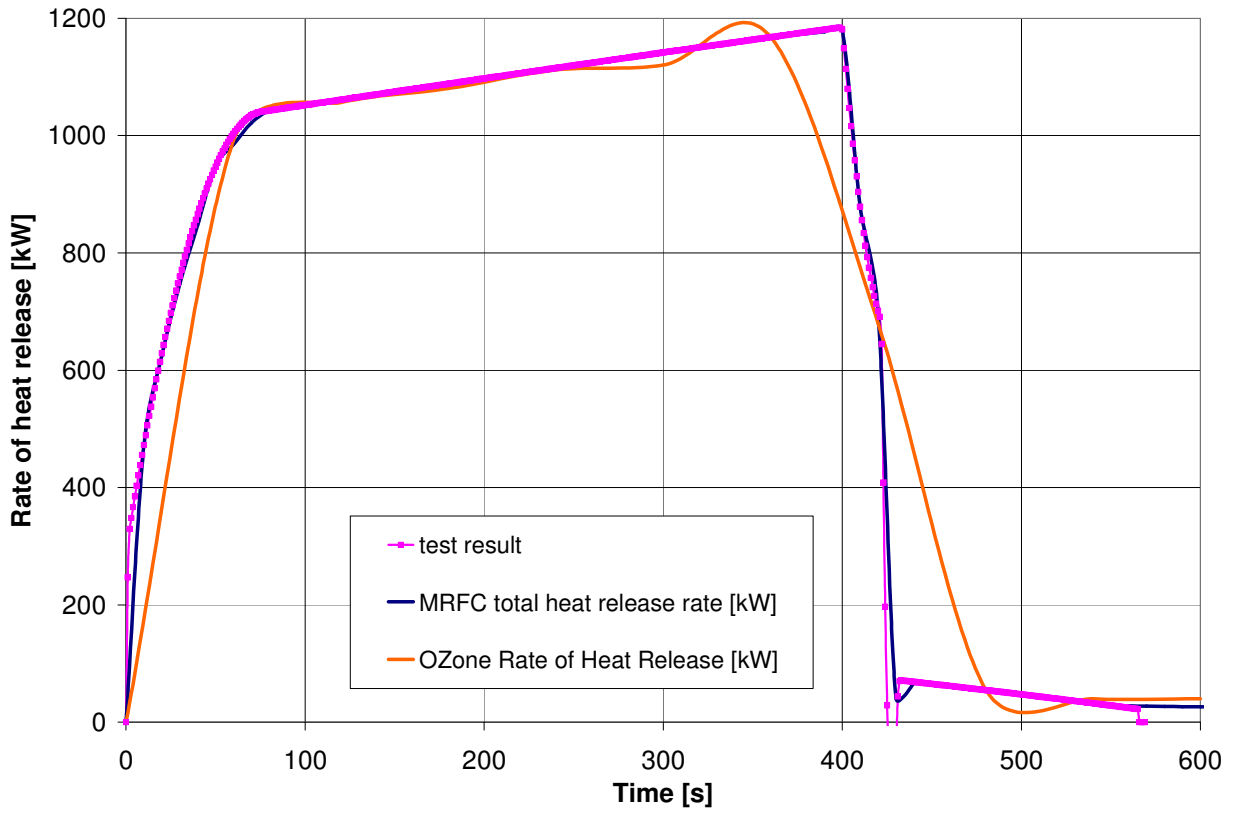


Figure D.44 – rate of heat release VTT test #9 ^[AGB]

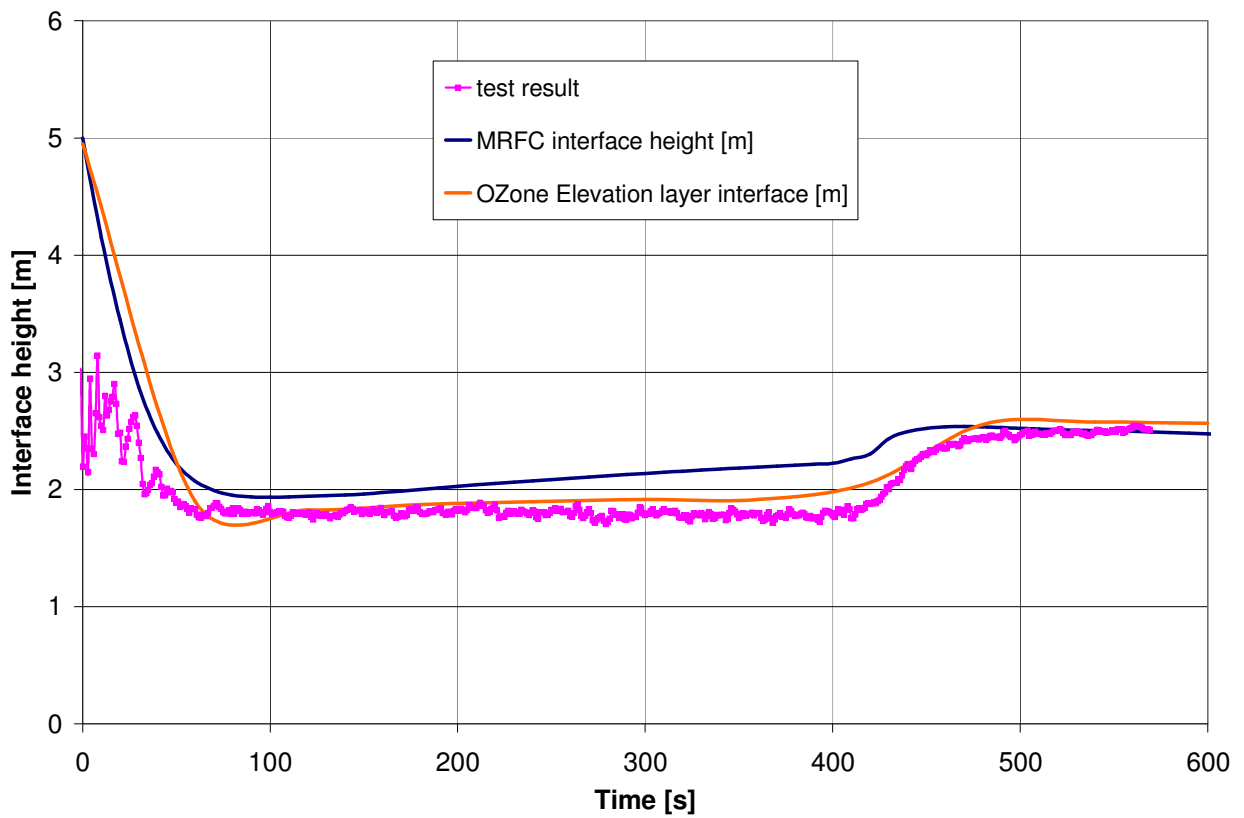


Figure D.45 – interface height VTT test #9 ^[AGB]

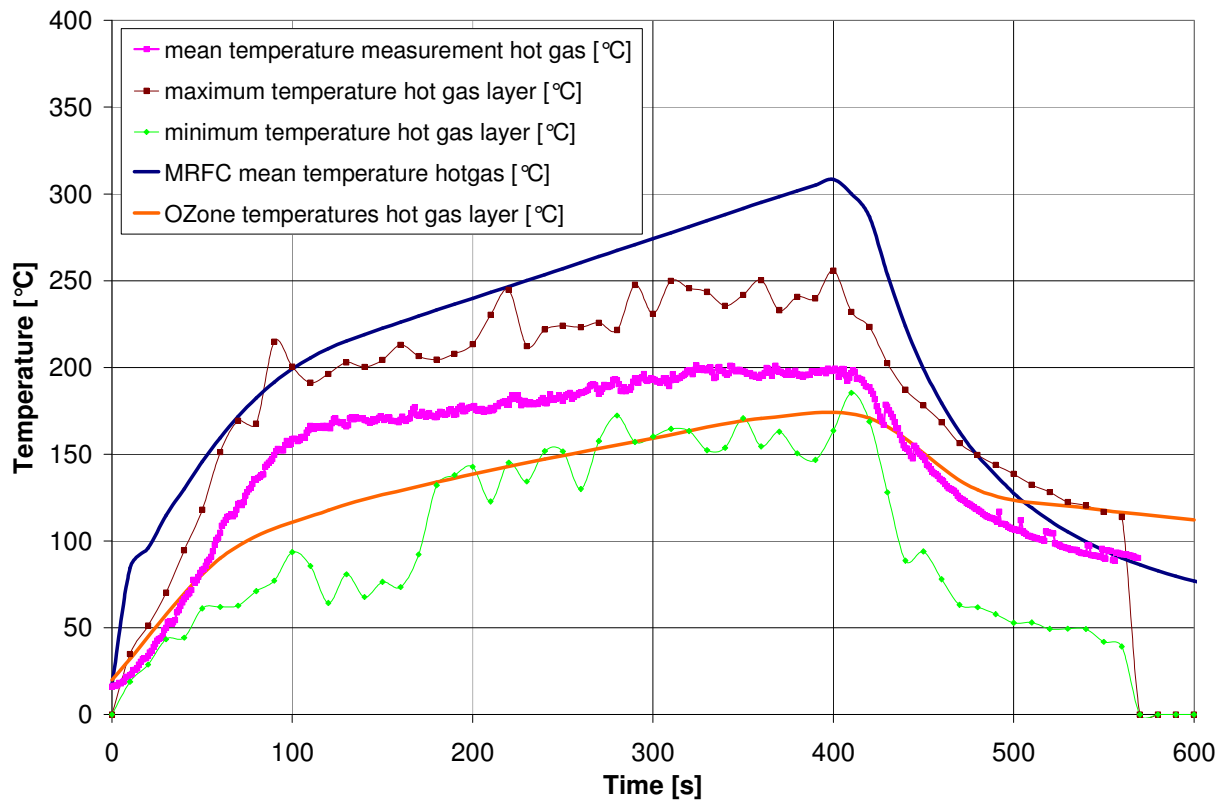


Figure D.46 – temperature of hot gas layer VTT test #9 ^[AGB]

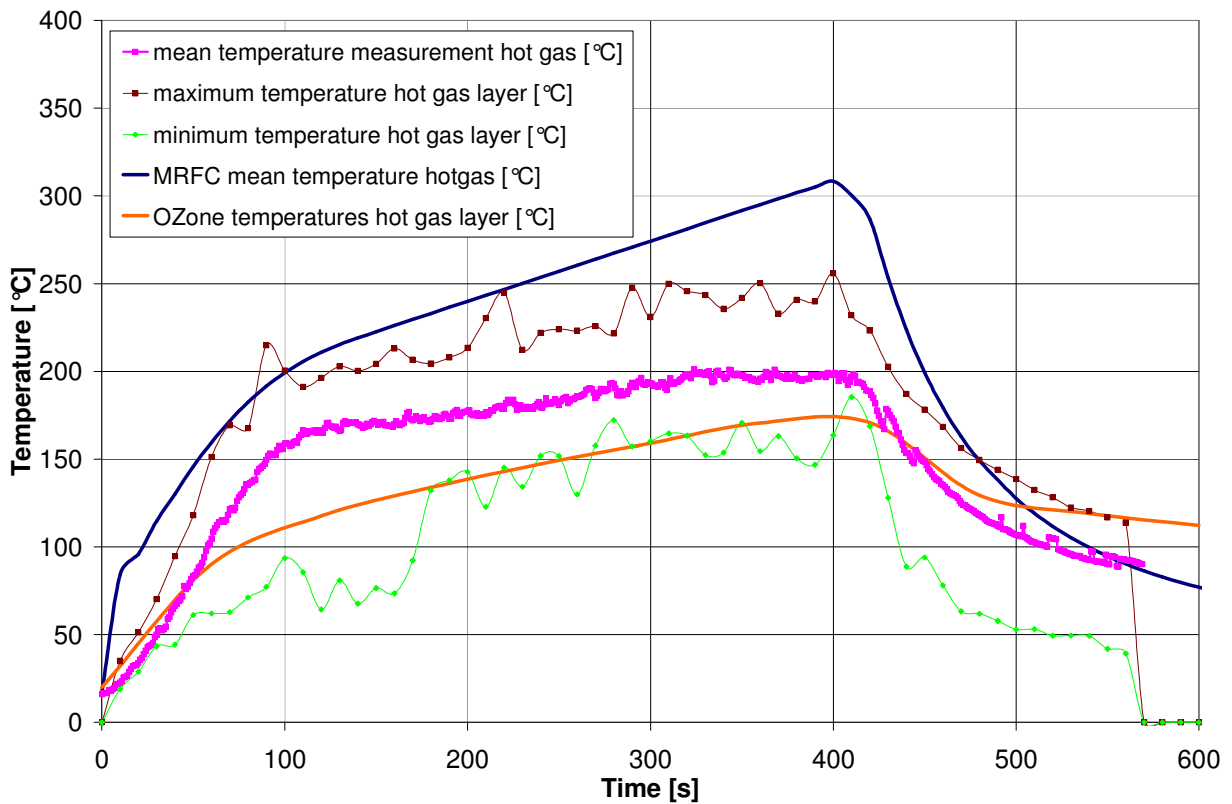


Figure D.47 – temperature of lower layer VTT test #9 ^[AGB]

Even if all input data that can be influenced by the user for the code OZone is essentially the same, there are some inevitable differences between codes according to physical modelling of the phenomena for mass and heat transfer to the ambient environment and/or to the enclosure boundaries. Different formulae are used in MRFC and OZone to describe the pressure distribution over the height above the floor of the compartment. In MRFC a linear distribution is assumed while OZone uses an exponential distribution in the height z above the height z_0 of the floor, which is of the form:

$$p(z) = p_0 e^{-\frac{g(z-z_0)}{RT}} \quad (\text{D.2})$$

In MRFC the following linear formulation is used:

$$p(z) = \frac{p_{floor} - z\rho_u g}{p_{floor} - (z'\rho_u - (z - z')\rho_l)g}, \text{ for } \frac{z \leq z'}{z' \leq z \leq h} \quad (\text{D.3})$$

with:

p_{floor}	=	reference pressure in the height of the floor
z	=	height above floor
z'	=	interface height above floor
h	=	height of ceiling above floor
ρ_u	=	density of upper layer
ρ_l	=	density of lower layer
g	=	acceleration due to gravity

The ambient pressure is 10^5 Pa and the distribution of pressure is nearly linear even with the exponential formulation (equ. D.2). Numerically there can be problems associated with calculating small differences of large numbers but it is considered that this aspect is not the source of any significant differences in the calculated results.

In the description of the heat transfer to the building material there is a major difference between zone model MRFC and OZone. In MRFC the convective heat transfer is calculated depending on the gas temperature. The same formulation is used as in CFAST for temperatures which are lower than 200 °C. A formulation according to forced flow with a constant defined velocity to a plate is used for temperatures which are higher than 600 °C. A linear interpolation is performed between these temperatures. In OZone a constant heat transfer coefficient is defined for the hot and cold gas layers, which is not changed during the calculation. In MRFC the parameters for the building material are changed according to actual temperature of the material. The temperatures of MRFC seem to be too high at lower hot gas temperatures.

The assumed value of 25 W/m²/K as convective heat transfer coefficient for the hot layer leads to temperatures which are too low; in further trials it was found that the temperatures can rise if a value of 12 W/m²/K is used, but they remain too low.

The use of temperature-dependant material properties in MRFC tends to improve the results if higher gas temperatures are reached.

CFD simulations with SOFIE

VTT large room test 8 was selected for performing CFD simulations by using the SOFIE code, via the graphical user interface JOSEFINE. Summary information about the test required for the SOFIE simulation is included in table D.9.

Description	Pool fire in large room - test 8			
Date of test	19 October 1998			
Fire source	0.61 m ² pool fire (diameter 0.88 m), 0.21 m above the floor, centrally			
Fuel	Heptane			
Nominal heat release rate	1440kW			
Geometry	Internal room geometry 10 m long, 7 m wide and 6 m high. Doorway opening on both front walls 2.4 m wide by 3.0 m high.			
Materials	Light-weight concrete			
Material properties	Material	Conductivity (W/m/K)	Density (kg/m ³)	Specific heat capacity (J/kg/K)
	Lightweight concrete	0.12	475	900
Test data	The average compartment temperature reached 350°C after 10 mins			

Table D.9 – summary of VTT room test 8

A brief summary of the main SOFIE model parameters is presented in table D.10:

Default numerical grid	61 x 36 x 36 = 79056
Discrete transfer rays	2 x 4
Numerical solver	TDMA
Prescribed soot mass fraction	0.088
Absorption coefficients	Truelove CH4+soot

Table D.10 – model parameters for SOFIE simulation of VTT room test 8

A grid sensitivity study was undertaken to investigate the influence on the results of the mesh resolution. Illustrative simulation results for the VTT room fire test 8 are shown in figs. D.48 and D.49 below, for two different fire locations:

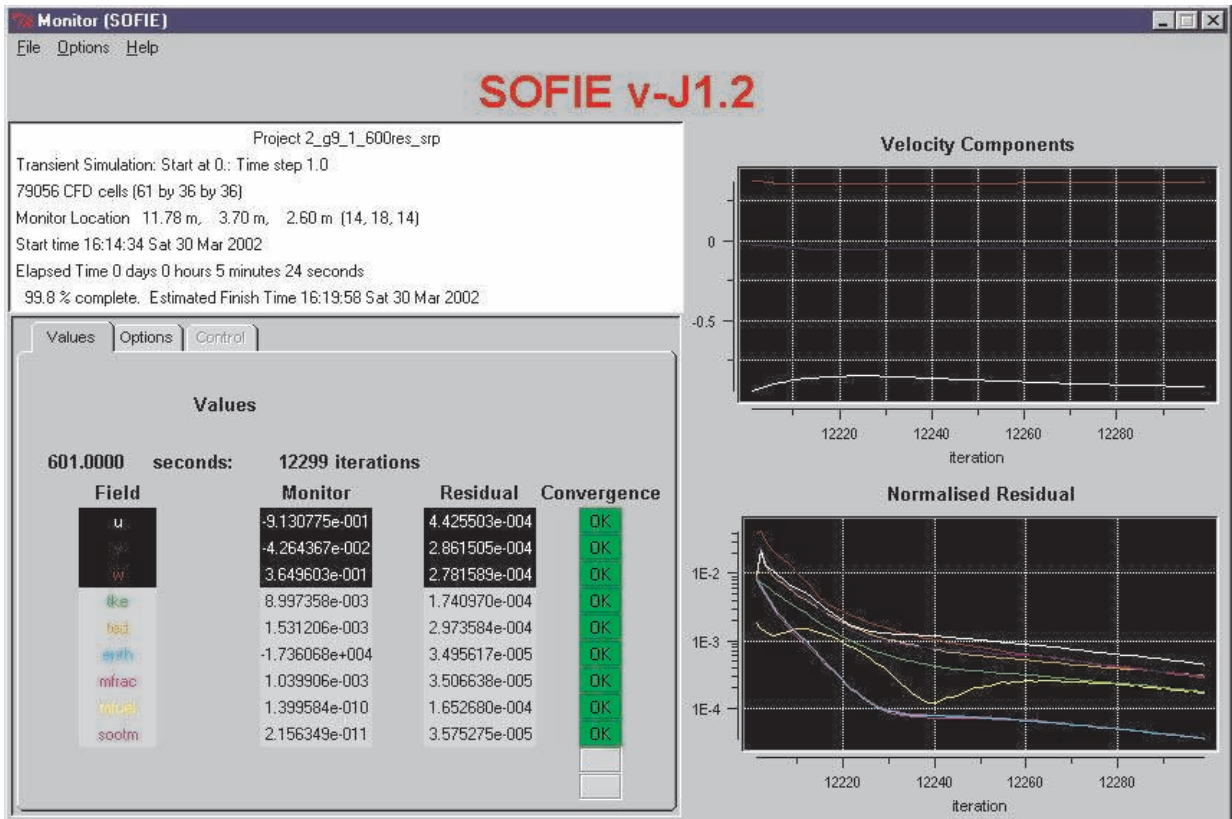


Figure D.48 – SOFIE monitor window at 600 seconds [AGB]

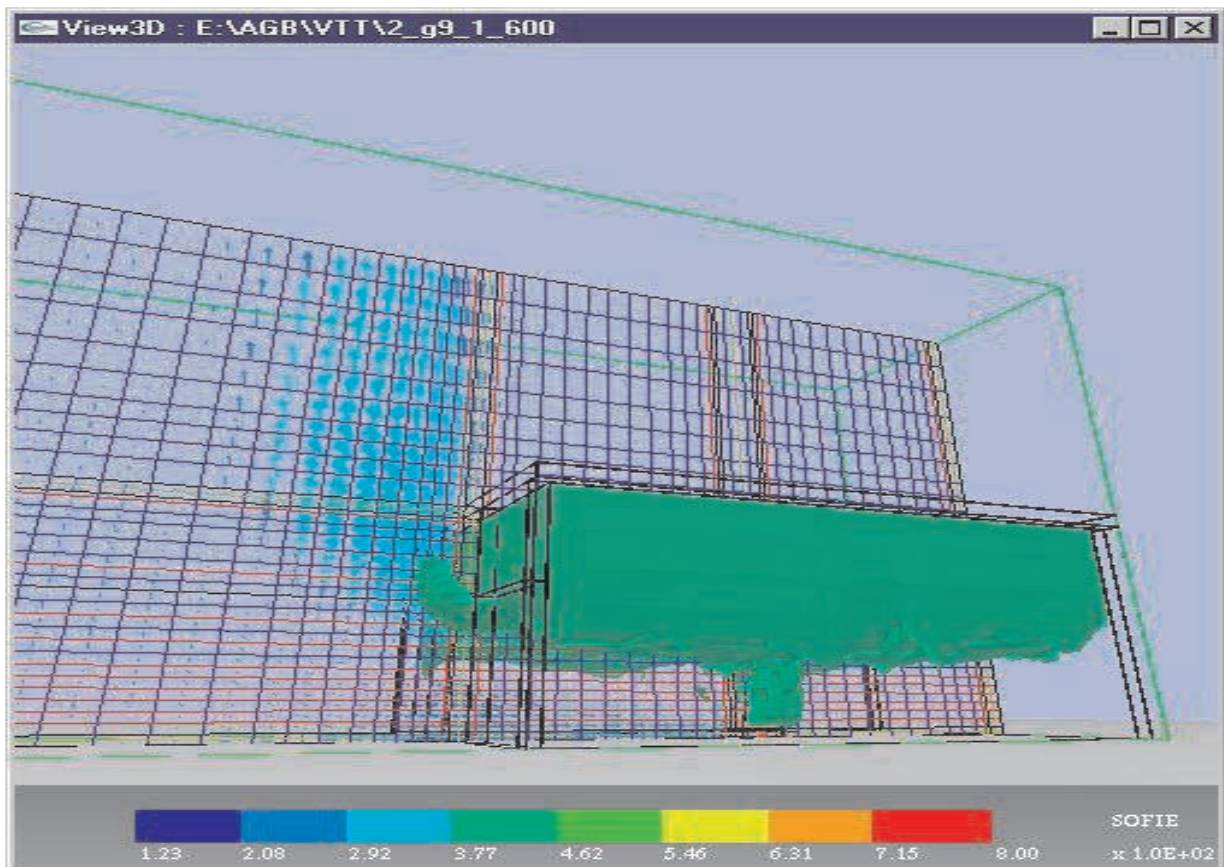


Figure D.49 – temperature iso-surface (800K) and velocity vectors [AGB]

Fig. D.50 shows the effect of the grid sensitivity and comparison of the transient simulations with measurements. Figs. D.51 and D.52 show the comparison of the predicted temperature and velocity profiles in the doorway with measurements at 500s when the gas-phase conditions in the room have reached the steady state. It can be seen that the CFD model has reproduced reasonably well the transient evolution of the thermal flowfield conditions of the large room fire test. Figs. D.53 – D.56 show the surface convective heat transfer coefficient distributions on the inner walls of the compartment. Summary information on these values is presented in table D.11. The overall average value, weighted by surface area, is $5.9 \text{ W/m}^2/\text{K}$.

Wall	Minimum	Maximum	Overall average
Back	2.5	8.4	5.7
Side	2.7	9.1	4.6
Front	3.2	10.7	6.8
Ceiling	3.8	10.7	6.8

Table D.11 – summary information on convective heat transfer coefficients ($\text{W/m}^2/\text{K}$) for VTT test 8

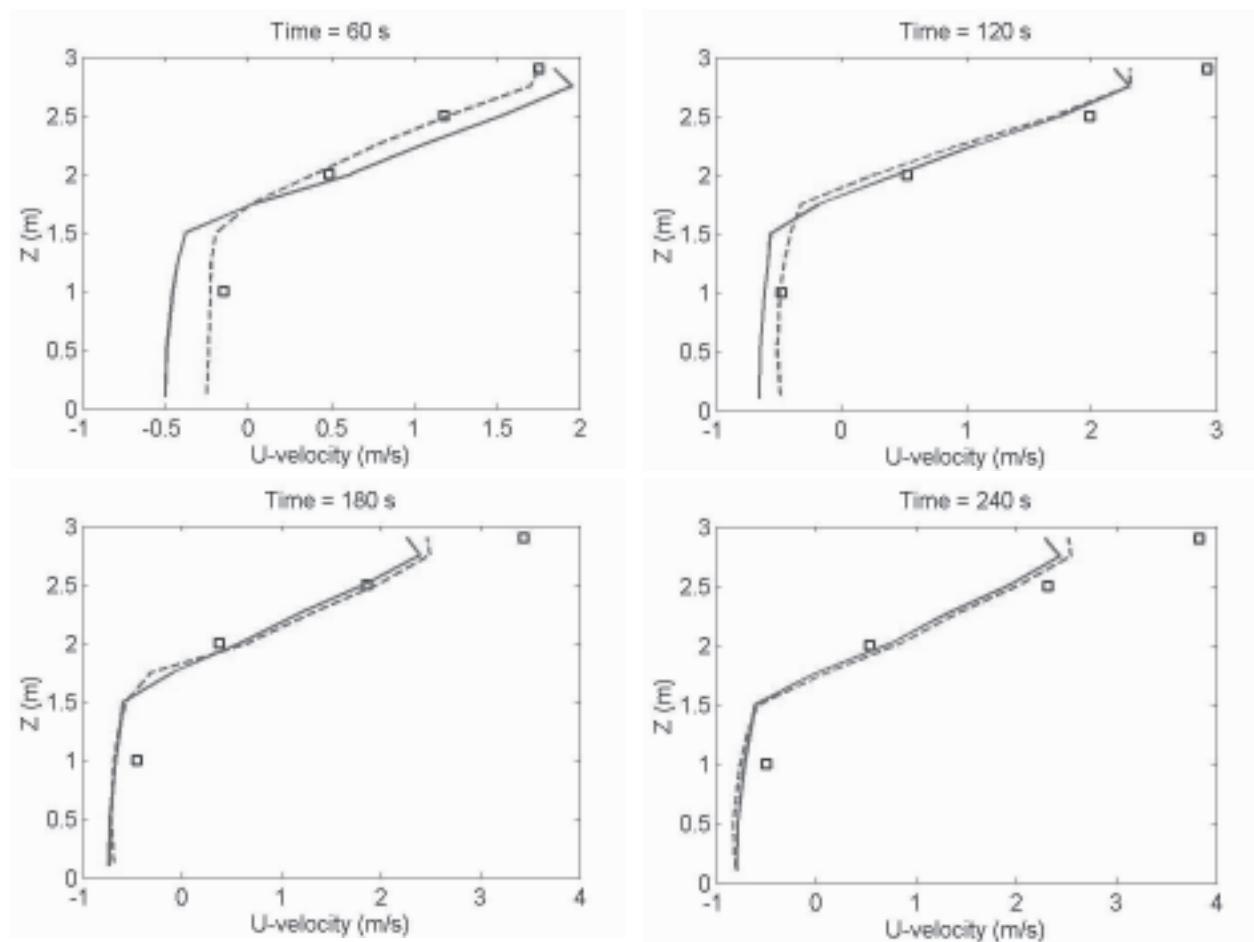


Figure D.50 – comparison of grid effect on door jet velocities at four time points ^[VTT]

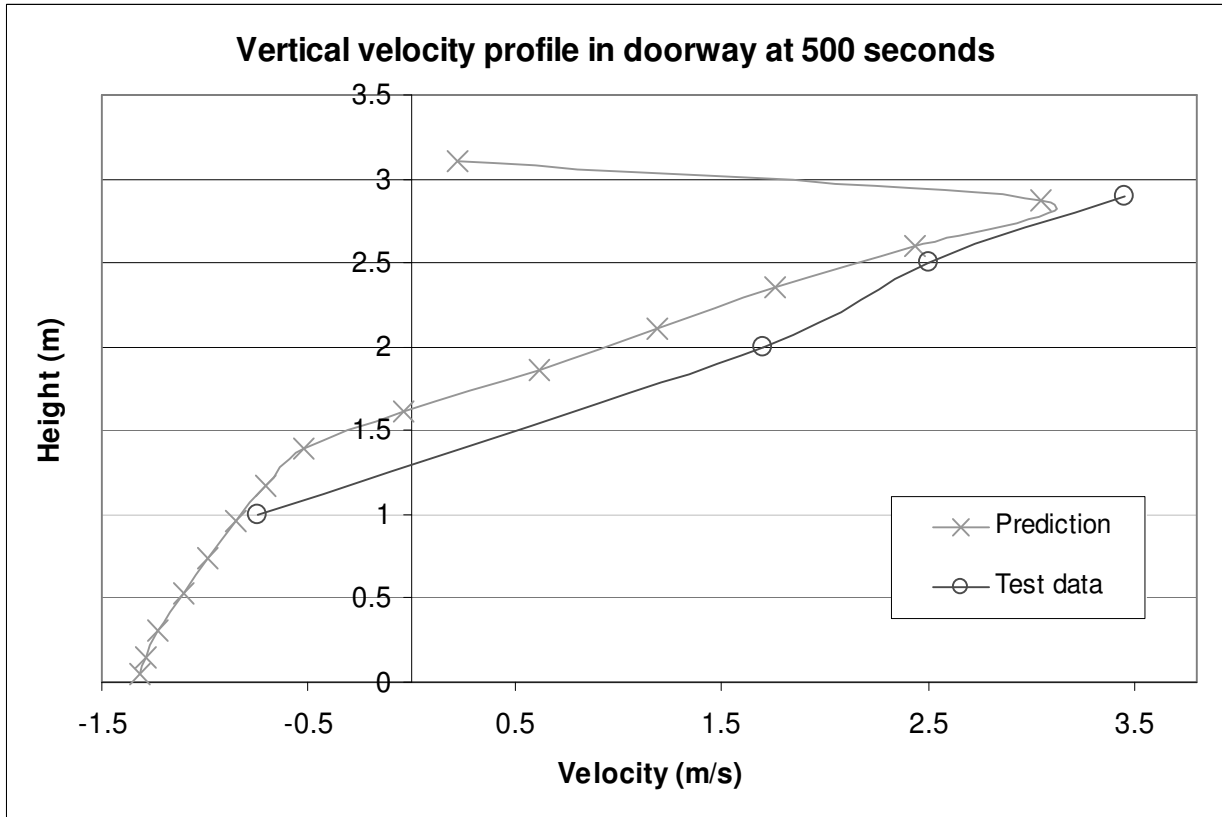


Figure D.51 – vertical velocity profile in doorway ^[BRE]

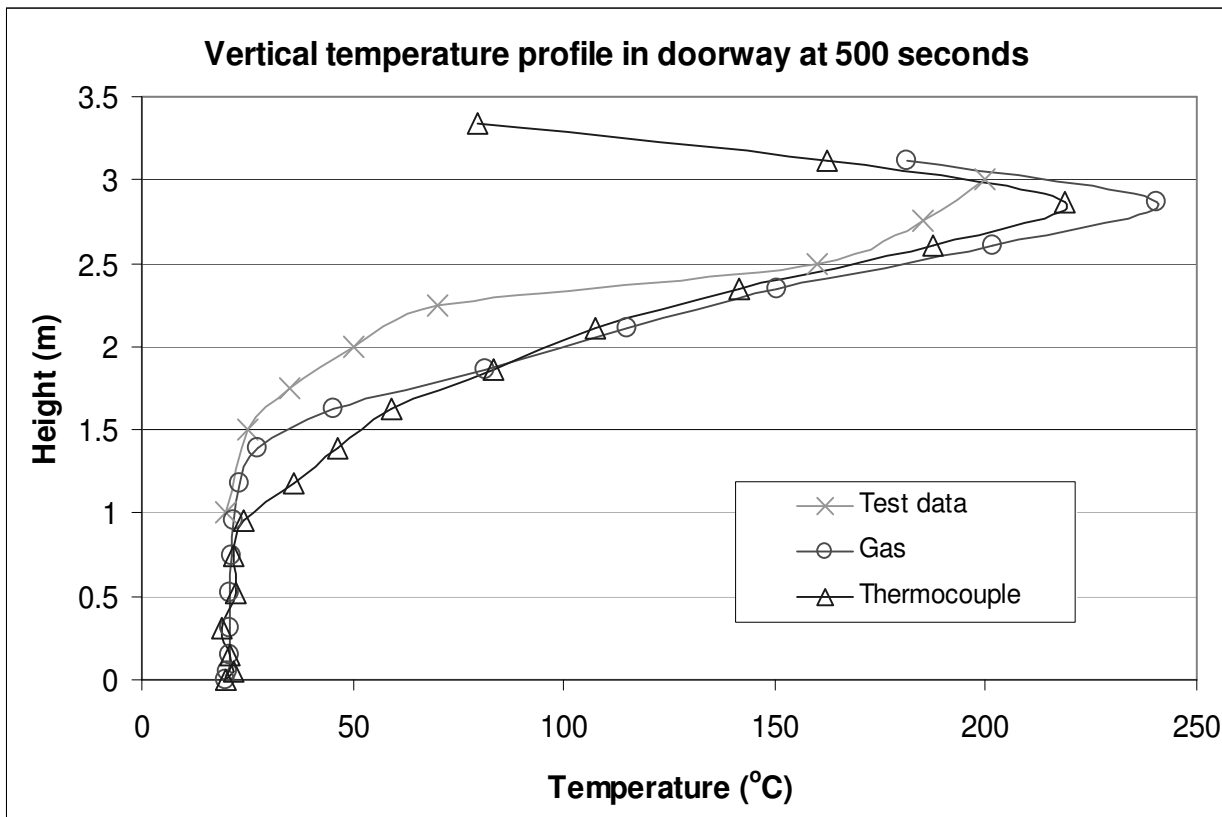


Figure D.52 – vertical temperature profile in doorway ^[BRE]

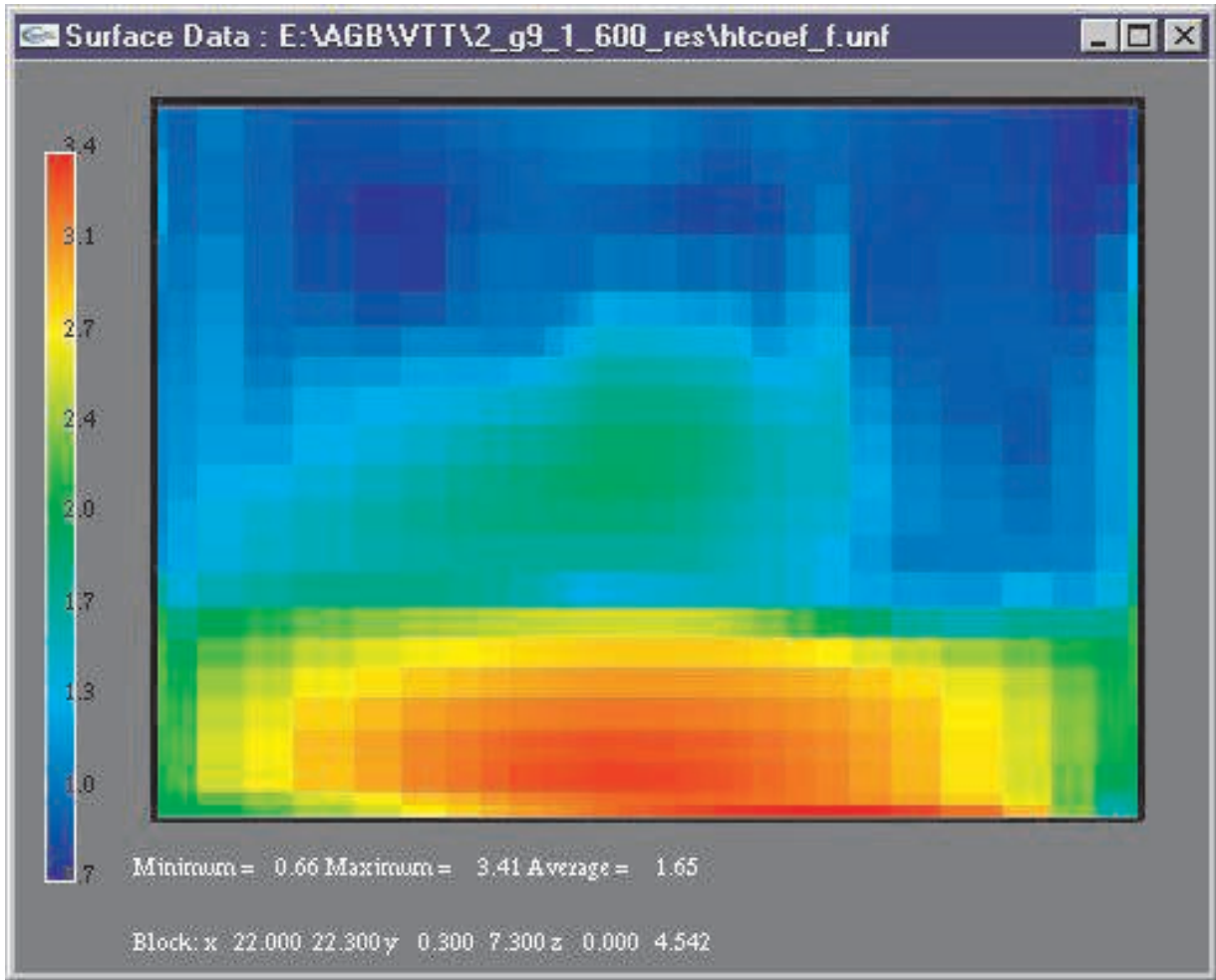


Figure D.53 – convective heat transfer coefficient inside rear wall of compartment ^[AGB]

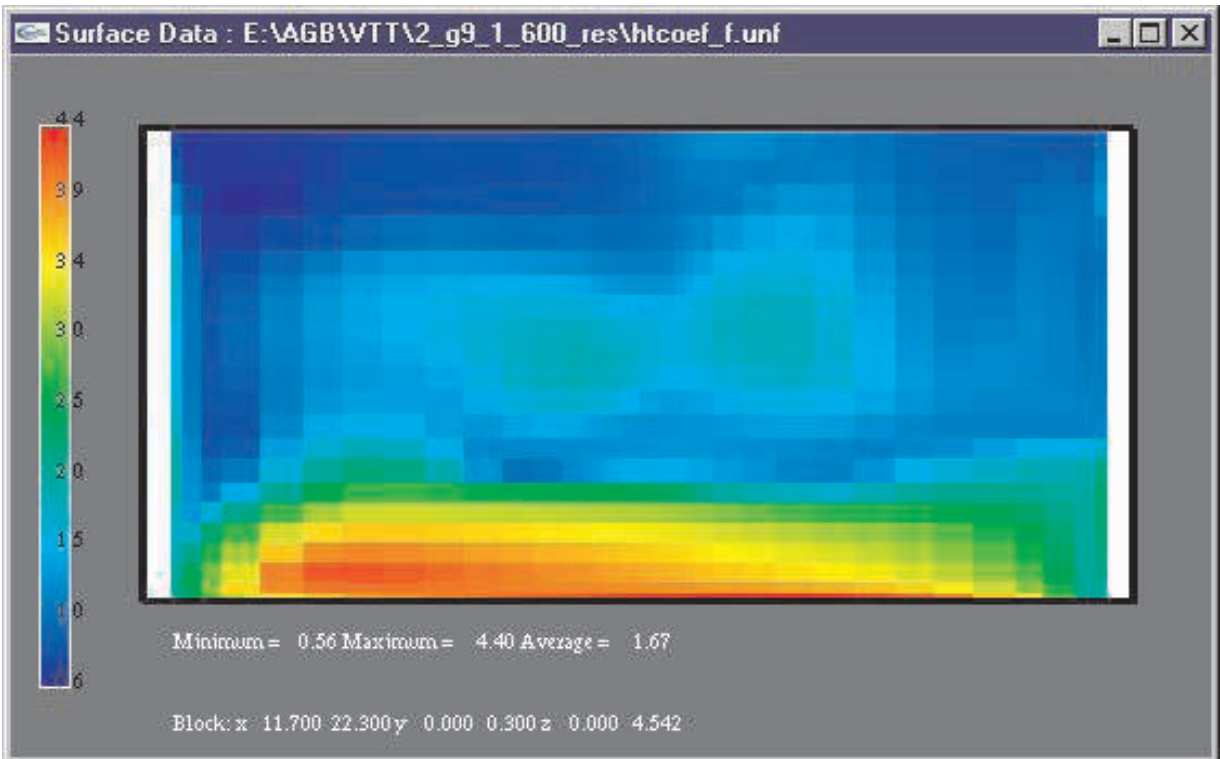


Figure D.54 – convective heat transfer coefficient inside side wall of compartment ^[AGB]

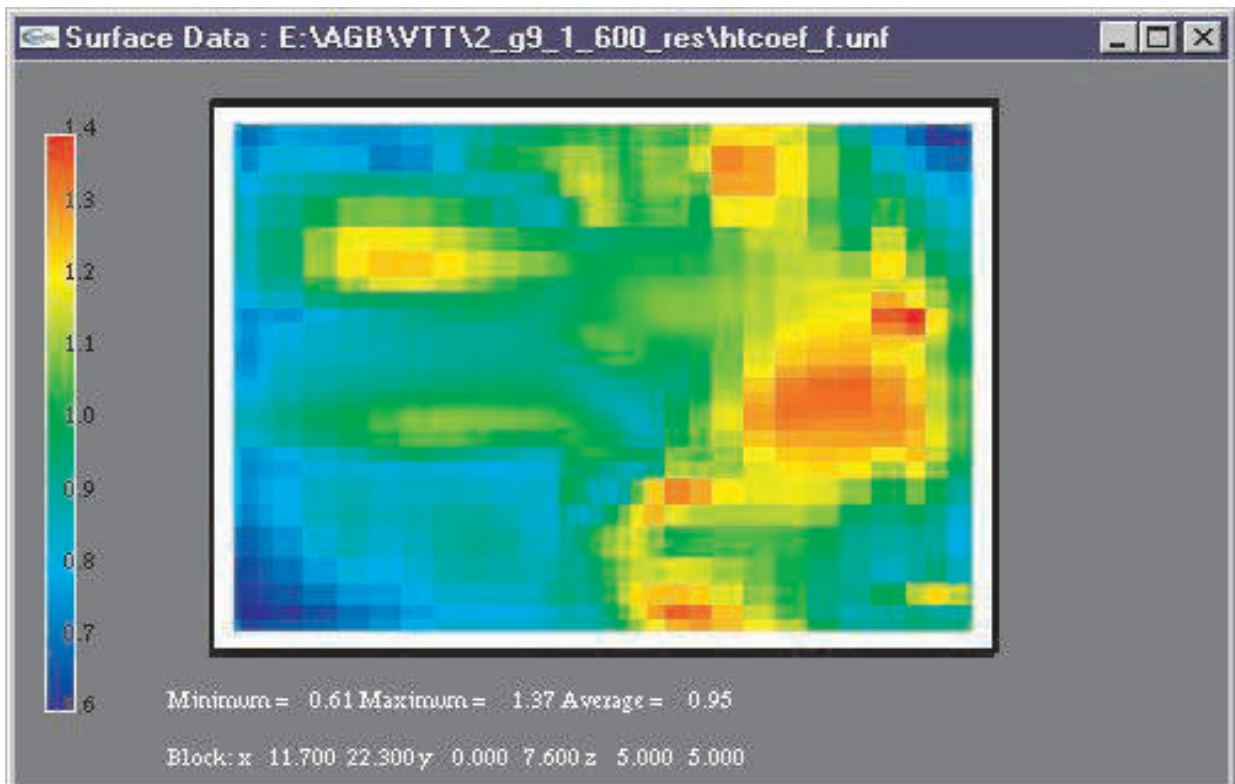


Figure D.55 – heat transfer coefficient on underside of ceiling of compartment ^[AGB]

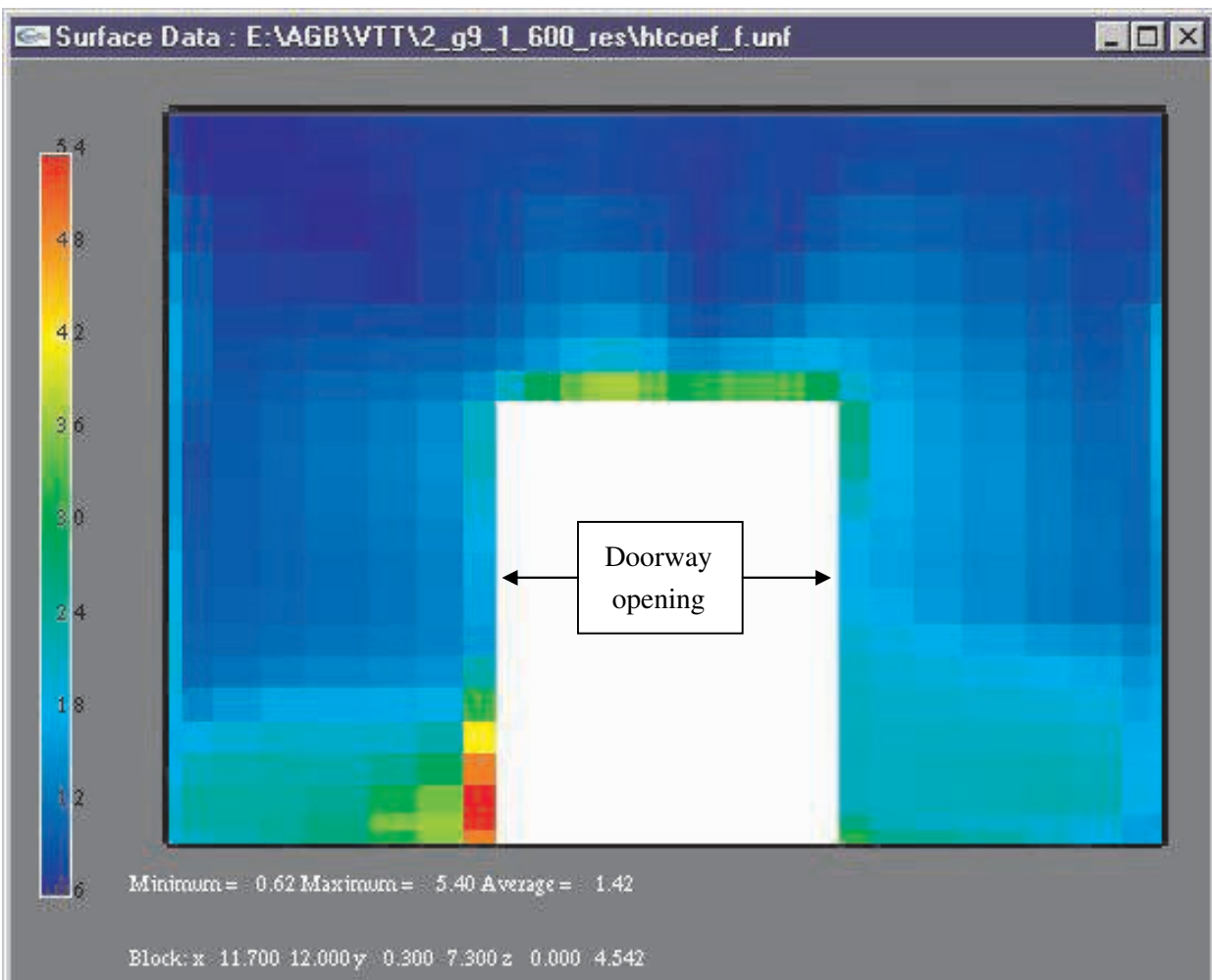


Figure D.56 – convective heat transfer coefficient inside front wall of compartment ^[AGB]

BRE large compartment fire tests

Experimental details

This test programme is summarised in table D.12 below. The relevant parameters investigated were location of ventilation opening, type of fire load and thermal properties of the compartment linings. The quantity of fuel load, opening factor and size of compartment were fixed for all tests. The distribution of fire load was the same in all cases, as was the method of ignition. Instrumentation locations were also kept constant throughout the experimental programme.

Test number	1	2	3	4	5	6	7	8
Fire load type	<i>W</i>	<i>W</i>	<i>W+P</i>	<i>W</i>	<i>W+P</i>	<i>W</i>	<i>W+P</i>	<i>W+P</i>
Boundaries	<i>I</i>	<i>HI</i>	<i>HI</i>	<i>HI</i>	<i>HI</i>	<i>I</i>	<i>I</i>	<i>I</i>
Opening	<i>F</i>	<i>F</i>	<i>F</i>	<i>F+B</i>	<i>F+B</i>	<i>F+B</i>	<i>F+B</i>	<i>F</i>

Table D.12 – BRE large compartment test series

Key: *W* = 100% wood
W+P = 80% wood, 20% plastic
I = compartment lining - insulating
HI = compartment lining - highly insulating
F = opening at the front only
F+B = openings at both front and back

Table D.13 below shows the relevant parameters for ventilation for the cases of front opening and front & back opening. Tests 4 to 7 all had openings at both the front and back of the compartment while Test 8 had the opening only at the front of the compartment.

Ventilation Characteristics		
Parameter	Front opening	Front & back opening
Area of vertical openings on all walls, A_v [m ²]	24.48	24.48
Opening height, h_{eq} [m]	3.4	1.7
Total surface area, A_t [m ²]	451.2	451.2
Opening factor ($A_v\sqrt{h_{eq}}/A_t$), O [m ^{1/2}]	0.1	0.07

Table D.13 – BRE large compartment test series – ventilation characteristics

The compartment was well instrumented for temperature and load cells were used to measure mass loss of certain timber cribs. Additional instrumentation included thermocouples and velocity probes in the doorway and total heat flux meters in the compartment walls and ceiling.

Test 8 of the NFSC2 series of tests on the BRE large compartment was previously selected as the main test case for model validation for this scenario. Simulations were also run for test 6 with openings at the front and the rear of the compartment giving nominally the same total opening area.

A series of photographs showing pre-test conditions and fire development for test 8 are shown in figs. D.57 – D.60.

The heat release rate curves required for the CFD simulations can be derived from mass loss data measured in the tests. In test 8, two different fuels were burnt - "plastic" (= polypropylene) and "wood", with the weight of plastic having been determined in advance to provide an equivalent energy content when burnt to that of the wood (4900 kg wood, 490 kg plastic, c.f. Schleich et al., 2000). Since the heat of combustion values for these two combustibles are significantly different, a substantially smaller mass of plastic is needed to provide the same energy content as the wood. When this plastic burns, its contribution toward the overall mass loss rate will be consequently reduced by the ratio of the values for heat of combustion. Therefore, determination of the evolution of the heat release rate depends on an assumption about the burning histories of the two different materials.

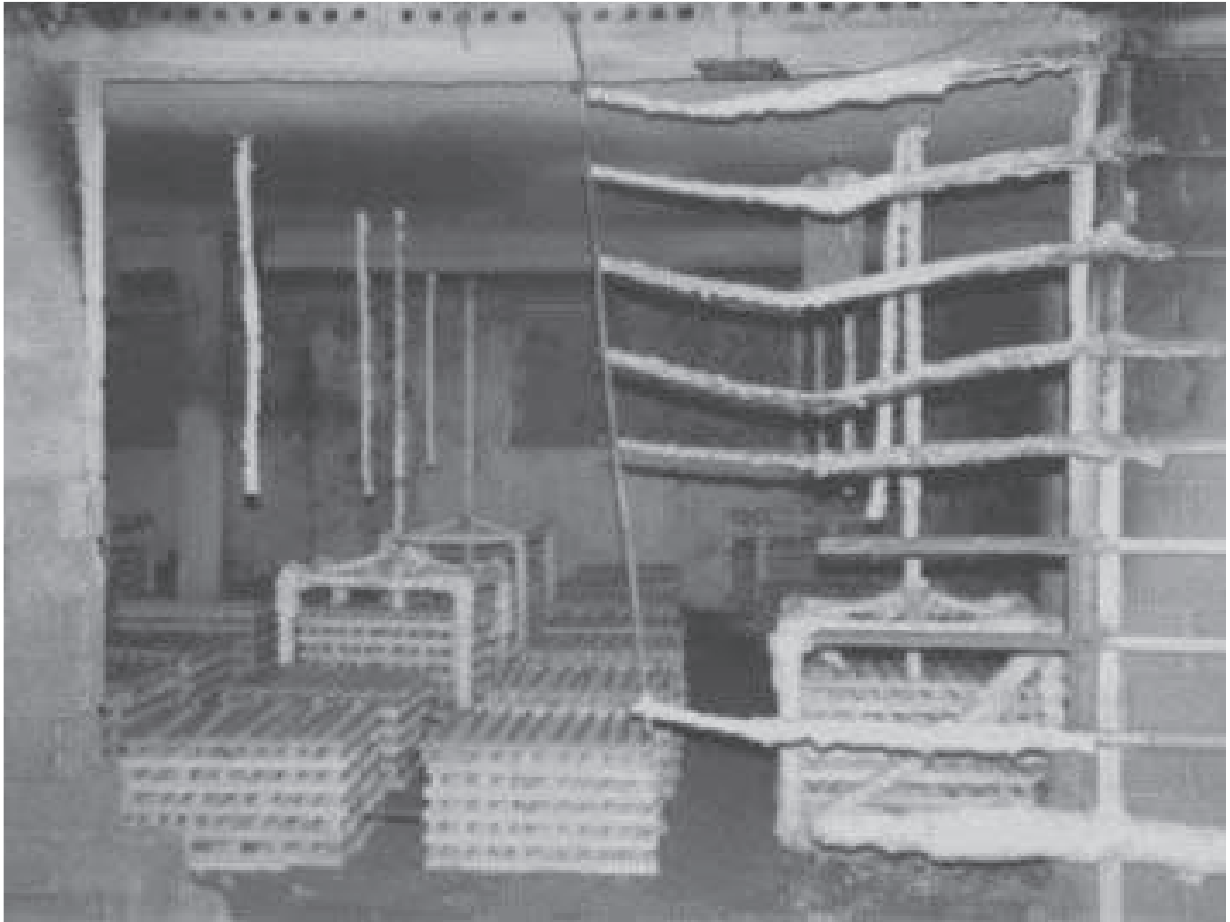


Figure D.57 – right-hand opening in BRE large compartment prior to test 8 (17/2/00)



Figure D.58 – right-hand opening showing early fire development in test 8



Figure D.59 – front openings showing later fire development in test 8



Figure D.60 – front openings showing flashed-over burning in test 7 (6/1/00)

It might be expected that the plastic material would burn off more vigorously than the cellulosic and this is borne out by the test data (e.g. average temperature just exceeded 600°C at 5 minutes in test 2 (wood only) whilst it exceeded 900°C at this time in test 3 (identical conditions, but with a wood and plastic fuel load). Furthermore, the plastic was located on top of the cribs, thus exposing it more effectively to the incoming air.

In order to derive an estimate of the actual heat release rate an assumption was made that the plastic burnt off preferentially at the beginning of the test, but that the proportion of plastic burning thereafter was proportional to the mass of plastic remaining. This meant that the early part of the heat release curve was dominated by the plastic contribution.

The calorific values (heat of combustion) and combustion efficiencies (equivalent to the "m combustion factor" of EC1 Annex E) were assumed to be:

polypropylene	43 MJ/kg	0.9
wood	17 MJ/kg	0.95

The value for polypropylene is a typical literature value, and it should be noted that it differs from the value of 34 MJ/kg stated in Schleich et al. (2000).

The heat release curves obtained in this manner are shown in figs. D.61 and D.62 for test 6 and test 8 respectively. These curves are consistent with the test measurements of velocity: wood and plastic have very similar heats of combustion *per unit mass of oxygen*, so on the basis of the heat release curve defined so as to accommodate the differential burning rates, similar air entrainment rates would be expected from both (neglecting the oxygen content of the wood itself). This is indeed observed in the test data for opening velocities.

Fig. D.62 also shows the original heat release curve derived from the mass loss data presented in Schleich et al. (2000); peak values are quite similar, but the early fire development was not well represented by the original curve.

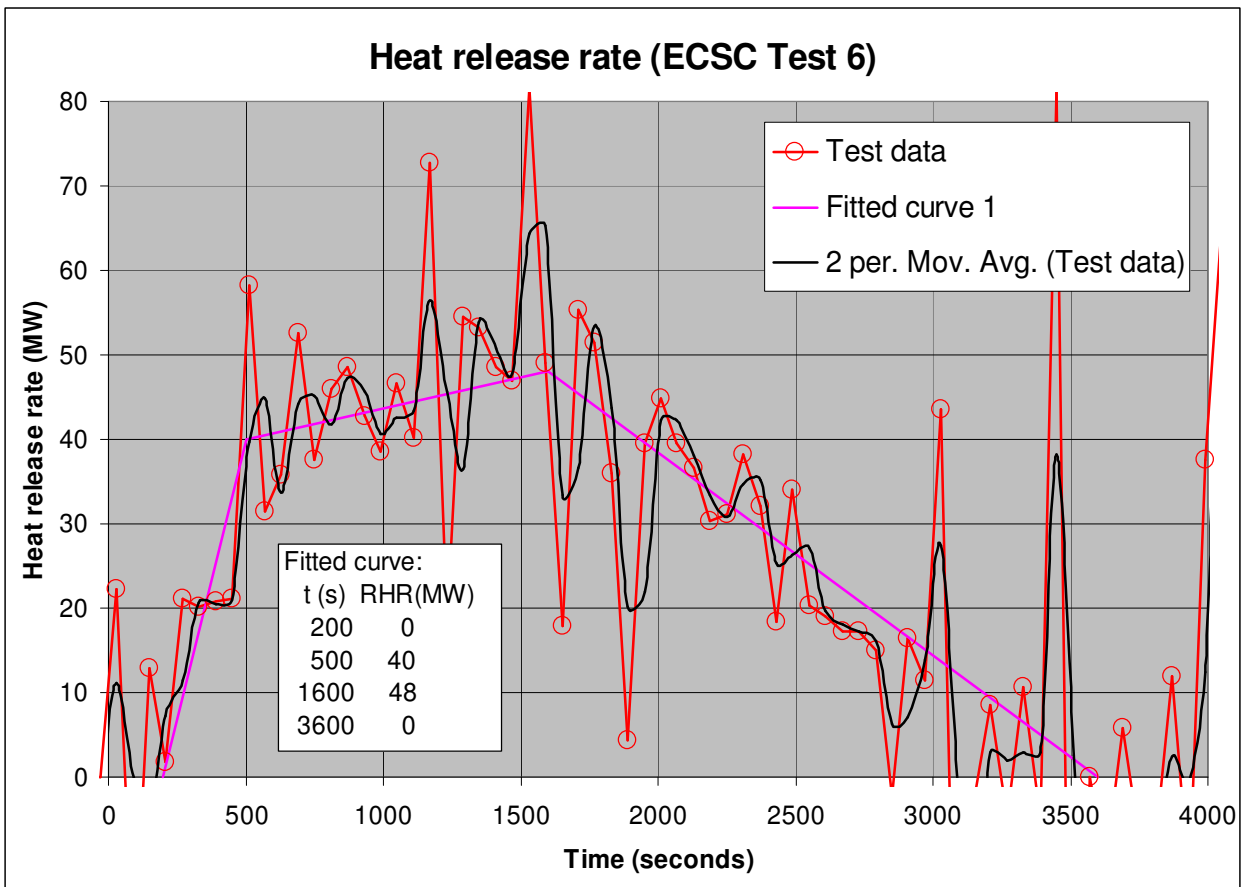


Figure D.61 – approximate heat release rate curve for BRE large compartment test 6

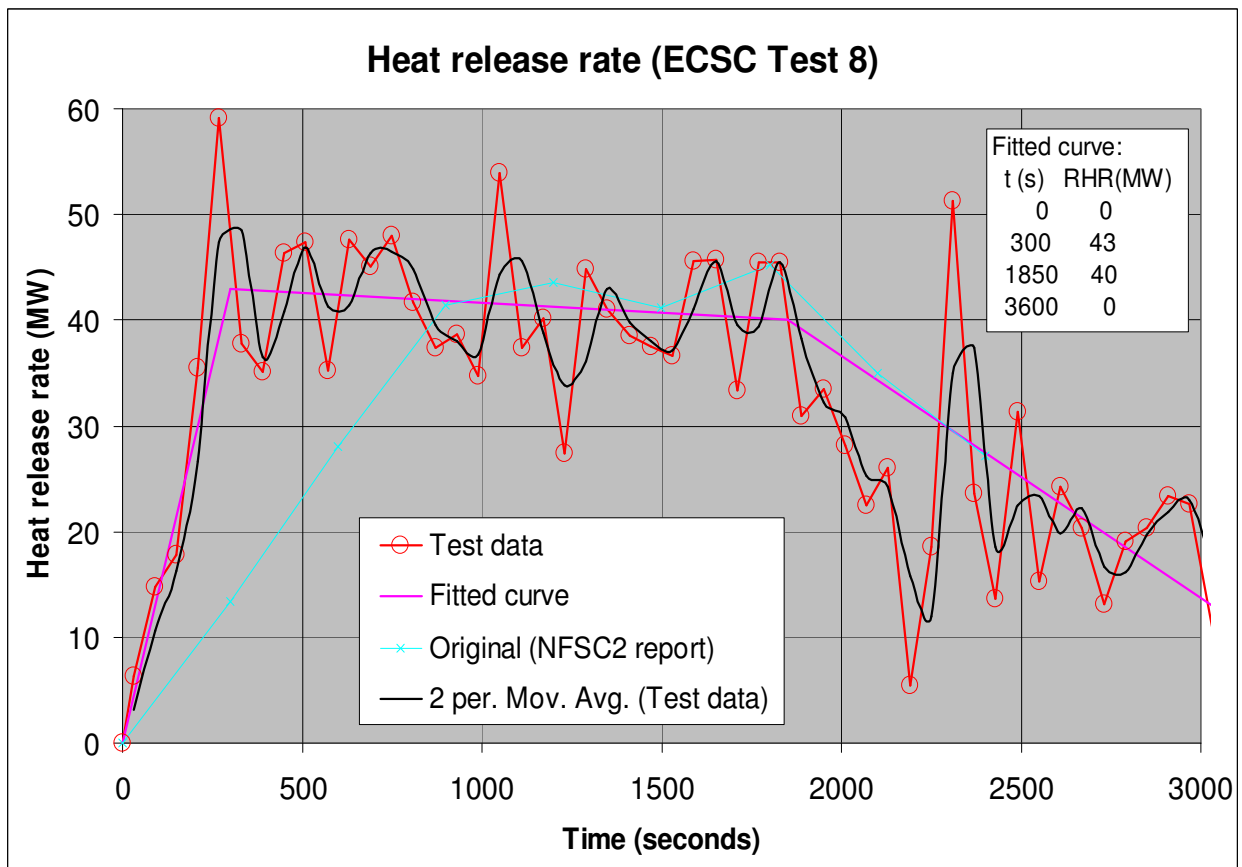


Figure D.62 – approximate heat release rate curve for BRE large compartment test 8

Revised summary information about the tests is presented in Tables D.14 and D.15 for test 6 and test 8 respectively.

Description	Wood crib fire in large compartment			
Date of test	11 November 1999			
Fire source	49 stick cribs of dimensions c. 1 m square arranged in 7 rows of 7 parallel to the compartment walls, with the central crib built around the main supporting column			
Fuel	Wood cribs			
Nominal heat release rate	There was a longer initial delay in this test, with no significant rise in compartment temperatures until about 200 seconds after "ignition". Thereafter, heat release rate rose to 40MW at 500 s and continued to rise to 48MW at 1600s before a linear decay (see fig. D.61)			
Geometry	Internal room geometry nominally 12 m x 12 m plan by 3.4 m high. Two openings on both front and rear walls each nominally 4 m wide over the upper half of the opening arranged symmetrically around the compartment centreline. Measurement of the actually geometry in situ showed that the opening height was only 1.4 m, whilst the opening width was 3.6 m.			
Materials	Light-weight concrete - used for the masonry walls - 0.19m thick Precast concrete - used for the ceiling slabs - 0.15 m thick Steel - 254x254UC73 section used for main beams and columns Sprayed fibre fire protection material (Fendolite MII) applied in nominal 25 mm thickness over underside of ceiling slabs and on beams and columns			
Material properties	Material	Conductivity (W/m/K)	Density (kg/m ³)	Specific heat capacity (J/kg/K)
	Lightweight concrete	0.42	1375	753
	Precast concrete	1.5	2400	1500
	Fendolite MII	0.19	680	970
Test data	The average compartment temperature reached 1000°C after 10 minutes and continued to rise to a peak of c. 1220°C at 42 minutes, falling off exponentially; the peak temperature at 42 minutes was c. 1300°C, near the rear wall of the compartment.			

Table D.14 – summary of BRE large compartment test 6

Description	Wood and plastic crib fire in large compartment			
Date of test	17 February 2000			
Fire source	As above			
Fuel	A combination of wood and plastic sticks having an equivalent total calorific value in the ratio wood 80% to plastic 20%			
Nominal heat release rate	Variable, peaking soon after the start of the test (300s) at about 43 MW, but displaying a reasonably stable burning plateau until 1850 seconds (see fig. D.62)			
Geometry	As above			
Materials	As above			
Material properties	As above			
Test data	The average compartment temperature reached 1000°C after 10 minutes and continued to rise to a peak of c. 1130°C at 45 minutes, falling off exponentially; the peak temperature at this point was c. 1330°C, near the rear wall of the compartment.			

Table D.15 – summary of BRE large compartment test 8

Fig. D.63 shows the recalculated velocity curve in which the best estimate of true gas temperatures was used in computation of the velocity (making reference to the difference between gas and thermocouple temperature in the predictions), rather than the measured thermocouple temperatures as previously. This introduces a correction which can be quite significant in the inflow. The recalculated curve was therefore used in subsequent comparisons with the model predictions, but any second-order effects due to further change of the results were neglected.

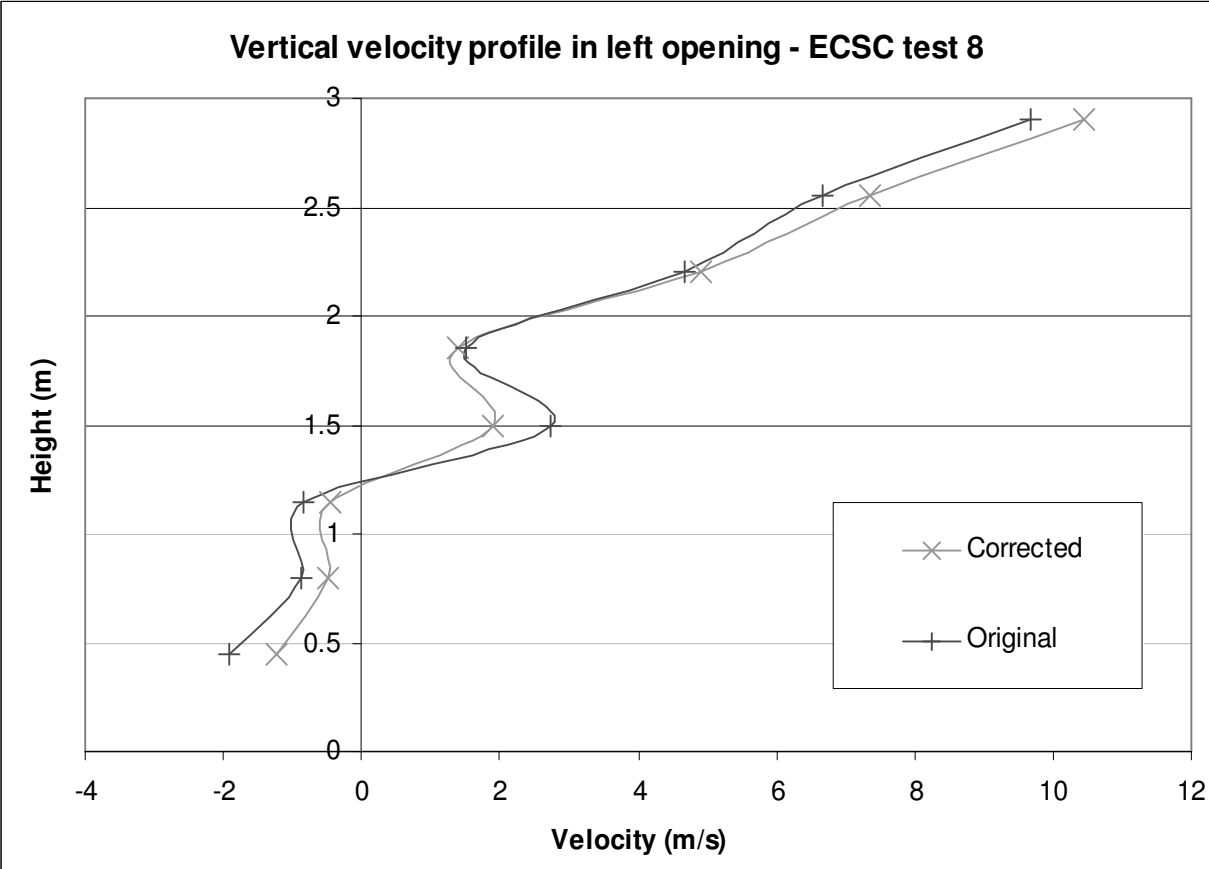


Figure D.63 – doorway centreline velocity curves from test for which thermocouple temperatures (original) and estimated gas temperatures (corrected) were used ^[BRE]

OZone simulation results

Each test was simulated with OZone. The results generally agreed well with the test data, though there were some differences in the shape of the temperature curves. Peak temperatures were within 10% of the experimental values in five cases out of eight, with the other cases showing rather higher temperature. Peak temperature was underpredicted in only two of the eight cases.

MRFC simulation results

The MRFC zone model was applied to test 8. A light-weight concrete with 20 mm insulation was used and a normal concrete of 100 mm thickness. For the contraction coefficient a value of 0.6 was defined. The fundamental parameters used for the calculations are mostly the same as previously. The protection is modelled using the temperature correlation for vermiculite, which is included in the program. The values for ρ and c_p are modified with two parameters $f_\lambda = 0,778$ ($\lambda = 0.19$ W/m/K) and $f_a = 0,836$ ($\rho = 680$ kg/m³, $c_p = 970$ J/kg). The chosen correlation produces constant parameters during the whole simulation time and temperature area.

In defining the heat release rate, it was considered that for wooden fuel the effective heat of combustion should not be constant during the whole time of burning. At the beginning of the fire the moisture content of the wood is pyrolyzed together with some light components of wood. Therefore the effective heat release rate should be lower in this phase of the fire. At the end of the fire there is mostly char (with a higher value for the heat of combustion) burning, so that the rate of heat release should be higher

The simulation results showed that there was not enough oxygen available for complete burning of the pyrolyzed fuel. Therefore the amount of oxygen in the hot gas goes to zero and a large amount of carbon monoxide is produced. Only a small amount of heat is going to the surfaces, most of the heat is flowing to outside through the opening.

After 12 minutes of simulation there is found to be only one layer inside the compartment. Up to 40 minutes this temperature agrees very well the average temperature derived from all measured temperatures in the compartment, as shown in fig. D.64.

Temperatures in the protected beam were computed and found to be overpredicted by about 100 °C (i.e. 25%), even though the calculated mean gas temperature fits quite well with the measured mean temperature in the compartment.

The temperatures of the unprotected beam and the surface temperatures of ceiling, wall and floor are also overpredicted during the initial phase with two layers in the compartment. Thereafter, the calculated temperatures are mostly too low. This results from the use of a single mean temperature in the compartment which does not take into account the fact that the temperatures are higher near the ceiling than at a lower location in the experiment.

The overall evaluation of the calculation shows that the temperatures for both the gases and the solid materials could be adequately reproduced. The accuracy reached is sufficient for practical application and on the safe side, if some rules for application are considered.

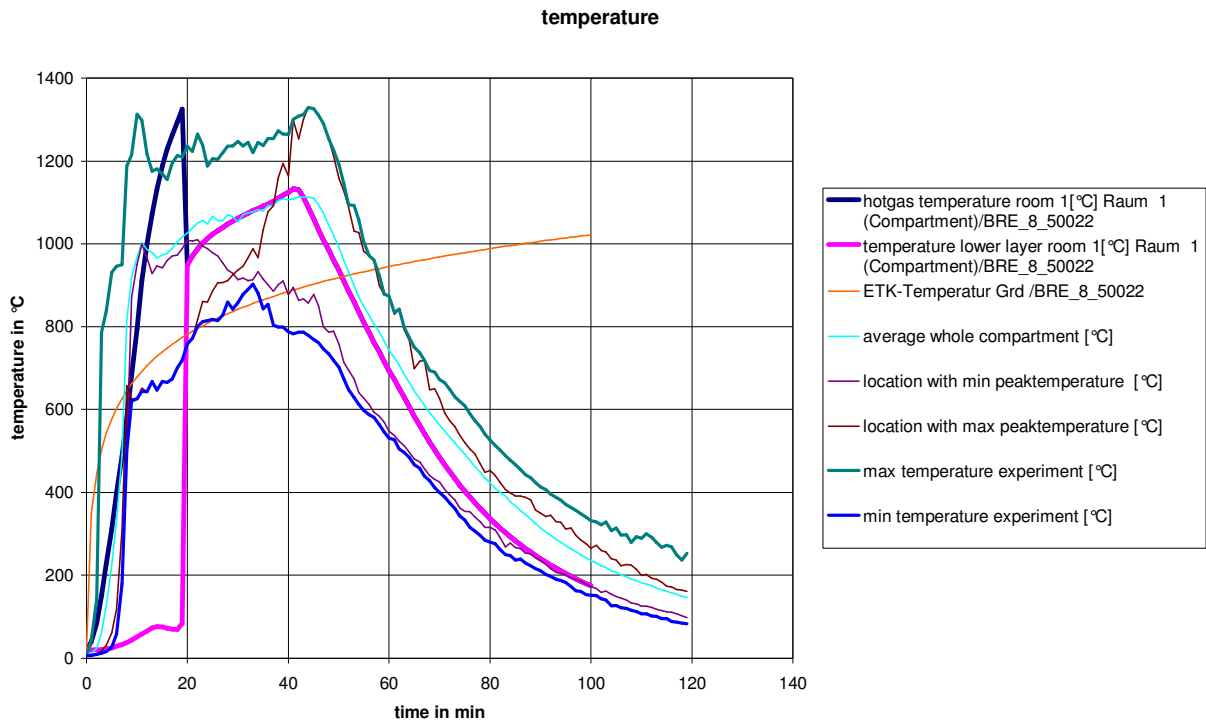


Figure D.64 – comparison of MRFC temperature prediction and experiment for BRE large compartment test 8 ^[AGB]

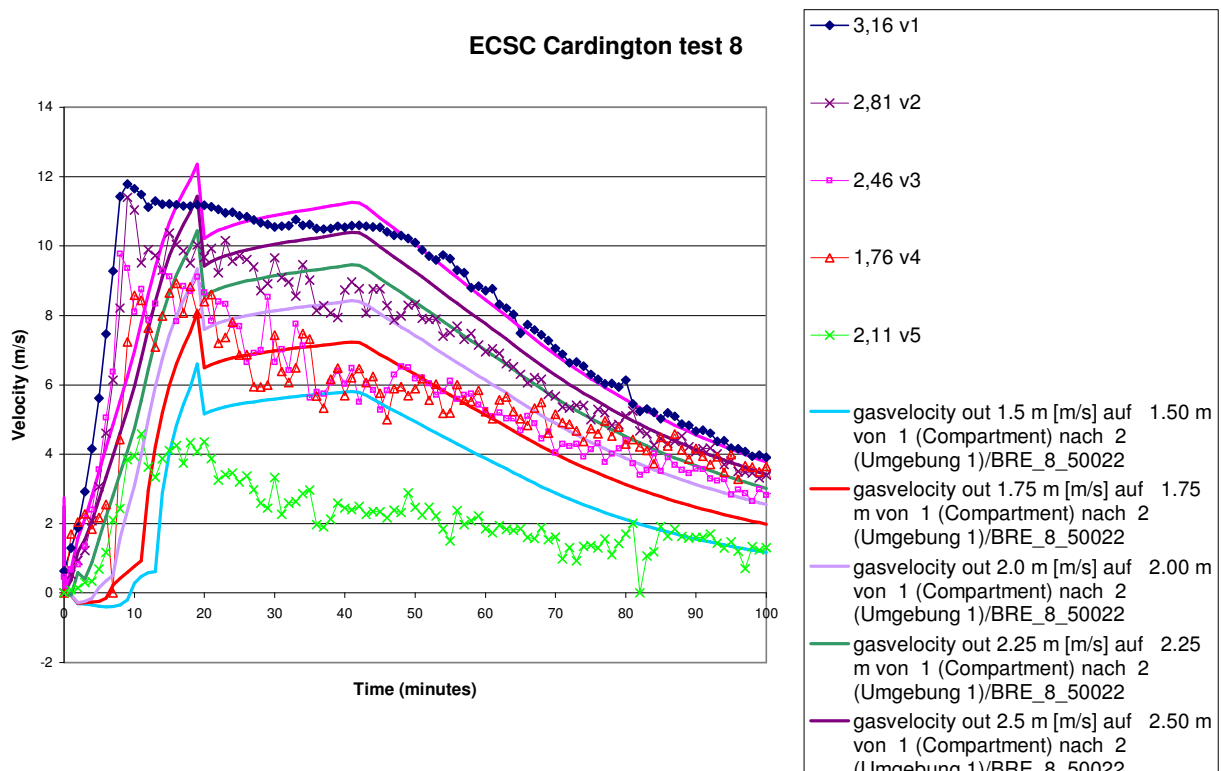


Figure D.65 – comparison of MRFC velocity prediction and experiment for BRE large compartment test 8 ^[AGB]

SOFIE simulation results - test 8 (front opening only)

For the simulations, the heat release rate was implemented via definition of crib burning rates for 7 rows of 7 fires. The burning rates were weighted (linearly) such that the peak burning zone moved progressively into the depth of the compartment whilst maintaining the correct overall heat output.

A brief summary of the main model parameters is set out in table D.16:

Numerical grid	32 x 47 x 39 = 58656
Discrete transfer rays	2 x 4
Numerical solver	sip3d
Prescribed soot mass fraction	0.035
Absorption coefficients	Truelove CH4+soot

Table D.16 – model parameters in SOFIE simulation of test 8

Fig. D.66 shows the SOFIE monitor window for the end of the simulation, indicating a reasonably good level of convergence:

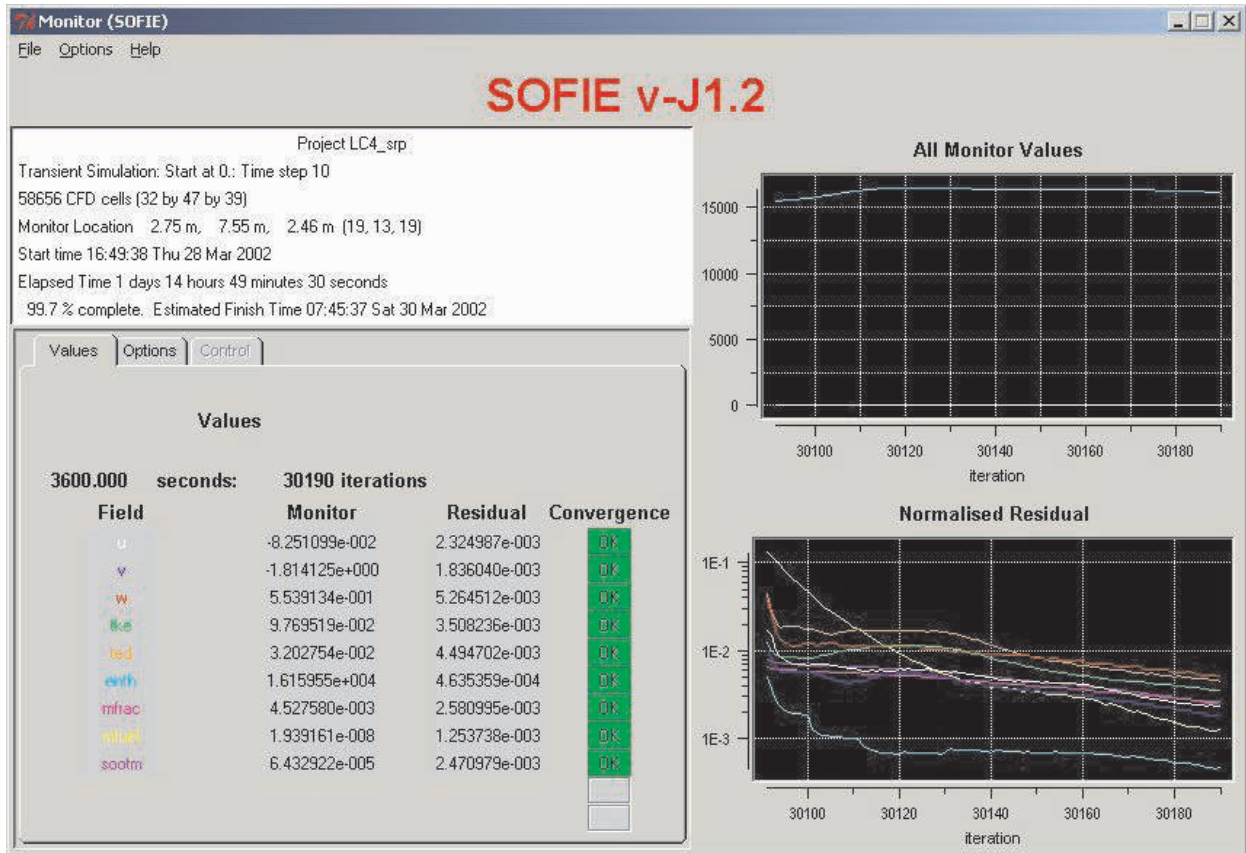


Figure D.66 – SOFIE monitor window for BRE large compartment test 8 [BRE]

Figs. D.67 and D.68 show the comparison of velocity and temperature for test 8. The results obtained with the JASMINE CFD code are also included in fig. D.67 for comparison, demonstrating that very similar predictions can be achieved by two completely independent codes.

Fig. D.68 shows predictions of both gas and thermocouple temperatures. A curve fit to the latter is included as the predictions show some scatter, due to the fact that the value is a function of the number of DT rays passing through a cell. Since relatively few rays were used in this simulation (c.f. table D.16) some non-uniformity is manifested which is entirely numerical. Considering the smoothed curve, the predicted thermocouple temperatures are in reasonable agreement with the experimental data, but still rather high in the hot layer and on the low side in the inflow.

A comparison between the value of the effective radiative temperature and the thermocouple temperature is shown in fig. D.69. Fig. D.70 shows a contour plot of the gas temperatures.

Fig. D.71 shows the results obtained for the convective heat transfer coefficient on the rear wall of the compartment in the simulations. Figs. D.72 - D.74 show the same data for the side wall, the ceiling and the front wall.

Summary information on the heat transfer coefficient values is presented in table D.17:

Wall	Minimum	Maximum	Overall average
Back	3.0	7.7	5.6
Side	2.3	4.8	3.5
Front	1.8	5.7	3.4
Ceiling	2.2	10.5	3.6

Table D.17 – summary information on convective heat transfer coefficients ($W/m^2/K$), BRE test 8

The average value, weighted by surface area, is $3.8 W/m^2/K$. For the same test, but using an independent simulation, partner LABEIN from minimum, maximum and average values to be 2.4, 17 and $6.8 W/m^2/K$ respectively, so average values considering both simulation results can be determined as 2.1, 13.8 and $5.3 W/m^2/K$ respectively.

For these tests, a lot of the burning clearly occurs outside the compartment, as can be appreciated from earlier figs. D.59 and D.60. The JOSEFINE interface allows the user to determine energy balances over regions and surfaces and in the case of test 8, it was found that 11% of the chemical energy in the fuel was emerging from the doorway unburnt.

Finally, figs. D.75 and D.76 shows the development of temperature in the protected steel indicative and a comparison with the test data, respectively. The latter demonstrates a relatively good agreement between the predictions and experiment and quite a low sensitivity to the relevant grid resolution and number of DT rays.

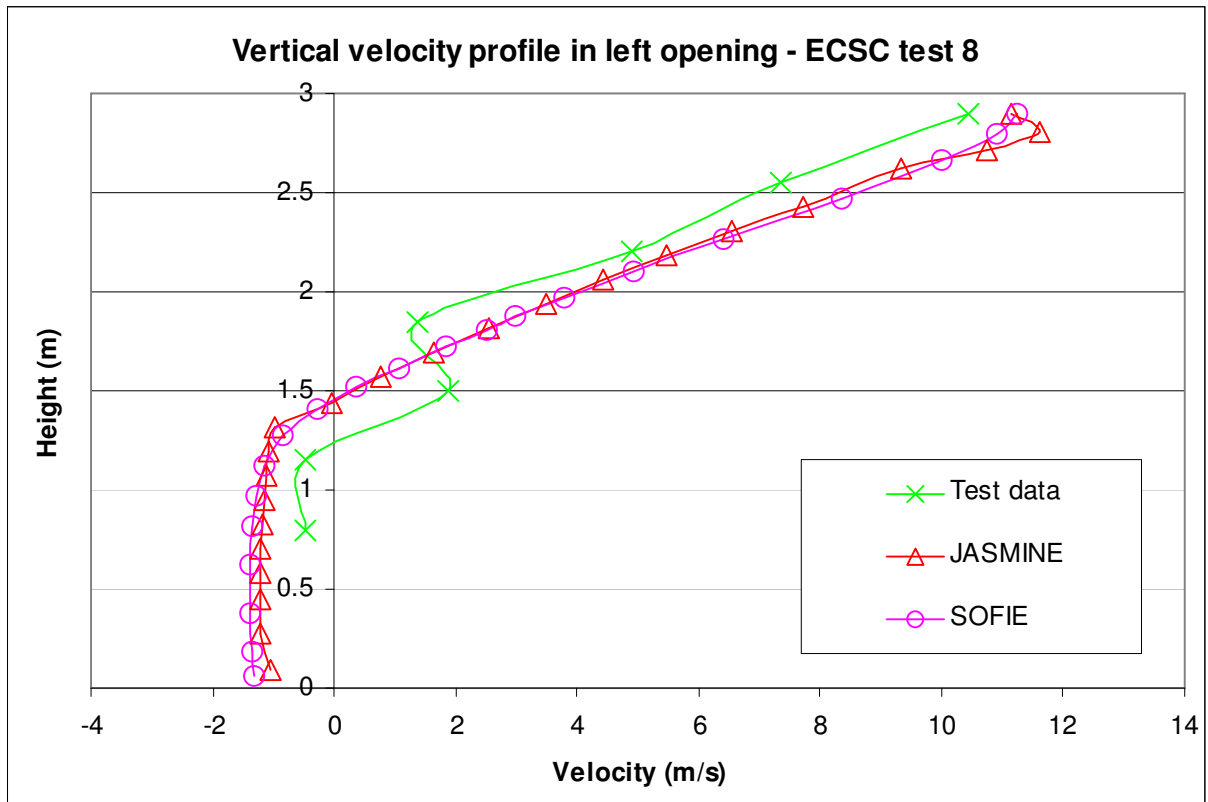


Figure D.67 – comparison between prediction (SOFIE and JASMINE CFD codes) and experiment for velocities on doorway centreline, BRE large compartment test 8 ^[BRE]

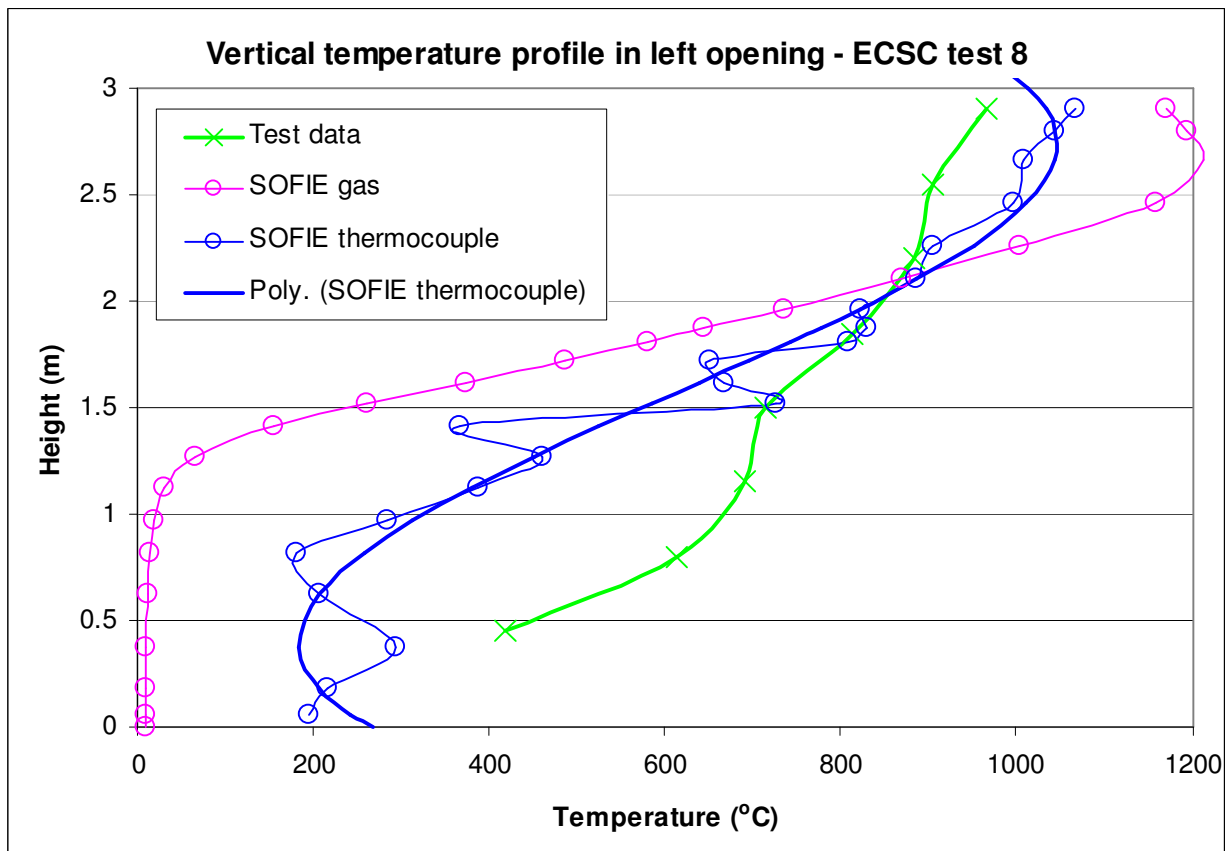


Figure D.68 – comparison between prediction (SOFIE CFD code) and experiment for temperatures (°C) on doorway centreline, BRE large compartment test 8 ^[BRE]

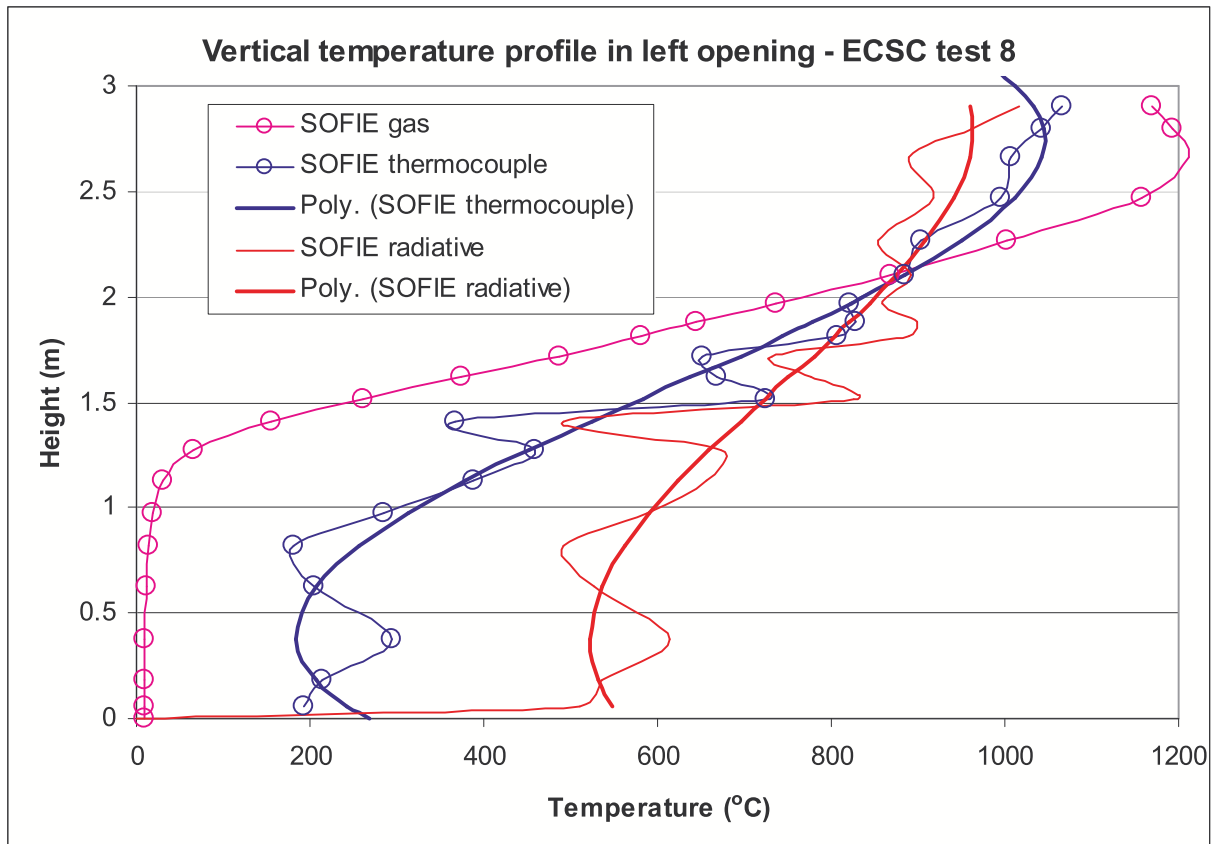


Figure D.69 – comparison of predicted gas, thermocouple and radiative temperatures (°C) on doorway centreline, BRE large compartment test 8 ^[BRE]

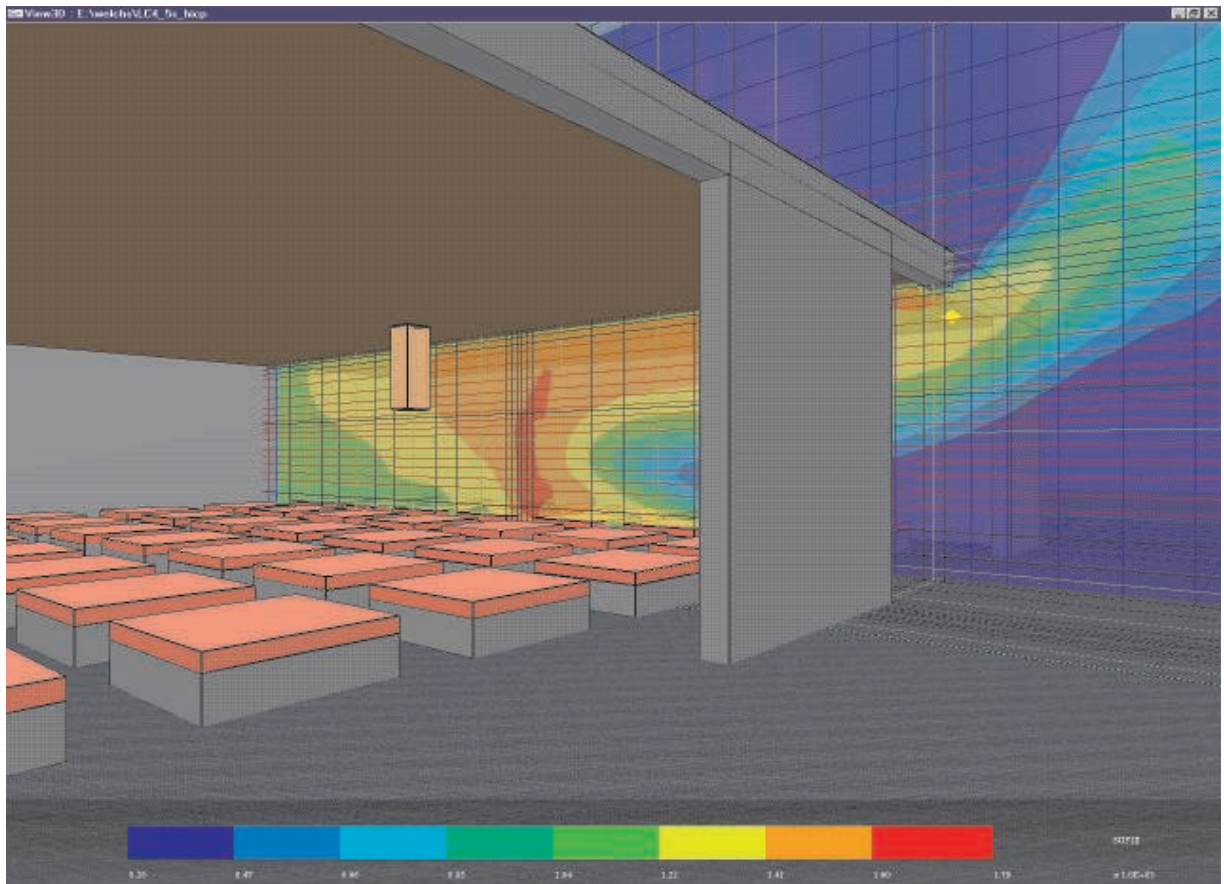


Figure D.70 – predicted gas temperatures (K) on doorway centreline at 10 minutes, BRE large compartment test 8 ^[BRE]

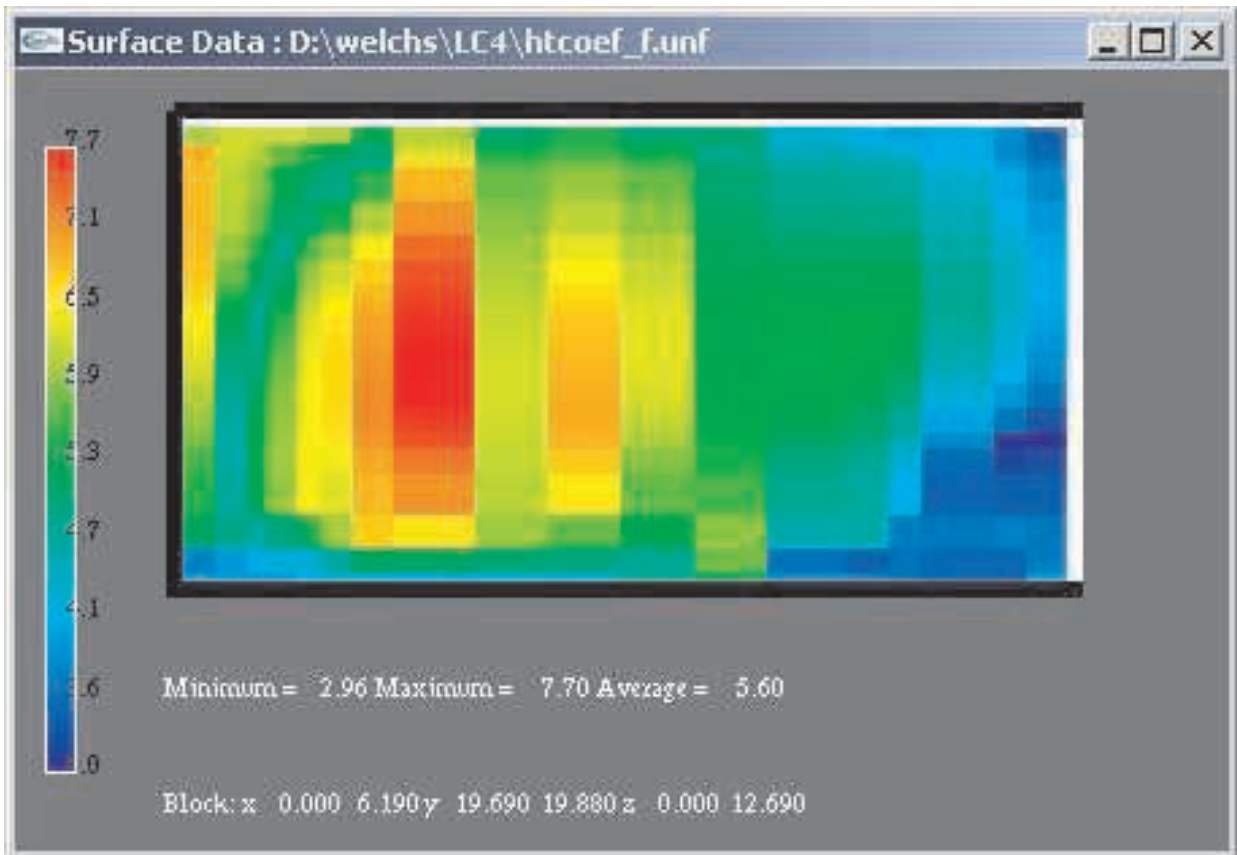


Figure D.71 – convective heat transfer coefficient inside rear wall of compartment, BRE large compartment test 8 ^[BRE]

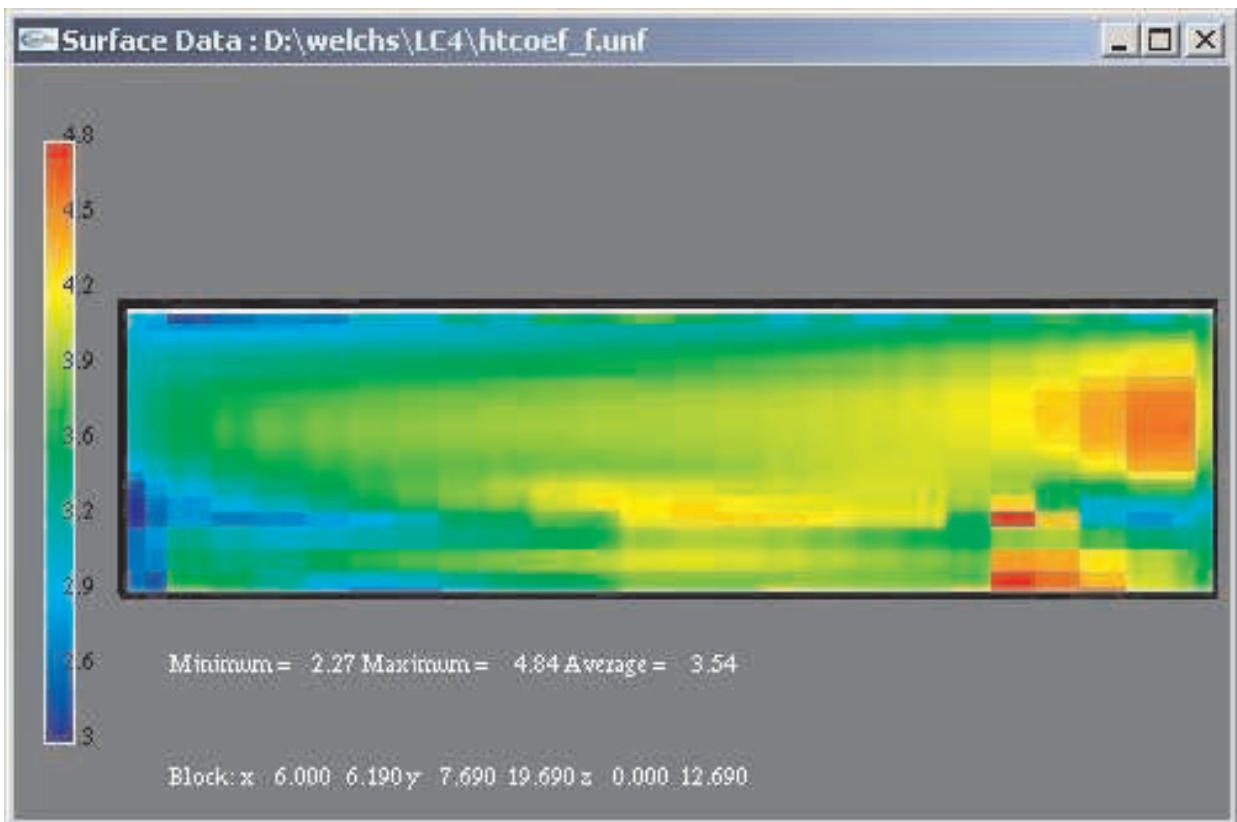


Figure D.72 – convective heat transfer coefficient inside side wall of compartment, BRE large compartment test 8 ^[BRE]

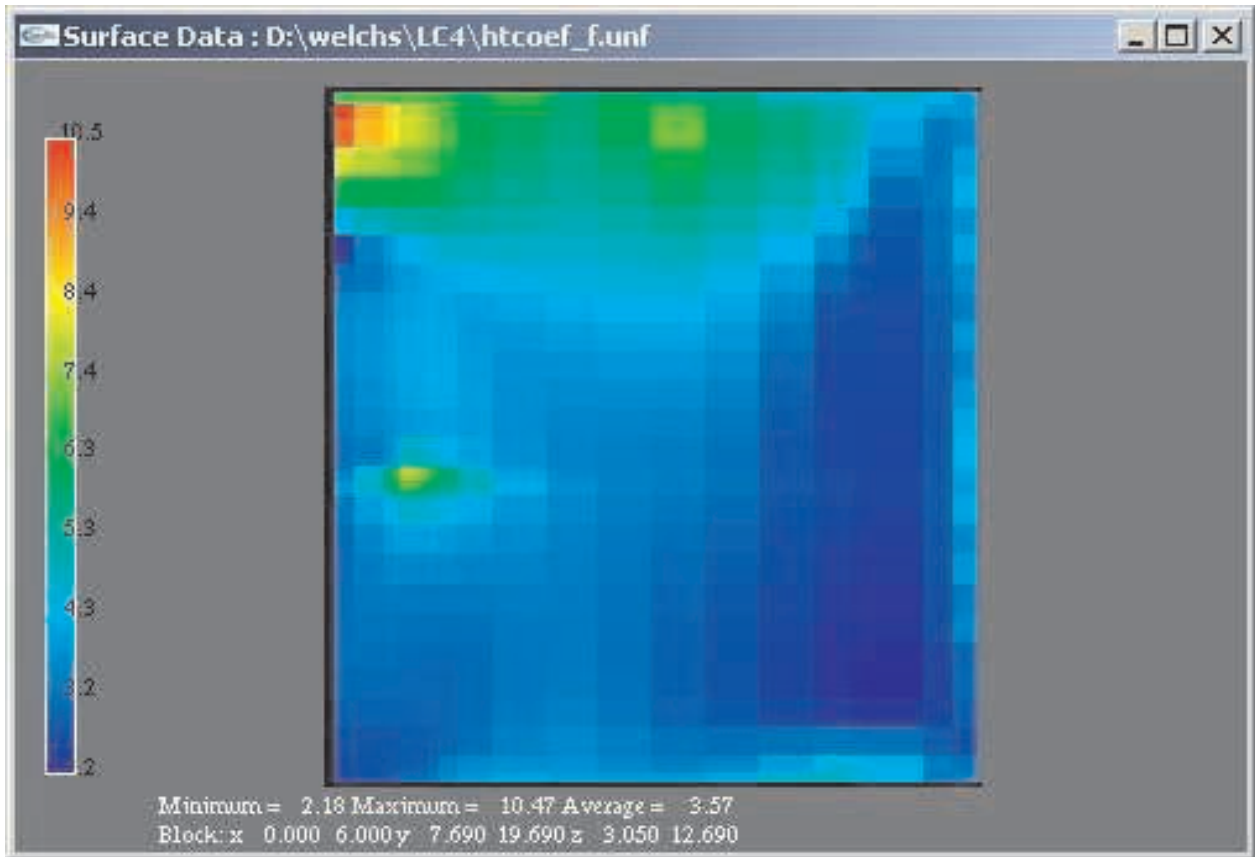


Figure D.73 – heat transfer coefficient on underside of ceiling of compartment [BRE]

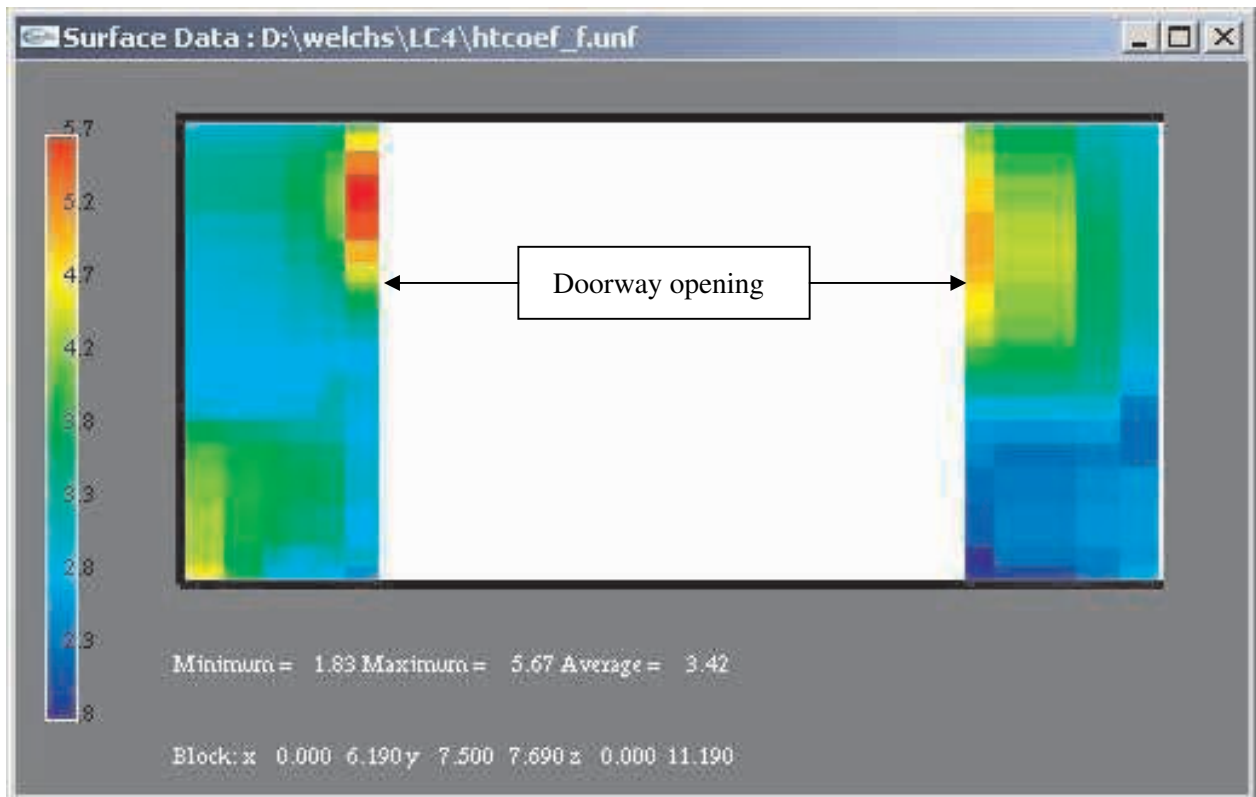


Figure D.74 – heat transfer coefficient inside front wall of compartment [BRE]

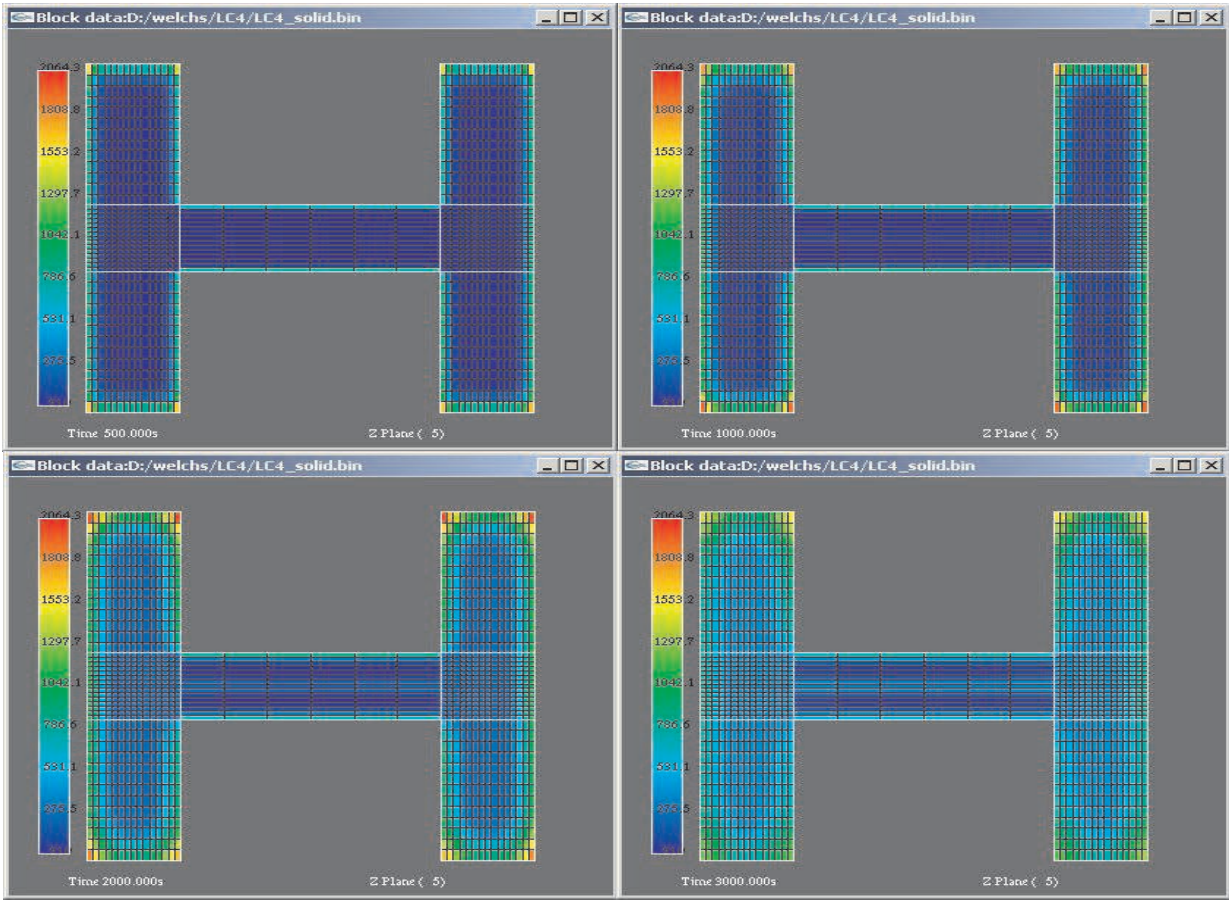


Figure D.75 – temperature development within protected indicative - BRE large compartment test 8 ^[BRE]

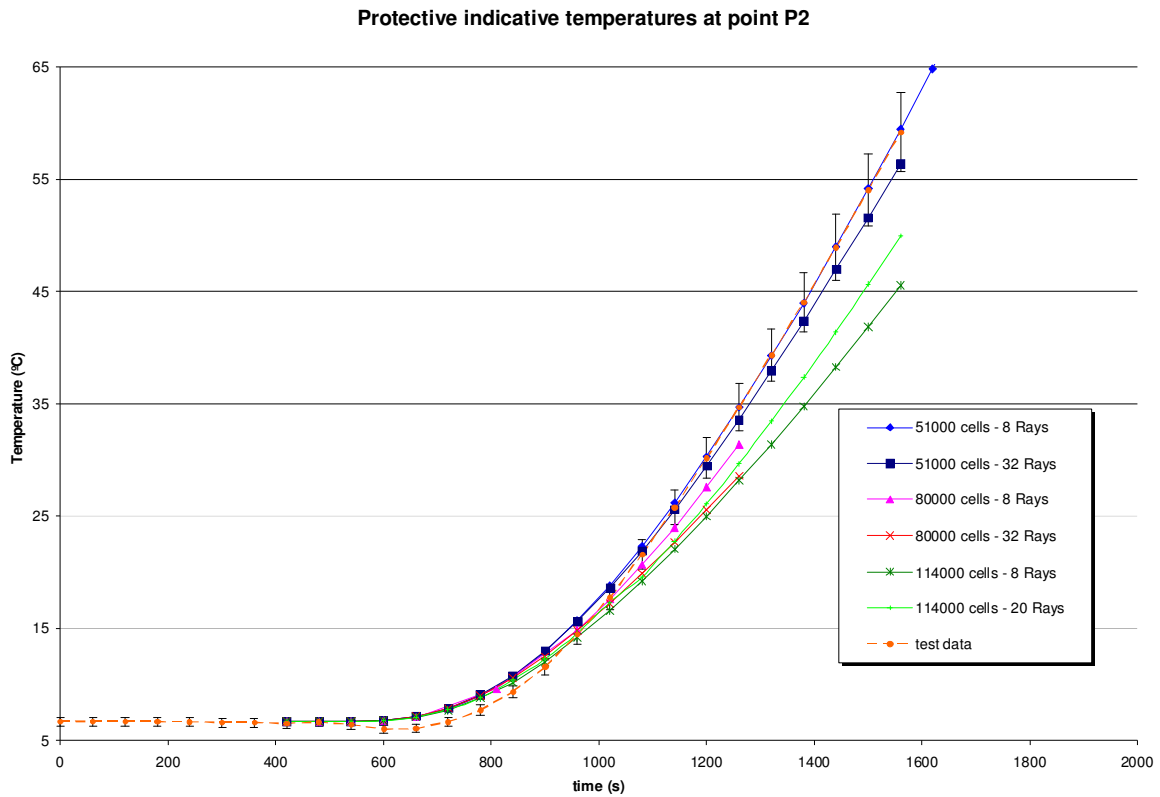


Figure D.76 – protective indicative temperatures at point P2 – grid & DT ray effects ^[LABLEIN]

SOFIE simulation results - test 6 (front and rear openings)

In this case, the burning rates of all cribs were assumed identical and a finer grid was used, c.f. table D.18 below. Note that a different solver (tdma) was adopted for this case, with emphasis on stability rather than efficiency, c.f. sip3d for test 8 simulations, as per table D.16.

Numerical grid	50 x 93 x 33 = 153450
Discrete transfer rays	2 x 4
Numerical solver	tdma
Prescribed soot mass fraction	0.035
Absorption coefficients	Truelove CH4+soot

Table D.18 – model parameters in SOFIE simulation of test 6

Note also that in this case the surfaces of the neighbouring buildings were included in the computational domain, thereby contributing to the larger number of cells. Fig. D.77 shows the computed gas temperature at a time of 500 seconds, i.e. at the start of the temperature plateau (HRR = 40MW). The temperature scale is ambient to 1500K. Some asymmetry in the flowfield can be seen, with the hottest combustion region offset towards the rear of the compartment, away from the test indicative.

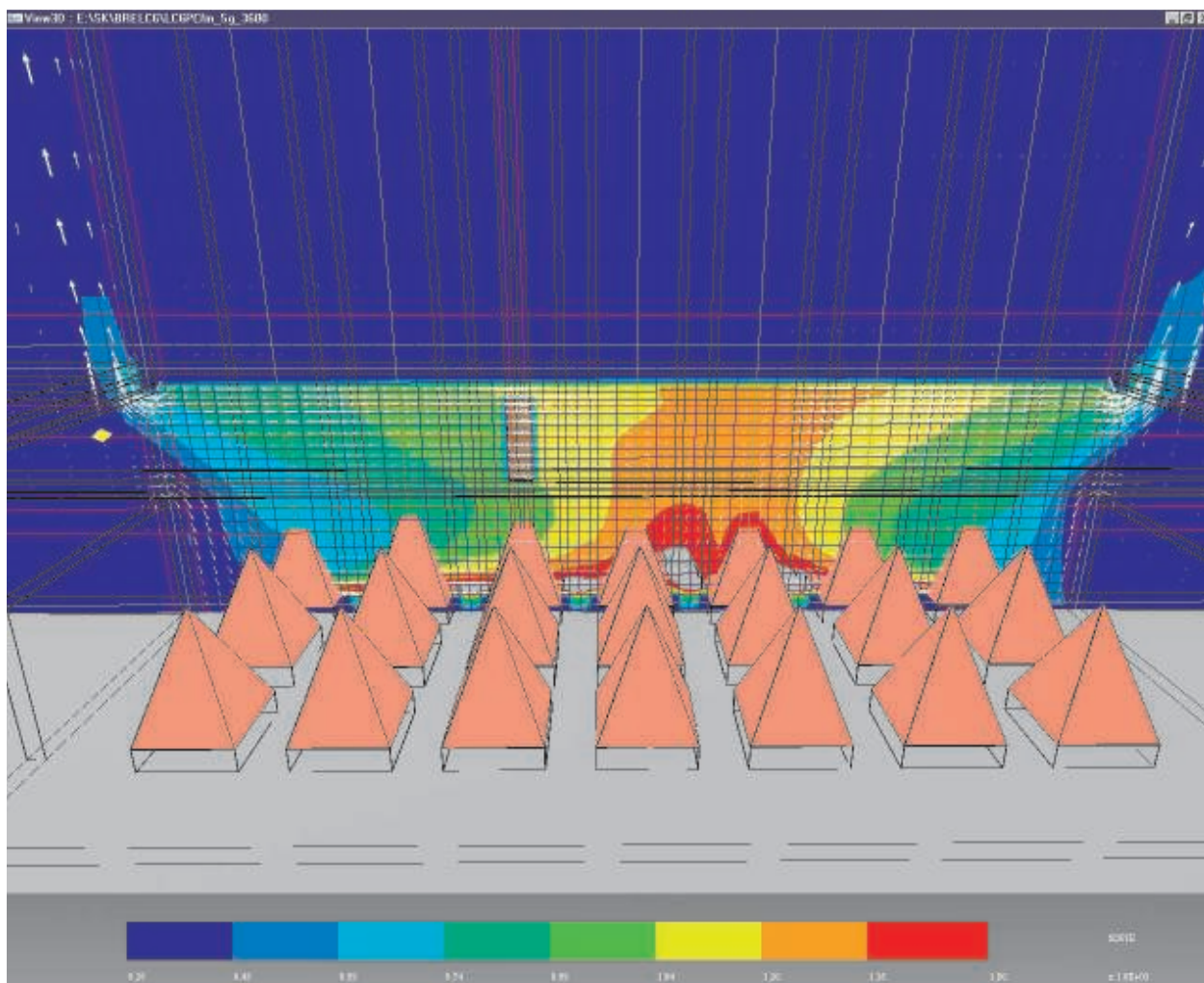


Figure D.77 – computed gas temperature field for BRE test 6 (front and rear openings) [BRE]

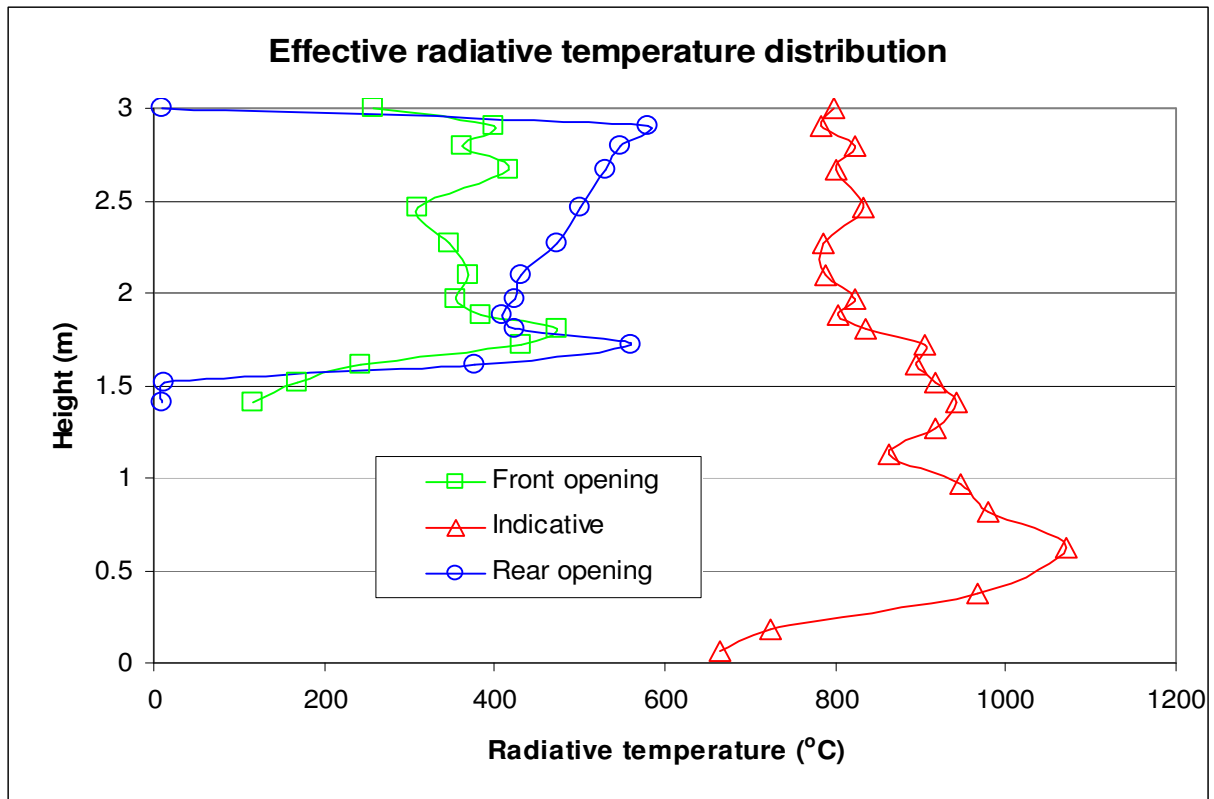


Figure D.78 – effective radiative temperature profiles at three positions in the compartment at 500s, BRE large compartment test 6 ^[BRE]

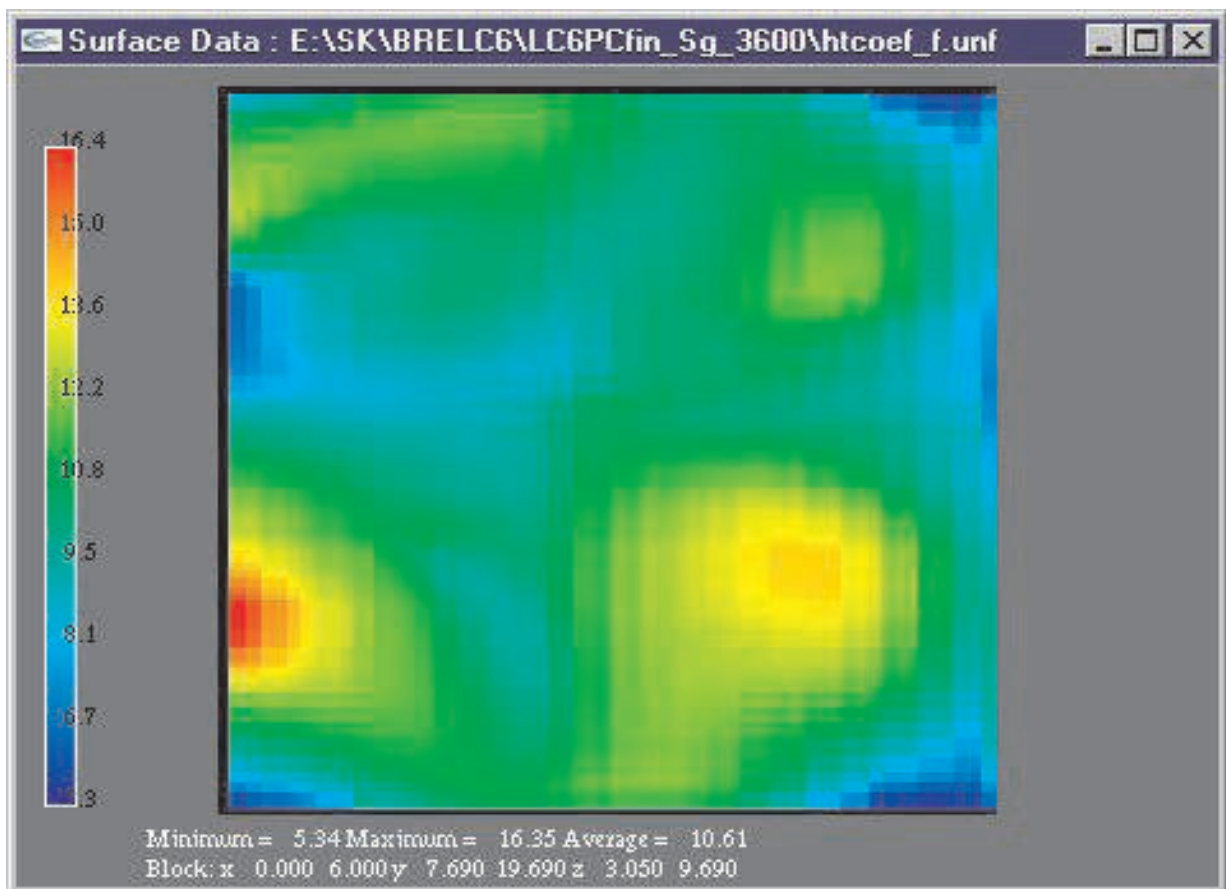


Figure D.79 – computed convective heat transfer coefficient values on underside of ceiling (front of compartment towards top of page) at 500s, BRE large compartment test 6 ^[BRE]

Fig. D.78 shows the computed radiative temperature values at the front and rear openings and near the compartment centreline where the steel indicatives were located. Fig. D.79 displays the distribution of the convective heat flux over the underside of the compartment ceiling.

Summary information on the convective heat transfer coefficient values on the other surfaces is presented in table D.19, for a simulation time of 15 minutes.

Wall	Minimum	Maximum	Overall average
Back	3.1	14.0	6.5
Side	3.9	9.3	5.6
Front	3.5	11.8	6.4
Ceiling	3.3	12.1	7.0

Table D.19 – summary information on convective heat transfer coefficients ($W/m^2/K$), BRE test 6

The overall average value, weighted by surface area, is $6.6 W/m^2/K$.

Looking at the data in a different manner, fig. D.80 presents a histogram of the predictions for test 8 from results produced by a different partner (LABEIN) with different model parameters. The actual values ranged from 2.4 to 17 $W/m^2/K$ with an average of $6.8 W/m^2/K$.

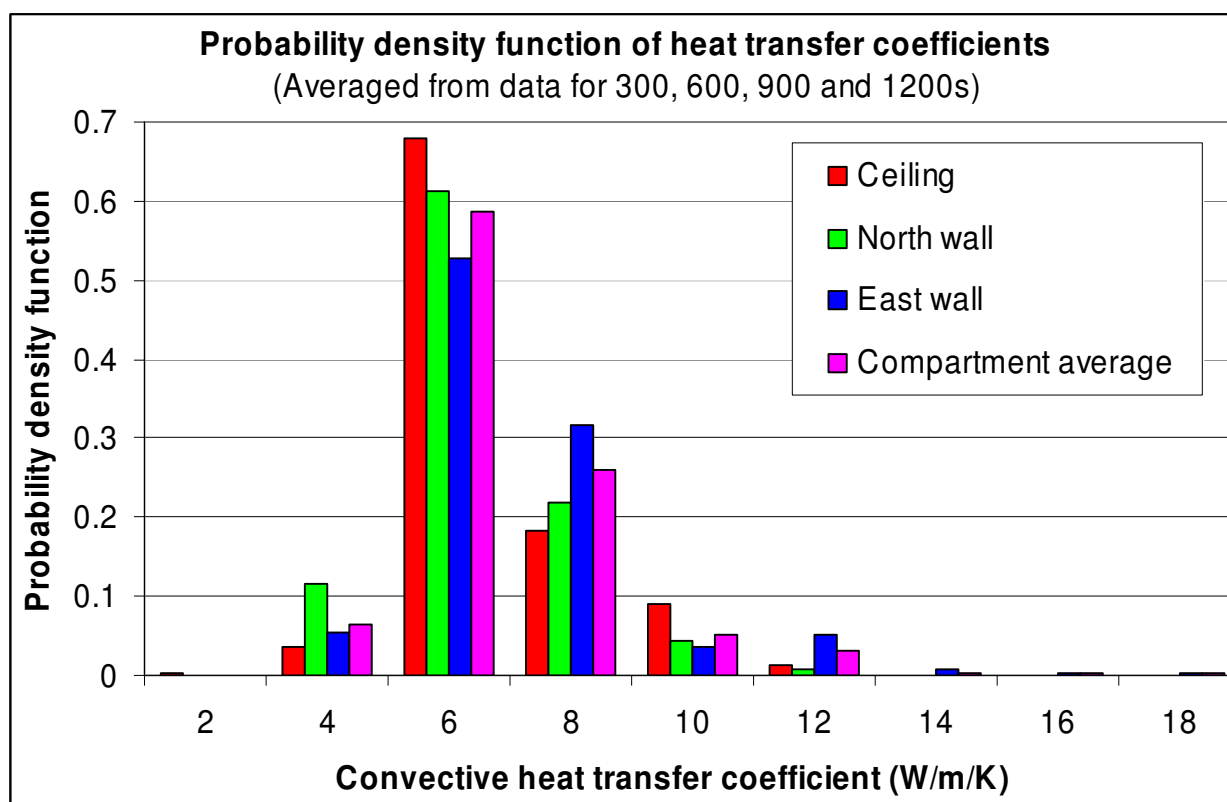


Figure D.80 – convective heat transfer coefficient for 51000 cells and 8 rays SOFIE simulation at 600 seconds (ceiling) ^[LABEIN]

Discussion

The results presented above for both the VTT large room and the BRE large compartment demonstrate that, overall, a reasonable representation of the thermal environment within the compartment has been achieved. Detailed comparisons with the test data show that (thermocouple) temperatures have generally been overpredicted in the hot layer and underpredicted in the lower incoming flow, whilst velocities reported from the test (which include an approximate correction to the thermocouple radiation error in their derivation) are reproduced rather better in the simulations.

Examination of the "effective parameters" results, i.e. computed radiative temperature and convective heat transfer coefficient, shows that the values and distributions can be interpreted and explained in terms of the details of the computed flowfields.

For instance, the flowfield in the VTT room is clearly layered, and this is reflected in the computed values of the convective heat transfer coefficient. For the BRE large compartment, a not insignificant component of the combustion takes place outside the compartment and the convective heat transfer coefficient values are rather more uniform over the inner surfaces of the walls as the burning regime is clearly post-flashover. In the case where there were front and rear openings, there is asymmetry in the computed flowfield (due to the fact that the neighbouring buildings, the "concrete building" in front and the "steel-framed building" behind, were different distances away from the openings (7.5 m and 3.5 m respectively)). This asymmetry was also observed, qualitatively, during the test.

The average values of convective heat transfer coefficient are all in the range 5 to 7 W/m²/K:

BRE test 8	5.3 W/m ² /K
BRE test 6	6.6 W/m ² /K
VTT test 8	5.9 W/m ² /K

The reasons for the differences between these values are not yet well-understood and further sensitivity analyses including the effect of grid resolution and number of discrete transfer radiation model rays would be required to properly explain them.

The temperatures of the steel indicatives develop in the expected manner, though the temperatures reached are rather higher (hence conservative) compared to the test data. One of the reasons for this must be to do with the remaining uncertainty in the value of the thermal properties for the protection material, and in particular it seems that a significant moisture plateau was shown in the test data. For the simulations reported, the solid-state solver was still limited to constant property values but it was subsequently modified to include a method of incorporating moisture effects via modification of the specific heat capacity, and thermal conductivity, c.f. Welch (2000). In order to investigate this aspect of the problem, BRE had earlier undertaken additional finite-element simulations of protected steel members using a prescribed temperature-time curve taken from the average of the test data.

Soot loading

The SOFIE CFD code has the capability to predict soot concentration using the flamelet-based model due to Moss (e.g. Moss & Stewart, 1998). A flamelet for the moderately sooting fuel, heptane, was developed in earlier work (Welch & Marshall, 2003) and is the default soot model recommended for use via the JOSEFINE interface.

Simpler soot models are also available in SOFIE - the two-equation model due to Tesner and a simple conserved scalar model referred to hereafter as "prescribed source". The latter is not a predictive model, but simple accommodates the effects of soot by means of a constant inflow over the burner surface at a prescribed concentration.

The Moss and Tesner models, while potentially describing the distribution of the soot concentration within the compartment, may not be the most appropriate for use in this type of study. This is because they were not developed in the context of post-flashover fires and their performance in this type of

environment is not well-established. However, these models can be used to study the effects of soot concentration in simpler test scenarios, thus identifying appropriate soot concentrations to specify for the prescribed source model.

In order to examine the influence and sensitivities of the method used to represent the sooting processes simulations were run of unbounded plumes. These are reported below, though they fall outside the main model validation exercise. In the case examined in detail the fire size was 2 MW and the size of the fuel tray was adjusted so as to achieve a heat release per unit area of 1653 kW/m² in accordance with test data.

The discrete transfer radiation model was adopted, with 4 x 8 DT rays, an additional polar ray and the "Oil+soot" Truelove coefficients.

For the prescribed scalar model, the soot concentration can be adjusted by changing the value at the inflow boundary condition. Taking a soot mass fraction value of 0.2 produced the following typical soot concentrations in the fire plume (table D.20):

Prescribed source soot mass fraction	Soot mass fraction				
	1st cell	1/4 plume height	1/3 plume height	1/2 plume height	flame tip
0.2	0.052	0.021	0.018	0.011	0.0027

Table D.20 – soot mass fraction with prescribed scalar models at various heights

Expressing these results in other terms, at the 1/2 plume height position, which is very close to a stoichiometric fuel location, the soot volume fraction was 1.7e-6, corresponding to a soot concentration of 21% of stoichiometric fuel carbon.

The Moss model describes the soot particle number density and mass fraction in terms of flamelet-derived properties. The values for the heptane model constants used in this study were derived by comparison with the propylene and methyl methacrylate (MMA) values measured by Moss & Stewart (1998), though the value of the surface growth constant was taken to be 8.5x10⁻¹⁶ (m³ K^{-1/2} s⁻¹) by default. The soot production was adjusted by introducing an additional scaling factor in the surface growth term. Note that all of the simulation results reported here were run with the "banded" radiation model, which was found to give lower radiative loss values than the lumped parameter models.

The results for the full-scale simulation using the non-adiabatic flamelet (NAF) model are shown below in fig. D.81. The pair of plots of radiative loss against soot concentration on the right of the figure are set out using two different scales for the prescribed soot concentration. The first (the lower pair of plots) is the "absolute peak" soot concentration, i.e. the maximum value, which is always obtained in the first cell in the domain above the inflow. Since the value in the higher temperature regions of the plume, where radiation is dominant, is significantly lower it is more informative to cross-plot the Moss soot concentration with an equivalent prescribed value obtained from the high radiative loss regions. This parameter has been obtained by deducing a simple scaling factor relating the peak value and the value pertaining at about 2% of the plume height which conveniently works out at around 2 (fig. D.81).

On the left of the figure the centreline soot concentrations are plotted against height for the default Moss model case and two selected prescribed soot model cases. These prescribed soot concentrations have been chosen to bound the Moss model predictions (for the baseline case, i.e. default model constants) and have the following source soot mass fraction values:

Prescribed (60%)	0.100
Prescribed (45%)	0.075

The equivalent locations are indicated on the "radiative loss v soot concentration" plots by means of coloured symbols. The results demonstrate that in this application, the radiative loss prediction effectively saturates at not much higher than 20% fuel carbon. Saturation is more obvious with the Moss model, where the loss apparently then begins to fall again, but is clearly exhibited by the prescribed model predictions too.

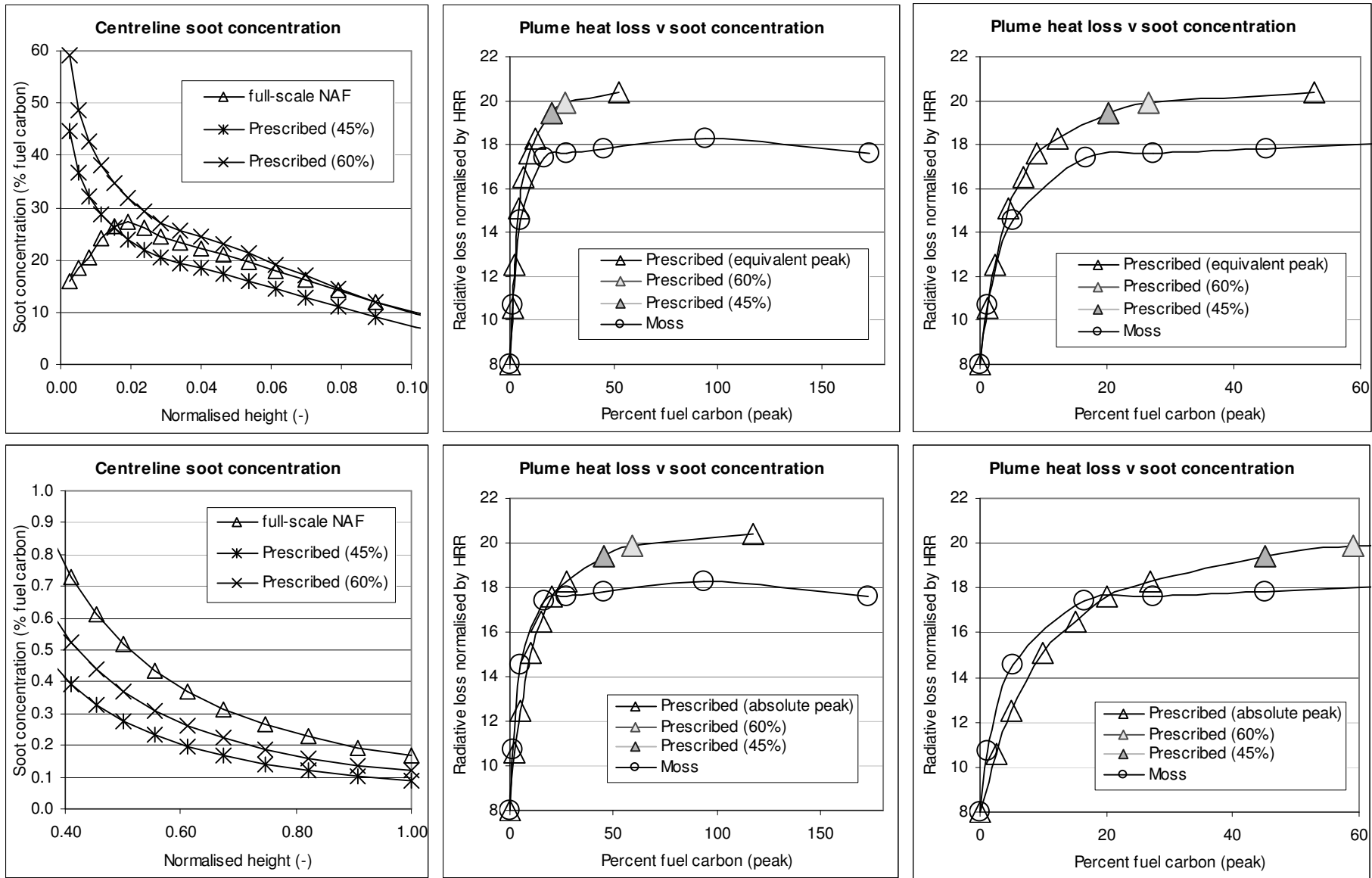


Figure D.81 – effect of soot concentration and soot model choice on heat loss from simple fire plume [BRE]

The other conclusion is that in the soot-dominated regime, i.e. on the plateau of the heat loss curves, the Moss model yields about 20% less loss compared to the prescribed model. This difference is not very large and suggests that in some applications, the prescribed model could be usefully adopted to represent the effects of radiative loss with significant computation savings, whilst adding little error in the prediction.

In light of the above findings, it was decided that prescribed source concentrations might be simply linked in the model to fuel type, using text-book data for peak soot yields to scale the values. This model was implemented in the JOSEFINE code, so that sensible default values of soot concentration are suggested, though the user retains control for investigating other possibilities.

Furthermore, a threshold is set in the code for the selection of the appropriate set of Truelove absorption/emission coefficients for the model, i.e. whether oil or methane, according to the above prescribed source values. This automates another aspect of running the simulation, reducing the scope for errors.

Supplementary cases of model validation

ProfilARBED have performed SOFIE simulations for two supplementary cases, namely, car fire tests and external steel column fire tests.

The open car park scenario is shown in fig. D.82. Some results for this case are shown in figs. D.83 and D.84, showing that the peak convective heat transfer coefficient was determined as $12.9 \text{ W/m}^2/\text{K}$.

In the scope of the ECSC research project “Fire resistance of external steel columns” (1981), about 20 fire tests were carried out on steel columns situated outside a fire compartment. These experimental tests were carried out at the test laboratory of the CTICM in Maizières-lès-Metz (France). The tests have been performed in a furnace of which the internal dimensions are 3.65 m x 3.65 m surface area and 3.13 m height (see fig. D.85). The walls are composed of ordinary bricks of 115 mm thickness (on the outside) and heavy fire-resistant bricks of 160 mm thickness (on the inside). The front façade, in which the ventilation opening is situated, is composed of cellular concrete blocks of 20cm thickness. The ceiling consists of 175 mm thick hollow-core slabs. A fire-proof screen 3 m high prolongs the façade of the furnace and simulates the upper storey. The ventilation opening has a surface area of 3.60 m^2 and a ventilation factor of $0.061 \text{ m}^{1/2}$. In order to place the 4 m long column under the most unfavourable conditions in terms of thermal exposure, it is positioned on the axis of the ventilation opening. The fire load consists of wood cribs laid out in different heaps on the floor, and varies between 29 and 58 kg of wood/m². The temperatures were measured by thermocouples placed inside the chamber, in front of the furnace and near the column.

The results for the external column fire test case are shown in figs. D.85 to D.90. It can be seen from fig. D.90 that the predicted results are in good agreement with measurements, thus demonstrating that the CFD model has reproduced well the thermal conditions for the column test.

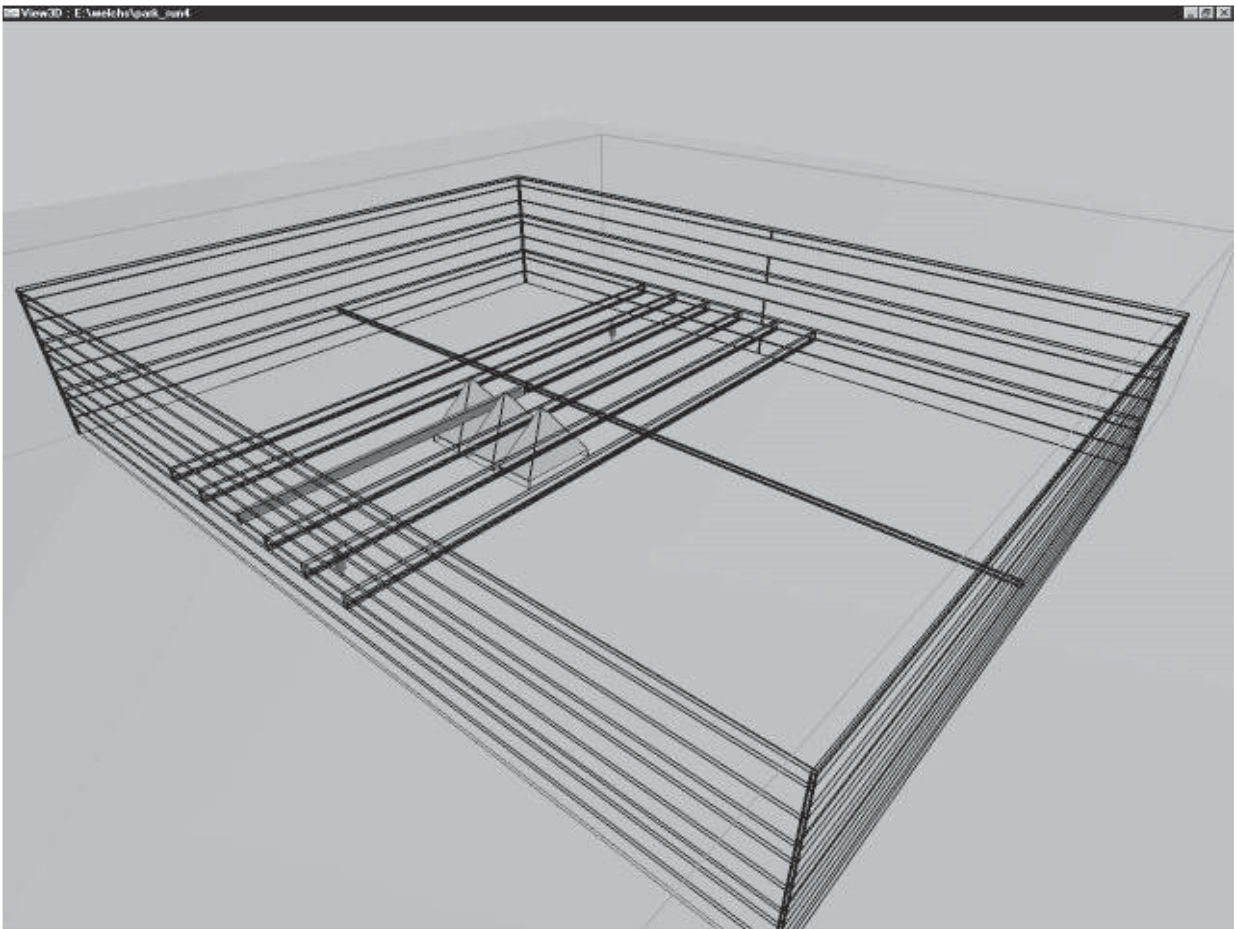
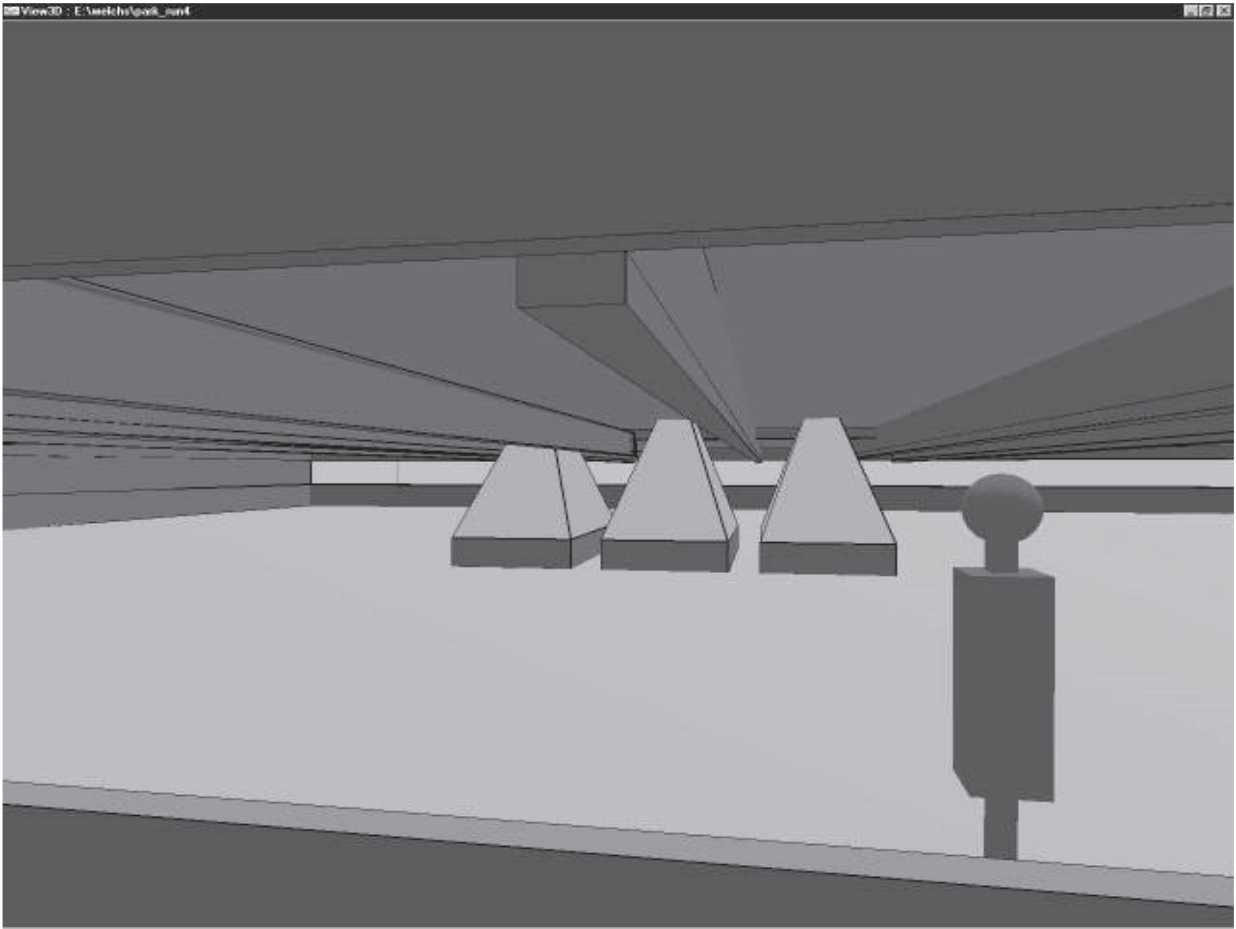


Figure D.82 – an open car park ^[ProfilARBED]

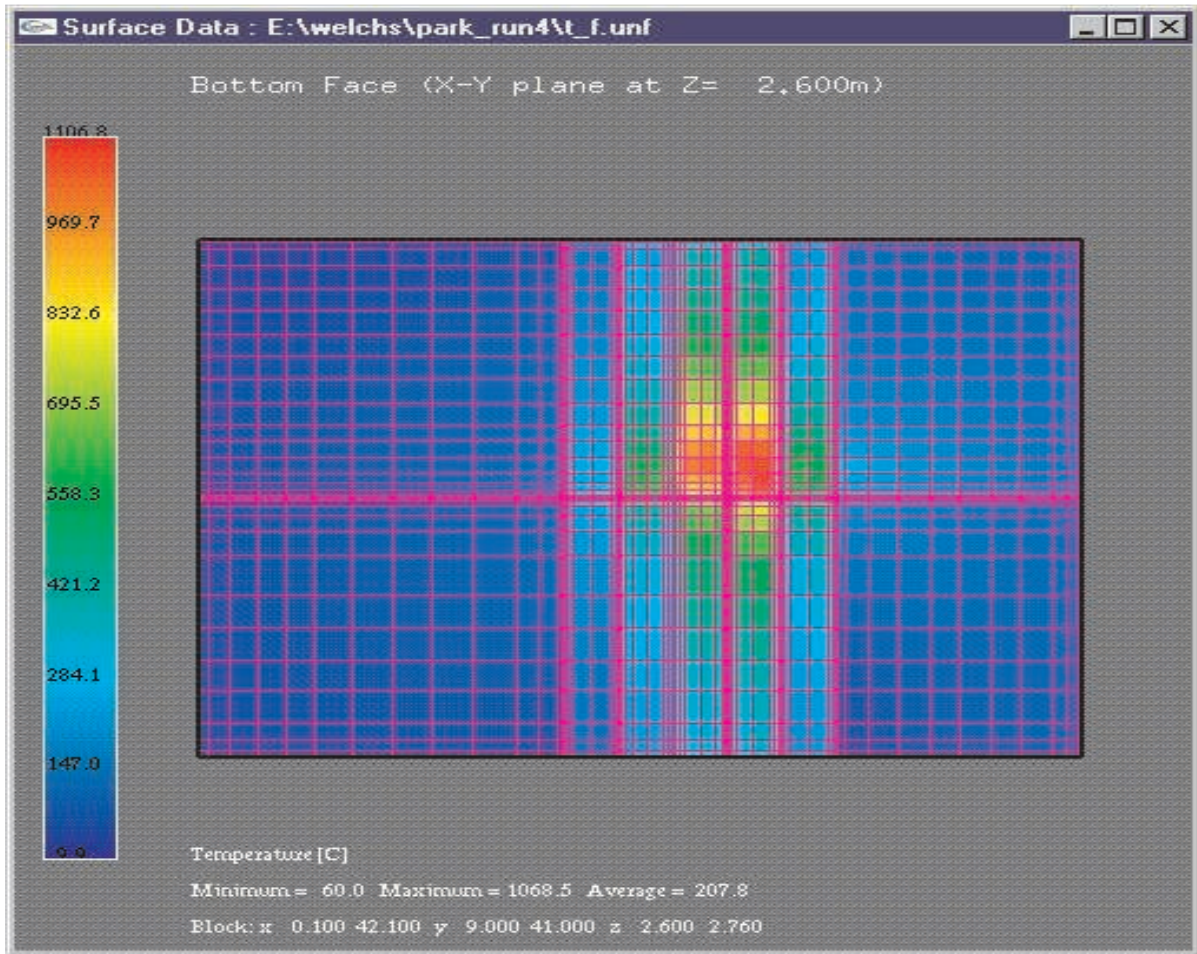


Figure D.83 – surface temperature distributions in open car park [ProfilARBED]

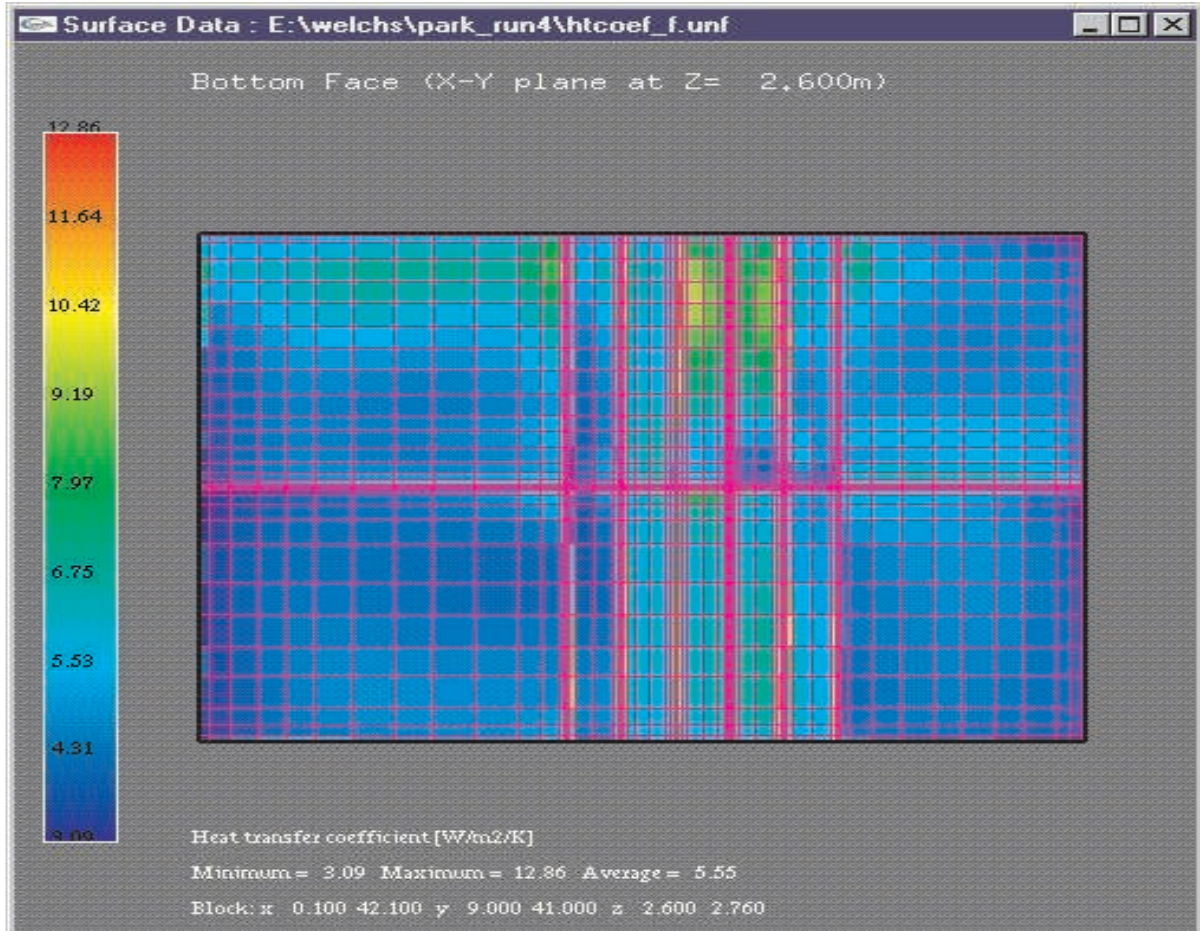


Figure D.84 – convective heat transfer coefficient distributions in open car park [ProfilARBED]

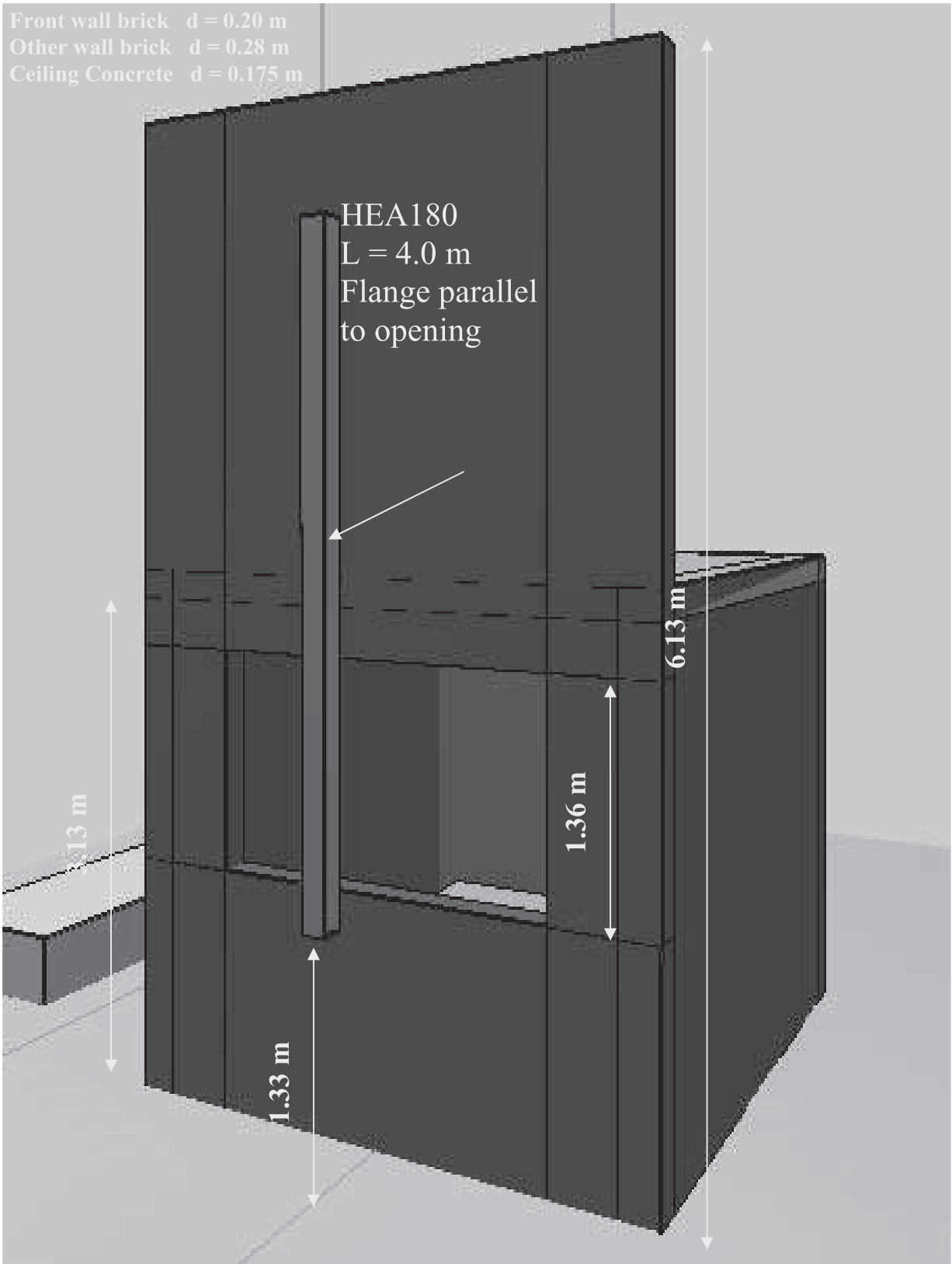


Figure D.85 – CTICM external column fire test rig [ProfilARBED]

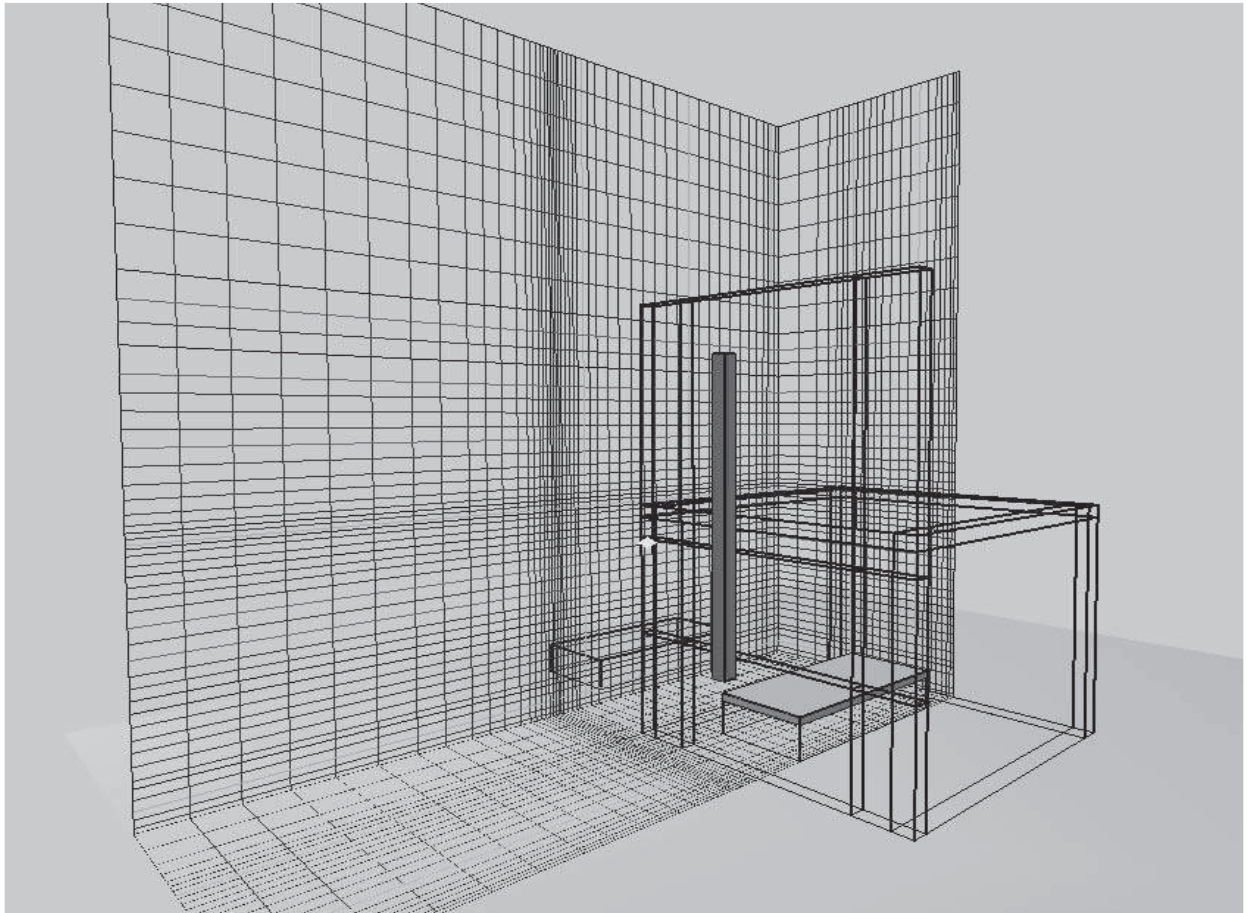


Figure D.86 – numerical grid for CTICM external column fire test case [ProfilarBED]

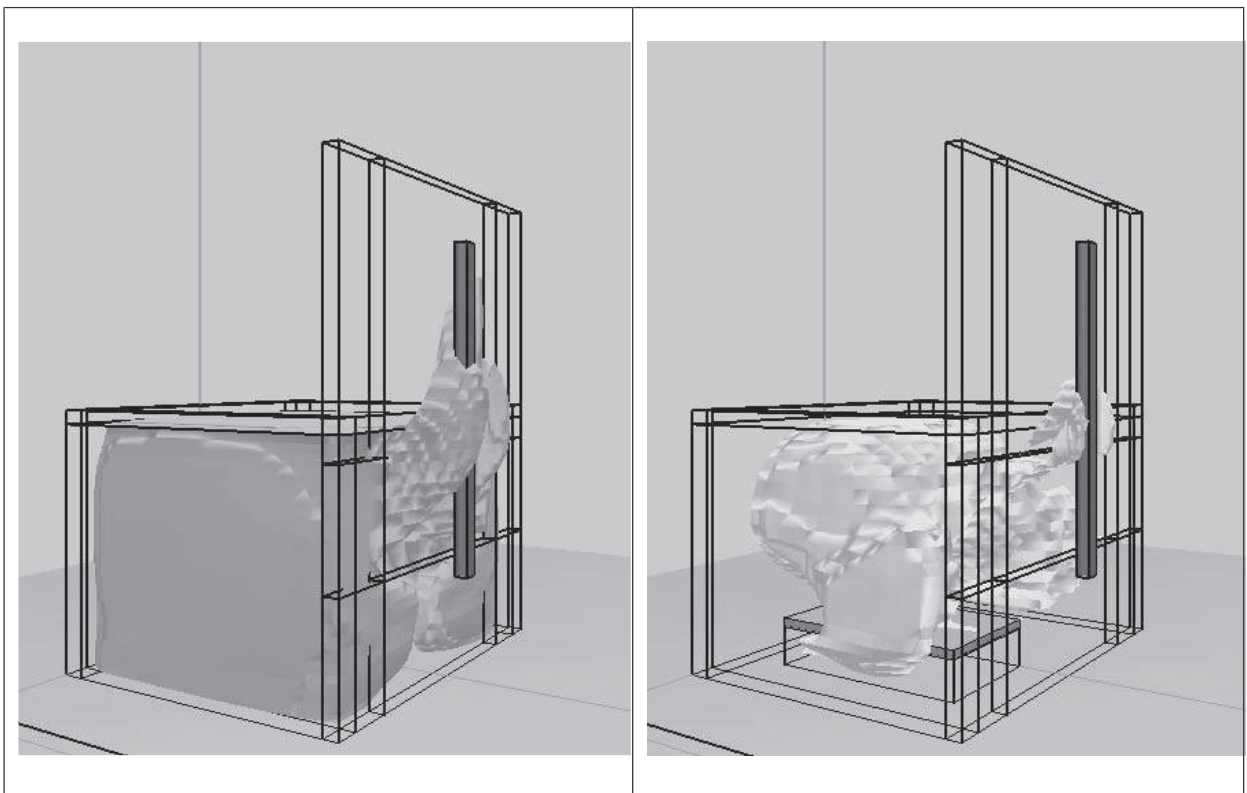


Figure D.87 – temperature isosurfaces for CTICM external column fire test case:
a) 927 °C, b) 1227°C [ProfilarBED]

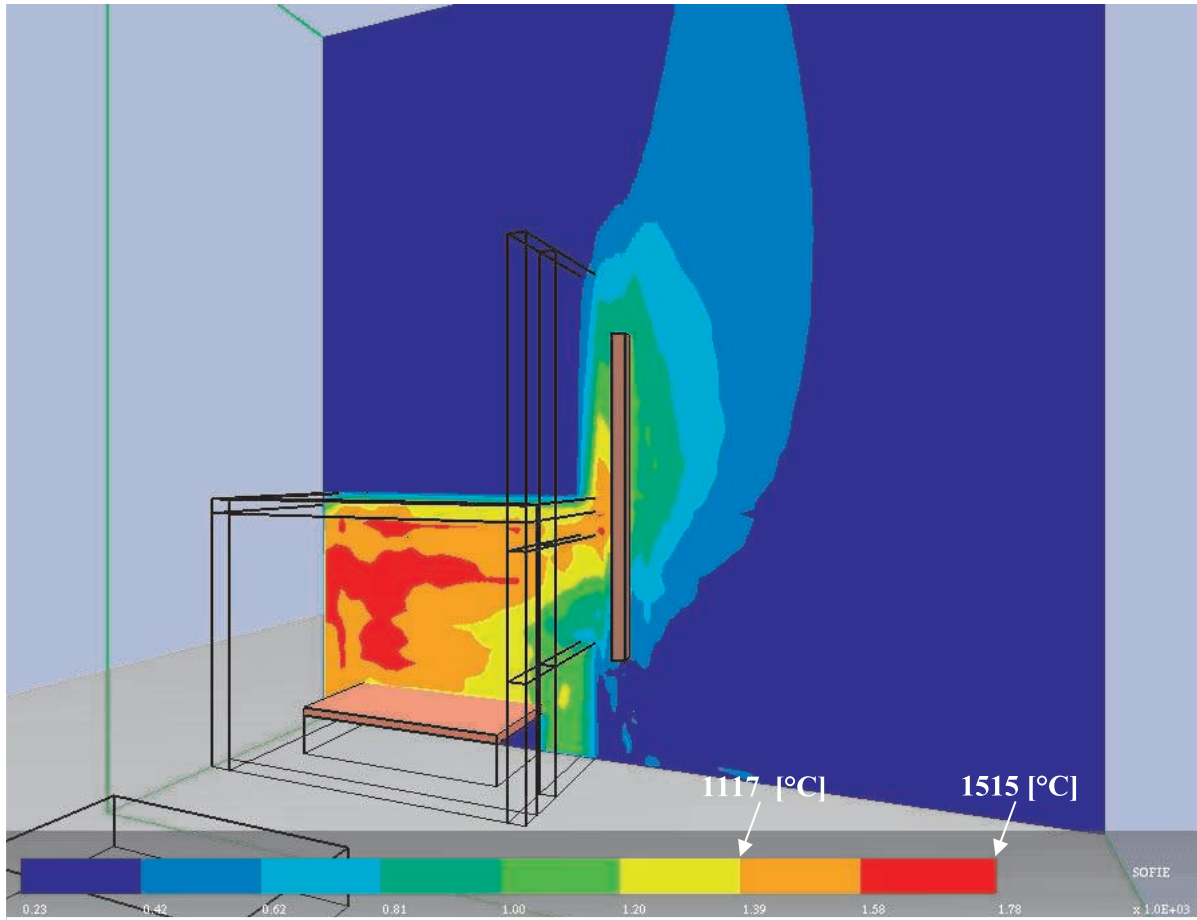


Figure D.88 – thermocouple temperatures (K) after 14 minutes (plane YZ) [ProfilARBED]

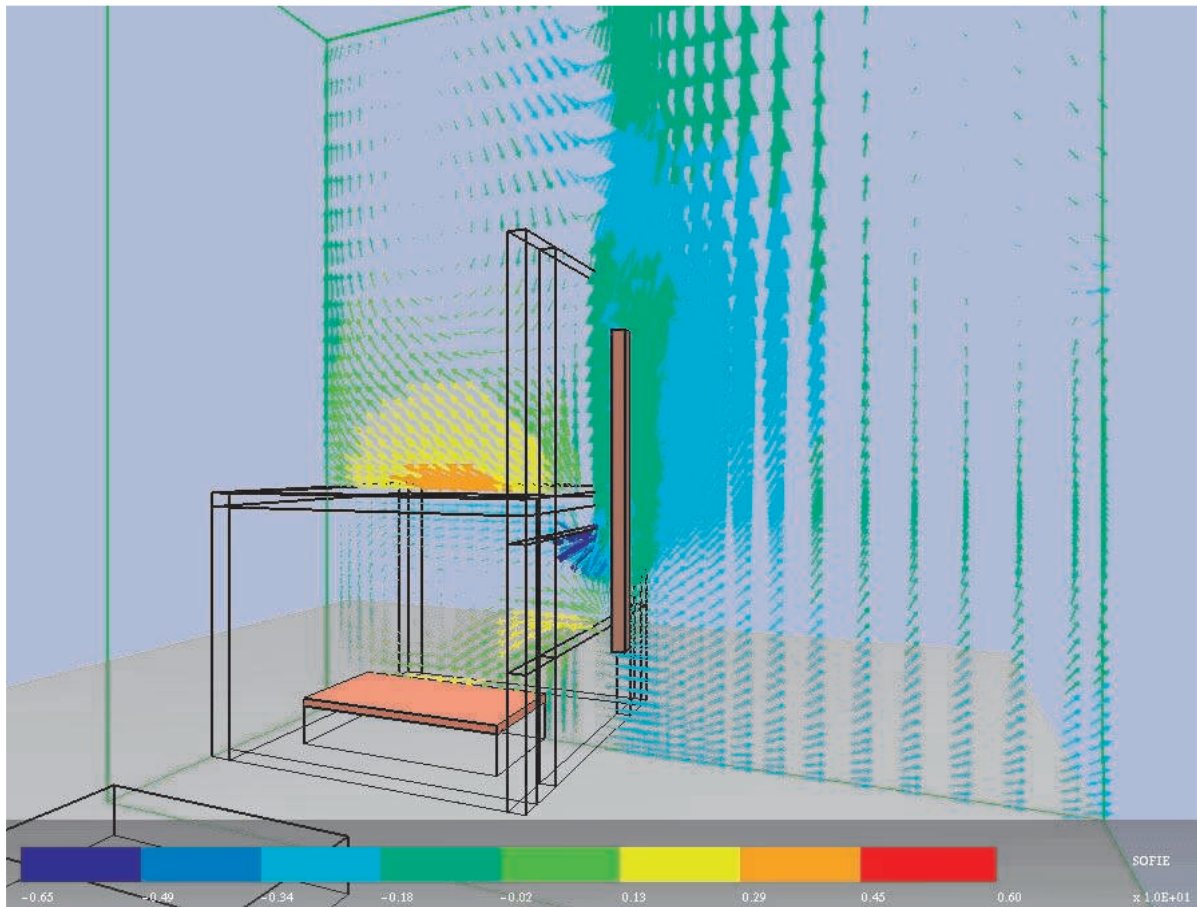


Figure D.89 – thermocouple temperatures [K] after 14 minutes (plane YZ) [ProfilARBED]

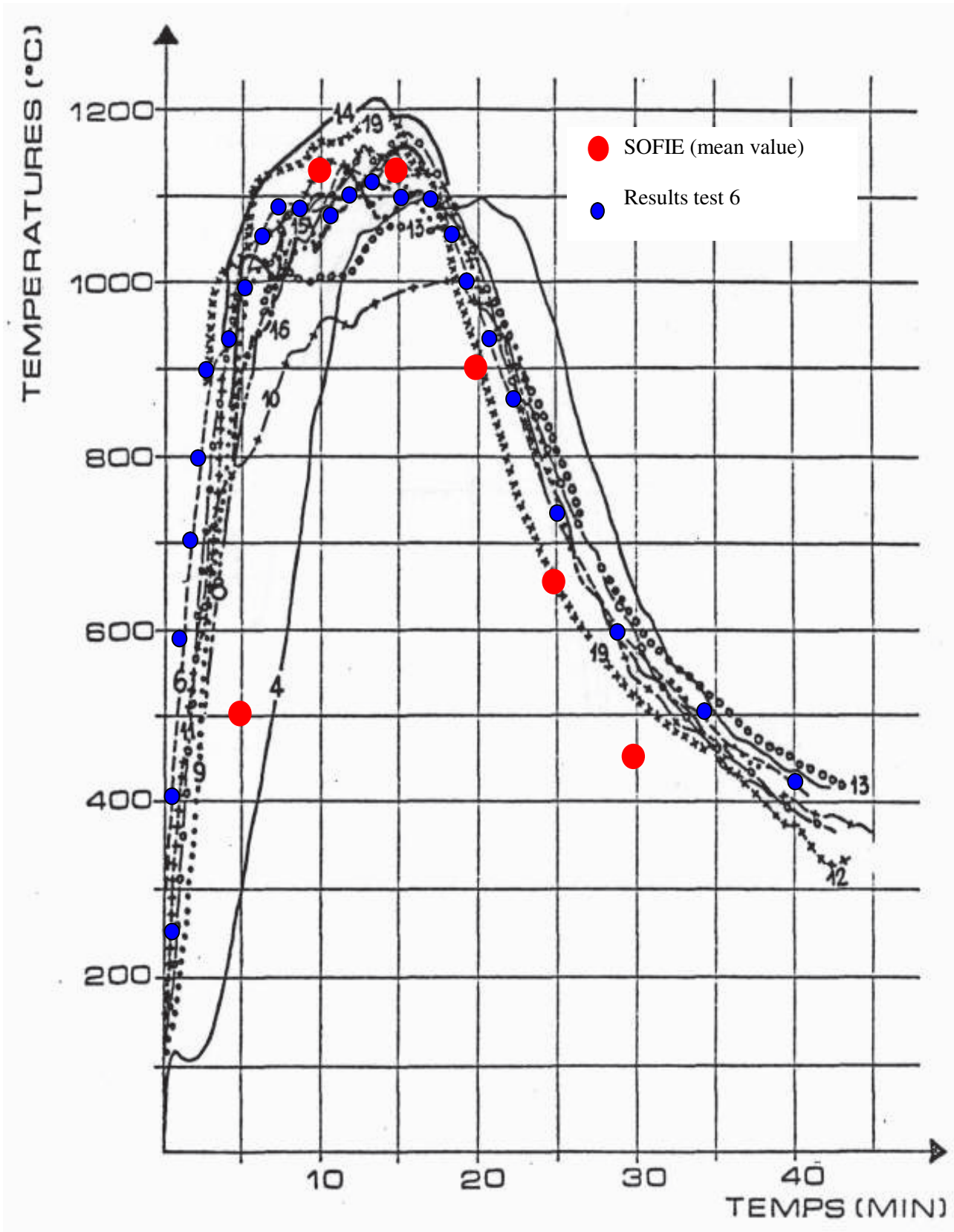


Figure D.90 – comparison with test data for CTICM external column test ^[ProfilARBED]

Appendix E – Analysis and review

This task is concerned with the analysis and review of the simulation results.

Supplementary cases of model application

A hypothetical scenario involving burning car fires in the underground car parks was considered of interest to the steel industry. A further very relevant case concerning the external column fire tests performed by CTICM was included later. The results for these cases are included above at the end of Appendix D.

Results analysis: equivalent parameter values

One of the specific objectives of the project concerns application of the CFD-based methodology developed to the assessment of some of the parameters adopted in the design codes (e.g. EC1 and EC3). At the time of drafting the proposal, this objective reflected the current state of development of the draft version of that document (i.e. EC1 Part 2.2, 1996), stating:

To apply the model for the assessment of the calibration and sensitivity of empirical design parameters, such as the convective heat transfer coefficient and safety factors used in the design guides (Eurocodes EC1 and EC3).

The project partners re-examined the relevant draft Eurocodes (EC1 Part 1.2, 2001) at the project meeting in November 2001. It was noted that no reference was now made to the "safety factors" mentioned in the earlier draft, and that the fundamental part of the "actions for temperature analysis (thermal actions)" guidance consisted of the following set of heat transfer equations⁵:

$$\dot{h}_{net}^{\&} = \dot{h}_{net,c}^{\&} + \dot{h}_{net,r}^{\&} \quad (E.1)$$

$$\dot{h}_{net,c}^{\&} = \alpha (\theta_g - \theta_m) \quad (E.2)$$

$$\dot{h}_{net,r}^{\&} = \Phi \epsilon_m \sigma ((\theta_r + 273)^4 - (\theta_m + 273)^4) \quad (E.3)$$

Following careful examination, it was agreed that the main parameters of relevance in the current project can now be defined as:

- convective heat transfer coefficient, α
- configuration factor, Φ , used in radiation equation (EC1 Part 1.2 equ. 3.3) (which is in turn a function of the fire development/exposure history - in turn a function of fire load, compartment geometry and protection material etc.)
- the effective radiative temperature, θ_r , (assumed in EC1 to equal the gas temperature)

The latter two parameters are interrelated and are not easily decoupled.

Therefore, in order to make comparisons between the results obtained from the CFD-based methodology and some of the simpler methods available in the design guidance, it is necessary to extract from the CFD results the values of some relevant "equivalent parameters". The information generally required by simpler models includes the value of the convective heat flux, and the effective radiation temperature (c.f. eqs. 3.1 to 3.3 in EC1 Part 1.2). Thus, the JOSEFINE post-processor was developed to permit extraction of surface values of convective heat transfer coefficient, temperature and heat fluxes.

⁵ It was subsequently noted that the definitions changed again in the final draft of EC 1 Part 1.2 (Stage 49 10 January 2002) with reintroduction of a factor for emissivity of the fire into equation (3); however, this value is to be taken as unity.

Furthermore, coding was written for the determination of an effective "radiative temperature". This field parameter is a measure of the effective temperature of radiation which can be seen from any point in space and is derived simply from the relationship:

$$T_{rad} = \left(\frac{\dot{q}_{rad}}{\sigma} \right)^{1/4} \tag{E.4}$$

where: \dot{q}_{rad} is the total flux arriving at any point in space
 (in practice, at each grid cell in the computational domain)
 σ is the Stefan-Boltzmann constant [$5.67 \times 10^{-8} \text{ W/m}^2/\text{K}^4$]

Results analysis: critical design parameters

Detailed assessment of the results for the purpose of identifying the critical design parameters affecting the thermal action on the steel/composite structures has now been undertaken. Results from these studies are presented below and a summary of the impact of the results is presented in Appendix F.

Summary results

The following is a summary table of convective heat transfer coefficient values, as values averaged over all exposed surfaces (in $\text{W/m}^2/\text{K}$):

Scenario	Minimum	Maximum	Overall average
BRI localised beam fire	3.0	25	4.0
VTT scale fire-resistance furnace (column)	5.0	33	12
Standard fire-resistance furnace (wall)	4.5	7.5	6.0
VTT room – test 8	2.5	11	5.9
BRE large compartment – test 6	3.1	14	6.6
BRE large compartment – test 8*	2.1	14	5.3

* - considering average of results obtained by partners BRE and LBEIN

Table E.1 – summary values on convective heat transfer coefficient for selected test cases

The averaged values for plane walls are fairly consistent at around $6 \text{ W/m}^2/\text{K}$. Where there are direct impingement flows, in the localised beam fire and the scale furnace, higher values are found.

Appendix F – Impact assessment

The verified CFD modelling methodology has the potential to overcome many of the current limitations and will provide an improved method for evaluating the thermal action of fires on building structures, encompassing heating regimes beyond those used in standard fire tests. The tasks undertaken in this task are as follows:

Review of Eurocodes procedures

The procedures set out in the Eurocodes have been reviewed in the light of the CFD data (predicted results) (see discussion above in Appendix E). The main conclusion of this exercise has been that it is easier to make a clear connection between a simple methodology and the advanced methodology developed in this work when there are fewer parameters involved in the simple equations. Throughout the duration of this project, the simple heat transfer equations in Eurocode 1 Part 1.2 (now eqs. 3.1 to 3.3) have been subject to review and modification. In earlier versions, safety factors (gamma values) were included but these have now been removed. However, having at one time resorted to a simpler version of the equation, the final form agreed upon (by the relevant CEN committee, TC250) involves more terms again.

This state of affairs does mitigate against exploitation of the more advanced models in deriving equivalent parameters, since it is necessary to decouple the complex three-dimensional fields which give rise to the effective fire temperature, configuration factor and (potentially) fire emissivity in the simple method. Given the complexity of this procedure, it has been considered to be more effective to concentrate on deriving the values of equivalent parameters which are of relevance to the original reduced form of the simpler methodology, involving a parameter we have termed the “radiative temperature”. This parameter encompasses the influence of all three of the above factors, and therefore makes it far easier to relate the advanced methodology developed in this work to simple model equations that are accessible to designers.

Recommendations - simplified models

In this section, further explanation and justification is given for the summary recommendations on “simplified models” given in the main body of the report. The context of the discussion is the relevant parts of the latest versions of the structural Eurocodes.

The following abbreviations are used:

EC1 ≡ Eurocode 1: Actions on structures Pt 1.2 General actions - Actions on structures exposed to fire
EC3 ≡ Eurocode 3: Design of steel structures Pt 1.2: General rules - Structural fire design

Comments on Eurocode guidance for simplified models

This section deals with recommendations for “*Simple calculation models*” described in part 4.2 of *Eurocode 3: Design of steel structures Part 1.2: General rules - Structural fire design* (hereafter, EC3). For thermal analysis (4.2.5 *Steel temperature development*) these methods refer to the basic heat transfer treatment set out in *Eurocode 1: Actions on structures Part 1.2 Actions on structures exposed to fire* (hereafter EC1) section 3 “*Thermal actions for temperature analysis*”. Whilst there is no precise correspondence between these simple models and the “*Advanced calculation models*” referred to in EC3 part 4.3, the information obtained from the CFD analyses in this project does enable some general comments to be made, as per below.

Heat transfer coefficient

EC1 section 3 “*Thermal actions for temperature analysis*” provides guidance on values of convective heat transfer coefficient to be used for various applications, as follows:

Exposure condition	Heat transfer coefficient, α_c
Standard temperature-time curve	25 W/m ² /K
External fire curve	25 W/m ² /K
Hydrocarbon curve	50 W/m ² /K
Natural fire models – simplified fire models	35 W/m ² /K
Natural fire models – advanced fire models	35 W/m ² /K*
None (unexposed face)	4 W/m ² /K

*unless more detailed information is available

Table F.1 – convective heat transfer coefficients from EC1 section 3

In the current project a fundamentally-based methodology was used to determine the convective heat transfer coefficient at all solid phase boundaries [Jayatileke, 1969]. For compartment test cases with both localised and post-flashover fires the predicted values were in the range 1.5-15 W/m²/K, with the average being around 6 W/m²/K. For the cases of a structural member exposed directly to flames from a localised fire (100 kW), and in a furnace, values reached as high as 25 and 33 W/m²/K, respectively, in the impingement region. This observation is consistent with the expectation that the value of the convective heat transfer coefficient should increase slightly with local flow velocity. Since velocity could be higher in larger fires, it therefore seems that a value of 35 W/m²/K might indeed be justifiable as an upper limit for the natural fire case, with the *proviso* that this is most appropriate for regions of high velocity, e.g. regions of direct flame impingement.

Considering the more general case of convective heat transfer to the boundaries of an enclosure it is apparent that if a high value is adopted this may result in non-conservative values of gas temperature, depending on the approach used to describe wall heat transfer. For example, in a zone model with the convective part of the wall heat transfer governed by the convective heat transfer coefficient, the overall heat loss from the compartment will tend to be increased. All things being equal, this implies that the predicted gas temperatures will be lower than would otherwise be the case. This is a non-conservative limit and in order to accommodate it a suggestion is made that a minimum value of the convective heat transfer coefficient should also be specified. This could justifiably be as low as 4 W/m²/K, the Eurocodes value for the unexposed surface. An even more conservative limit is available from the assumption of adiabatic walls, i.e. with convective heat transfer coefficient (and radiative exchange) effectively equal to zero - and this case would normally be adopted to provide a check on upper bound temperatures.

Gas-phase emissivities

The final version of the radiative transfer equation in EC3 is:

$$\dot{q}_{net,r} = \Phi \epsilon_m \epsilon_f \sigma (T_r^4 - T_m^4) \quad (F.1)$$

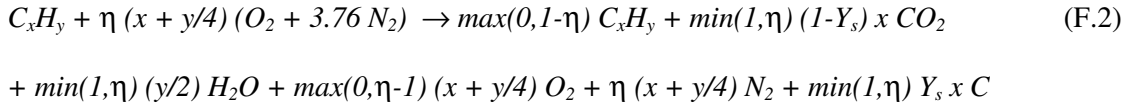
In earlier drafts of the document the ϵ_f and ϵ_m parameters had sometimes been combined into a single "effective" parameter. It is however helpful to distinguish the member and fire emissivities in this manner because the engineer/designer can thereby take account of known variation in each parameter independently. Under many circumstances, there is a large uncertainty in the fire gas emissivity so unless the fuel is particularly clean-burning it can often be conservatively assumed to be unity.

However, if more detailed information *is* available, including an estimate of the soot concentration, then an engineering calculation can be used to make a more accurate assessment of the fire emissivity. In this project an analysis exploiting a detailed radiation model was made in order to derive a generalised chart from which this type of information could be determined if a few simple assumptions are made. The development and justification for the analysis are described below.

Computation method

The narrow band model RADCAL was used for the computation of effective absorption coefficients inside a uniform gas-soot mixture corresponding to the combustion products.

The radiating medium was assumed to consist of a mixture of combustion products and air at some elevated temperature. The combustion reaction is approximated as:



where η determines the amount of air. For stoichiometric ratio $\eta = 1$. Y_s is the fraction of fuel mass converted to soot, i.e. soot yield. The simple soot yield is a very crude but effective approximation. As the spectral absorption coefficients are not generally available for hydrocarbons, the spectral information of methane is used for fuel.

RADCAL calculates the spectral intensity of a radiation beam penetrating through a uniform layer of gaseous combustion products and soot. The total intensity is calculated by integrating the transmitted intensity over the wavelength. From the total intensity i , the effective mean absorption coefficient a_e is then calculated as:

$$i = \frac{\sigma}{\pi} \left[(1 - e^{-a_e L}) T_g^4 + e^{-a_e L} T_w^4 \right] \quad (F.3)$$

where L is the path length and T_g and T_w are the gas and wall temperatures, respectively. Here, the wall temperature is assumed to be 20 °C. A schematic picture of the geometry is shown in fig. F.1.

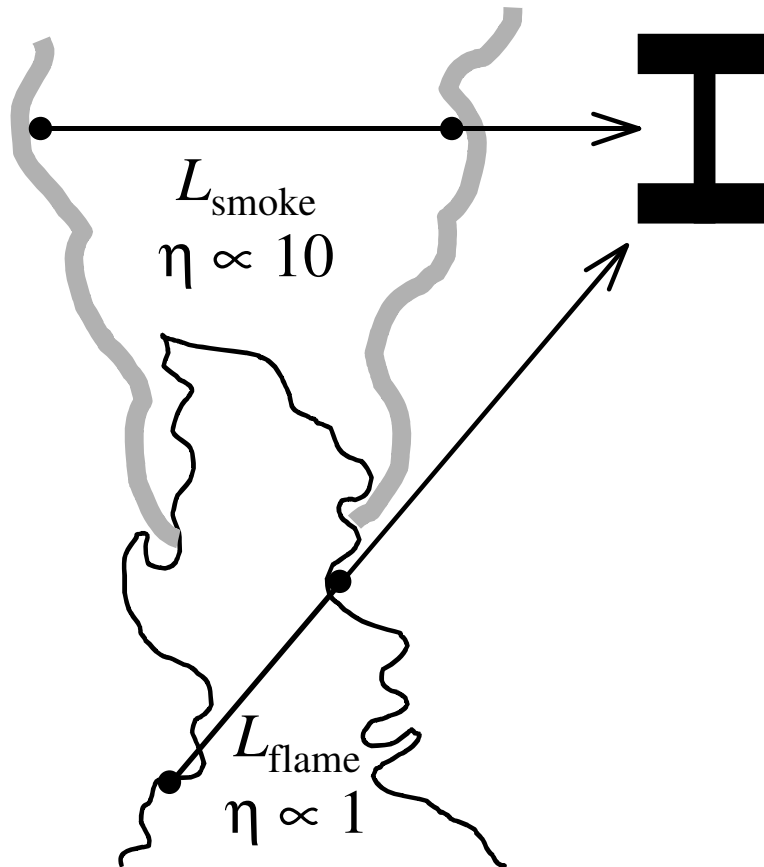


Figure F.1 – schematic picture of the geometry assumed in the emissivity computation

Finally, the emissivity of the gas layer is calculated as:

$$\varepsilon_f = 1 - e^{-a_c L} \quad (\text{F.4})$$

Note that RADCAL assumes that the soot consists of small particles only, which is typical for flaming regions. The results are not very suitable for smoke layers, where soot consists of large particles. Therefore, the following emissivity results should be treated as lower limits, in a conservative manner.

Results

Emissivities of a flame region at different soot yields are given in fig. F.2. The results are presented as a function of path length at two gas temperatures: 1000°C and 300°C respectively. As can be seen by comparing the two figures, emissivity depends strongly on the soot yield and path length at both ambient temperatures, but only very weakly on the temperature itself. The amount of excess air has also very strong effect on the emissivity. As the excess air dilutes the mixture, it is expected to have an opposite effect to increase in path length.

This intuitive result is shown to be true in fig. F.3, which shows the emissivity at a gas temperature of 800°C and various different soot yields. At each soot yield, the emissivities were calculated for a wide range of different L and η . When emissivities are plotted against the ratio L/η , the points corresponding to the same soot yield collapse to the same curve. So each curve of fig. F.3 is actually a family of curves calculated with different (L,η) -combinations. The emissivity of the flame, smoke plume or smoke layer can be found from the figure very easily, if the path length, excess air ratio and soot yield are specified.

A simple method to approximate the air excess ratio η is given in fig. F.4, where η/Z is plotted as function of $Z/Q^{2/5}$. The fire plume mass flow was calculated using Zukowski's and McCaffrey's fire plume models. The stoichiometric amount of air was taken to be $Q/3000$ kg/s, where Q is in kW. The applied normalisation of the height and heat release rate allows the representation of the plume variables with only one curve for all heat release/height combinations. The same curve also applies to the smoke layers, as the η -value inside the smoke layer is approximately the same as inside the smoke plume, at the height of the layer interface. The uncertainty of method is illustrated by the difference of the curves given by the two different plume models.

Example

A steel beam is heated by a 1.0MW heptane fire from below. What is the emissivity of the radiating flame, seen by the beam?

From fig. F.4 we can see that the height of the continuous flame is $0.08 \cdot 1000^{2/5} \text{ m} = 1.3 \text{ m}$ and the height of the intermittent flame region is $0.2 \cdot 1000^{2/5} \text{ m} = 3.2 \text{ m}$. The mean path length of the radiation is taken to be the average flame height, 2.2 m. Also from fig. F.4 we can see that inside the flame region an approximate value for η is 2.75 (using the average of the two curves). Assuming a 2% soot yield, the emissivity can be read from fig. F.3, giving the result $\varepsilon_f \approx 0.45$. The conservative approximation would be $\eta = 1$, which would give result $\varepsilon_f \approx 0.7$.

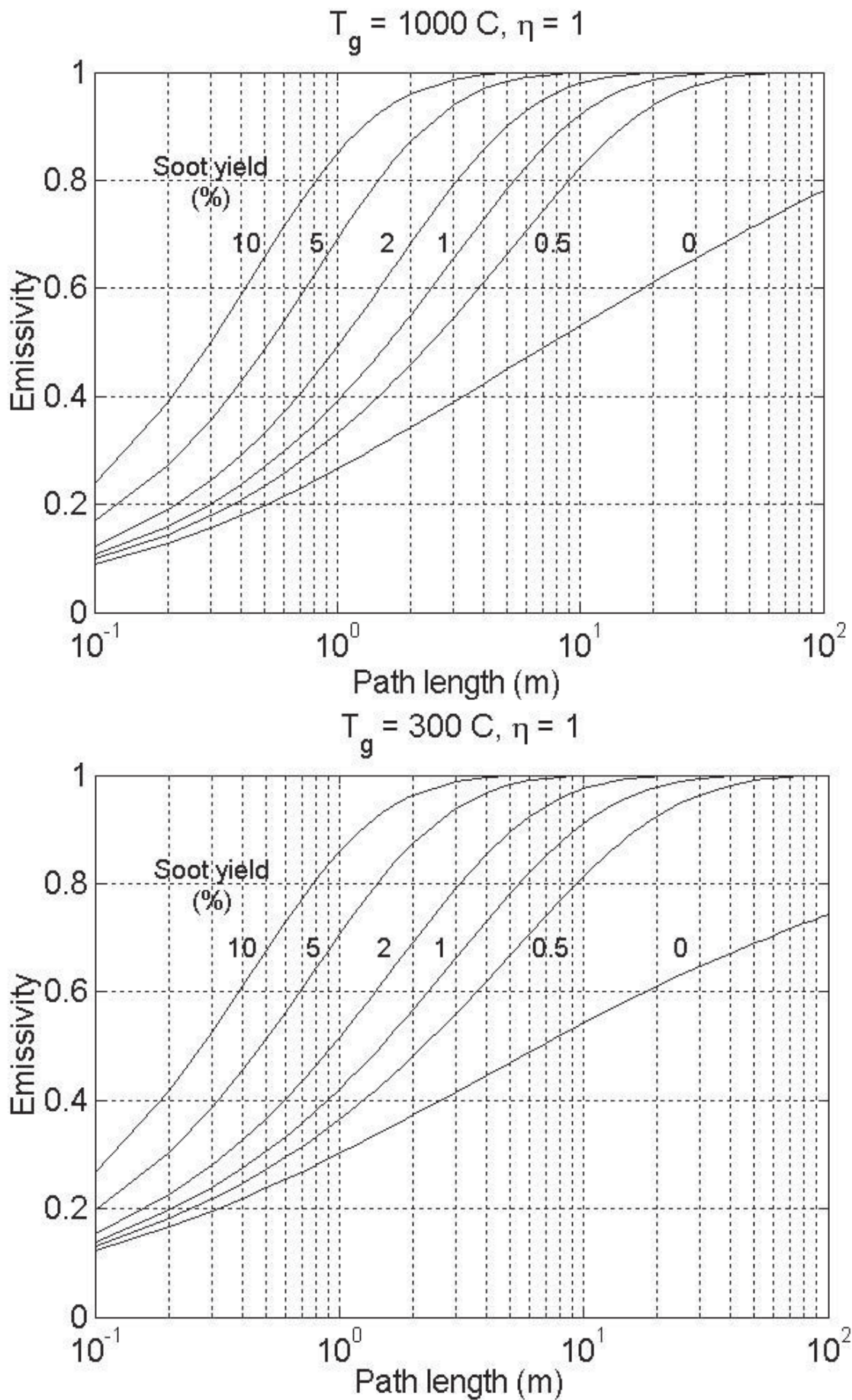


Figure F.2 – emissivity of a soot-gas mixture in reaction region, where $\eta \approx 1$; results are given for different soot yields and gas temperatures of 1000°C (top) and 300°C (bottom)

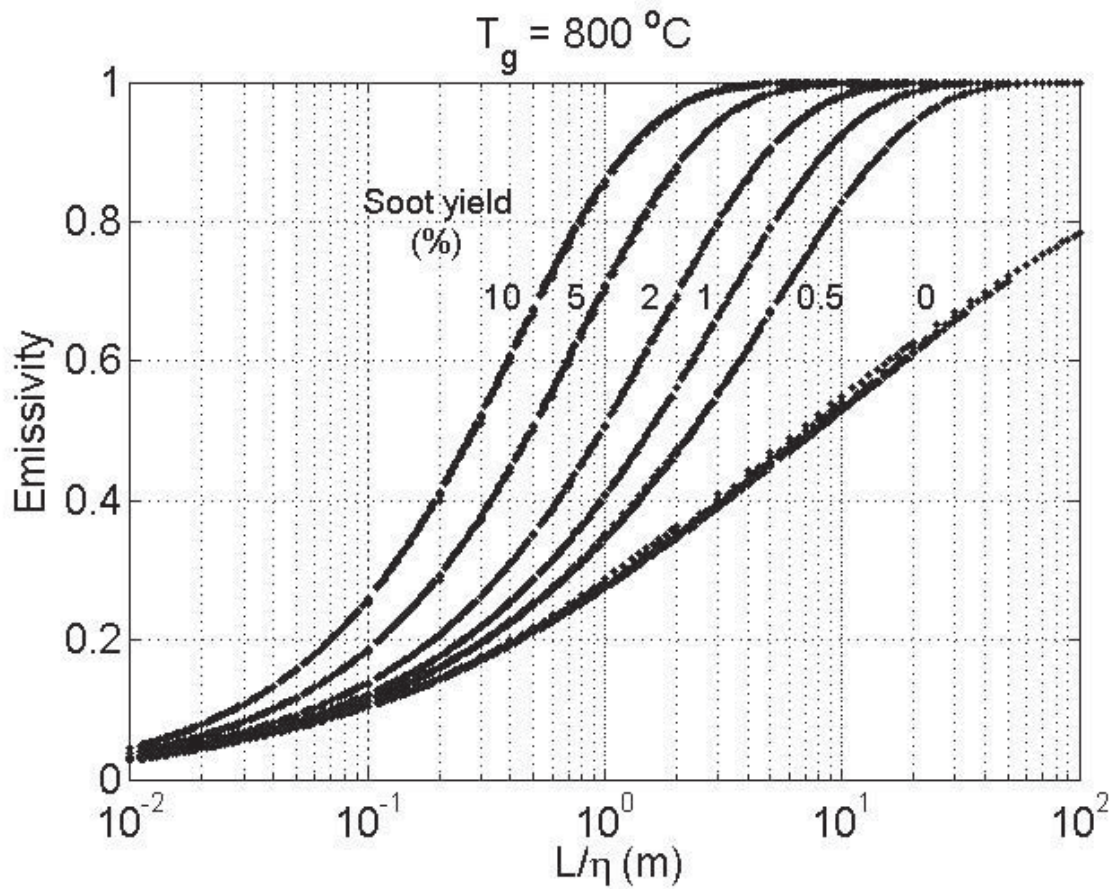


Figure F.3 – emissivity of the mixture of soot and combustion products at temperature of 800 °C, for different soot yields

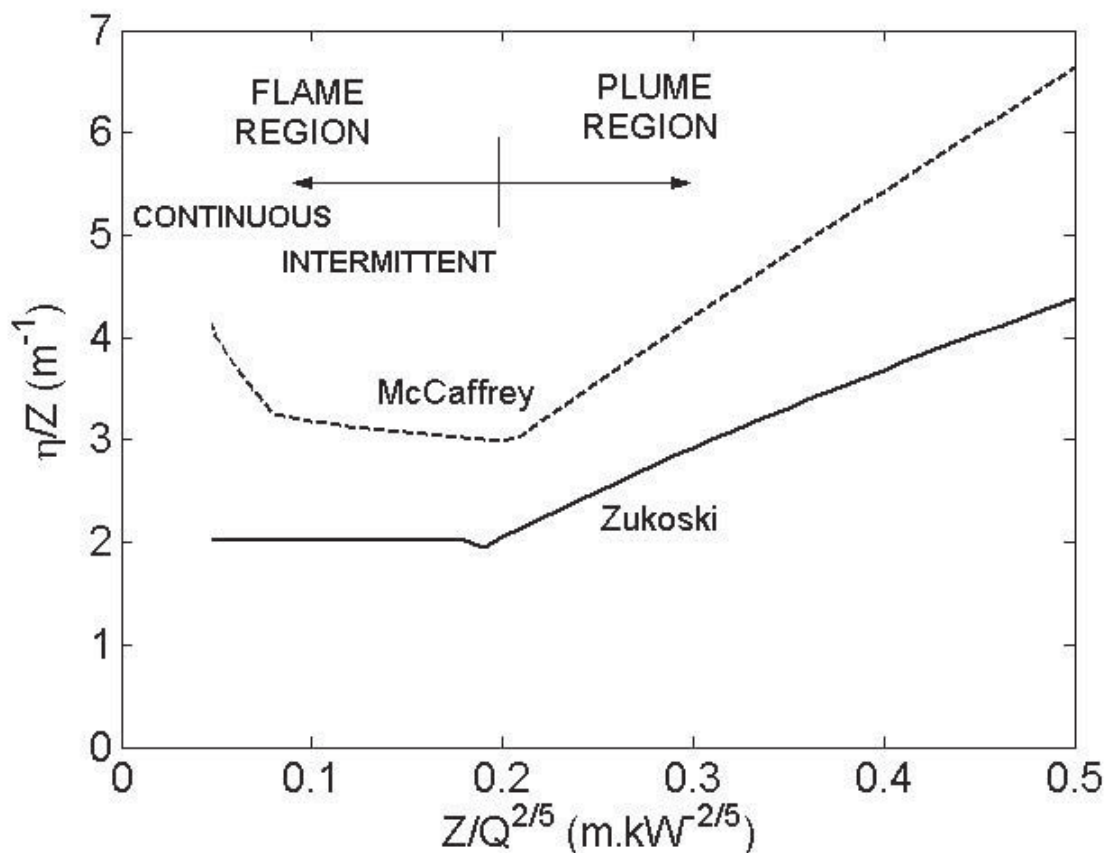


Figure F.4 – dependence of air excess factor η on the heat release rate and height

Member emissivity

More accurate information is sometimes available for a material or coating, together with its material and temperature dependence, and this can in principle be used in either the simplified or advanced models. However, if the member becomes blackened with soot deposits during the fire its emissivity will also tend to unity, and this provides a conservative upper bound value.

Configuration factor

This parameter is explicit in the simple equation for radiative heat transfer (equ. F.1 above) but is implicit in the CFD approach so no *direct* information can be obtained from the latter.

Procedures for determining the value of this parameter are described in *EC1 Annex G Configuration factor*. Distinctions are made between localised and fully-developed fires, i.e. the “position effect”, and also according to the geometry of the receiving object (convex or concave) due to “shadow effects”.

The first distinction is easy to understand, providing that the localised fire is not impinging on the member of interest and also that any influence of a hot layer is not significant. The latter distinction is more complex, as even for convex members there is generally an orientation effect, i.e. with a localised fire, only one aspect of the component is exposed to the fire. If the shape is not convex, e.g. the typical I- or H-beam, the computation becomes more complex and a local "shadow factor" must be accounted for (NB - this is not the same as the k_{shadow} parameter introduced in the main heat transfer equation (equ. 4.24) in EC3). Both the orientation and any local shielding should be taken into account explicitly in performing the overall heat transfer calculations.

Radiative transfer equation

The net radiative heat flux to a solid surface is defined as the sum of the incoming and outgoing radiative heat fluxes:

$$\dot{q}_{net,r} = \dot{q}_{in,r} - \dot{q}_{out,r} \quad (F.5)$$

In principle, the incoming radiation can be calculated by integrating the radiative transport equation (RTE) over the space seen by the surface element, and then integrating over all directions. Actually, this is what the CFD codes do.

In the Eurocode methodology, both integrals are simplified for practical reasons. The RTE integration over the space is replaced by assuming some emissivity and effective radiation temperature for the radiation source at each direction. This idea is illustrated in fig. F.6, which shows how solid angle $d\Omega$ has ϵ and T associated with it. If the radiating surface is perpendicular to the direction vector s and the reflections from other sources are neglected, the incoming radiative heat flux can now be written as:

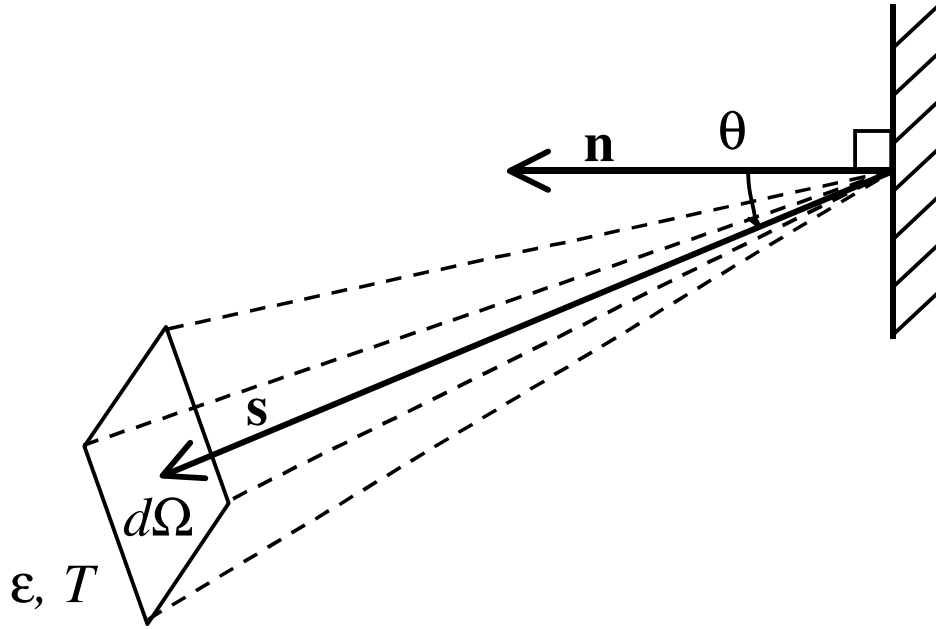


Figure F.5 – integration element of the solid angle

$$\dot{q}_{in,r}^{\&} = \epsilon_m \int_{2\pi} \epsilon(\Omega) \sigma T^4(\Omega) \frac{\cos(\theta)}{\pi} d\Omega \quad (\text{F.6})$$

where ϵ_m is the emissivity of the steel member, and θ is the angle between the wall normal n and direction vector s . In practice, the integral is calculated as a sum over the different radiation sources, and separate configuration factors are used for each source. Configuration factors are available in analytical form for many geometries. The formula for incoming radiation is:

$$\dot{q}_{in,r}^{\&} = \epsilon_m \sum_i \Phi_i \epsilon_i \sigma T_i^4 \quad (\text{F.7})$$

Typical radiation sources are fire, hot layer, walls, floors and openings. The outgoing radiative flux is simply:

$$\dot{q}_{out,r}^{\&} = \epsilon_m \sigma T_m^4 \quad (\text{F.8})$$

In Eurocode EN 1991-1-2, the formula for net radiative heat flux is (equ. 3.3):

$$\dot{q}_{net,r}^{\&} = \Phi \epsilon_m \epsilon_f \sigma (T_r^4 - T_m^4) \quad (\text{F.9})$$

where Φ is the configuration factor and T_r is the effective radiation temperature. The Eurocode also states that, for fully engulfed members, T_r may be represented by gas temperature T_g around the member. However, this equation contains two ambiguities: firstly, the fire configuration factor Φ and emissivity ϵ_f multiply both the incoming and outgoing terms. Secondly, there are no instructions how to take into account sources of radiation other than fire. A more accurate form of the Eurocode equ. 3.3 could be:

$$\dot{q}_{net,r}^{\&} = \epsilon_m \sum_i \Phi_i \epsilon_i \sigma T_i^4 - \epsilon_m \sigma T_m^4 \quad (\text{F.10})$$

For practical application, an even more simplified version can be obtained by using only two terms in the sum, representing "fire" and "the rest of the visible world". The properties of the surrounding space, not being part of the fire, are represented by emissivity ϵ_a and temperature T_a . Net radiative flux is now:

$$\dot{h}_{net,r}^{\&} = \Phi_f \epsilon_m \epsilon_f \sigma T_f^4 + (1 - \Phi_f) \epsilon_m \epsilon_a \sigma T_a^4 - \epsilon_m \sigma T_m^4 \quad (F.11)$$

The problem still remains as to what values should be used for ϵ_a and temperature T_a . However, reasonable estimates can be obtained even by assuming $\epsilon_a = 0$ and $T_a = 293$ K. This formula has no theoretical sources of uncertainty, unlike the Eurocodes equation, and the embedded assumptions are not hidden. The only, non-obvious, simplification is the neglect of the reflection sources.

It is very probable, that during a typical application of equ. F.9 (the Eurocode heat flux equation), T_r is simply represented by the fire temperature T_f , because other options have not been introduced or suggested. In this section we study the magnitude of the errors introduced by the two theoretical sources of uncertainty, explained in the previous section. The errors are studied in a practical situation, where the member is at a temperature of 100°C, and is heated by a relatively distant ($\Phi_f = 0.1$) fire, with a flame temperature of 900°C. For the analysis, we write:

$$\underbrace{\Phi_f \epsilon_m \epsilon_f \sigma (T_f^4 - T_m^4)}_{\text{Eurocode heat flux}} = \underbrace{\Phi_f \epsilon_m \epsilon_f \sigma T_f^4 + (1 - \Phi_f) \epsilon_m \epsilon_a \sigma T_a^4 - \epsilon_m \sigma T_m^4}_{\dot{h}_{net,r}^{\&}} + E \quad (F.12)$$

where E is the error of the Eurocode formula, defined as:

$$E \equiv (1 - \Phi_f \epsilon_f) \epsilon_m \sigma T_m^4 - (1 - \Phi_f) \epsilon_a \epsilon_m \sigma T_a^4 \quad (F.13)$$

Next, the magnitude of the relative error:

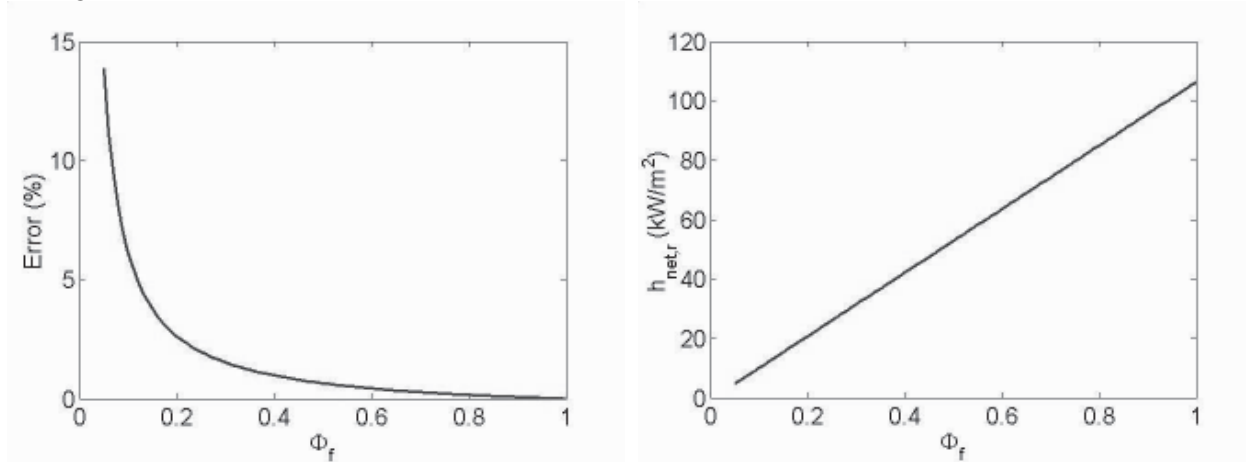
$$\text{Error (\%)} = 100 \cdot \frac{E}{\dot{h}_{net,r}^{\&}} \quad (F.14)$$

is calculated using the following parameter values:

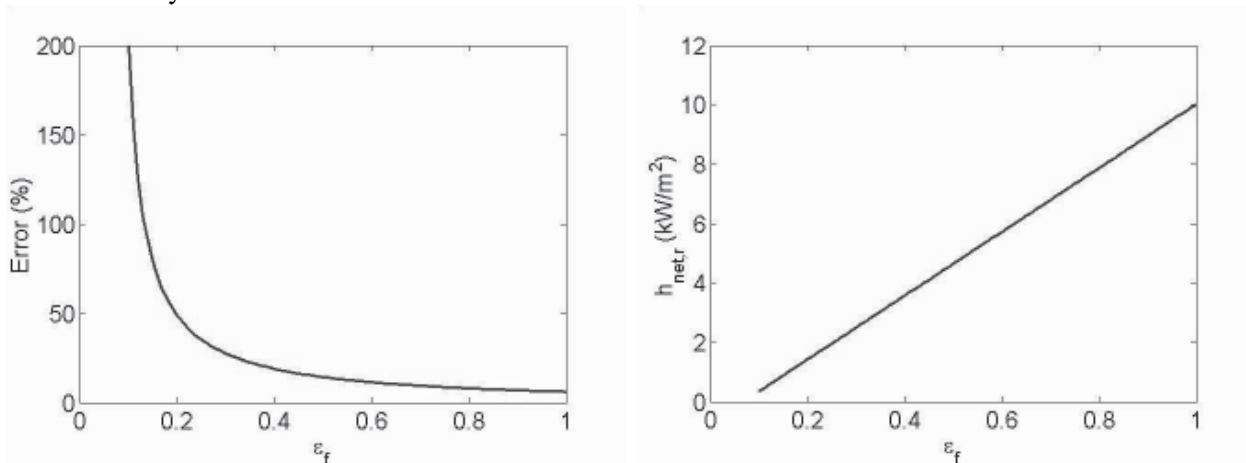
$\Phi_f = 0.1$	$T_f = 900 \text{ }^\circ\text{C}$
$\epsilon_f = 1$	$T_m = 100 \text{ }^\circ\text{C}$
$\epsilon_a = 1$	$T_a = 20 \text{ }^\circ\text{C}$

The effect of each parameter on the relative error is studied by varying each of them in turn within their typical ranges, keeping other parameters constant. The effects of the configuration factor and emissivities are shown in fig. F.6. The corresponding values of $\dot{h}_{net,r}^{\&}$ are shown on the right-hand side of the same figure.

Configuration factor



Fire emissivity



Ambient emissivity

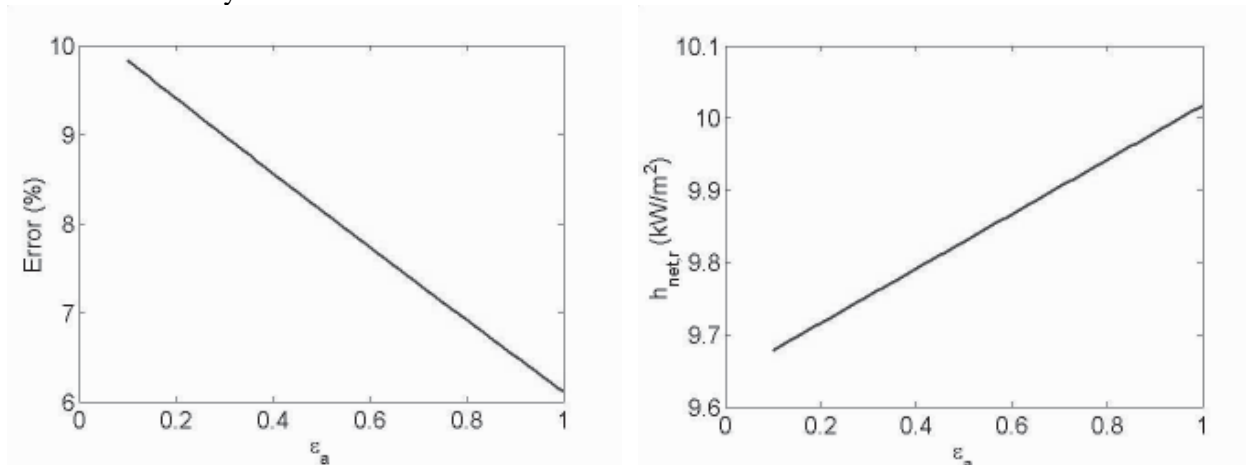
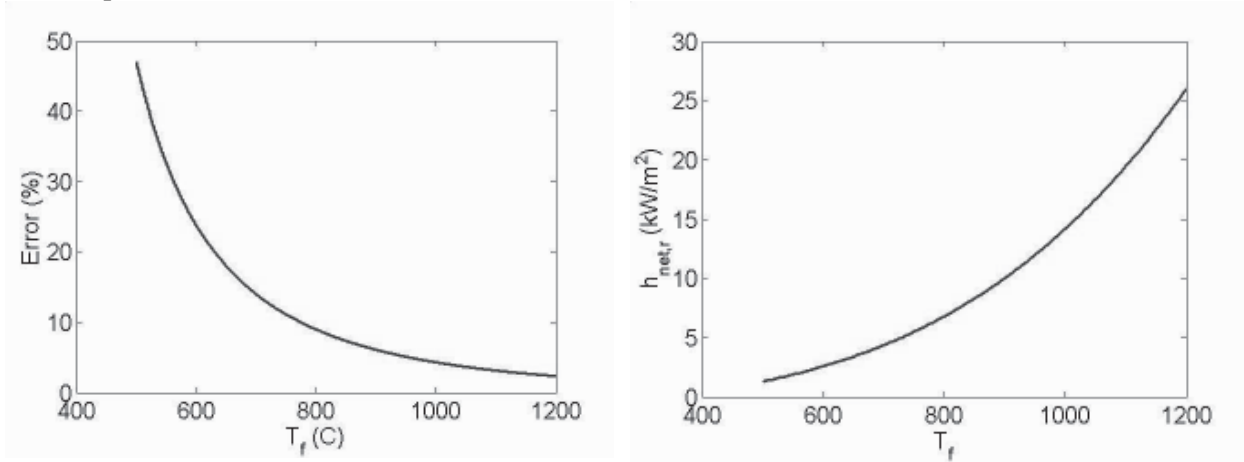


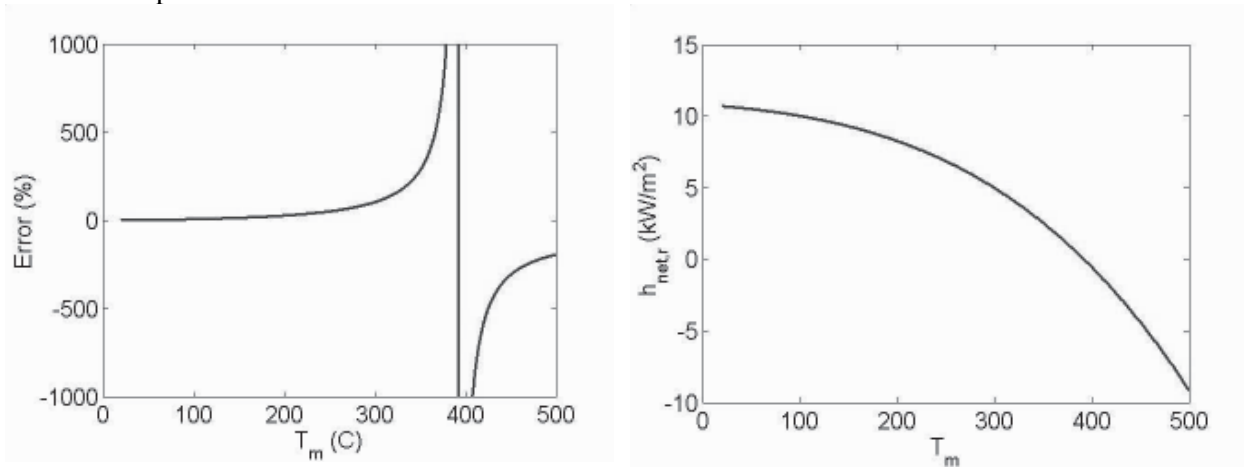
Figure F.6 – the effect of the radiation parameters Φ_f , ϵ_f and ϵ_a on the error in Eurocode equ. 3.3

The corresponding results for the temperature parameters are shown in fig. F.7. As can be seen, the error can be tens or even hundreds of percents under certain conditions. However, in some cases, such as for variation of the member temperature, the high relative errors are found when the denominator ($h_{net,r}$) goes to zero.

Fire temperature



Member temperature



Ambient temperature

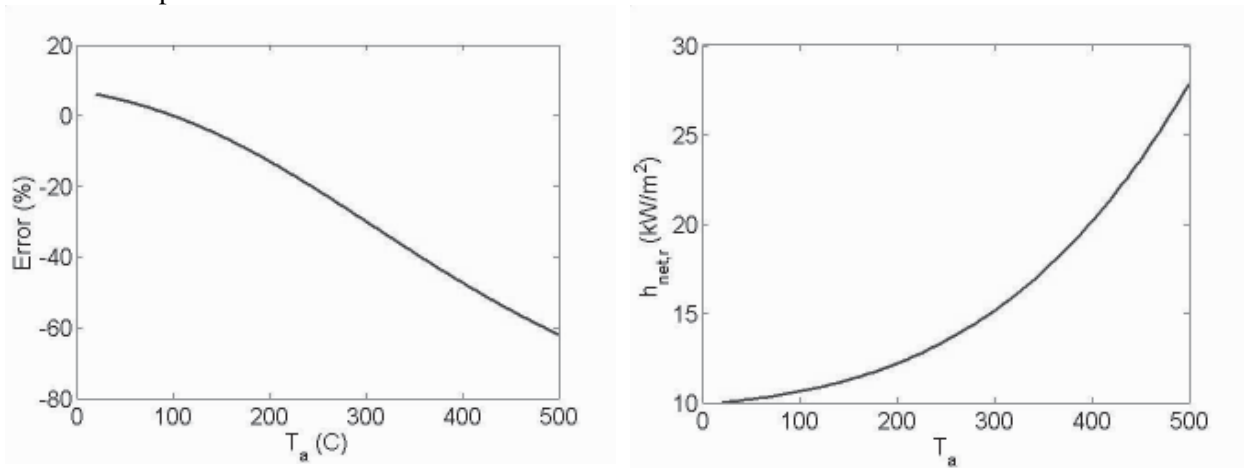


Figure F.7 – the effect of the radiation parameters T_f , T_m and T_a on the error in Eurocode equ. 3.3

Effective radiative temperature/flux

During the project some attention was given to the prediction of an “effective radiative temperature”. This field parameter is a measure of the effective temperature due to radiation which can be seen from any point and is derived simply from the relationship:

$$T_{rad} = \left(\frac{\dot{q}_{rad}}{\sigma} \right)^{1/4} \quad (F.15)$$

where: \dot{q}_{rad} is the total flux arriving at any point in space (automatically determined in a CFD code)
 σ is the Stefan-Boltzmann constant [5.67×10^{-8} W/m²/K⁴]

The effects of emissivity and spatial dependence via the configuration factor between the receiving body and each infinitesimal component of radiating mixture is automatically included within the flux term, \dot{q}_{rad} . Therefore, T_{rad} is a useful measure of thermal exposure severity for radiation-dominated flows, as it will reveal the distribution of the radiative heating impact. It has some parallels with measured thermocouple temperatures (see Appendix C), differing only in the convective term, so that there will normally be a good degree of correspondence between these two fields. Consistent with this observation is the fact that thermocouple temperatures will give a much better representation of thermal severities than gas temperatures.

Due to potential confusion with physical temperatures, it is not recommended that the radiative temperature parameter be routinely used for assessing thermal severities, due to potential confusion with gas temperatures. Whilst there will be significant regions of flow where the radiative temperatures greatly exceed the local gas temperatures, due to remote radiative heating, e.g. in a cold inflow through a doorway, there will also be regions within hot layers and flame plumes where radiative temperatures are actually lower due to the influence, in radiative transfer terms, of a cool surroundings, e.g. a cold layer or ambient environment. There is a clear danger for the latter condition in using radiative temperatures instead of gas temperatures, for example in a zone model, as the former are not conservative in terms of radiative heating.

There will however be circumstances where it is useful to exploit the predicted radiative flux field itself, i.e. the distribution of \dot{q}_{rad} . This parameter can be termed the effective radiative flux. Considerable attention was devoted to examining the accuracy and sensitivities of the flux distribution predictions during the course of this project, as described in Appendix B, section 2.1, and this information is normally directly accessible from a CFD code. The only weakness with CFD treatments is the need to apply smoothing when insufficient numerical rays had been adopted or could be afforded. When this “ray effect” is severe, some averaging may be required in order to determine realistic levels at all points in space.

Recommendations - CFD models

These recommendations are intended to provide some useful general guidance for running problems specifically concerned with structures in fire to those already familiar with the basics of the methodology.

The performance of CFD methodology depends on the proper description of physical and chemical processes combined with appropriate initial and boundary conditions, for the particular problem. For application to structural fire safety, it is essential that the model is able to provide a realistic treatment of the fire source and its interaction with its surroundings. Validation of fire models is vital for achieving confidence in their predictive capabilities.

In view of the complex nature of the modelling methodology, a critical analysis of the predicted results is essential to ensure that the results are used correctly for design purposes. This can be achieved by

checking that the important characteristics of the individual fire components are simulated realistically. The components characterising the fire behaviour are usually the same zones or sub-models used in the zone modelling approach, e.g., the fire source, the fire plume, the ceiling jet, upper hot layer, wall flows and vent flows.

For ensuring 'correct' use of CFD fire safety design and assessment, consideration should be given to various essential components, including the treatment of the 'fire science' together with fire/structural specific issues, the scope and method of attack on a particular problem, the physical and numerical models and the relevant validation.

The best practice guidance on these essential components, aimed at ensuring 'correct' use of CFD, is summarised below (see also references Kumar & Cox (2001), Cox & Kumar (2002)).

General fire science

1. Check that Q^* , the non-dimensional heat release rate, is representative of the fire of concern, where for buoyant fires $Q^* < 2.5$.
2. Account for radiative loss from the flaming region. A fire greater than 1 m in diameter will lose between 20% and 45% of its heat by radiation, the lower limit being for clean burning fuel such as methane and higher limit for a highly sooty fuel such as polystyrene.
3. Ensure that boundary heat losses are properly accounted for.
4. Predicted temperatures must be within physically expected limits (normally well below "adiabatic flame temperature").
5. Compare flame temperature, flame height, plume entrainment, upper layer temperature, ceiling jet properties, etc. with empirical correlations.

Fire/structural specific issues

Smoke

The concentration of smoke produced by a fire can have a big impact on the heat transfer to structural components. This is because the smoke particles take part in the radiative heat transfer, providing a source of radiant energy but also absorbing radiation. The amount of smoke produced depends on the fuel type and the ventilation levels, among other things. If it is likely to be important in a particular application, it should be included in the simulation. Within the scope of the current project a simple method for linking soot yields to fuel type was implemented, based on scaling from literature yield data [Tewarson, SFPE, 1988].

A conservative limit is often to assume a high soot concentration – which maximises heat loss – though it has been determined in this work that beyond a source soot mass fraction of 0.1 little further increase in radiative loss is produced for well-ventilated fires.

High-temperature material properties

In order to accurately predict heat loss into solid boundaries it is highly desirable to have accurate information available concerning the thermal properties of the participating solids. The main properties of relevance are the thermal conductivity and the specific heat. This information is often available at room temperature conditions but not for the sort of temperatures likely to be encountered during a fire. Therefore, particular effort might have to be made in order to address this problem.

A conservative limit on compartment temperatures can be produced by assuming adiabatic (no heat loss) boundaries, effectively defining them to be perfect insulators.

Moisture/intumescence

Materials containing moisture (e.g. concrete, plasterboard and many fire protection materials), or which are by nature intumescent, may exhibit greatly retarded conductive heat transfer due to the absorption of energy in the relevant phase change processes which occur under heating. These effects must be adequately represented in order to satisfactorily reproduce the thermal response.

Remote burning

Fires burn where air and fuel are able to mix in the right proportions. CFD codes employ combustion models to predict the location of this burning and under ventilation controlled conditions it may often be far removed from the actual fire source or the site of volatile release. This fact must always be taken into account where relevant and a combustion model must be used (rather than a simple heat source, as simpler option provided in some codes).

Fuel chemistry

It is a particular problem of fire engineering that real fires often involve combustion chemistry which is complex and poorly known (in contrast to many experimental fires for which pure fuels are often used). Since the nature of the combustion kinetics has important consequences for things like soot production and flame temperatures methods of tackling these problems are required.

Running simulations

Area of application

The overall scope of the problem must first be assessed. Is it a requirement to predict the effect of a localised fire on a single member, or a case where full engulfment of all relevant components is anticipated in a “post-flashover” scenario. This allows a decision about the required size of the computational domain.

Requirements/applicability

Determining how to tackle simulation of a particular fire is often a delicate balance between various requirements pulling in different directions.

1. First it must be decided if a transient simulation is required. This would normally be the case if steel temperatures are of interest, as quasi steady state information may be overly conservative. Taking into account also how long (real time) any transient simulation must be, the user ought to be able to work out how many cells they can afford (from past experience, or estimate provided by code itself). Given a domain size, it is then possible to determine the approximate cell size for a given number of cells. If this is too large then an alternative solution must be sought. One would normally look for a typical cell size of a half a metre or so, perhaps up to one metre in large domains, though finer cell divisions of the order of 0.1 m are necessary near solid boundaries and around objects of interest like the fires source (if localised).
2. If cells of sufficient resolution cannot be afforded, alternatives, such as reducing the size of the domain to be simulated, should be investigated. One option to reduce the overall size of the computational domain may be to investigate use of mirror symmetry boundaries. Savings can also be made by performing initial studies for the steady state conditions – in order to check the overall flowfield and convergence, before proceeding to a full transient simulation for the particular case of interest. Steady-state simulations usually provide a conservative bound on thermal exposures since they tend to overestimate wall temperatures, thereby reducing heat loss from a compartment.
3. A final point to consider here is the computation of the burning location. CFD codes with combustion models predict this on the basis of the calculated intermixing of fuel and air, together with information on turbulence parameters which affect the burning rate. In some cases the fire size will depend on the nature of the incoming airflows so that simple prescription of the fire is hazardous.

General procedure

In order to run CFD simulations a certain minimum amount of training is required. Nevertheless, there are a few helpful comments that can be made about the procedure in general, in order to best tackle particular problems.

The first general point is that in tackling a new problem an approach should be adopted whereby increasing complexity is added to the simulation progressively. For instance, it may be expedient to start with a steady state case and to omit entirely simulation of radiation, or wall heat transfer, in initial

simulations. Once the user is convinced that they have a good flowfield solution, they can switch to transient mode and add in the heat transfer factors, preferably one at once, by turning on the relevant physical models.

Regarding transient solutions, it may suffice to run a coarse simulation with large timesteps and relatively high threshold for convergence before running a very intense and long duration simulation in an attempt to produce better accuracy.

Regarding cell size, this should be progressively refined. However, it should be noted that when running problems in 3D the scope for refining grids in all three co-ordinate directions is rather limited as a two-fold increase in resolution in each direction yields an eight-fold increase in the number of cells. Sometimes it may be necessary to move in the other direction to a coarser grid in order to prove grid independence of a solution.

Similar considerations apply to selecting the number of DT rays. Computation costs soon become prohibitively expensive if ray numbers are doubled in both theta and phi directions simultaneously.

A final general point here is that there will often be a trade-off between accuracy and computation time. In order just to obtain a rough solution it may sometimes be necessary to make some compromises on the level of convergence enforced, but if accurate results are required all necessary requirements must be fulfilled.

Physical models

Combustion

It is recommended that for structural fire engineering a proper combustion mode (in RANS codes, eddy breakup or flamelet and in LES codes, flamesheet) should be used. This allows a proper coupling between local airflow and distributed heat release (unlike in the simple “heat source” model).

Radiation

Consideration should be given to the spectral dependency of the radiative transfers. More accurate results can be obtained by using “banded” models though there is a hierarchy of complexity here as explained in Appendix D of this document.

Consideration should also be given to the method used to determine the path length. Exact models are available but these have higher computational overheads than those which simply assume a single nominal value for the whole domain.

With the discrete transfer method (DTRM, Lockwood) ray number sensitivity must be examined. The minimum number of rays that can be used is 2×4 , but more is preferable.

Thermocouples

If comparisons are being made with experimental data then it is necessary to include a thermocouple simulation in the computer model. Though it might be possible to estimate heat fluxes and thereby correct back experimental values to gas temperatures this is a much more cumbersome and uncertain procedure than doing the reverse whereby the computed radiation field is used in the CFD code in order to determine a general “thermocouple temperature field”. If this feature is not available in a CFD code it should be added if possible.

Solid-phase heat transfer

If conjugate heat transfer is used in transient simulations, consideration should be given to the fact that large inaccuracies will result if the cells are not small compared to the thermal wave moving it to the material, as this must be adequately resolved if the wall temperature and heat loss is to be correctly described. In order to determine what size is “small” a engineering check should be made on the thermal penetration depth versus time. Thermal penetration depth is given simply by:

$$\delta \approx \frac{2}{\pi^{1/2}} \left(\frac{k_s t}{c_s \rho_s} \right)^{1/2} \quad (\text{F.16})$$

Numerical models

Grid

1. The most basic consideration here is that of grid resolution. This factor must never be overlooked and in theory a grid refinement study using at least three different grid resolutions should be performed - ideally by doubling the grid cells in all directions. For these buoyant flows special attention should be given to the vertical mesh spacing. In practice, this is a very demanding requirement but some attempt to examine sensitivity should always be made. The only exception might be problems which are very similar to cases for which grid independence has previously been shown with the code in question.
2. Resist the temptation to undertake two-dimensional simulations. These can provide physically misleading solutions. Think where the air entrained into the fire would come from if the problem were really two-dimensional.
3. Particular attention should be paid to those regions of interest where high accuracy is important, e.g. the fire plume and near any solid boundaries or openings in an enclosure.
4. Wherever possible aspect ratios should be maintained within a factor of 50. Change of cell size should be progressive, not sudden.

Interpolation schemes

It is likely that a first-order numerical differencing scheme would be used at least initially since it is stable, but if possible as convergence is approached use a second-order or higher-order scheme.

Pressure boundaries

Ensure that 'free' boundaries are chosen carefully. A free pressure boundary should be far enough from any ventilation openings not to affect flows through them (for example, in a simple room fire, this should at least be equal to the length of the room). Avoid steep pressure gradients near the free-pressure boundary and ensure that simulations are reasonably insensitive to the boundary position.

Timestep

In transient simulations, be sure that the time-step is adapted to the choice of the grid and check the influence of the time-step on the results. For a rapidly developing fire more iterations per time step are generally needed.

Convergence

1. Normalised mass and momentum continuity errors, and residual errors for all the solved variables should be less than about 0.01, preferably less than 0.001. In an ideal simulation the residuals will decrease steadily.
2. Examine convergence by following data, especially pressure, at critical locations (e.g., in the plume, in the hot layer and in ventilation openings). Monitor values should gradually settle down to their converged levels.
3. Global mass and heat balance should be better than about 95% in one or more analysis regions. One of these regions should encompass the entire enclosure or building.
4. Explore difficulties in achieving a steady-state solution by utilising transient simulations. There may be no steady solution if physical oscillation is present.

Validation

1. To ensure trust and confidence in the model predictions, model validation must always be undertaken by means of comparison of simulation results with test data for a case which is similar enough to the case of interest that there is no doubt that it is physically relevant.
2. Further checks can be made by means of empirical and theoretical engineering correlations, e.g. for flame height, entrainment, layer depth etc. Some of these might be best performed by using a zone model, provided that the basic assumptions underlying that particular modelling approach (normally that the flow can be effectively partitioned into one or two zones) are not violated.

Annex 1 – Technical Annex

TITLE: Natural Fire Safety Concept - The Development and Validation of a CFD-based Engineering Methodology for Evaluating Thermal Action on Steel and Composite Structures

AIMS

The overall objective of the proposed project is to develop an engineering methodology, exploiting the advanced capabilities of computational fluid dynamics (CFD), for determining the thermal behaviour of structural elements in steel/composite-framed buildings. Specific objectives of the project are as follows:

- To develop a verified CFD-based engineering methodology for simulating the thermal action on steel/composite structures,
- To apply the methodology for evaluating the effect of fire loading, ventilation and compartment construction on the thermal action on steel/composite structures,
- To identify the essential elements of the methodology developed and provide guidance on its 'correct' use, i.e. defining the range of applicability and the sensitivity to various input parameters,
- To apply the model for the assessment of the calibration and sensitivity of empirical design parameters, such as the convective heat transfer coefficient and safety factors used in the design guides (Eurocodes EC1 and EC3).
- To contribute to the development of the design guides.

DESCRIPTION OF WORK

The technique of computational fluid dynamics will be applied to develop a thermal model for evaluating the performance of steel/composite structures in natural fires. Model development will focus on the computation of convective and radiative heat transfer to the structural envelope and the refinement of description necessary in both the gas phase and solid boundaries - for example, radiative properties of the participating gas-phase medium including particulate soot and combustion products, the necessary spatial grid resolution in the solution for radiative exchange and the treatment of turbulent heat transfer to the compartment boundaries. Key numerical sensitivities of the model will be determined by means of sensitivity studies and the effect of the interaction between the gas and solid-phases will be studied.

A progressive model verification exercise is proposed. This will involve simulation of steel behaviour in fire tests for which experimental data is available - a localised beam fire test, standard fire-resistance furnace tests and full-scale tests involving natural fires. The methodology will also be compared with the alternative zonal calculation method (OZone) developed in the previous ECSC programme for evaluating the standard fire-resistance test with real fire exposure conditions. In addition, use of alternative zone models will be examined.

The predicted data from the model will be used to determine equivalent values for the convective heat transfer coefficient, resultant emissivities and other empirical factors used in heat transfer calculations. Detailed assessment of the results will then be made to identify the critical design parameters affecting the thermal action on the steel/composite structures.

The procedures set out in the Eurocodes will be reviewed in the light of the CFD predictions. Recommendations will be made on improvements to the parameters used in the standards procedure and/or extension of the methodology as necessary.

WAYS AND MEANS

Project co-ordination will be undertaken by BRE.

In the model development phase, an existing fire-specific CFD code will be further developed in those areas which are deemed necessary for application to prediction of the thermal response of structural elements in steel/composite framed buildings. Where necessary additional material property information will be incorporated into the model. At each stage of the model development, internal verification will be undertaken as a matter of course. The application and performance of the models developed will be undertaken by means of sensitivity studies.

In the model verification stage, test data will be collated for each of the three classes of test case identified and, where necessary, data processing will be undertaken. Simulation results will be carefully compared to the experimental results, permitting identification of the key model dependencies and critical parameters in use of the model. The results will also be compared with those available from the alternative zonal calculation methods. Further test cases will be studied as necessary.

The model results will be used to determine equivalent values for heat transfer parameters and identify critical design parameters. Consequently, the implication of the results will be assessed and recommendations made regarding both the methodology developed and the design codes methodologies.

PROGRAMME BAR CHART

Tasks, partner assignment, duration		1999-2000		2000-2001		2001-2002	
Work package	Partner (man months)	1st semester	2nd semester	3rd semester	4th semester	5th semester	6th semester
Work package 0 Administration	BRE 4	[shaded bar]		[shaded bar]		[shaded bar]	
Work package 1 Model development	BRE 12	[shaded bar]					
Work package 2 Model validation	BRE 12 ARBED 11 LABEIN 11 VTT 5 AGB 7			[shaded bar]			
Work package 3 Analysis and review	BRE 4 LABEIN 5 VTT 6					[shaded bar]	
Work package 4 Implications of the results	BRE 3 ARBED 8 VTT 2 AGB 2					[shaded bar]	
Work package 5 Information dissemination	BRE 1 ARBED 1 LABEIN 1 VTT 1 AGB 1					[shaded bar]	

The results of the project will be the subject of a publication in the "Technical Steel Research" series. The research described above will be placed in the area covered by the Executive Committee (or the Expert Group): F6

Contents

FINAL SUMMARY	3
Objectives of the project	3
Comparison of planned activities and work accomplished	4
Description of activities and discussion	5
1. Model development	5
2. Model validation	5
3. Analysis and review	6
3.1 Supplementary cases of model application	7
3.2 Results analysis: equivalent parameter values	7
3.3 Results analysis: critical design parameters	8
4. Implications of the results – impact assessment on the Eurocodes	8
4.1 Review of Eurocodes methodology	8
4.2 Recommendations and extension to Eurocodes methodology	8
5. Information dissemination	10
Conclusions	11
Assessment of exploitation and impact of the research results	13
Nomenclature	15
Glossary	17
List of figures and tables	19
References	23
APPENDICES – Scientific and Technical Description of the Results	25
Appendix A – Technical background	27
Zone models	27
CFD models	27
Zone model OZone	28
Zone model MRFC	31
CFD model SOFIE	31
Radiation model	32
<i>Radiation model fundamentals</i>	33
<i>Discretization scheme</i>	35
<i>Radiation transfer equation (RTE) solution</i>	37
CFD model JASMINE	38
Appendix B – Model development	39
STELA Composite solid solver	39
JOSEFINE Graphical User Interface (GUI)	40
Appendix C – Thermocouple temperatures	45
Theory	45
Thermocouple model	47
Appendix D – Model validation	49
Localised beam fire tests (BRI beam fire test)	49
Experimental details	49
CFD simulations with SOFIE	51
Fire-resistance furnace tests (VTT scale furnace; Standard fire-resistance furnace)	62
VTT scale furnace	62
<i>Experimental details</i>	62
<i>CFD simulations with SOFIE</i>	62
<i>Boundary conditions</i>	64
<i>Steel columns</i>	64
<i>Simulations results - gas phase</i>	66
<i>Simulations results - solid phase</i>	67
Standard fire-resistance test furnace	68
Large room & large compartment fire tests (VTT large room; BRE large compartment)	74
VTT large room fire tests	74
<i>Experimental details</i>	74

<i>Fire source</i>	75
<i>Instrumentation</i>	77
<i>Zone model simulations with Ozone and MRFC</i>	79
<i>CFD simulations with SOFIE</i>	90
BRE large compartment fire tests	96
<i>Experimental details</i>	96
<i>Ozone simulation results</i>	103
<i>MRFC simulation results</i>	103
<i>SOFIE simulation results - test 8 (front opening only)</i>	105
<i>SOFIE simulation results - test 6 (front and rear openings)</i>	112
<i>Discussion</i>	114
<i>Soot loading</i>	115
Supplementary cases of model validation	118
Appendix E – Analysis and review	125
Supplementary cases of model application	125
Results analysis: equivalent parameter values	125
Results analysis: critical design parameters	127
Appendix F – Impact assessment	127
Review of Eurocodes procedures	127
Recommendations - simplified models	127
Comments on Eurocode guidance for simplified models	127
Heat transfer coefficient	127
Gas-phase emissivities	128
<i>Computation method</i>	129
<i>Calculations</i>	130
<i>Example</i>	130
Member emissivity	133
Configuration factor	133
Radiative transfer equation (RTE)	133
Effective radiative temperature/flux	138
Recommendations - CFD models	138
General fire science	139
Fire/structural specific issues	139
<i>Smoke</i>	139
<i>High-temperature material properties</i>	139
<i>Moisture/intumescence</i>	139
<i>Remote burning</i>	140
<i>Fuel chemistry</i>	140
Running simulations	140
<i>Area of application</i>	140
<i>Requirements/applicability</i>	140
<i>General procedure</i>	140
Physical models	141
<i>Combustion</i>	141
<i>Radiation</i>	141
<i>Thermocouples</i>	141
<i>Solid-phase heat transfer</i>	141
Numerical models	142
<i>Grid</i>	142
<i>Interpolation schemes</i>	142
<i>Pressure boundaries</i>	142
<i>Timestep</i>	142
<i>Convergence</i>	142
Validation	143
Annex 1 – Technical Annex	145

European Commission

EUR 21444 — Steel products and applications for building, construction and industry
**Natural fire safety concept — The development and validation of a
CFD-based engineering methodology for evaluating thermal action on steel
and composite structures**

*S. Kumar, S. Welch, S. Miles, L.-G. Cajot, M. Haller, M. Ojanguren, J. Barco, S. Hostikka,
U. Max, A. Röhrle*

Luxembourg: Office for Official Publications of the European Communities

2005 — 150 pp. — 21 x 29.7 cm

Technical steel research series

ISBN 92-894-9594-4

Price (excluding VAT) in Luxembourg: EUR 25